IMPERIAL COLLEGE OF SCIENCE TECHNOLOGY AND MEDICINE

University of London

THE PROPAGATION OF LAMB WAVES THROUGH METALLIC AIRCRAFT FUSELAGE STRUCTURE

by

Roger P. Dalton

A thesis submitted to the University of London for the degree of

Doctor of Philosophy

Department of Mechanical Engineering

Imperial College of Science Technology and Medicine

London SW7 2BX

January 2000

Abstract

Owing to their unique potential for long-range, in-plane propagation through thin plates, guided waves seem to offer an obvious solution in the development of an on-board structural health-monitoring (SHM) system, to provide assurance of structural integrity for ageing metallic aircraft. This thesis evaluates the potential of guided waves for this application, by focusing on their propagation through the fuselage structure.

The fuselage structure of all semi-monocoque aircraft is characterised by a number of simplified structural features and the acoustic properties of constituent materials are measured, enabling dispersion curves of the associated waveguide systems to be plotted. Dispersion predictions, supported by experiments, are used to identify the most promising modes in each of the structural features. For joints where dispersion curves cannot adequately describe the mode interaction with the discontinuous geometry, dynamic finite-element modelling is employed and model predictions are also validated by experiment.

The investigation found that the simple, painted and tapering skin presents little problem for long-range propagation, providing dispersion is avoided. The application of sealant layers, however, causes severe damping of virtually all modes, except at very low frequencies. The transmission efficiency of modes across joints was found to be critically dependent upon the behaviour of 'carrier modes' in the overlap region. For narrow joints, including aircraft stringers, the sensitivity of carrier-mode interference to joint parameters effectively prevented propagation across a succession of joints, though excellent transmission across a single joint was demonstrated. Active SHM systems, requiring long-range propagation, are therefore not considered viable, owing to the high density of structural features. A brief study of the modal characteristics of acoustic emission employing numerical predictions and experiments, utilising simulated AE signals, found that AE signals are not impeded by twinned carrier-mode interference, owing to their low frequency. As a result of this work possible improvement of current AE defect location methods is suggested.

Acknowledgements

I would like to thank my supervisors, Prof. Peter Cawley and Dr. Mike Lowe for their guidance and support throughout this project and I especially wish to acknowledge the judgement, encouragement and patience of Prof. Cawley, to whom I am deeply indebted.

For all their generous advice, assistance and companionship, I also thank my colleagues in the Non-Destructive testing group at Imperial College. I particularly appreciate the efforts of Dr Brian Pavlakovic who wrote the excellent software that has supported both my work and that of the rest of the group. I should also like to thank a former colleague, Dave Haddock of RAF Brize Norton, who provided numerous skin samples, finished in various aircraft paint schemes, and the members of RAF NDT Squadron for their advice and for providing samples of aircraft fuselage structure.

This work was funded by the Department of Trade and Industry (DTI) and managed by the Defence Evaluation and Research Agency (DERA) under the Civil Aircraft Research and Technology Demonstration (CARAD) programme.

Finally, I want to thank my family for their enduring patience and encouragement and in particular my wife, Sue, for her reassurance and inspiration.

Contents

Appendix A.

Appendix B.

References

List of figures

List of Tables

1. Introduction and overview

1.1 Background

1.1.1 Smart Structure

A fully automated onboard system to monitor the structural health of an aircraft has the potential to reduce operating costs, increase flight safety, and improve aircraft availability and, in the case of military aircraft, improve survivability. It is not surprising therefore, that considerable effort is currently being focused on the development of such a system.

In the aircraft of the future this health-monitoring system may be linked with developing integrated actuators (Chopra (1996)), designed to effect changes in the skin profile and thus a means of flight control. An inductive method of powering and interrogating low profile sensors embedded in composite structure has been demonstrated by Spillman and Durkee (1994) and a skin containing integrated actuators and embedded sensors might form what is fashionably called a ‘Smart Structure’ or even a ‘Smart Material’. Considerable controversy has arisen over the use of these terms, which have been used increasingly to cover a very broad range of loosely related work in many disciplines, since the late 1980’s. A review of work on ‘Smart Structures’ can be found for example in Culshaw (1996). Despite the efforts of many such as Ghandi and Thompson (1992) and more recently Spillman, *et al.* (1996), there is as yet no agreed definition. Although sensor technology is well advanced and it is claimed that data transport and computer technology is already sufficiently developed to meet this task [Culshaw (1996)], actuator technology significantly lags the progress on sensory systems. A review of the state of the art of so-called smart actuator technology can be found in Chopra (1996). It is unlikely that a fully adaptive smart structure will see service for many years, but such systems are not only required for future aircraft design. A closer examination of aircraft design policy and particularly the current provision for structural health monitoring will reveal the urgent need for a reliable automated system that can be retro-fitted to ageing aircraft.

1.1.2 Aircraft Design Philosophy and Structural Health Monitoring of Ageing Aircraft

As the cost of assuring the airworthiness of ageing aircraft fleets spirals, there is perhaps a more pressing need for a simple sensory system to monitor the progress of damage in these aircraft. Such damage primarily consists of cracks, corrosion and disbonding, but could also include scores, loose rivets and in the case of military aircraft battle damage. Most aircraft now in service were designed under the ‘fail-safe’ or ‘damage-tolerant’ design. Fail-safe design superseded the ‘safe-life’ design philosophy in the 1950’s following the Comet disasters [HMSO (1955)]. Under the safe-life policy the expected period of defect free operation would be calculated for each component of the structure. This was termed its ‘life’ and the component was replaced on life expiry. This philosophy was flawed for three main reasons:

- It hinged on the accurate calculation of life. This was far from an exact calculation and was unable to account for variations in operating environment and loading.

- It took no account of incidental damage that might occur during, for example, routine maintenance.

- It was costly, particularly since apparently flawless components were replaced at the end of their life.

Fail-safe design recognised that defects in the structure were inevitable and aimed to mitigate their effect. The essential characteristics of fail-safe design are:

- Low design stress levels.

- Slow crack propagation rates.

- High fracture toughness materials - In particular the new fatigue resistant aluminium/copper/manganese alloys replaced the stronger, but less resistant, aluminium/zinc alloys.

- Crack arrest features.

- Redundant load paths - The aircraft had to be shown to be capable of recovery and landing following the failure of any single structural component.

- Structural health monitoring - Structural inspection was essential to identify defects in order that remedial maintenance could be undertaken before flaws reached critical size.

Fail-safe design can be very robust, as is testified for example by the passengers of Aloha Airlines flight 243, which landed safely after a large section of the upper fuselage was lost in flight (NTSB (1989)). This single incident in 1988 precipitated much of the recent research in the field of aircraft NDE. In this case the structural health-monitoring system, which is a corner stone of the design policy, clearly failed and the passengers were extremely lucky. The National Transport Safety Board identified several factors that contributed to the incident, in particular:

- Numerous small cracks emanating from the fasteners in the main fuselage lap joints that run the length of the fuselage were found and it was the very rapid joining of these cracks that resulted in loss of the upper fuselage section.

- The aircraft had not been operated as the designers had anticipated and it had accumulated a much higher ratio of cabin pressurisation cycles to flying hours than the servicing policy allowed for.

Currently, structural health monitoring is primarily based on visual inspection. Spencer (1996) reports that in recent experiments conducted by the FAA, the success of visual inspection was found to be highly variable, depending very much on the experience of the inspector and other factors such as the conditions under which the inspection is carried out. Experienced inspectors located between 44% and 69% of the sample defect set. In order to allow for the possibility of inspectors failing to find a defect, the structurally significant components are first identified and the critical defect size calculated for each. An estimation of the time taken for a defect to grow from the minimum visually detectable size, to the critical size is then made and this is divided by three to give the inspection periodicity. Thus the inspection program has three chances of finding a defect before the component fails. NDT is employed only when the minimum visually detectable size is found to be greater than the critical size or if the determined inspection period is too short for practical purposes. NDT techniques effectively reduce the minimum detectable size.

The problem with this policy lies firstly in the estimates of fatigue growth rate and secondly in the cost of visual inspection and current NDT techniques, in terms of both man hours and aircraft down-time. Despite recent advances in the field of fracture mechanics, little progress has been made on the calculation of fatigue crack growth rate under in-service conditions. These conditions are characterised by random loads of variable amplitude, frequency and level under varying environmental conditions. At least to some extent the estimation of crack growth rate required for damage tolerant design is more robust than the crude cumulative damage methods employed under the safe-life policy. This is because no calculation of the time for defect initiation and its growth to the minimum detectable size is required. The initiation time is exceedingly difficult to predict accurately and the early growth/time dependence is non-linear. Like the safe-life calculations however, the growth rate calculations are highly dependent upon the complex effects of the loading regime and environmental conditions. Apart from the predictable loads due to flight manoeuvres and the ground/air/ground cycle which, in the case of the fuselage includes, pressurisation, landing, and take-off loads, one has to calculate the significant effect of gusts that primarily impose bending loads on the fuselage. These have traditionally relied upon data collected from gust recorders carried on sub-sonic aircraft, flying various routes during 1950’s and early 1960’s (ESDU (1969)). The reliability of this data, which is expressed in terms of gust frequency (the number of gusts of a given velocity per 1000 gusts of a standard velocity) and gust exceedance (the number of gusts having a velocity greater than or equal to a given velocity encountered per kilometre of flight), is dubious to say the least.

To make matters worse, this data is used in conjunction with the expected flight profile of the aircraft. Unfortunately, although the aircraft operators pledge to operate the aircraft in a particular way (For aircraft certified in the UK, this is specified in a document called the

'Statement of Operating Intent'), the changing demands of passenger travel and commercial pressure means that this can be compromised. This was the case with the Aloha Airlines 737 which had been operated on short flights between the Hawaiian islands, rather than on long-haul flights assumed by the servicing policy. The flight profiles of military aircraft are even more difficult to anticipate accurately.

1.1.3 Global Structural Health Monitoring

1.1.3.1 System Requirements

The need for a reliable, automated system of structural health monitoring has been shown but there are many possible approaches for such a system and a number of peripheral issues have still to be considered:

- What defects must the system sense and what will be the required sensitivity and resolution?
- Is the entire structure to be monitored or just the structurally significant areas?
- Will the system operate in flight or just as a built-in test system for use by maintenance staff?

Ideally the system would be capable of monitoring the entire aircraft structure and this global approach was the one taken by the Federal Aviation Authority (FAA) following the NTSB's report on the Aloha accident. The report recommended that the FAA "assume the lead role in encouraging further research of advanced and automated inspection equipment for the development of improved economical state-of-the-art methods which minimise human performance inadequacies".

The variation in aircraft performance and usage together with the complexity of aircraft structural design makes the task of defining general specifications for a structural health-monitoring system (SHMS) very difficult. However, under the American Joint Air Force contract: 'Smart Structures Concept Requirements' (SSCORE) an attempt was made by

Northrop corporation to outline some basic system requirements for military aircraft Kudva, *et al.* (1994) . A global system was envisaged with rugged, reliable sensors, capable of detecting cracks of 0.05 inches in length (~ 1.25 mm) in geometrically complex locations, close to fastener holes, apertures and sharp edges. The system should also detect corrosion and skin stiffener separation, though no limits are given for these. The skin temperature range for a Mach 2 military aircraft is specified as -65°F to 375°F (-54°C to 191 °C), thus defining the operating temperature range. The SSCORE requirements also indicate the need to monitor loads and stresses so that real time growth rate calculations can be made to estimate the time remaining before a flaw becomes critical. Finally the system should feature the following:

- Minimum maintenance,
- Redundancy and fail-safe operation,
- Use of standard aircraft power supplies,
- Easy installation and modification
- No interference with other on-board systems.

A number of further considerations are highlighted in a more general review of the problem of aircraft structural health monitoring not directly concerned with an integrated system [Smith (1996)]. In general the system must be capable of coping with the following features which provide difficulty for current techniques:

- Multiple layers of dissimilar material. The system must be capable of detecting flaws in the sub-layers.
- Tapering thickness material.

- Inconsistent geometry and material. The system should be able to cope with inconsistencies introduced by repairs where component geometry and material may not conform to those of adjacent components.
- Complex geometry. In particular the system should be capable of detecting cracks in poorly shaped fastener holes and in components with short hole-to-edge distances.

In defining a reasonable limit for the detection of multi-site damage, the FAA argues that if cracks could be detected before they emerge from beneath the rivet head, then failure due to crack linking is very unlikely. Perhaps more importantly, since repair manuals allow for the over-sizing of rivets, cracks that are discovered before they reach a length of 0.03 inches (0.762mm) are repairable simply and cheaply by over-sizing. These are very demanding limits for crack detection in a global health-monitoring system.

The FAA considers that aircraft can operate safely with skin thinning of up to 10%. This might reasonably constitute a limiting specification for the detection of corrosion. However, in the author's experience the acceptable damage limit for skin thinning in UK military aircraft given in the Structural Repair Manual is generally found to be 5%.

Disbonding in the skin joints is identified as a problem area, since loads transferred to the fasteners often cause failure. In such riveted adhesive joints, disbonding over an area covering more than 5% of the rivets in any continuous load path should be detectable, particularly where disbonds extend to the skin edges.

1.1.3.2 The development of Structural Health Monitoring of Aircraft

The infamous Aloha incident in 1988 caused widespread concern over the structural integrity of ageing aircraft, particularly with respect to multi-site fatigue damage in lap joints. Since then a great deal of research effort has been directed to improving and developing non-destructive evaluation techniques to meet this problem. Only a small proportion of this work was concerned with development of an integrated system, though so called wide-area or large-area techniques may be closely related. These include thermal wave imaging [Han, *et al.* (1997)], laser shearography [Hagemaier (1991)], and optical holographic methods [Schubert, *et al.* (1997)], which have all entered service in one form or another. These systems, which currently rely on remote imaging of the skin surface, usually the external surface, are not suitable methods for development into an integrated system, though they can claim to have significantly reduced inspection time and maintenance costs.

Of the relatively few methods that are contenders for implementation into an integrated health-monitoring system, acoustic emission (AE) is probably the most developed. Commercial AE systems that are not permanently fitted, but are nevertheless designed to monitor the entire fuselage of a small airliner, have been available since the late nineteen eighties [Carlyle (1989)]. One of these, featuring some 300 channels, was used by the RAF to provide structural integrity assurance of the VC10 aircraft fuselage during proof pressure testing [Odell (1991)]. AE is closely related to the work of this project, since it effectively excites low frequency guided modes in the aircraft structure. This will be discussed more fully in chapter 6. Despite the use of AE for non-destructive testing over many years, researchers in this field largely ignored the modal aspects of AE data. Recently however, AE has been placed on a more scientific footing with the consideration of AE event signals in terms of propagating guided modes, in what is now generally called 'modal acoustic emission' Gorman (1991). Despite these advances however, the considerable problem of noise has still to be overcome. This continues to cause difficulties, even in systems used during ground maintenance, where it takes the form of signals from, for example, chaffing and rubbing of components, air leaks and dust or rain driven against the skin. Many more sources would arise in a flying system and some means must be found to filter the required event signals.

Another contender is the detection of defects from changes in the modal vibration or resonance characteristics of a structure. A prototype system described by Hickman (1991) featured a 50" dummy section of wing leading edge, comprising skin and support structure, that was fitted to the wing of a Twin Otter aircraft. Pattern recognition software was trained to recognise cracks and loose rivets from the signals received by eight piezoelectric sensors (2 per panel) and a success rate of 100% was claimed for the different defect configurations tested in flight trials when the system was excited by an electromagnetic coil transducer. The results were less encouraging when the system was naturally excited by noise, because aircraft noise has a limited bandwidth that does not excite the higher structure modes required for accurate defect characterisation. The problem with such a system and the many other systems that rely on neural networks and pattern recognition software, is the need for training to provide a database of defect characteristics. In the tests described, three crack defects and three rivet failure defects were introduced, but the permutations of all the possible defects and worse still combinations of defects, is limitless and seems to suggest that a very large or perhaps infinite training data set is required. Obtaining good quality training data presents another difficult problem.

Spillman and others believe that optical methods offer the best means of implementing global health monitoring of aircraft, and will probably prove the most suitable for fully adaptive smart structure. Such a system would sense damage indirectly through an incidental parameter such as strain. In his review paper Spillman (1996) describes how optical strain sensors can be configured to provide point measurements using single or multimode optical fibres by means of Bragg gratings or Fabry-Perot techniques. Signals from these sensors can be multiplexed in the fibre optic channel to delineate the sensing region. Alternatively long gauge-length sensors can be created using Michelson Interferometry. Optical methods offer a number of important inherent advantages over most other methods:

- Wide bandwidth allowing multiplexing of more signal channels.

- Safe power transmission with virtually no loss.

- Freedom from the effects of electromagnetic radiation, (which is of particular concern in military aircraft).

- Optical fibres can be easily introduced into fibre composite materials without degrading structural performance.

However, optical systems do suffer some drawbacks, not least the problem of temperature/strain crosstalk (which also affects other systems) and the relative fragility of optical fibres.

Contemporary aircraft design incorporates an increasingly large proportion of advanced composite structure and it is not surprising therefore that considerable research effort is directed towards the problem of embedding sensors within this material and integrating the data transfer and acquisition system. Objects introduced into the composite structure generally tend to impair the structured performance to some extent and so the volume of sensors and associated connecting channels must be reduced. Several workers have attempted to remove the need to directly connect to the sensors. Spillman and Durkee (1994) have designed and tested a simple solution that allows both power and data transfer to an embedded resistive strain gauge by means of mutually inductive embedded and surface mounted coils. In the ultrasonic field others are working on the possibility of using radio telemetry to connect to embedded interdigital ultrasonic sensors [Whiteley, *et al.* (1999)]. Such a system would dispense with the need for a physical data channel for most of the network and thus should save weight and greatly simplify repairs to the structure. Progress has also been made on the development of low volume sensors. Low profile interdigital transducers utilising the piezoelectric polymer: PVDF [Monkhouse, *et al.* (1997)] and the more robust piezoelectric ceramic: PZT [Gachagan, *et al.* (1996)] have been developed for the excitation of guided waves. A further interdigital method that should allow the selective excitation of several different guided modes by means of a series of embedded wires is also under development [Atkinson and Hayward (1999)]. These low profile sensors could also be surface mounted and used on metallic aircraft skin.

A somewhat subjective assessment of the general state of the art of structural health-monitoring system (SHMS) technology was attempted by Kudva, *et al.* (1993). This alleges that while sensor technology is roughly 40% mature, computers are 75% mature with respect to SHMS development. The supporting analysis algorithms are believed to be only 40% mature, and system integration is less than 40% ready.

1.1.3.3 Work on a guided wave systems

The potential use of ultrasonic guided waves for non-destructive evaluation was probably first realised by Worlton (1957) who noted that Lamb waves effectively revealed sub-surface laminar flaws and overcame some of the problems encountered in conventional ultrasonic testing such as near-surface defects. In recommending Lamb waves he neglected however, to mention the most valuable property of guided wave testing. This lies in the fact that instead of simply interrogating the structure immediately below the transducer, as is the case of conventional ultrasonics, guided waves propagate along the plane of the plate and thus interrogate a line or an area of the plate. Thus, guided waves have a considerable advantage in terms of efficiency over other more localised methods. It is for this reason that guided waves have strong potential for use in global SHM systems. This potential for long range propagation and testing of structure has already been exploited in a number of areas of industry. A system for testing pipes over tens of meters is marketed by TWI/Plant Integrity under the trademark of 'Teletest' and a more sophisticated system for the same purpose featuring defect recognition, location and classification elements of 'smart' technology has been developed by 'Guided Ultrasonics Ltd'. Pipes, which are essentially one dimensional in the sense that waves are propagated in one direction only, are ideal specimens for guided wave techniques. The two-dimensional problem posed by plates is more difficult and despite considerable research effort, the author is aware of no commercial long-range system, even for simple plate structures, currently in existence. A contemporary review of the progress of ultrasonic guided wave NDE, which includes some ageing aircraft inspection, can be found in Rose (1995). This shows that much of the success of guided waves techniques in two-dimensional structures is confined to short range applications, including material and defect characterisation as well as flaw detection. This project examines the feasibility of a long-range guided wave system in two-dimensional aircraft structure.

1.2 Project Aims and Organisation

The work in this project was funded by the Department of Trade and Industry (DTI) under the Civil Aircraft Research and Technology Demonstration Program (CARAD) scheme, and the Defence Evaluation and Research Agency (DERA) were appointed project managers. Originally, the project aim was the development of an aircraft smart structure utilising guided waves. This however, proved too ambitious given the current state of maturity of this field, and the resources and time constraints of the project. It was subsequently agreed therefore, that work should concentrate on studying just the propagation of guided modes through metallic aircraft structure, with a view to identifying modes with potential for long-range propagation. Since weight is a crucial factor in aircraft design, the weight of transducers and their associated data transfer and power supply systems must be minimised. Cost and maintenance considerations also demand a minimum density of transducers, and the greater the number of transducers employed, the greater the burden on data distribution and signal processing systems. It is therefore vital that selected modes are able to propagate efficiently through the structure, negotiating the high density of structured features indicated in figure 1.1. A rough estimate of the fuselage surface area of the relatively small Boeing 737 aircraft indicated that for a transducer pitch of one meter about 400 transducers would be required and for a Boeing 747 four times this number would be needed. It was consequently decided that efficient propagation over at least a meter was an essential requirement and it was necessary to set a limit for the attenuation of potentially useful modes. From the findings of recent development work for guided-wave pipe inspection systems [Alleyne, *et al.* (1996)], defect echoes of roughly –20 dB above the noise floor are required. The signal-to-noise ratio is significantly improved when tone burst excitation is employed, particularly when modulated by an envelope function such as the Hanning function. Anticipating say a ten cycle Hanning windowed tone burst excitation, current transduction techniques would be expected to achieve a signal-to-noise ratio of at least 60 dB measured close to the transducer. It was therefore decided that the signal should decay by no more than 40 dB over the propagation distance. The primary objective therefore was to identify modes having an effective attenuation of less than 40 dB/m. The term ‘effective attenuation’ includes signal attenuation owing to losses, such as reflections, incurred at the boundaries of structural features along the propagation path. The strategy employed was to use these somewhat arbitrary and subjective limits to net all potentially viable modes, given that long range propagation underpins the viability of any mode. A further selection might then be made based on other factors such as defect sensitivity, excitability and interaction with fasteners.

Although the problem is simply one of mode selection, unfortunately in any given system, a potentially infinite number of guided wave modes exist. It has been shown by Alleyne and Cawley (1992) that in general the success of guided wave NDE depends on excitation of a single mode, in order to simplify the received signal as far as possible. Since the number of possible modes in a given system increases with frequency it is sensible to examine the lower frequencies first and work in this project focussed primarily on frequencies below 5 MHz.

The course of the investigation began by considering modes in a single skin before moving on to more complex multi-layered systems. The majority of the fuselage structure was assumed to feature a single supported skin and in order to study the effective attenuation it was important to study the transition of signals from the single skin into each of the structural features. Efficient propagation in the single skin must therefore be a pre-requisite of any mode considered as having potential.

The first phase of the work was to measure the acoustic properties of the aircraft materials discussed in section 1.3, in particular the sealant: PRC 1442 B2 and the adhesive: Redux 775, so that modal analysis could be carried out. Aircraft paint was also considered. Subsequent phases of the work were roughly defined by consideration of each of the structural features in turn. The results from these phases prompted a brief investigation of acoustic emission in the structure.

The work of each phase of the project generally began by modelling the system by means of dispersion analysis for systems with a uniform geometry, or by dynamic finite-element analysis for systems with more complex geometry. Dispersion analysis was facilitated by a computer program called ‘Disperse’ developed at Imperial College by Pavlakovic, *et al.* (1997).

For most of the experiments, single modes were excited in the plate using the coincidence or wedge method explained in chapter 2. However, the internal reverberation in the coupling medium tended to result in a confusing train of signals and some work was therefore carried out to eliminate this problem.

1.3 Characterisation of Aircraft Fuselage Structure

It is fortunate that the ageing aircraft group in which we are interested generally exhibits very little variation in design, both in terms of the arrangement of components and the materials used. There seems to have been reluctance on the part of designers to experiment with composite materials and contemporary alloys that were available. Perhaps this cautious approach is understandable in the aerospace industry where mistakes are invariably very costly. Although some steel, titanium and magnesium alloys are found, the vast majority of the structure is composed of aluminium alloy both in forged and plate form. Over the past forty years three main groups of alloy have been used in aircraft construction [Megson (1990)]:

i) Nickel free Duralumins.
ii) Duralumins with 1.2% of nickel and a large magnesium content
iii) The aluminium-zinc-magnesium group

The last of those has a very high static strength and the 7000 series alloys developed from this group were used in the more recent designs, where high strength was required. Duralumin alloys containing about 4% copper have better fatigue performance but poorer strength compared to the 7000 series and Duralumin with a high percentage of magnesium forms the 2000 series. The alloy chosen to represent aircraft skin is 2014 which together with the slightly more fatigue resistant 2024 are the materials most commonly found in fuselage skins. More recent design might include the aluminium-lithium alloys and certain aircraft have had specially developed alloys, such as for example concord, which has hidaminium skins that have improved high temperature performance. The variation in the elastic properties of these materials results in a relatively small variation of the acoustic properties and so the 2014 alloy, with the British standard (Aerospace) BS L157, reasonably represents any metallic aircraft skin likely to be found.

Semi-monocoque fuselage skins are by definition supported by a sub-structure that is usually made up of frames and stringers as shown in figure 1.1. Very often the material used in sub-structural components is the same as that used for the skin, and for simplicity this assumption was adopted for the purposes of this project. Furthermore, it was also assumed for simplicity, that the material thickness used in the sub-structure was the same as that of the skin. This is not always true, particularly in the case of frames.

Skin thickness varies substantially in wing structure, where machined skins usually taper in a spanwise direction. However, in the fuselage this is not usually the case and where required, thickened regions are obtained by applying added layers of skin. The thickness of a single layer of fuselage skin varies, but a skin thickness of 16 swg (1.63mm) or 18 swg (1.22 mm) is commonly found in commercial airline aircraft. The later was adopted for the generic skin in this project.

The general method of fuselage construction is described by Megson (1990) and is the same for aircraft of widely differing roles. The frames are positioned vertically in the fuselage jig and stringers and longerons, which pass through cut-outs in the frames, are riveted to the frames by means of short brackets called ‘frame ties’. Subsidiary frames that surround doors, hatches, and windows are then bolted or riveted into position and finally the skin panels are riveted to the frame and stringer flanges. Before assembly the structural components are given an anti-corrosion treatment and have a coating of primer paint applied. Jointing compound is usually applied between riveted joints. Several different jointing compounds are used but the most common for pressurised fuselage joints are ‘Thiakol’ and ‘PRC’. These are trade names for polysulphide sealants that are also used to seal integral fuel tanks. In this case the sealant is applied to the internal surface along the joint lines, and sealant is often daubed over the rivet heads to a depth of up to about 5mm. The thickness of the jointing layer in riveted joints made with PRC 1442-B2, was found to be thinner close to the rivets. The degree of thinning varied, but away from the rivets the joint thickness was fairly consistent at 0.3 mm. It was felt that, at least for initial analysis, rivets should be excluded for the purposes of this investigation. A standard sealed joint would therefore simply feature a jointing layer of PRC 1442-B2 with a thickness of 0.3mm. A more accurate joint specification, including fasteners, could later be tested with modes that were found to propagate well across the simplified joint. It subsequently transpired from the results, that this was not necessary.

In some aircraft the stringers are bonded to the skin rather than riveted. The lap joints (which are formed at the boundaries of skin panels), and the frame-to-skin joints may be both bonded and riveted. A number of different adhesives have been used the most popular being AF163 and Redux. Redux is a phenolic resin adhesive that was developed during the second world war and was widely used in the Comet aircraft and many others. Initially the method of use was to brush on a coat of phenol-formaldehyde to the anodised surfaces and then the polyvinyl-formal (PVF) component in the form of a powder would be shaken on to the surface. The joint surfaces were then brought together with a pressure of 7 bar and cured at a temperature of 150^{o}C for 30 minutes [Beevers (1995)]. In recent years the components of Redux adhesive are supplied in the form of a single film which is cured under similar conditions set out in the DTD 775B specification. Since this method gives more consistent joint thickness, the joints made for experiments in this project utilised Redux 775 film. Bonded joint specimens, used in experimental work and described in chapters 4 and 5, were all made to DTD 775B except that a light grit blasting was substituted for the anodic treatment to save time. This would have made no significant difference to the acoustic properties of the joints. It was found that when cured, the jointing layer had a mean thickness of 0.25 mm which was declared the nominal thickness of a bonded joint.

Having outlined the method of aircraft construction and determined nominal specifications for the sealed and bonded joint types, the problem of characterising the structural detail of aircraft constructions must be addressed. A reasonable compromise must be reached such that the results obtained reflect propagation in a real aircraft fuselage, whilst meeting the resource and time constraints of the project. The complexity of the fuselage structure illustrated in figure 1.1 is formidable and in order to simplify the problem, a number of essential structural features were identified which together characterise the semi-monocoque fuselage of any aircraft. Although there is a high density of structural features, almost all fall into one of the six types shown in figure 1.1, each of which presents a different system in respect of guided wave propagation. Since the essential function of these generic structural features is simply to provide insight into the signal propagation, each is to some extent idealised as listed below:

- No paint or anti-corrosion treatment was applied to the surfaces. The effect of applying paint layers to a free plate was investigated separately and is discussed in chapter 3.

- No rivets were included. This significant simplification was part of the strategy to identify any guided modes with potential, before the scattering problem of rivets was considered.

- All of the plates featured were of the aluminium alloy: BSL157 and are 1.2 mm thick. This was deemed to be the specification of a single skin. In practice skins of varying thickness and possibly different material may be encountered.

- In the case of the stringer joint a simple strip of skin represents the sub-structural member. In practice these members may have a ‘Z’ ‘C’ or ‘Top hat’ cross-section.

- The maximum number of skin layers shown in figure 1.1 is two. However, more than two skins are often found and as many as six have been used around large apertures in the fuselage.

- In real aircraft structure some of these features may be combined. For instance the double-skin feature may also have sealant applied to one surface and one of the skins could be tapered.

Given the scope and time constraints of the project, these idealisations were necessary in order to reduce the structural permutations to a manageable set, without unduly compromising the relevance of the results.

Each of the features illustrated in figure 1.1 can be found in any real aircraft structure. A large proportion of the fuselage structure features a supported single skin, so a free plate is the simplest generic feature. The skin, with a layer of PRC sealant applied to one surface, represents the application of sealant in the belly of the fuselage, in what is termed the ‘bilge’ area. Here the sealant protects against accelerated corrosion owing to the collection of liquid such as condensation, hydraulic fluid, galley waste and toilet waste. This also represents the system found in integral fuel tanks. The double-skin feature represents reinforced areas around fuselage apertures such as hatches, doors and windows, where several extra skin layers may be applied. The lap joint is commonly found at the boundaries of skin panels, while the stringer joint represents any point at which a structural member is attached to the skin. Acoustically, the essential difference between the two is that in the case of the lap joint, propagation across the joint entails crossing the jointing layer, which is not the case for a stringer joint. Tapered skins are most commonly found in the wings, but the tapered skin feature also represents the chamfered boundaries of fuselage panels and doubler plates (added skin layers) may also be tapered.

1.4 Outline of the Thesis

The project work naturally fell into phases defined by the establishment of the acoustic properties of aircraft materials and the examination of each of the structural features previously outlined. These phases of work therefore form the subsequent chapters of this thesis, which are presented in roughly chronological order.

Since, in general terms, the same experimental and numerical techniques were applied throughout the project, these are described in chapter 2, together with the preliminary measurement of the acoustic properties.

Lamb waves, which are the guided modes of a free plate, are considered in chapter 3, where attention focuses on the factors influencing attenuation in the single skin. The tapered skin is a closely related system and the results of finite-element analysis of the reflections from the change of section are also presented in this chapter and compared with experimental results.

Chapter 4 examines propagation in the multi-layered systems beginning with skin with overlying sealant and paint layers before moving on to the two double-skin systems jointed with PRC sealant and Redux adhesive respectively. For each case the dispersion curves are presented and validated at selected points by experiment and this is followed by a discussion of mode selection.

Chapter 5 deals with the lap and stringer joints, again considering both sealant and adhesive joining. The important interaction of principal carrier modes with similar wavenumbers, that can dominate the efficiency of wave propagation across joints, is revealed. Carrier-mode interference results in very poor propagation across a succession of joints, but commercial acoustic emission systems rely on receiving low amplitude acoustic emission event signals over several meters. The reason for this is shown in chapter 6, which presents the results of numerical and experimental examination of simulated AE propagation across joints, and suggests how current systems might be improved.

Lastly, chapter 7 presents the conclusions of the project regarding the use of ultrasonic guided waves for aircraft structural health monitoring, for both active and passive systems. The project approach and method is also critically reviewed in this chapter and a number of avenues of further work are suggested.

1.5 Summary of contributions made by this work.

The main contribution of this work lies in its analysis of long-range propagation, specific to metallic aircraft structure. Whilst considerable work has been done on relatively short range ultrasonic interrogation of aircraft structure, there has been very little research on the problems associated with guided wave propagation across the high density of structural features commonly found in aircraft. This work highlights the problem of attenuation caused by the common application of sealant to the internal skin surface, and sheds useful light on propagation in painted skin and tapering skin. In particular the analysis of joints contributes to the field of smart structure development by showing how the interference of modes in joints can be used to produce excellent transmission across a single joint, but effectively prevents transmission across a series of joints. Ultimately, the work showed that an active structural health-monitoring system for metallic aircraft that relies on long-range guided-wave propagation is not viable. This should save considerable time and expense in the future development of aircraft smart structure.

In addition, the work has made several significant subsidiary contributions in various fields. A short analysis of acoustic emission that was necessary to resolve questions arising from conclusions of the main investigation threw useful light on modal aspects of the acoustic emission signal propagation across joints, and included the quantitative modelling of transmission coefficients. This section of the work also suggested a potentially useful means of improving AE source location. The work on tapered skins usefully compared a stepped-element scheme for finite element modelling of tapering regions with an alternative tapering-element scheme. Finding the tapering-element scheme many times more computationally efficient, this result, and the method of validation employed, should prove useful in this field. A contribution to the transduction of guided waves is made by the development of local immersion baths made from wax. These absorb reverberations in the water path, providing a much ‘cleaner’ transmission and receipt of signals. Finally during the measurement of the acoustic properties of PRC a useful variation of a conventional technique was employed to overcome the problem of coupling variation.

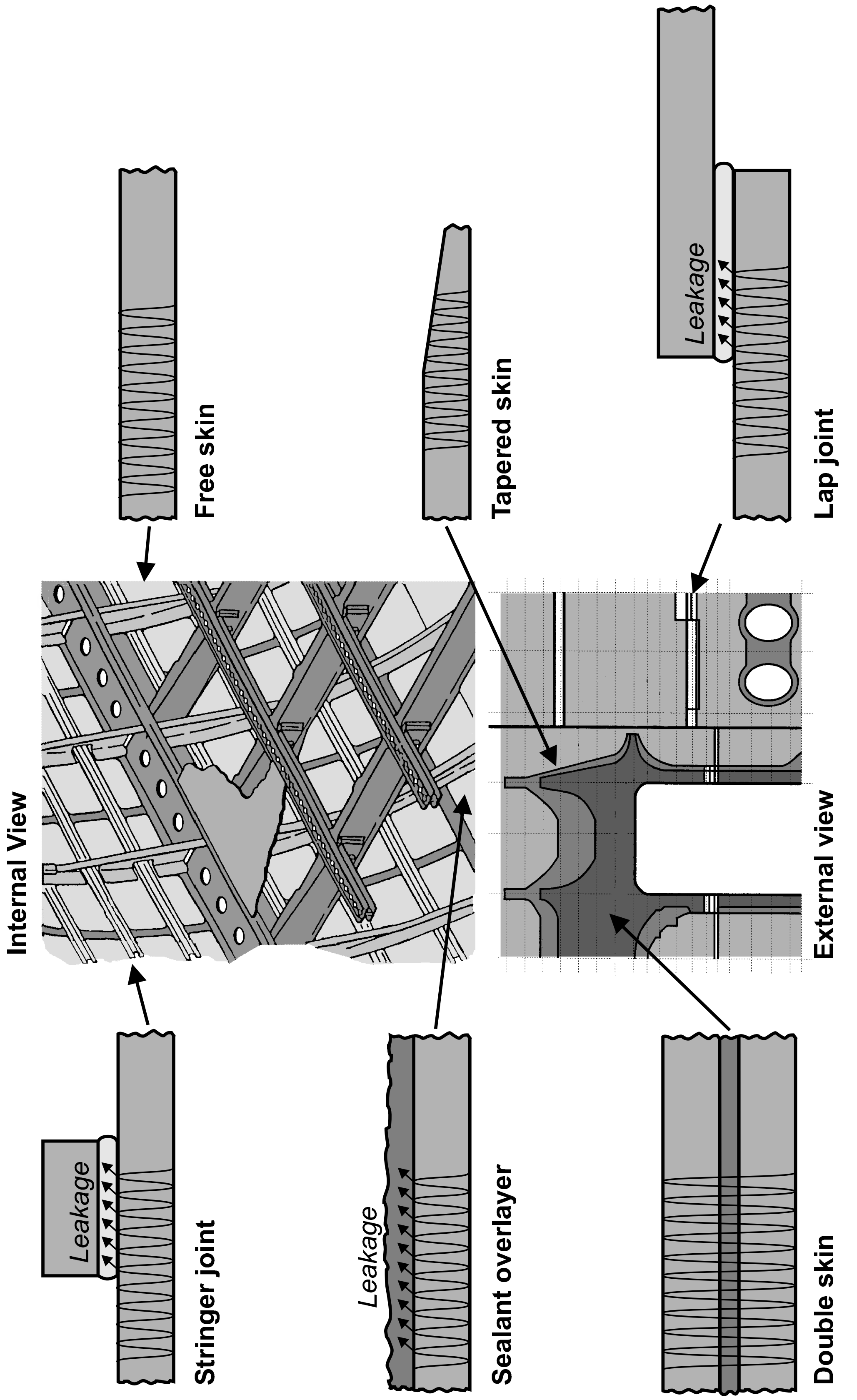

Fig 1.1. Semi-monocoque fuselage construction and the structural features examined.

2. Experimental and numerical techniques

2.1 Introduction

Much of the work of this project involved the validation of dispersion curves and finite-element analysis by experimental measurement. In general, the same experimental and numerical analysis techniques were used throughout, with little variation, and so it is convenient to set out the general details of these techniques in an early chapter. The aim of most of the experimental work was to validate dispersion curves or numerical analysis in respect of certain modes. These modes were primarily selected on the basis of group velocity and attenuation (as described in chapter three) and it is therefore sensible to validate the models by means of the same parameters where possible. Consequently, most of the experiments were directed at the measurement of group velocity and attenuation of guided modes. The dispersion predictions of the various structural systems were derived using the 'global matrix method', which is implemented in the software program: 'Disperse'. This method is discussed further in appendix A. The global matrix method requires a complete definition of the elastic properties of each layer of the system in order to determine the roots of the governing characteristic equation, giving the modal solution. Although slight anisotropy of the skins is caused by rolling during manufacture and some inhomogeneity is often introduced into the sealant and adhesive during preparation, (for example by the introduction of air), the aircraft materials detailed in chapter 1 may reasonably be considered homogeneous and isotropic. The elastic properties of these materials are therefore completely defined by the velocity and attenuation of the longitudinal and shear bulk waves through the material, together with the material density. Before describing the experimental and numerical techniques it is appropriate to briefly mention the measurement of these acoustic properties, a more detailed discussion of which is presented in appendix B.

2.2 Measurement of acoustic properties of aircraft materials

2.2.1 Bulk wave velocities

The simplest method of bulk wave velocity measurement is made by determining the time of flight of a sharp pulse through a known thickness of material. In practice it is often easier to measure the time difference between successive reverberations of a pulse across the thickness of the test specimen. This method is only appropriate however, if the material is non-dispersive so that the shape of the pulse remains unaltered during transit. In addition, of course, the pulses must be separated in time and the specimen must therefore have sufficient thickness. Where the material under test is attenuative, a short path length is required, in order to receive a well-defined return pulse above the noise floor. The result of these two competing requirements is that often, successive reverberations cannot be separated in the time domain and frequency domain methods must be employed. Two well-known spectral methods are the 'Amplitude Spectrum Method' and the 'Phase Spectrum Method'. These are discussed in detail by Pialucha, *et al.* (1989).

The Phase Spectrum Method has the advantage that it produces many more points across a given frequency band, giving an almost continuous function, but it has the disadvantage that it requires that successive pulses be separated in time.

The 'Amplitude Spectrum Method' does not require the separation of successive pulses and provided that the material is not too dispersive or attenuative, the number of points obtained is generally acceptable. At least one resonance is required within the frequency bandwidth of the input signal (preferably many) and so a very short, broadband pulse must be employed. Since a Fourier transform of the entire time trace can be used, the method is simpler to process and is more appropriate for thin samples. Consequently, the Amplitude Spectrum Method was used to determine both the longitudinal bulk wave phase velocity in the PRC sealant and the longitudinal and shear wave velocities in the Redux adhesive. A 5 MHz probe was used to obtain longitudinal velocity measurements over the frequency band from about 2 to 6 MHz in the PRC and Redux specimens. Further measurements were made on an aircraft joint sample using a 50 MHz probe gave the longitudinal velocity in Redux for frequencies up to 80 MHz. A 6 MHz shear probe was used to establish shear velocity over the band from 3.5 to 10.5 MHz in Redux. The velocities can be considered non-dispersive over the frequency range of interest (0-5 MHz).

The shear wave velocity in PRC was not obtainable by the amplitude spectrum method owing to the very high shear wave attenuation such that, even in very thin specimens, the available shear probe received no reverberation signal. In this case the velocity spectrum was calculated from the reflection coefficient between a specimen of Polycarbonate (PC) bonded to a specimen of PRC. This shear velocity in the frequency range 1-2 MHz was obtained using a 6 MHz shear probe, the higher frequencies being effectively filtered by the material. This measurement showed considerable dispersion, but in view of the very high measured shear wave attenuation, indicating negligible shear wave propagation, a mean value of 200 m/s was ascribed. A more detailed explanation of these measurements together with a discussion of the results can be found in appendix B.

The bulk wave velocities for the materials concerned are presented in table 2.1 at the end of section 2.2.

2.2.2 Bulk wave attenuation

The decay of a bulk wave introduced into in a material by the coupling of a transducer is the result of energy losses due to a combination of:

- Beam spread (diffraction).
- Redistribution of energy through reflection, transmission and mode conversion at material boundaries.
- Viscous damping and scatter within the material.

However, the attenuation coefficients of transverse and longitudinal waves, required for dispersion analysis, account for the last of these three mechanisms only and contributions from the others must be eliminated in the measurement process or by subsequent manipulation of the results.

In order to measure attenuation, several methods have been established. Essentially it is necessary to compare the amplitude of two signals with differing propagation path lengths within the material and to isolate the damping factor from other attenuating factors along the signal paths. Some methods, such as those described by Krautkramer and Krautkramer (1983) are designed to provide rough measurements using commonly found industrial field NDT equipment. Papadakis (1990) details methods which are more suited to industrial applications with an ongoing requirement for attenuation measurement of process material. These methods require special equipment designed for the purpose and/or permanently bonded transducers. A number of laboratory measurement methods are usefully reviewed by Guo, *et al.* (1995), who introduces a variation of the amplitude spectrum method, called the 'Normalised Amplitude Spectrum' method that measures attenuation from the level of the minima (or maxima) in the amplitude spectrum. Guo also describes two important and commonly used 'echo' techniques that rely on comparison of the amplitude of two echoes that have different path lengths through the specimen.

A straightforward method of measuring attenuation is termed the 'Double Through Transmission' (DTT) method, which was adapted by Drinkwater (1995) for the measurement of longitudinal wave attenuation in rubber. Guo reviews two commonly used variations of this technique, which he terms the $F_0/B_1/B_2$ method and the $F_0/F/B_1$ method. The former, which requires two successive reflections from the far face of the specimen, was adopted successfully to measure both longitudinal and shear wave attenuation in Redux adhesive as detailed in appendix B. The longitudinal attenuation measurements were made using a 20 MHz probe giving values from 15-50 MHz, which were extrapolated to low frequencies. A 6 MHz shear probe was used to obtain the shear wave attenuation in Redux from about 3.5-10 MHz (see figures B4 and B5). The much higher attenuation in PRC sealant however, demanded the latter method, which requires only one backwall reflection. Since it was necessary to develop a variant of this technique, both the original technique and the variation will be described below.

The ray paths of the $F_0/F/B_1$ method, described by Guo, are illustrated schematically in figure 2.1, and Guo's notation has been retained as far as possible. The reflection coefficient between a sample of the coupling material (c) and air (b) is assumed to be unity, and a separate reference measurement of the reflected amplitude (F_0) at this reference interface (position 1) will effectively reveal the amplitude of the incident wave (I) in figure 2.1:

$$F_0 = -I \tag{2.1}$$

It is assumed that the incident wave in the reference measurement at position 1 is the same as that in the main test in position 2. Having made the reference measurement, the amplitudes of the front and back reflections (F and B_1 respectively) from a specimen of known thickness are measured in position 2. The thickness of coupling material in positions 1 and 2 must be identical. These measurements allow the double transmission decay factor through the specimen material (A_α^2) to be calculated:

$$A_\alpha^{\ 2} = -\frac{B_1}{F}\frac{R_{ca}}{R_{ba}(1-R_{ca}^{\ 2})} \tag{2.2}$$

where:

$$R_{ca} = -\frac{F}{F_0}$$

and

$R_{ba} = R_{ca}$ for immersion coupling

$R_{ba} = 1$ for air backed specimens.

Finally the attenuation coefficient (α) is given by:

$$\alpha = \frac{1}{2L}\ln(A_\alpha^{\ 2}) \tag{2.3}$$

where L = specimen thickness.

Often water is used for the coupling medium and when the specimen and transducer are immersed, or when a local bath is used, the coupling efficiency will be constant, giving consistent measurements. However, water is a poor choice of coupling medium if the impedance of the specimen is very different from that of water and particularly if it is also highly attenuative. The coupling material must be chosen such that the reflections from the front and back faces of the specimen are measurable. Too close an impedance match between the coupling and the specimen results in a diminished front face reflection, while too poor a match causes insufficient energy to be transmitted, with the result that echoes from the specimen backwall will be too heavily attenuated by the specimen to be measurable. In the case of PRC sealant, which is highly attenuative and therefore requires good transmission of energy at the coupling/specimen interface, a polycarbonate (PC) coupling layer bonded to the air-backed specimen was found to give the best results. Provided a thin, uniform bond is achieved, the coupling efficiency between the specimen and the coupling layer will not vary and the reference reflection can be from an air-backed portion of the coupling medium. Using a solid obtained from coupling material may also allow measurement of the shear wave attenuation.

A small quantity of coupling gel is applied to the surface of the solid coupling layer, at the measuring point, in order to couple the transducer. One of the problems with this method is that, in order to make the reference reflection measurement, the transducer must be moved. The use of coupling gel often results in a difference in the coupling efficiency between the two measurements, causing erroneous results. Thus the implicit assumption of the method; that $I[position{:}1] = I[position{:}2]$, is generally invalid. The method was therefore modified to remove this problem and the modified $F_0/F/B_1$ method used to measure the longitudinal wave attenuation in PRC is described below.

2.2.2.1 Attenuation in PRC sealant

In order to overcome the coupling problem, an extra interface was created by the addition of an extra layer of coupling material. The reference reflection was then normalised using the reflection at this interface. A diagram of the test specimen and equipment is shown in figure 2.2(a) and the relevant signal paths are shown in figure 2.2(b). Normalising the reference reflection (F_0[*position:*1]) by multiplying by (F_R[*position:*2]/F_R[*position:*1]) eliminates the problem of coupling variation:

$$F_0\,(normalised) = F_0[\text{position} : 1]\frac{F_R[\text{position} : 2]}{F_R[\text{position} : 1]} \tag{2.4}$$

Since, from consideration of figure 2.2(b), the reflection coefficient (R_{ca}) is given by:

$$R_{ca} = \frac{F}{F_0\,(normalised)} \tag{2.5}$$

then

$$R_{ca} = -\frac{F}{F_0[\,position : 1]} \times \frac{F_R[\,position : 1]}{F_R[\,position : 2]} \tag{2.6}$$

If the loss factor for a single transmission across the PRC specimen is A_α then the double transmission loss is given by:

$$A_\alpha{}^2 = -\frac{B_1}{F}\frac{R_{ca}}{1 - R_{ca}{}^2} \tag{2.7}$$

Finally the attenuation coefficient (α) is calculated from A_α^2 and the PRC specimen thickness (L) using:

$$\alpha = \frac{1}{2L}\ln\left(A_\alpha{}^2\right) \tag{2.8}$$

Polymethyl-methacrylate (PMMA) and Polycarbonate (PC) were chosen to form the interfaces required. It is important that these materials have similar, but not identical impedances, that are close to that of PRC. This allows reasonable transmission across the interfaces giving a well-conditioned measurement. Earlier attempts with a number of other materials including aluminium, glass and polystyrene failed, owing to poor conditioning. The interface between the PMMA and PC was made by applying a thin coating of solvent to one surface and then pressing the two surfaces together for several minutes in order to obtain a bondline thickness of less than five micron, which is negligible compared with the wavelength. The PRC was prepared from the two-part mix as specified by the manufacturer and applied to the PC surface. Since the method relies upon a consistent reflection from the lower surface of the PRC, it is important that this surface is as smooth as possible, so that scatter due to surface roughness is not a significant factor. In addition, the thickness of the PRC, which is measured, must be consistent. These conditions were met by using a flat plate of glass smeared with release agent, together with spacers to trap the PRC layer during curing. Care was taken to eliminate air from the PRC as far as possible. Finally the thickness of the PRC layer was measured using a micrometer.

Using a transducer with a centre frequency of 5 MHz, a measurement of the pulse/echo time response was made in positions (1) and (2) in figure 2.2, and the resulting time traces were captured by digital oscilloscope and stored on a PC, where signal processing was carried out. In order to obtain the frequency spectrum of the attenuation coefficient, the manipulations given in equations 2.4 to 2.8 were performed in the frequency domain, by means of fast-Fourier transform (FFT) of the relevant temporal signals. The resulting spectrum of longitudinal attenuation in PRC is shown in figure 2.3. Over much of the frequency band presented in figure 2.3, the longitudinal attenuation in PRC is an approximately linear function of frequency. This allows the attenuation to be expressed as a single wavelength dependent parameter: 0.2Np/m (1.74 dB/m), which is shown in table 2.1.

Attempts were made to measure the shear wave attenuation by the same method, utilising shear transducers coupled to the specimen via a delay line and using treacle as a shear couplant between each. Unfortunately no clear backwall echo was obtainable from any sample since the shear attenuation was clearly very high. Further attempts were also made using the normalised amplitude spectrum method mentioned previously. This requires that the reflection coefficient R_{ca} in figure 2.1 is known a-priori, but efforts to establish this by comparison of the front face reflection and a reference reflection from the air-backed end of the delay line failed, once again due to poor conditioning. Similar problems were encountered when trying to find R_{ca} using the well known expression for the normal incidence reflection coefficient in terms of the material impedances, by means of the published impedance of PC and the measured shear velocity and density of PRC. Small errors in the last two parameters led to unreliable results. Finally it was conceded that the shear wave attenuation was sufficiently high to assume that shear wave propagation through PRC is negligible. Accordingly, a very high value of 1 Np/ λ (8.686 dB/λ) was assumed for the shear wave attenuation coefficient in PRC.

2.2.3 Density measurement

While the density of PRC samples was simply established from measurements of sample volume and weight, bulk samples of cured Redux of sufficient size to enable similar measurements were found to be very different to very thin samples cured in joints. This was probably because the pressure and temperature conditions used in the standard curing procedure could not be reproduced during the curing of thicker specimens. Under standard curing the adhesive thickness is determined simply by pressure, but for thicker specimens, spacers had to be used. Temperature gradients, set up by the curing reaction, would also have been different in specimens of different thickness. It was therefore necessary to obtain the Redux density indirectly from the normal reflection coefficient between a joint cured Redux sample and water, together with knowledge of the impedance, of water and the longitudinal bulk wave velocity in Redux. The measured densities of PRC sealant and Redux adhesive are shown in table 2.1.

Structure	Material	Spec.	Density (kg/m^3)	Longitudinal velocity (m/s)	Shear velocity (m/s)	Longitudinal Attenuation (np/λ)	Shear Attenuation (np/λ)
Skin	Duralumin	**BS L157**	**2700** (3%)**	**6348** (1%)**	**3133** (3%)**	**negligible***	**negligible***
Jointing /Sealant	Polysulfide Sealant	**PRC 1422B2**	**1527 (7%)**	**1500 (16%)**	**200 (40%)**	**0.2 (31%)**	**1*** (50%)**
Bonding Adhesive	Phenol-formaldehyde polyvinyl-formal	**REDUX 775**	**1036 (10%)**	**2829 (3%)**	**1325 (6%)**	**0.12 (8%)**	**0.29 (15%)**

* compared with the other materials ** Published data ***Assumed (too high to measure)

Table 2.1 Acoustic properties of aircraft skin system materials. (Maximum percentage errors are shown in brackets.)

2.3 Experimental techniques

2.3.1 General Excitation and reception of guided waves

Guided waves are very easily generated in a plate, simply by applying a force of sufficiently short duration to either the surface or edge of the plate. Such non-resonant excitation takes place, for instance, when simulated acoustic emission event signals are generated by the breaking of a pencil lead on the plate surface described in chapter 6. However, unless a controlled spatial distribution of harmonic forces, with restricted frequency bandwidth, is applied, there will be no control of either the number or the propagation direction of modes generated and the efficiency of mode generation will be poor. Apart from passive acoustic emission systems, practical guided wave applications usually require some measure of mode selection and directional control, to enable analysis of received signals. The experimental work of this project was no exception.

The displacement mode shape of S_0 tends to purely in-plane displacement with decreasing frequency. For example, at 1MHz the surface out-of-plane displacement of the S_0 mode in the skin is about 50% of the amplitude of the in-plane displacement, whereas by 0.5MHz this has fallen to 18%. In cases where a predominantly extensional S_0 mode at low frequency was required, excitation was achieved simply by coupling a conventional ultrasonic transducer directly to the plate edge and controlling only the frequency. Usually, however, and particularly when exciting modes above the A_1 cut off frequency, it is necessary to control both frequency and wavenumber in order to isolate a particular mode. Some general theoretical analysis of this can be found in Viktorov (1965) and Ditri, *et al.* (1994). Guided wave transducers fall into two main groups: those that operate on the coincidence principle and those that employ what is commonly termed an interdigital method. Both of these methods are reviewed in Viktorov's paper.

2.3.2 The local immersion technique based on the coincidence principle

The local immersion method of excitation is a particular implementation of the coincidence principle. The coincidence principle applies a surface force distribution indirectly, through the impingement of bulk waves on the plate surface, as shown in figure 2.4(a). The bulk waves are generated by an ultrasonic transducer oriented at a particular angle with respect to the surface, such that the phase velocity of the resulting travelling sinusoidal disturbances at the plate surface match that of the mode required. The bulk wave incident angle (θ) and the phase velocity of the guided wave mode (c_m) are simply related to the bulk wave phase velocity (c) by Snell's law such that:

$$\theta = \arcsin \frac{c}{c_m} \tag{2.9}$$

The value of c depends upon the properties of the coupling medium between the transducer and plate and the type of bulk wave considered. Many different coupling mediums have been employed. Solid coupling mediums, of which the more common are PMMA and acrylic, are discussed from a practical standpoint by Alleyne and Cawley (1994). Although such transducers are easier to use in practical NDT, they have two disadvantages over other coupling mediums. Firstly, a solid coupling wedge will support both longitudinal and shear wave propagation. Each of these bulk waves is likely to generate a separate guided wave signal on reaching the plate surface, and several modes may be excited. This prevents the generation of a simple single-mode signal. Secondly, the necessity to use a further couplant between the transducer, the wedge, and the plate, causes coupling variation when the system is moved to different locations on the plate, and the resulting signal amplitudes are not strictly comparable. A further problem is that some energy is reflected at the plate surface, leading to reverberations within the wedge. These may eventually strike the plate surface at either the same angle, or a different angle, generating further guided wave signals of the same mode, or of other modes. This also occurs with the local immersion technique, but is not usually a problem where more general immersion in a liquid couplant is employed. Theoretical analysis of liquid coupling has been presented by Jia (1997) , who computes the amplitude of resulting guided waves and includes the effect of specular reflection at the plate surface. The problem with this method is one of attenuation due to leakage. Since the guided modes in the plate have been generated by energy transfer from the liquid, the reciprocal process can also occur with equal efficiency. As the mode propagates beneath the liquid, energy will leak into the liquid, generating bulk longitudinal waves that propagate away from the plate at the same angle as that used for excitation, and the guided wave will very rapidly decay. To overcome this problem the extent of the liquid coupling is restricted to just that required at the excitation area. This technique, known as 'local immersion', is shown in figure 2.4(b), and is discussed by Alleyne and Cawley (1992) . A theoretical analysis of similar system comprising a vertically orientated, partially submerged plate is advanced by Briers, *et al.* (1997) though this configuration is of limited practical use. Alleyne fitted the liquid baths with seals that allowed them to be slid along the plate over small distances without draining them. The problem of reverberating reflected energy, seen in the wedge method, is particularly severe in this method owing to the greater mismatch in the impedances of the plate and the couplant. This problem is addressed in the work presented in the next section.

Local immersion transduction results in a considerable reflection of energy at the plate surface [Kino (1987)], which reverberates in the coupling bath and generates unwanted signals as described previously. This problem can be markedly improved by designing the local immersion baths to reduce the reverberations. The strategy employed was to construct the bath from a material that would absorb and dissipate the energy reflected from the plate. This involves finding a highly attenuative material, with an impedance as close as possible to that of the water (1.46 MRayl), so that maximum transmission into the material occurs at the water-solid interface. In respect of the longitudinal wave, paraffin wax has an impedance of 1.76 Mrayl with an attenuation of 105 dB/m at 1 MHz, and is therefore well suited to this purpose. Paraffin wax is also cheap and has a low melting point (57 °C), which allows it to be simply moulded into the required shape as described below. Indeed, the wax can be reused to mould further baths with different incident angles and it has even proved simple to make baths with bases that conform to the radius of pipes.

In addition to solid and liquid coupling, successful air coupling of transducers to guided waves in plates has been reported by Castaings [Castaings and Cawley (1996), Castaings and Hosten (1998)]. In these cases, high power electrostatic transducers are employed in order to offset the primary limitation of the acoustic impedance mismatch between the solid materials and the air. Rubber membranes may also be interposed between solids and air, in order to help match the impedances and improve the transmission of energy.

2.3.2.1 Experiments using local-immersion wax baths

The local immersion technique is a particular variation of the coincidence principle. Figure 2.5 shows the general pitch/catch arrangement employed in many of the experiments carried out to measure the group velocity and attenuation of a particular mode in a region of a plate or joint specimen. First, two wax baths were produced, as illustrated in figure 2.6(a), each with an incident angle (θ) corresponding to the phase velocity of the transmitted and received modes respectively. This angle is calculated by equation 2.9. A mould was manufactured from Perspex in order to cast the wax baths and this is shown in figure 2.6(b). The pipe seen in the figure was cut at the required incidence angle from a length of MDPE pipe of the same diameter as the transducer and was held in place in the mould by means of 'Blu Tack' in the pipe bore and at the lip of the mould. The mould and pipe were coated in a release agent (oil) and paraffin wax was then melted over boiling water before being poured into the mould. After setting, the bath was released from the mould and the pipe removed. Finally a 2 mm 'O'ring seal was let into position around the aperture in the base. This was done simply by sweating the seal into the base as shown in figure 2.6(a). Once the wax baths have been moulded, the upper surface of the transducer aperture is scoured with a hacksaw blade to allow air to escape and a 3 mm hole was drilled from the depression formed on the surface of the bath when the wax sets, through to the transducer aperture. The surface depression forms a reservoir that is used to ensure the bath remains full.

The plate specimen was prepared by marking a guideline on the plate surface indicating the path over which attenuation was to be measured. The wax baths fitted with appropriate transducers were placed on the plate and aligned by means of a wooden straight edge shown in figure 2.5, that was held in position by means of clamps (not shown). The baths were also weighted to ensure a good seal at the plate. Both excitation and receiver transducers were connected to a 'Wavemaker Duet'. This is a bespoke signal generator/receiver produced by Macro Design. It is capable of providing a range of waveforms from a simple pulse to rectangular, triangular and Hanning windowed tone bursts of between 5 and 20 cycles in the frequency range 40 kHz to 4 MHz. The excitation output can be balanced across two channels in anti-phase for use with interdigital transducers or output from a single channel employed in this case. The Wavemaker has both pitch/catch and pulse/echo modes of operation. In pulse/echo mode, an adjustable gate controls the duration of the transmission phase of operation. Beyond the gate time the instrument is switched to receive and the output amplifier stages are switched off in order to reduce noise. The received signal may be passed through an internal agile bandpass filter slaved to the excitation frequency, which further reduces noise. When operating in pitch/catch mode the receiving transducer is connected to the input of the internal amplifier and may, once again, be passed through the internal bandpass filter. In the arrangement shown in figure 2.5, the Wavemaker is operating in pitch/catch mode with the transmitter connected to the unbalanced signal generator output channel and the receiver connected to the amplifier input channel. The amplifier output was connected to a LeCroy 9000 series digital oscilloscope, which was, in turn, connected, via a GPI bus, to a personal computer (PC).

The PC was used for storage and processing of the received signals. Time domain processing involved the estimation of the amplitude and arrival time of time-separated tone bursts. This was usually achieved by isolating the required tone signal and applying a Hilbert transform to obtain the envelope [Hahn (1996)]. The maximum amplitude and its associated time-of-flight are then easily found. This method is only accurate for non-dispersive signals. When it was necessary to establish the time-of-flight of a significantly dispersive signal it had to be estimated from the leading edge of the signal envelope. A threshold amplitude was set slightly greater than the noise level and the first crossing of this threshold was used to define the time-of-flight that was acceptable for comparative purposes. Where the attenuation of a dispersive signal was required, the target signal was isolated and Fourier transformed. Attenuation was then established from the amplitude of a particular frequency component, (usually the centre frequency), measured at two (or more) spatially separated locations on the signal path.

Except where otherwise stated, the excitation signal used in all experiments was a Hanning-windowed tone burst, which depresses the sidebands to less than –32 dB with respect to the centre frequency amplitude. The number of cycles in the toneburst varied between experiments, depending on the conflicting needs of avoiding dispersion and maximising resolution. In order to establish the attenuation over a region of plate a series of signal records were made at incremental distances (usually of 10mm) from the transmitter. The receiver bath was slid along the straight edge to each incremental position marked on the plate as shown in figure 2.5 and the received time record was saved. To avoid any liquid on the signal path, that would cause erroneous attenuation, the receiver bath was always moved towards the transmitter. A plot of amplitude versus distance was thus obtained.

Some pulse/echo experiments were also made using a local immersion transmitter/receiver. In these cases the arrangement was similar to that shown in figure 2.5 with the receiver removed. The Wavemaker was switched to pulse/echo mode with the gate activated.

2.3.3 Receiving guided wave signals by Laser

Pulsed lasers have been employed as broadband non-resonant transducers for the generation of fundamental modes by Hutchins, *et al.* (1989), Klein and Bacher (1998) and low power laser inteferometry is commonly used for broadband, non-resonant receipt of Lamb modes. Lasers have also been used as resonance transducers for the generation of specific Lamb modes by employing periodic arrays of spot or line sources in an interdigital arrangement [Costley and Berthelot (1992)]. A laser interferometer manufactured by Polytech (model OFV 512) was used in some of the experiments of this project. This equipment incorporates a 1mW helium-neon (633nm wavlength) laser in a vibrometer in which the user has access to both the probe beam and a reference beam. An interferometer measures the dynamic Doppler shift from the vibrating object and this is processed by separate unit (OFV2700-1) to produce an analogue vibration displacement signal. Having a bandwidth from 50 kHz to 20 MHz it has two basic modes of operation. In single-beam mode a retro-reflecting stationary reference mirror is fitted to the end of the reference beam fibre. All measurements are then made relative to the (stationary) reference mirror, and the output is the component of displacement of the probe beam reflector (the specimen) along the beam axis. In differential mode both beams are utilised and the output is the difference in the displacements of the probe and reference beam reflectors. This allows difference vibration measurements to be made between any two points on the structure. The equipment is able to resolve out-of-plane displacements at the plate surface of the order of 0.1nm. However, it can also be configured to measure just in-plane displacement as described in section 2.3.3.1 below. Use of the laser has the advantage that measurement is possible very close to plate boundaries such as the edge of a joint, which is not possible with the local immersion method. In addition the measurement is absolute and so comparisons made, for example, across joints are more reliable than in the case of local immersion owing to the possibility of disturbing the bath configuration when it is drained, moved and refilled. Nevertheless the point measurement could on occasions be over-sensitive to position on the plate. In the case of the local immersion method, the signal is effectively averaged over the area of the footprint and it is therefore somewhat less sensitive to the beam pattern of the transmitter and extraneous reflections from the sides and corners of the specimen.

2.3.3.1 Out-of-plane operation

The Polytech laser features two probes, one of which provides a reference signal. To measure out-of-plane displacement, a mirror is fitted to the reference probe and the other probe is focused at normal incidence on the point of measurement on the plate, as illustrated in figure 2.7a). The reference signal is subtracted from that reflected from the plate surface to give a signal that varies with displacement. The output signal from the laser equipment, that is proportional to the displacement at the plate surface, is fed to the digital oscilloscope and finally to the PC. Polishing the plate surface at the measurement point significantly reduces the noise. However, it was generally found necessary to have the oscilloscope average the received signal over a number of sweeps (usually 1000), particularly for small displacement amplitudes, (in the order of a nanometre), where the signal to noise ratio may be as little as 0.5. The noise is primarily the result of imperfect specular reflection from the plate surface and therefore averaging does not change the absolute measurement of plate displacement.

2.3.3.2 In-plane operation

Removing the mirror from the reference probe and co-focusing the two probes on the measurement point with incident angles of +30° and –30° respectively with respect to the plate normal allows just in-plane displacement to be measured. This configuration is shown in figure 2.7b). An in-plane displacement (Δx) will cause a change in the signal from the data and reference probes of $\Delta x \sin 30°$ and $-\Delta x \sin 30°$ respectively. Since $\sin 30° = 0.5$, subtraction of the two probe signals yields a resultant signal proportional to Δx. In order that the light from each probe is reflected back into the same probe it is necessary to fix a small piece of retro-reflective tape to the plate surface. This inevitably damps the guided wave in the plate so that only relative measurements of in-plane displacement are possible. The extent of the damping of out-of-plane displacements by the tape, was measured using the signals employed in the experiments reported in this project. This was found to be around 5%. A clamp was manufactured to hold the probes at the required incident angle and this technique proved very useful for analysis of modes with predominantly in-plane displacements at the surface. Care was taken to ensure correct and consistent directional alignment of the probes, which is important in this configuration.

2.3.4 Mode identification

Most of the experiments were designed to generate, essentially, a single mode, or just the two fundamental modes and sufficient spatial distance was allowed so that different modes were separated in the time domain and could be identified by consideration of group velocity. Phase velocity could also have been measured, for example, by summing the received signal at two spatially separated locations and applying the amplitude spectrum technique, mentioned in section 2.2.1, to the resulting waveform. However, since, the modes were generally non-dispersive, the result would simply have been the same as the group velocity. Measurement of group velocity is both straightforward and quick. Where a number of possible signal paths in the plate caused confusion, particular reflections or signals were often identified simply by damping local areas of the plate with ‘BluTack’ and observing the change in amplitude of the received signal.

2.4 Numerical techniques

The range of cases amenable to an exact analytical solution is very limited, not least from a practical point of view. Each change in geometry requires the solution of a new set of field equations and as the geometry becomes more complex the boundary conditions become more difficult to satisfy. Approximate analytical methods such as the variational and perturbation methods may be useful for relatively minor deviations from the general system but become cumbersome for more complex geometries. These techniques do however, provide much clearer insight into the physical nature of the interaction of waves with changes in the system and therefore have a useful role. For accurate analysis of the complex geometries commonly encountered in industrial applications, numerical techniques are usually employed. Of these the finite-element (FE) method is the most popular. Finite difference (FD) schemes were found by Blake (1988) to be less stable and this was confirmed by Alleyne (1991). Nevertheless FD schemes are still employed for guided wave simulation owing to their speed and simple implementation compared with FE, see for example Balasubramanyam, *et al.* (1996). One of the disadvantages of all numerical techniques is the time taken to run each model. Recently this has been significantly improved by so called hybrid methods. Koshiba, *et al.* (1984) applied the hybrid method to a FE analysis of isotropic plates and Cho and Rose (1996) applied the hybrid method to a boundary element approach. The hybrid method utilises analytical methods for the simpler areas with uniform geometry together with numerical methods for localised areas where the geometry of the model changes. These two types of region are coupled by means of normal mode expansions at the boundaries of the numerically evaluated areas. Such formulations were not available to the author and purely numerical methods were employed at the expense of some additional computation time.

2.4.1 Dynamic Finite-element Analysis in this project.

The program 'FE77' was used for the numerical analysis in this project. This program was developed at Imperial College by Hitchings (1995) and offers an explicit time marching implementation of the finite-element method. This project generally employed two-dimensional, plane-strain models that model the propagation of plane waves with no components in the z direction. A typical arrangement for a simple plate, which, is modelled in cross-section, is shown in figure 2.8.

2.4.1.1 Mesh configuration

The first consideration in formulating a finite-element model is the configuration of the mesh and four-noded quadrilateral elements were chosen for the two-dimensional models presented in this work. These linear elements are stiffer and consequently less accurate than quadratic elements such as the eight-noded quadrilaterals, commonly used in static analysis. However, they offer a significant saving in computation time, particularly for the large models considered here, and their accuracy has been found in similar work to be acceptable [Alleyne and Cawley (1992)]. It is generally preferable to use square elements of the same size throughout the model, in order to avoid the possibility of erroneous reflections at the boundaries between regions with different elements. In most of the models representing aircraft joints, the jointing layer was comparatively thin with respect to the rest of the model and for some modes, the mode shape across jointing layer varied considerably. An efficient mesh size (determined by Blake's rules, outlined below), resulted in a jointing region of just two elements thick, and concern arose as to whether such a mesh could adequately model this layer. Consequently, several comparative models with four rectangular elements across the thickness of the jointing layer were run. The elements in the jointing regions of each of these models had an aspect ratio of two, retaining the same length in the propagation direction as those of the other regions of the model, as illustrated in figure 2.9. In each case the results were identical to the equivalent model with square elements, and so most of the subsequent modelling simply employed two square elements across the jointing layer. However, for some of the large acoustic-emission models, discussed in chapter 6, an efficient mesh size, would, have resulted in a jointing region of just one element thick and these were therefore modelled using the rectangular-element scheme.

In all cases the inter-nodal spacing in the propagation direction (Λ) was determined from the wavelength (λ_s) of the slowest mode within the bandwidth of the excitation signal. Applying the first of two rules-of-thumb established by Blake (1988) to assure accuracy and stability of finite-element models, such that:

$$\frac{\lambda_s}{20} < \Lambda < \frac{\lambda_s}{8} \tag{2.10}$$

a mesh size of $\lambda_s/10$ was usually employed. Finer mesh sizes than this require unnecessary computation time and may be less accurate, owing to rounding errors in the computation.

2.4.1.2 Time Step

To determine an appropriate time step the second of Blake's rules was applied. This states effectively that, for stability, the fastest mode must not cross the shortest distance between adjacent nodes (α) in less than 0.8 time steps, or:

$$\Delta t < \frac{0.8\alpha}{c_f} \tag{2.11}$$

where Δt is the time step and c_f is the velocity of the fastest mode within the excitation bandwidth. Thus, having determined the frequency and bandwidth of the input signal, the mesh size and time step are also established.

2.4.1.3 Excitation

The next consideration is the excitation function to be applied to each of the input nodes of the model (shown for example in figure 2.7), in order to generate just the required mode. Two possible schemes were employed. The simplest approach is to force each input mode with a windowed sinusoidal function of frequency equal to the centre frequency of excitation. The forcing amplitude for each input node is proportional to the relative displacement seen in the mode shape at the position of the node in the plate thickness and at the centre frequency of the input. This scheme, called 'centre frequency forcing', was used in cases where modes were well isolated.

A more rigorous excitation scheme that applies the exact mode shape over the excitation bandwidth is used where modes are less easily isolated [Pavlakovic, *et al.* (1998)]. Firstly, the excitation bandwidth is divided into a number of discrete frequency points, each of which is associated with a relative amplitude dependent upon the frequency spectrum of the excitation function (usually a Hanning windowed, sinusoidal tone burst). At each frequency point on the chosen mode, a separate mode shape is identified and for each through-thickness node point, an amplitude is assigned, as in the centre frequency forcing method. This is multiplied by the relevant amplitude from the excitation function frequency spectrum, giving a forcing amplitude for the particular node at each frequency within the excitation spectrum bandwidth. In this way, a frequency spectrum is obtained for the forcing function of each input node. An inverse FFT is then performed on each of these spectra, to obtain the temporal forcing function for each input node. This exact mode shape forcing scheme is only required for the higher order modes, which may otherwise be difficult to isolate, and when the excitation bandwidth extends over mode cut-off frequencies. In the latter case, instability would otherwise arise owing to the apparent infinite velocity of the cut-off mode, which would obviously violate the second of Blake's rules if it were generated.

2.4.1.4 Monitoring.

Finally, decisions have to be made regarding the monitoring scheme by which information is derived from the model. Stress or displacement in both in-plane and out-of-plane directions can be monitored at any node in the plate model over the time duration of the model. In this project, only displacements were required and there are, once again, several useful schemes that may be employed. In most instances, where a signal corresponding to that received in experiments by a laser or local immersion transduction is required, surface nodes are monitored. The position of the nodes and indeed the length of the model, were chosen such that the reflections of the modes from points of interest were adequately separated in the time domain. Where this was not possible, sufficient nodes were monitored to allow a two-dimensional Fourier transform (2DFFT) to be performed, in order to separate the modes in wavenumber-frequency space [Alleyne and Cawley (1991)]. In all cases, 64 nodes were used for this purpose, giving adequate wavenumber resolution; the range required in the wavenumber spectrum, determined the distance between each monitoring node. Similarly, the x and y displacements at each monitoring node were recorded at time intervals determined by the range required in the frequency spectrum. Clearly, the required spatial and temporal sampling intervals required were rounded to increments of the mesh size and time step respectively.

A simple way of separating symmetric and anti-symmetric modes is to monitor in-plane and out-of-plane displacements at the mid-plane of the plate, since at this position anti-symmetric modes have only out-of-plane displacement and symmetric modes exhibit only in-plane displacements. This method was therefore usefully employed in some models to separate the two fundamental modes. A further scheme is to monitor the *x* and *y* displacements at nodes with the same *x* co-ordinate through the thickness of the model. Since, according to normal mode theory [Auld (1990)], the displacement at a particular point in the system can be expressed as a sum of the normal mode components, it is possible to determine the relative amplitudes of the propagating modes at a given location, using a normal mode extraction technique [Pavlakovic (1998)]. However, current implementations of this technique were not able to operate on multiple layers and could not resolve wavenumbers of opposite sign. (ie waves travelling in opposite directions). Consequently, little use was made of this method.

Having devised a model of appropriate size and determined the mesh size, time step, excitation, and monitoring scheme, the model was run for an appropriate duration to allow sufficient propagation of modes of interest. The models took from between several hours to three days to run, after which, the results were processed in much the same way as described for experimental results, and the resulting group velocity and attenuation parameters were compared with those obtained from similar geometries by experiment.

2.5 Summary

This chapter began by discussing measurement of the acoustic properties of the aircraft materials identified in Chapter 1, namely, PRC sealant, and Redux adhesive (published data being accepted for Duralumin). Density was measured by the well-known liquid displacement method, and the bulk wave velocities and attenuation in cured samples of Redux adhesive were measured using the amplitude spectrum and multiple-through-transmission techniques respectively. These standard methods are detailed along with the results in Appendix B.

Whilst it proved possible to measure the longitudinal wave velocity in PRC using the amplitude spectrum method, measurement of the shear wave velocity necessitated a somewhat less reliable method based on reflection coefficient at a PRC/polycarbonate junction owing to the very high shear wave attenuation. Longitudinal wave attenuation in PRC was established by the $F_o/F/B_1$ method that requires only one backwall echo, however, attempts to measure the shear wave attenuation using an available 6 MHz shear wave probe did not succeed. Shear wave attenuation in PRC might perhaps have been measured by measuring the transmission coefficient of mode-converted shear waves, in a through transmission arrangement employing narrow band signals. Instead, an artificially high value was assumed, reflecting the fact that there is practically no shear wave propagation in PRC.

Following the discussion of acoustic property measurements, the general experimental techniques were described. The local immersion technique was generally used to excite and receive signals at the skin surface and special wax baths were developed to reduce or eliminate unwanted reverberations in the water path. In some cases a laser interferometer was employed as a receiver, and this equipment could be configured to measure either in-plane or out-of-plane surface displacements independently.

Finally the chapter introduced the numerical analysis employed at various stages of the project. Four-noded quadrilateral elements were used in finite element analysis, and the formulation of the models was discussed, including the determination of maximum element size and maximum time step from the velocities of the slowest and fastest waves respectively. The models generally employed a simple centre-frequency-forcing regime, discussed in the text, and the in-plane and out-of-plane displacements were usually monitored at surface nodes along the model. In some cases however, these displacements were monitored at the mid-plane in order to separate symmetric and anti-symmetric modes.

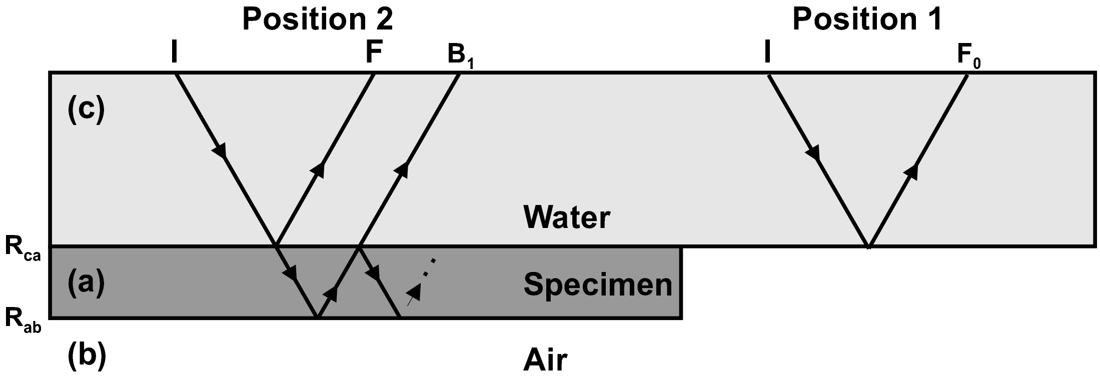

Fig 2.1 Ray diagram for the $F_0/F/B_1$ *method. (Rays are normal to the interfaces but are shown inclined for clarity.)*

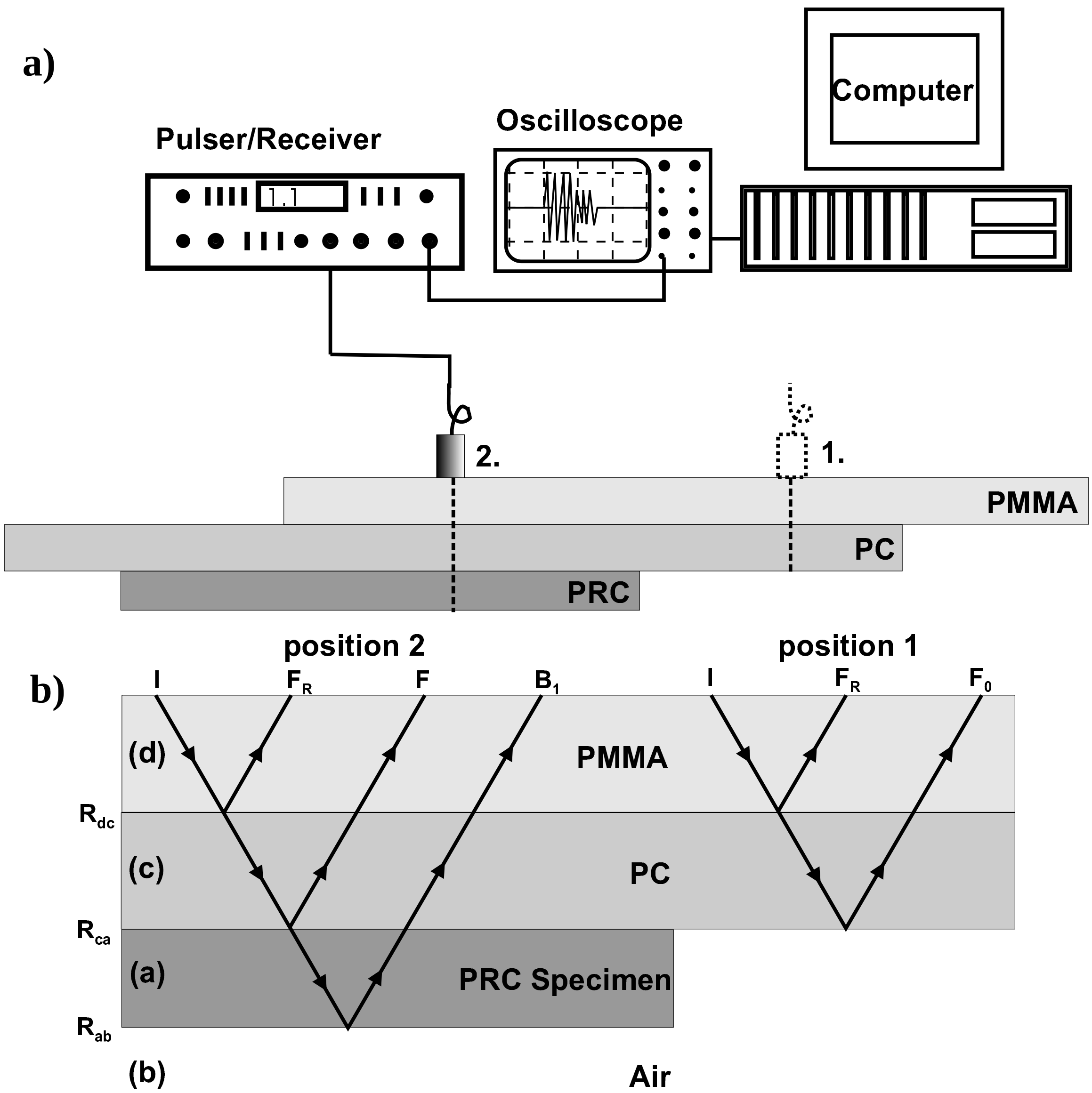

Fig 2. 2 (a) Schematic diagram of the equipment arrangement and specimen construction used in attenuation measurement of PRC sealant. (b) Ray diagram of the relevant signals and reflection coefficients in the attenuation measurement shown in (a).

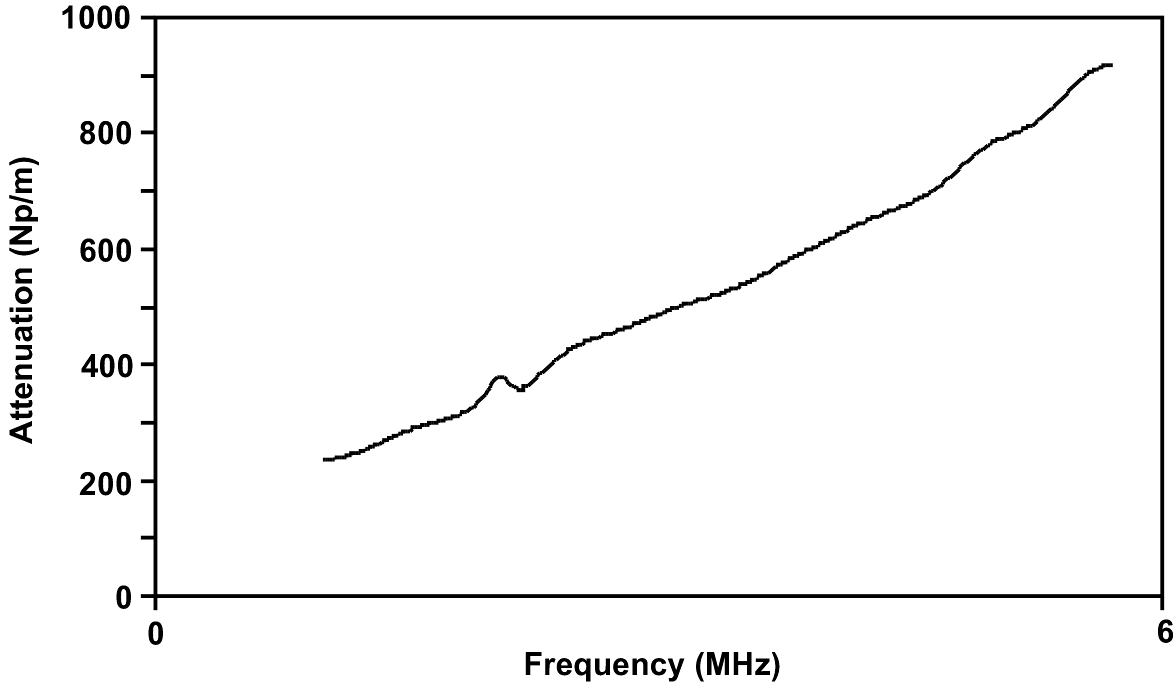

Fig 2.3 Spectrum of longitudinal bulk wave attenuation in PRC sealant.

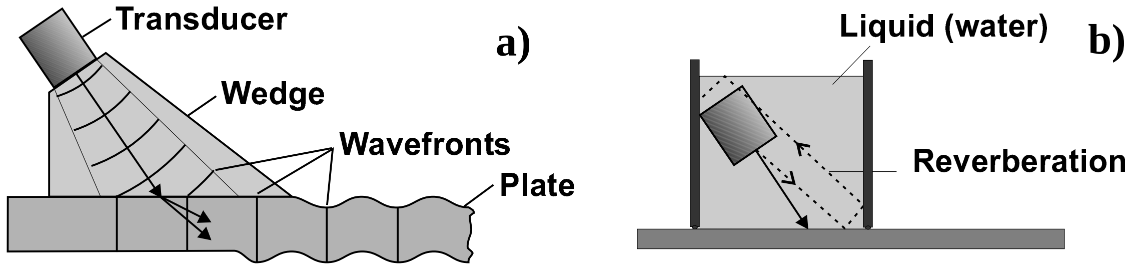

Fig 2. 4 Coincidence principle of guided wave excitation: (a) Solid or 'wedge' coupling (b) Local immersion coupling

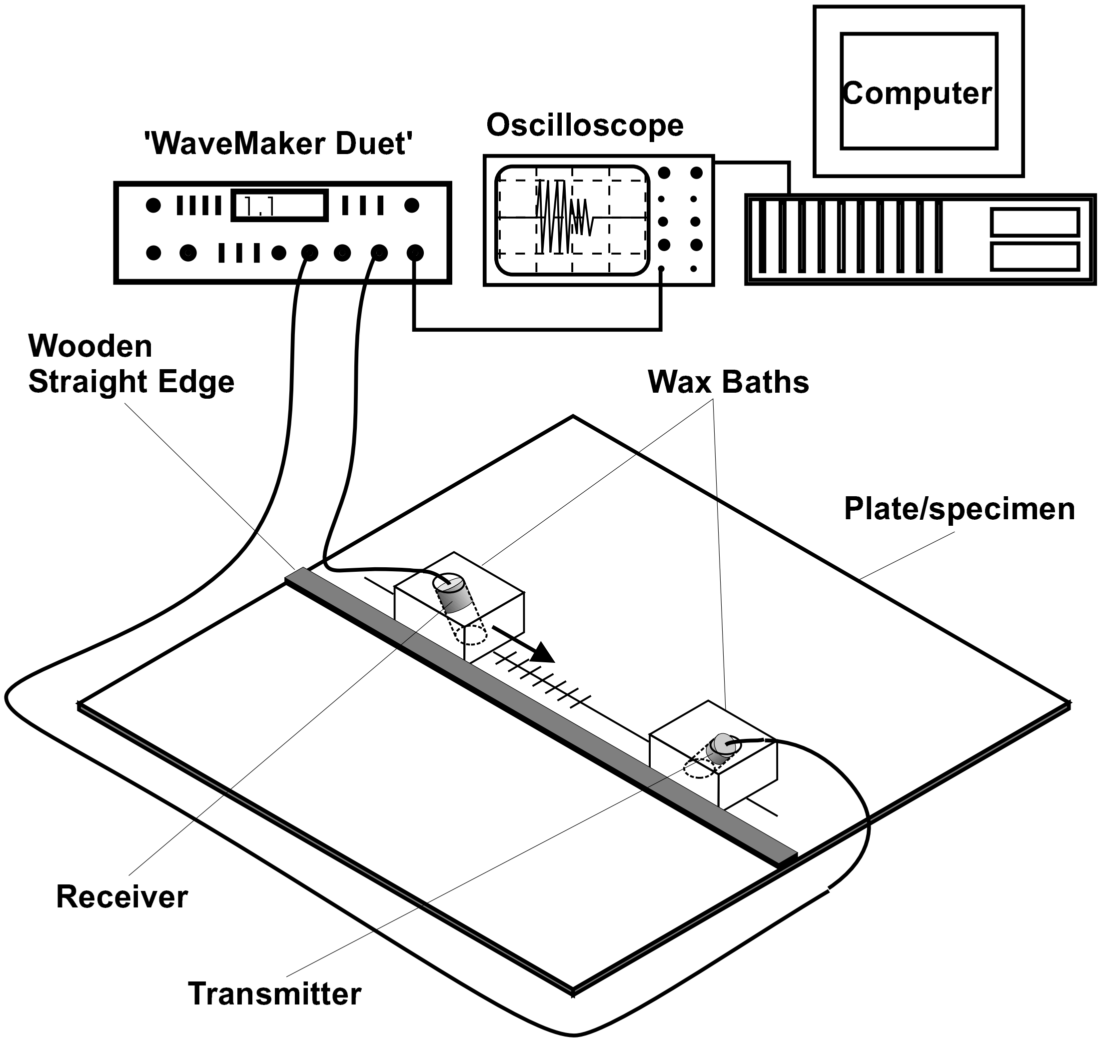

Fig 2.5 Schematic view of the pitch/catch arrangement used in experiments.

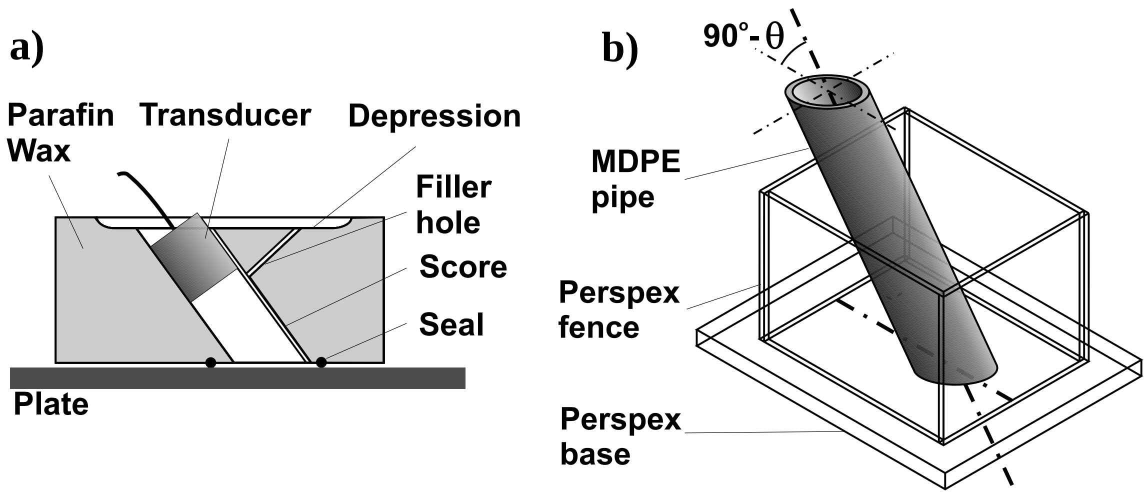

Fig 2.6 (a) Side view of wax bath for local immersion excitation. (b) Mould used to cast wax baths.

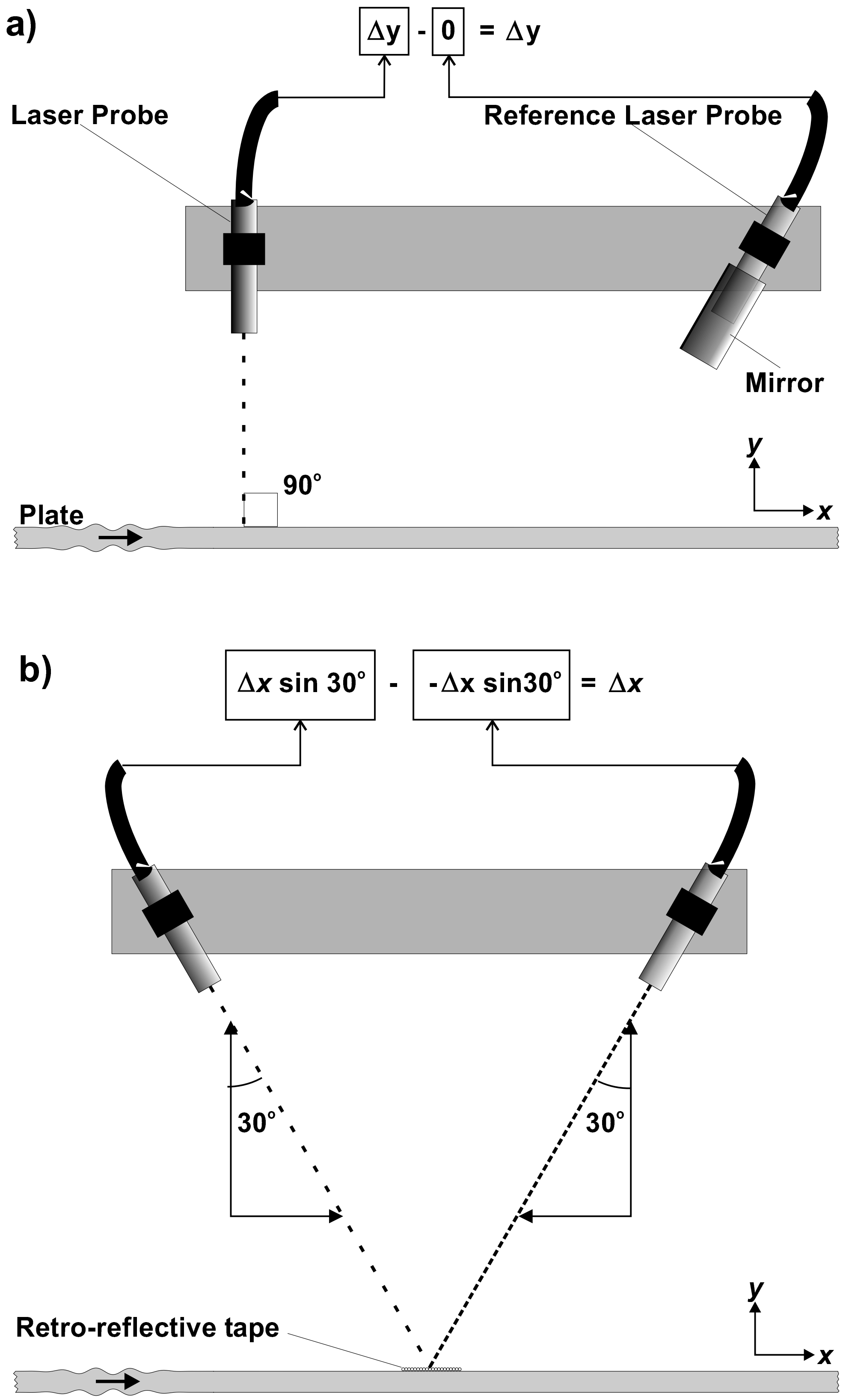

Fig 2.7 Laser measurement of signal surface displacement components: a) Out-of-plane b) In-plane.

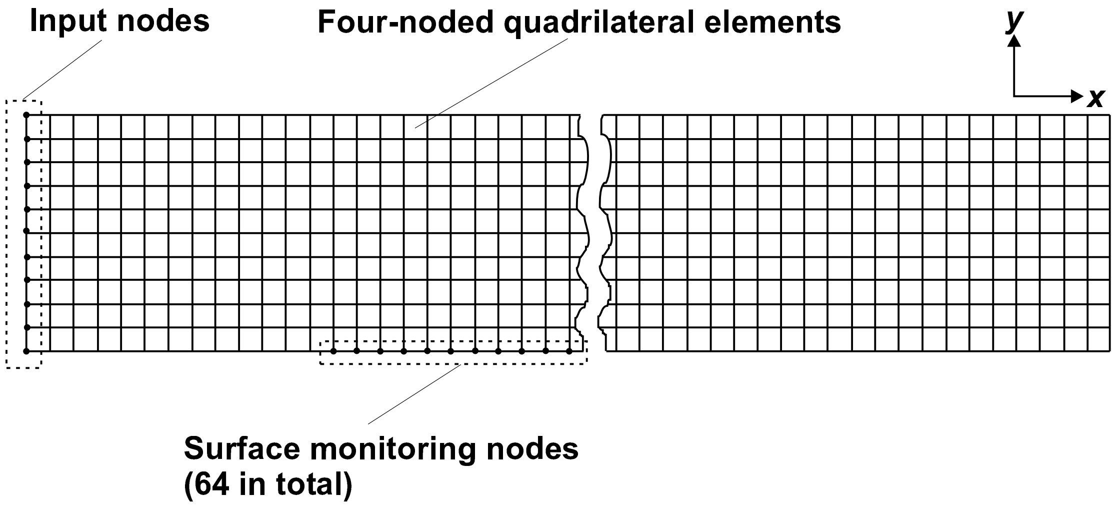

Fig 2. 8 A typical two-dimensional plane strain finite-element model of a simple plate employing four-noded quadrilateral elements and having a surface monitoring region for 2DFFT analysis. (The mesh size is exaggerated for clarity).

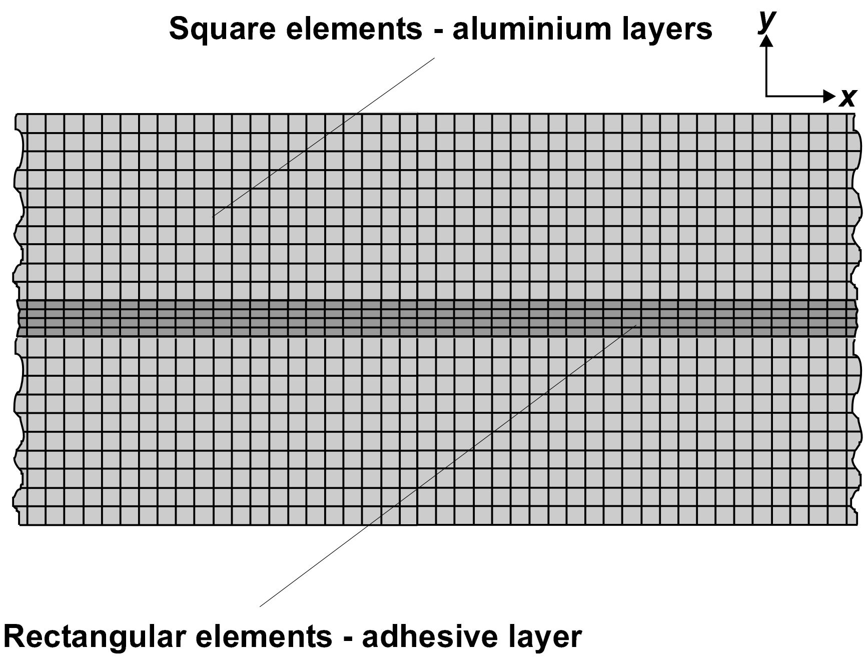

Fig 2.9 Finite-element mesh used to model double-skin systems in which the thin jointing layer is modelled by rectangular elements of aspect ratio = 2.

3. Guided waves in single skin

3.1 Introduction

Having discussed the techniques to be employed and established the acoustic properties of the materials involved, this chapter examines the first and simplest of the structural features: the single skin. The analysis of the free plate system, that is to say a plate in a vacuum, can be found in many standard texts including for example Graff (1973) . However, key features of the theoretical derivation of the dispersion curves, for the free plate system, are reviewed in Appendix A. The free plate case closely approximates the single-skin case owing to the very large difference in the acoustic properties of the air and the skin and so, for the analysis presented in this chapter, the free plate case is regarded as the single-skin case. It is worth reiterating the point made in chapter one, that a mode regarded as potentially useful in respect of propagation across any of the multi-layered systems, must also be capable of efficient propagation in the single skin which forms so much of the fuselage structure. The dispersion curves for a single skin are presented in figure 3.1 and this chapter is firstly concerned with the practical issue of identifying the potentially useful modes, on which, ideally, all further selection should be based.

Since tapered skin is effectively a single layered system, the focus of this chapter provides a convenient point at which to discuss the tapered skin case. The chapter therefore closes with an examination of asymmetrically tapering skin and focuses on the possibility of reflection and mode conversion at changes in section.

3.2 Mode Selection

3.2.1 Discussion of selection factors

The dispersion curves of any given waveguide system convey a great deal of information by which the potential of the various modes can be evaluated and compared, and they are invariably the first modelling tool used in the process of selecting the most promising modes for use in a practical application. Since the work of this project focussed upon long-range propagation, factors affecting mode amplitude are of primary concern.

The group velocity spectrum in figure 3.1b) gives an indication of dispersion. In order to transmit information about flaws in a component, it is necessary to employ a non-continuous signal, thus, a tone burst of finite duration is generally employed. Temporally limiting the signal duration causes its energy to be distributed over a band of frequencies centred on the excitation frequency, with a distribution function that is dependent upon the shape of the toneburst envelope and the tone frequency. It is consequently not possible to excite just a single point on the dispersion curve and significant excitation of frequency sidebands above and below the excitation frequency occurs. If the gradient of the dispersion curve is not zero, then the velocities of the sideband frequency components will not be the same as that of the centre frequency component. The result is that signal energy spreads spatially in the plate as propagation progresses. Since the original energy is now distributed over a wider area, the maximum amplitude of the signal is reduced. For example, figure 3.2 illustrates the change in a highly dispersive S_0 signal after propagating 100mm. Reducing the signal bandwidth by increasing the number of cycles in the excitation signal will reduce the effects of dispersion and in the case of non-dispersive points it is necessary to limit the bandwidth to the non-dispersive region of the group velocity curve. This is illustrated in figure 3.3, for the narrow non-dispersive minima on the S_0 curve. Both figures 3.2 and 3.3 are simulated signals that have been generated from the dispersion predictions for the single skin. In each case the input tone burst function is Fourier transformed and the frequency components delayed by an appropriate period according to their respective phase velocities and the required distance travelled. These delayed frequency components are then inverse Fourier transformed to give the predicted time domain signal, having propagated over the distance specified. In addition to the amplitude reduction, the ability of the signal to resolve closely spaced entities diminishes as the signal envelope extends. Wilcox (1998) showed that to maximise the resolution of a dispersive signal for a given propagation distance there is an optimum number of cycles in the tone that represents the best compromise between a short initial signal and the effect of dispersion. However, as will be seen, the need to isolate a mode also has a bearing on the length of the excitation tone. Furthermore, in a long-range structural health-monitoring system operating in pulse-echo mode, the distance to a flaw is of course unknown and may vary widely. It will not therefore be possible to arrange for the optimum excitation tone length. This reinforces the case for employing non-dispersive modes. The non-dispersive modes, (points of zero group velocity gradient), are marked in figure 3.1.

Two of the non-dispersive points shown in figure 3.1 occur at minima on the group velocity curves of the S_0 and A_1 modes. At these points, and particularly in the case of the S_0 minimum where the non-dispersive band is narrow, the lower amplitude sidebands of a broadband signal will travel faster than the centre frequency component. These sideband components will therefore be received before the main component and the received signal will appear similar to that shown in figure 3.3 (A) or (B) (depending on the length of the tone burst employed). This leads to confusion when, for example in the case of a reflected echo from a defect, the defect location is established from the time of flight of the leading edge of the signal. Also the minima, by definition, tend to have lower group velocities than non-dispersive maxima and this too is disadvantageous. Ideally, as indicated in chapter one, just a single mode is used in order to avoid complicated and confusing signals. However, the interaction of modes with structural features and defects results in mode conversion, and in most instances the received signal will comprise more than one mode. In these circumstances clarity is improved if the signals of different modes are separated in time as far as possible. Using the fastest possible mode for the excitation signal ensures that it will arrive ahead of any other mode, thus simplifying signal analysis. For this reason the non-dispersive maxima, that also represents the fastest possible mode at a given frequency, may be preferred to the other non-dispersive points and such points are seen on the curves of S_0: (point 1), A_0: (point2), A_1: (point 4) and S_1: (point 5) in figure 3.1b).

The dispersion curves of figure 3.1 also indicate another factor to be considered when selecting promising modes: the degree to which a mode can be isolated during excitation in order to achieve single mode generation. This depends upon the separation of the desired mode from other modes in both the phase velocity (or wavenumber) dimension and the frequency dimension and mode points in close proximity to those of other modes on the phase velocity spectrum are more difficult to isolate. It has already been observed that mode conversion is an inevitable consequence of guided wave interaction with structural features and in a linear system this is limited to other modes existing within the frequency bandwidth of the incident signal. Since the number of possible modes increases with frequency, lower bands may be preferred in order to minimise the number of mode-converted signals. The redistribution of energy to other modes depends on many factors, but, as will be seen in chapter 3, modes with similar phase velocity to that of the input mode may be preferentially excited by mode conversion. Mode purity is thus reduced and this then is a further reason for avoiding modes with similar phase velocity to others at the same frequency. The mode conversion issue plays an important part in the analysis of multi-layered systems and will be discussed more fully in chapters 4 and 5.

Whilst the dispersion curves are of crucial importance in mode selection, other important factors are not directly discernible from these curves. For the single-skin case such factors would include excitability and defect sensitivity, both of which are largely determined by mode shape. The first of these describes the efficiency of excitation of a given mode by the particular arrangement of forces applied to the plate by the transduction system. The second factor describes the degree of interaction between a mode and a particular type of defect. Such interactions are generally complex and are outside the scope of this work. It is, however, appropriate to consider that in order to interact with a flaw occupying a limited region of the plate thickness, wave energy must exist in that region. To take an obvious example, a surface wave on one side of the plate will not be sensitive to surface defects on the opposite side, because wave energy decays exponentially with distance from the surface. Not withstanding these considerations, dispersion is by far the most important and overriding factor where long-range propagation in the single skin is concerned, for it largely determines the signal attenuation with propagation distance. The frequencies of the modes shown in figure 3.1 do not exceed 5 MHz and in this frequency band, viscoelastic attenuation and that due to scatter are sufficiently low to be ignored. The dispersion curves of figure 3.1 are those of a plate in a vacuum and in this system no leakage of acoustic energy from the plate is possible. This is not strictly accurate for a plate in air, since some leakage into the surrounding air does occur. However, the very large impedance difference between the aluminium skin and the air results in negligible coupling and the attenuation (generally less than 0.1Np/m for frequencies of less than 5 MHz) is ignored. In the system considered in chapter 4, where the plate is bounded by a material other than air, significant leakage generally occurs.

The only other significant attenuation factor affecting the lower order modes in the single-skin system is that due to beam divergence. Generally, the acoustic signal generated by a transducer of finite size tends to be divergent. Consequently, the wavefronts extend with propagation distance and their energy is therefore more widely distributed, resulting in a decreasing amplitude with propagation distance. Guided waves propagating in all directions in the plane of the plate, from a point source, constitute the simple cylindrical wave case in which amplitude (A_r) decreases inversely with the square root of the radial distance (r) [Krautkramer and Krautkramer (1983)],

$$A_r = A_i\sqrt{\frac{1}{r}} \tag{3.1}$$

where A_i is the initial amplitude. The commonly used units of attenuation (Nepers), as detailed in appendix B, assume an exponential decay to which this mechanism clearly does not conform. The amplitude ratio of two points located in the cylindrical wave field depends upon the ratio of their respective distances from the source point, rather than an absolute distance. It is therefore difficult to express this function in terms of Nepers/m or dB/m. However, it can be seen that for points remote from the source point the attenuation will be very small. For example, considering two points located at distances of one and two meters from a point source, the relative attenuation due to beam divergence will be equivalent to 0.35 Np/m (3 dB/m). Beam divergence from real transducers is more complex and depends upon the particular characteristics of the transducer employed, namely the frequency, amplitude and distribution of forces applied to the plate. The cylindrical wave may be considered the worst case, and it roughly indicates the low order of decay expected.

3.2.2 Conclusions

Having discussed the factors considered in the selection of promising modes for long range propagation in a single skin and determined that freedom from dispersion is the principal criterion, it is concluded that the non-dispersive modes comprise a set of promising candidates, of which some have further advantages and disadvantages.

The S_0 mode at 0.5 MHz-mm (marked (1) at 0.42 MHz in fig 3.1) has the highest velocity and is non- dispersive over a relatively broad band. Many researchers have focused on the potential of this mode and some, for example Sun (1993), have studied its use in respect of aircraft structural defects. It has the simplest of mode shapes, dominated by in-plane (IP) displacement, such that the out-of-plane (OOP) displacement at the surface reduces as the mode tends to a purely extensional wave at zero wavenumber. Consequently, the OOP excitability of this mode is poor. The mode is very well isolated in phase velocity from the only other mode existing at this frequency: that of A_0.

The A_0 mode at 1.36 MHz-mm (marked (2) at 1.13 MHz in figure 3.1) is also well isolated from S_0 in phase velocity, but has much greater OOP excitability. This mode has been found by many workers to have excellent potential for the NDE of simple free plate systems. See for example Alleyne and Cawley (1992).

Although the S_0 mode at 2.48 MHz-mm (marked (3) at 2.07 MHz in figure 3.1) has excellent OOP excitability, the rather sharp minimum at low velocity is disadvantageous for the reasons previously explained, and it is therefore less well suited to long range NDE.

At 2.65 MHz-mm the A_1 mode (marked (4) at 2.21 MHz in figure 3.1) is poorly isolated from S_1 and unfortunately both modes have similar OOP excitability. This mode also exhibits very little displacement or strain energy at the mid-plane of the plate and therefore has little defect sensitivity in this region.

Despite its useful high velocity, the S_1 mode at 4 MHz-mm (marked (5) at 3.33 MHz in figure 3.1) has very poor OOP excitability. It is also poorly isolated from the A_1 mode, which has high OOP excitability. If this mode is employed, then surface mounted transducers would need to excite, and sense in-plane displacements at the plate surface.

The A_1 mode at 4.66 MHz-mm (marked (6) at 3.88 MHz in figure 3.1) has a high OOP excitability and is reasonably well isolated in phase velocity. However, its low group velocity is particularly disadvantageous at this higher frequency where many other modes exist and it would be important to ensure single mode operation if this mode was used.

In summary, it is apparent that for a transduction system sensitive to normal displacement at the plate surface, the A_0 mode at 1.36 MHz-mm is the most promising with the A_1 mode at 2.65 MHz-mm a possible second choice. However, if transducers that are sensitive to in-plane displacement at the surface are obtainable, the low frequency S_0 mode and S_1 mode at 4.01 MHz-mm may be preferred. In chapter 5, it will become clear that OOP excitability and leakage attenuation in multi-layered systems are closely related and since these factors are antagonistic, an IP transduction system may be essential. Provided dispersion is avoided there is no difficulty in achieving long range propagation with amplitude decay of less than 40 dB/m.

3.3 Tapering Skin

3.3.1 Introduction

Chapter one briefly indicated that skins of tapering thickness are commonly found in the wings, and are occasionally employed in reinforced areas of the fuselage. The boundaries of fuselage doubler plates may also be chamfered, so that this too forms an asymmetrically tapering skin thickness. Although the tapering skin case is not a common feature of semi-monocoque fuselage construction, it was felt that a brief investigation should attempt to ascertain whether a large reflection would be likely to occur at the change in section, at the boundaries of the tapered region. The degree of taper that might be expected is fairly arbitrary, ranging from very fine tapering indeed, in wing skins, to perhaps 1:5 in the case of chamfering. In order to limit the time spent, it was decided to study asymmetric tapers with gradients of 1:80, 1:40, 1:20, 1:10 and 1:5. The asymmetric taper represents the worst case because an asymmetric change in thickness allows mode conversion to all of the possible modes of the system, rather than just modes of the same type as the incident mode.

By the time that this work was undertaken, study of mode propagation across other systems had already indicated that, practically, only the fundamental modes need to be considered. Analytical study of tapering waveguides is difficult and appears currently to be limited to early and somewhat crude one-dimensional approximations for the acoustic field in a rectangular horn, such as may be found, for example, in Morse (1948). A numerical approach was therefore adopted. Since the work described below was completed, an experimental study of guided wave propagation in an immersed plate has been reported by Guillet, *et al.* (1999). Although approach of this work was somewhat different, the conclusions generally agree with the findings given in this section in respect of the fundamental modes.

3.3.2 Numerical Study of Asymmetrically Tapering Skin

The finite-element approach described in chapter two was used to model the five cases of varying asymmetric taper mentioned (1:80, 1:40, 1:20, 1:10, 1:5). Clearly, each one of these cases can be achieved by numerous choices of thickness variation. However, the simplest approach was to use the designated skin thickness of 1.2 mm and the double-skin thickness of 2.4 mm and simply vary the length of tapering region to suit the required gradient. This also simplified the meshing of the finite-element model.

In the design of both numerical and experimental tests, due consideration must be given to the effect of changes in frequency-thickness product across the regions of the model or specimen. For example, a mode existing in the input region may be forced below its cut-off frequency-thickness product in a region of decreasing thickness. This will inevitably result in mode conversion to other modes. In the work presented here, the input mode was generally chosen to be non-dispersive.

3.3.2.1 Validation of the meshing options

In general, four-node quadrilateral elements have proved to be the best compromise between accuracy and computational efficiency, as indicated in chapter two. However, use of these elements allows two possible schemes for meshing the tapered region, and these are illustrated in figure 3.4. Figure 3.4(a) shows the stepped element approach in which the gradient is modelled as a series of abrupt changes in thickness of no more than the depth of one element. Provided that the element dimensions are sufficiently small, the step changes should not perturb the model sufficiently to cause erroneous reflections. This approach has already been used successfully by Alleyne and Cawley (1992) to model cracks that are inclined with respect to the plate surface. The second possible meshing arrangement, shown in figure 3.4(b) utilises the possibility of tapering the elements to match the required gradient. It is generally good practice in FE modelling to distort the elements as little as possible. However, since any change in element geometry implies a change in element stiffness, it is possible that erroneous reflections could occur that are the result of the change in element geometry, rather that the sectional change in the plate. Consequently, a simple evaluation of these competing schemes was carried out, which comprised two parts.

In the first part, three stepped models like that illustrated in figure 3.4(a) were run. Each model had the same external dimensions with an input region 2.4 mm thick and an output region 1.2 mm thick. These were separated by a region of tapering thickness with a gradient of 1:20. The first stepped element model had ten elements through the thickness, stepping down to five elements, whilst the second and third models had twenty and forty elements stepping down to ten and twenty elements respectively. In each case centre frequency forcing was employed and the end nodes of the input region were forced with a twenty cycle Hanning windowed tone burst of 0.56 MHz. The forcing amplitude at each input node was such that the mode shape of the A_0 mode was applied across the plate thickness. (Centre-frequency forcing' is described more fully in chapter two). This particular excitation generated a non-dispersive A_0 mode in the thicker input region. The results of these models were compared with that of a tapered element model with ten elements through the thickness in all regions. In all models, the in-plane and out-of-plane displacements were monitored at surface nodes in the input and output regions as shown in the figures 3.4 (a) and (b).

The in-plane displacement function with respect to time obtained from the first input node is presented in figures 3.5(a), (b) and (c) for the stepped models with ten, twenty and forty input elements respectively. The many permutations of mode conversion and reflection from the relatively close boundaries of the model regions made identification of the source of the reflections difficult. However, S_0 signals can easily be differentiated from those of A_0 by comparing the in-plane and out-of-plane displacement traces. These are of similar amplitude in A_0 signals, but for S_0, the in-plane amplitude is considerably greater. In order to provide additional confirmation of the mode type and also the direction of propagation, a complex, two-dimensional Fourier transform (2DFFT) was performed on the results from the 64 surface nodes in each monitoring region and where possible, reflections were isolated by gating in the time domain. The 2DFFT procedure, described by Alleyne and Cawley (1991) , differentiates backward and forward propagating modes with similar wavenumber, but is not able to resolve signals of the same mode, propagating in the same direction, that cannot be separated in the time domain. Such signals are likely to result from reverberation across the tapered region.

The incident A_0 signal (marked (1) on figure 3.5a)) is seen centred at roughly 0.03ms and this is followed by a reflected A_0 signal (2) centred at about 0.07ms and a reflected S_0 signal (3) centred at about 0.095ms. Whilst consideration of the time of flight indicates that the A_0 reflection originates from leading edge of the tapered region, the S_0 reflection appears to be the result of mode conversion at the trailing edge of the tapered region, followed by reflection from the specimen end. When the stepped element model results are compared with the corresponding result for the tapered element model, presented in figure 3.5(d), it is clear that since figure 3.5 (c) and (d) are similar, the stepped element model converges with that of the tapered element model as the number of elements increases. In fact, figures 3.5 (c) and (d) still differ by about 35% in respect of the amplitude of the S_0 reflection, though the difference in the A_0 reflection is less than 1%. It is possible therefore that still larger stepped models would be required in order to converge the results to less than 1%.

The second part of the model evaluation provided further validation of the tapered element model. Two further models were constructed, both of which defined a simple plate of constant thickness. The elements of the first model were made to taper by varying degrees, as shown schematically in figure 3.6. The results of this model, in respect of the same A_0 input signal, were compared with those of the control model, which had simple square elements. The output displacement waveforms recorded at corresponding monitored points in both models were identical to within 1%.

The conclusion from these two validation exercises is that at least in this case, the use of tapering elements provides a sizeable saving in terms of computational effort. The stepped element model required twelve times as many elements as the tapered element model, to give reasonable convergence, and took three days to run, compared with the tapered element model, which took about two hours. The reason for such a large difference in computing time is that when the mesh size is reduced, the time step must also be reduced to meet the stability criterion given by equation 2.11. The second validation exercise suggests that elements with tapers of up to 1:5 can be used safely, however, this exercise has only considered one input mode. Although the results justify the use of the tapered element model for a particular mode point, any change to a different frequency-thickness product or a higher order mode, with a more complex mode shape, should be independently validated.

3.3.2.2 Numerical Simulation of Reflections from tapered regions of varying gradient

The relative reflection ratios from the various taper gradients outlined previously were investigated for three different input modes: A_0 at 0.56 MHz, S_0 at 0.5 MHz and A_1 at 2.2 MHz. A similar finite-element model to that used for the validation of tapered elements shown in figure 3.4(b) was used and in each case only the length and the number of elements across the tapered region were adjusted to achieve the required gradient. Time traces similar to those shown in figure 3.5(d) were obtained from surface nodes in the input monitoring region. As in the validation case, the possibility of interference of reflections from the leading and trailing edges of the tapered region meant that a precise reflection coefficient for each mode could not be established. Table 3.1 indicates the reflection coefficient of the maximum reflection from the tapered region calculated from the maximum out-of-plane amplitude of the reflected signal. Figure 3.7 shows a typical example of a result from a model with a 1:5 taper and an incident S_0 mode. The various signals are identified in the figure caption and the establishment of the reflection coefficient for table 3.1 is illustrated.

3.3.2.3 Experimental validation of the numerical results

In order to validate the finite-element analysis a practical experiment along similar lines was undertaken. Test specimens were constructed by milling five, 2.4 mm thick sheets of aluminium alloy to the dimensions shown in figure 3.8(a). Larger test specimens would have been preferred in order to allow separation of the A_0 and S_0 reflections in the time domain, but it was not possible to mill larger specimens on the available machine tools. As in the numerical tests, the length of the tapered region was adjusted to give gradients of 1:80, 1:40, 1:20, 1:10 and 1:5. Figure 3.8(b) shows the experimental arrangement employed. A Hanning-windowed, twenty-cycle tone burst of the A_0 mode was generated by means of the local immersion wax bath as described in chapter two. Both incident and reflected signals were received by two separate methods: On the upper surface of the input region a conical transducer was used to monitor out-of-plane displacements, while at the corresponding point on the lower surface two co-focused laser probes monitored the in-plane displacements, as detailed in chapter two.

An example of the in-plane and out-of-plane displacement/time plots for the 1:5 taper are shown in figure 3.9, this gradient having the greatest amplitude reflections. Once again the reflections are not fully separated in time, but the peak, labelled (1), centred at 0.14ms in figure 3.9(a) corresponds with the S_0 reflection seen in the numerical result and caused by mode conversion at the trailing edge of the tapered region followed by reflection from the plate end. For each gradient, the maximum reflection from the tapered region found in the experiment is indicated, in brackets, in the column for A_0 in table 3.1. The experimental results for the 1:20 gradient were disregarded because the specimen was defective.

3.3.3 Conclusions

Although the numerical and experimental results are not directly comparable, owing to differences in the interference of the reflections from the ends of the tapered region, it is clear that in both cases the amplitudes of the reflections are of a very low order (<3%) and are roughly similar. Interference also obscures the trend but, as expected, the reflection amplitude increases with gradient. In general the finite-element results indicate that a reflection of less than 10% can be expected for gradients of up to 1:5. In most cases the reflection is insignificant.

	Input Mode		
Taper Gradient	S_0 at 0.5 MHz	A_0 at 0.56 MHz	A_1 at 2.2 MHz
1:80	0.003	0 (0)	0.005
1:40	0.008	0.005 (0.018)	0.016
1:20	0.020	0.008 (disregarded)	0.027
1:10	0.034	0.027 (0.020)	0.064
1:5	0.048	0.030 (0.023)	0.104

Table 3. 1 Maximum reflection coefficient from the tapered region predicted by finite-element analysis considering out-of-plane displacements. Experimentally measured values for input A_0 *are shown in brackets.*

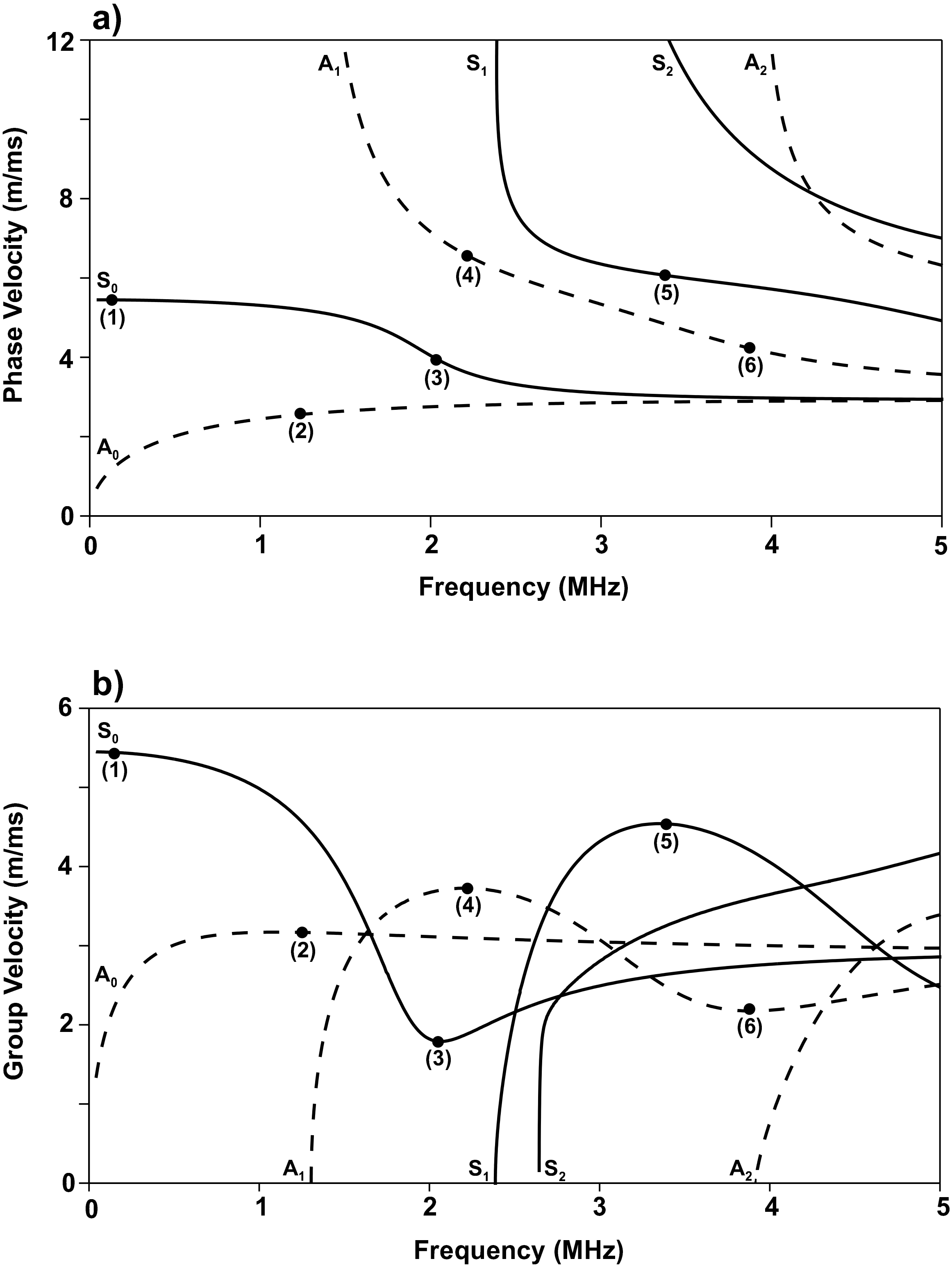

Fig 3.1 a) Phase velocity and b) Group velocity spectra for Lamb modes in an aircraft skin (1.2 mm thick).
: Anti-symmetric modes. : Symmetric modes.

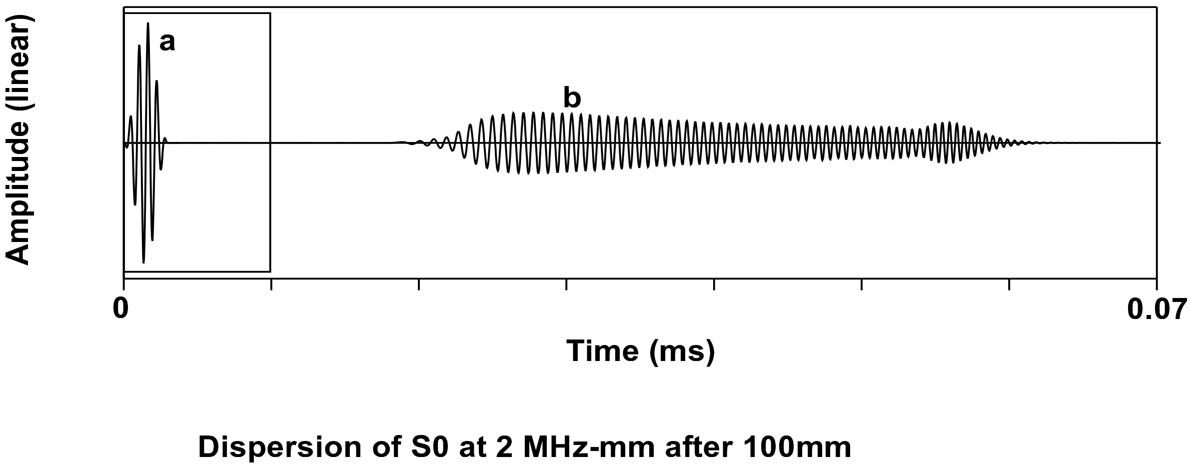

Fig 3.2 The highly dispersive S_0 mode at 2 MHz-mm (a) before propagation and (b) after propagating 100mm

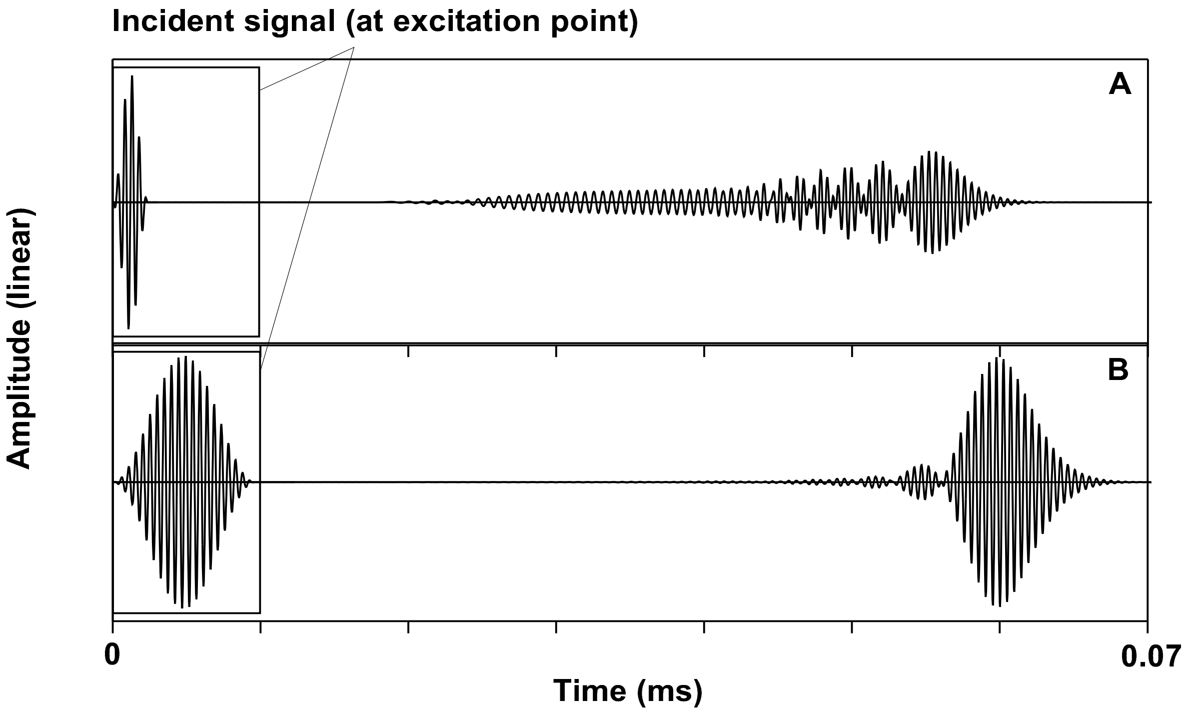

Fig 3.3 Propagation of the non-dispersive S_0 mode at 2.48 MHz-mm comparing the effect of excitation tone length. (A) Shows the case of a 5 cycle Hanning windowed tone burst and (B) Shows the case of a 20 cycle Hanning windowed tone burst. In both graphs the incident signal is shown followed by the signal after propagating for 100mm.

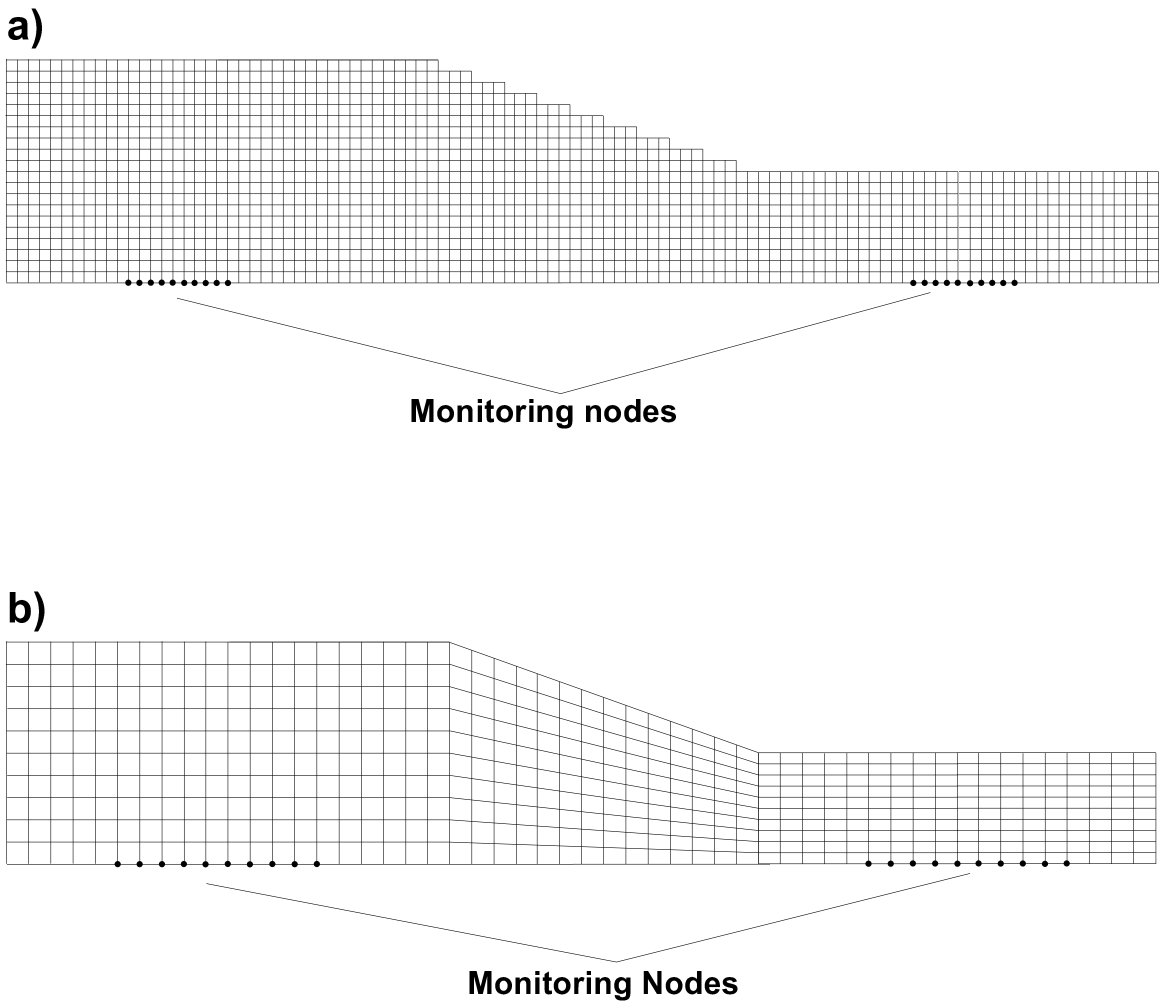

Fig 3.4 Finite-element mesh options for modelling a region of tapering thickness. (a) The stepped element model. (b) The tapered element model.

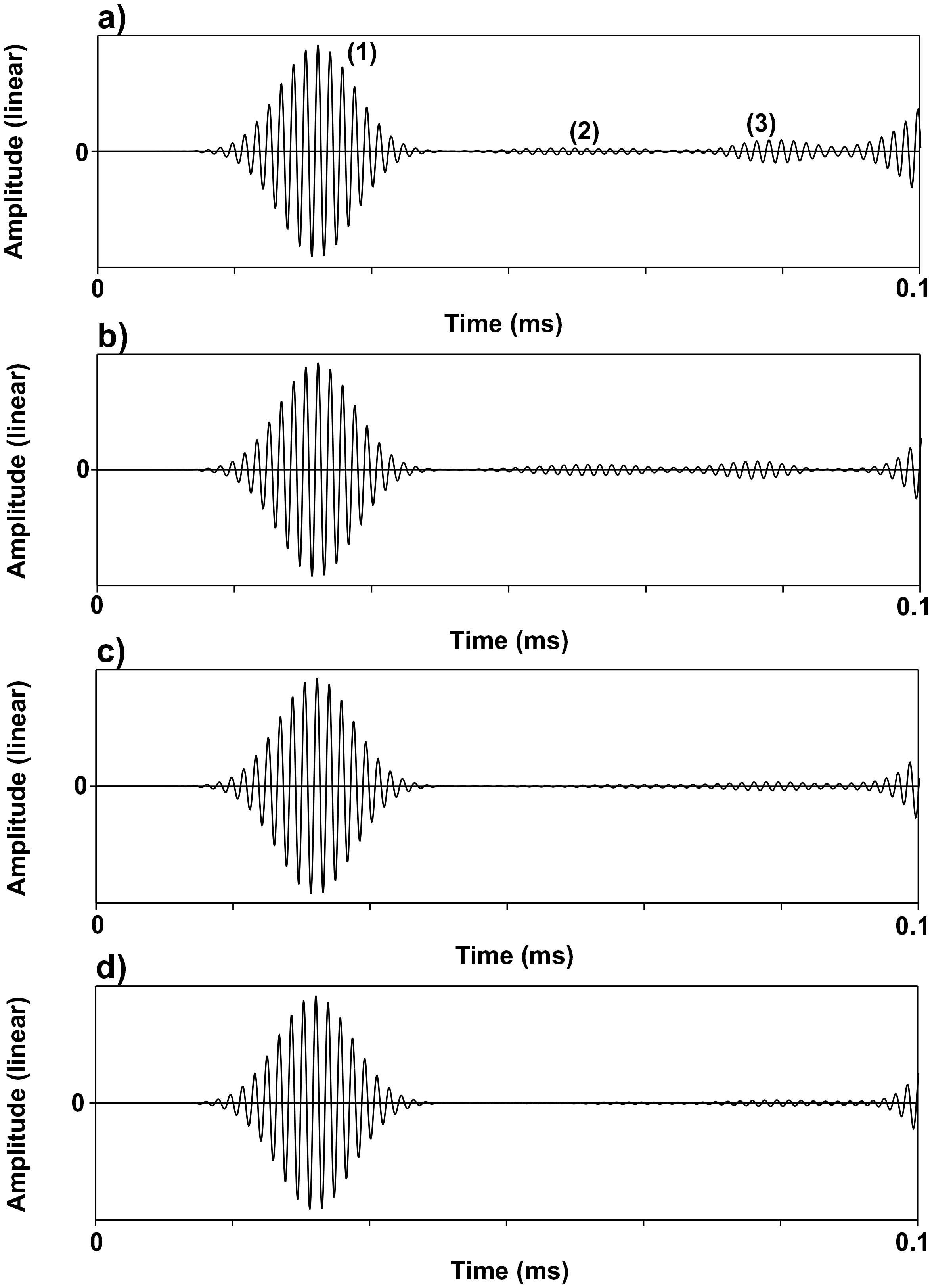

Fig 3.5 The in-plane displacement/time traces received from the first input monitoring node for: (a) the stepped *model with* ten *elements across the thickness of the input region, (b) the* stepped *model with* twenty *elements across the thickness of the input region, (c) the* stepped *model with* forty *elements across the thickness of the input region, (d) the* tapered *element model with* ten *elements across the thickness of all the regions.*

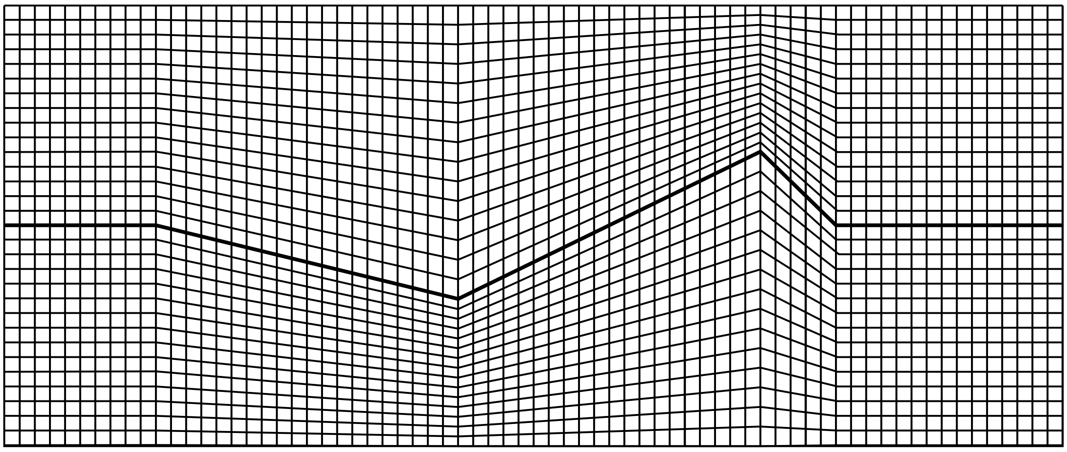

Fig 3.6 Plane plate finite-element model used to validate the use of tapered elements of varying gradients in subsequent modelling.

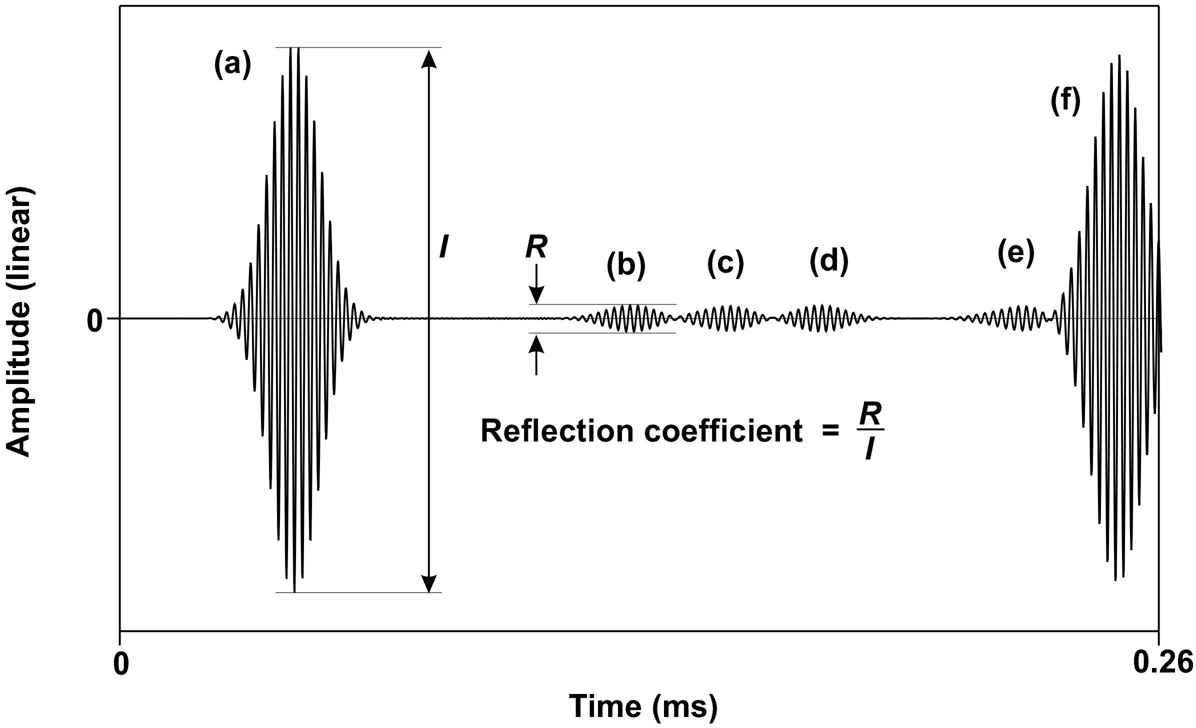

Fig 3.7 Out of plane displacement result from FE model with a 1:5 taper for input S_0 at 0.5 MHz defining the reflection coefficient. (a) is the incident S_0 signal; (b) is the is the direct reflection of S_0 from the tapered region; (c) is A_0 mode converted at the taper; (d) is S_0 reflected from the taper and the frontwall of the model; (e) is A_0 mode converted at the taper and reflected from the model frontwall and (f) is the reflection of the incident S_0 mode from the model backwall.

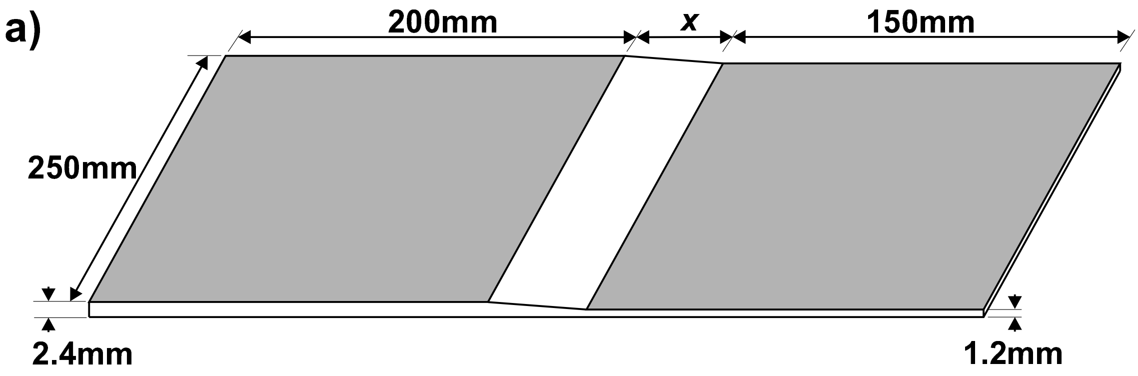

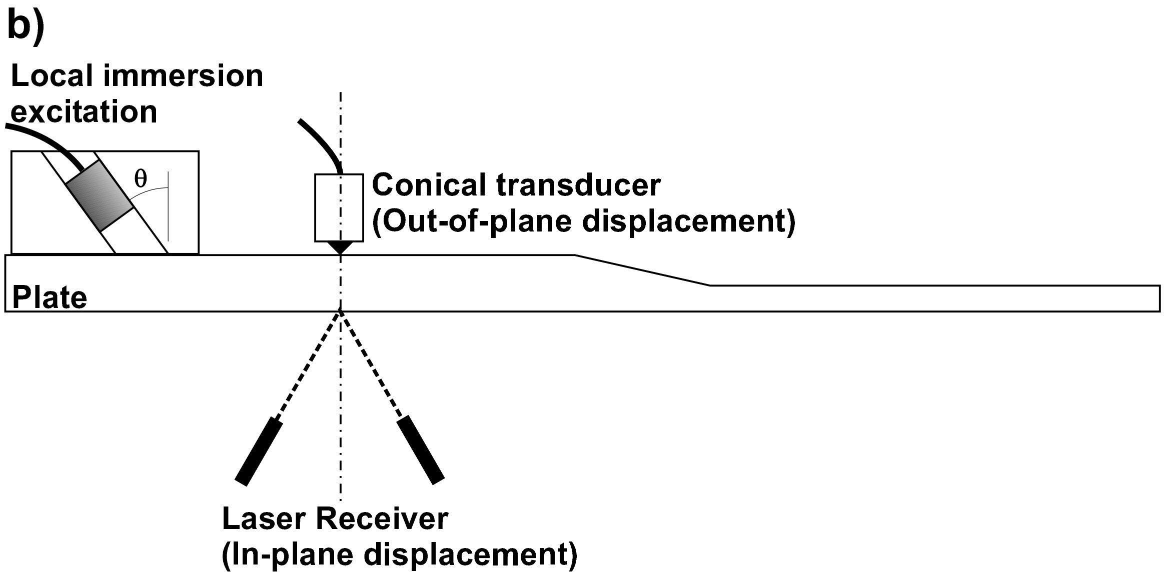

Fig 3. 8 (a) Tapered skin experimental test specimen. (b) Equipment arrangement for tapered skin experiments.

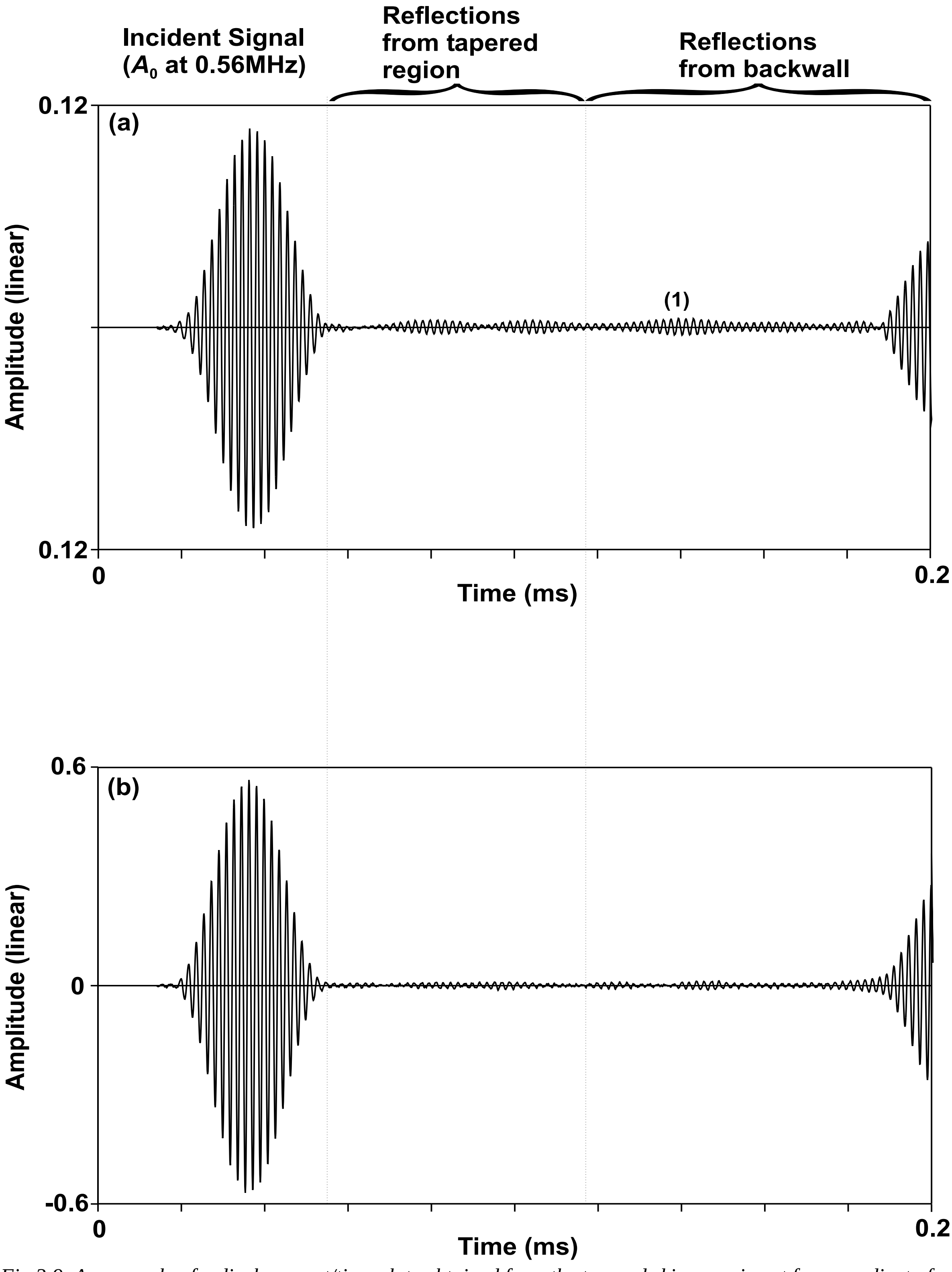

Fig 3.9 An example of a displacement/time plots obtained from the tapered skin experiment for a gradient of 1:5 (a) In-plane displacement. (b) Out-of-plane displacement.

4. Guided wave propagation in multi-layered aircraft structure

4.1 Introduction

In chapter 3 it was concluded that, provided that dispersion is avoided, there is little difficulty in achieving long-range propagation in a single skin, with an effective attenuation of less than 40 dB/m, as required. In chapter 1 however, it was shown that many areas of aircraft structure consist of several layers, comprising a skin with a surface layer of sealant or multiple skin layers that may have a sealant or an adhesive interlayer. This chapter examines the propagation characteristics of guided modes in these multi-layered systems.

The chapter begins by considering the case of a skin with a layer of sealant loaded on one surface. In one sense, since all aircraft structural components usually have some form of finishing layer applied, all areas might be considered multi-layered systems. Having discussed skin loaded with sealant, this chapter will then briefly examine the effect of paint layers, prior to considering systems with two jointed aluminium skin layers in the final section.

4.2 Skin loaded with sealant

The material property measurements presented in chapter 2 showed that, since PRC sealant supports little or no shear wave propagation, it might reasonably be considered a viscous fluid. Guided waves in plates loaded with an inviscid fluid, in particular water, have been thoroughly studied since the work of Osborne and Hart (1945), Osborne and Hart (1946), and the case of single sided fluid loading is essentially that formed by the co-incidence transduction system discussed in chapter two. When the fluid depth is infinite, (an infinite half-space) the dispersion curves reveal an extra anti-symmetric mode usually referred to as the Scholte mode [Scholte (1942)]. Sessarego, *et al.* (1997) showed that when the plate is loaded on both sides by a fluid half-space, a further symmetric mode is added in addition to the Scholte mode. This mode is co-incident in phase velocity with that of the fluid bulk wave, except at very low frequency-thickness products. Apart from the emergence of these additional modes, the main difference between the modes of the free plate and those of fluid loaded plates is one of attenuation.

Consider the propagation of a mode in a free plate as it passes into a region where the plate is loaded on one side by a fluid. Provided that the mode exhibits some out-of-plane displacement at the plate surface, displacement energy is coupled to the overlying fluid layer. If the phase velocity of the mode in the plate is greater than that of the bulk wave in the fluid, energy will leak from the plate, setting up bulk waves in the fluid that propagate away from the plate at an angle determined by Snell's law. (See equation 2.9) This leakage of energy, which of course, is the same mechanism used in transduction by the coincidence principle, causes considerable attenuation of the plate mode. When the plate is loaded by a solid half-space, modes with phase velocities greater than that of the bulk shear wave in the half-space leak shear-wave energy, while modes with phase velocities greater than the bulk longitudinal wave velocity in the half-space leak both shear and longitudinal wave energy. The case of a propagating A_0 mode leaking into a PRC half-space is illustrated in figure 4.1.

Next consider the case where the non-viscous liquid layer is fairly thin and no longer constitutes a half-space. In this case the leaked energy is reflected from the free boundaries of the liquid layer back in towards the plate. Energy no longer escapes the system and the reverberation between the free boundaries sets up one or more modes propagating in the double-layer system. These modes have no attenuation mechanisms other than those identified for the free plate. When the fluid layer is viscous however, the modes of the double-layer system have significant attenuation owing to viscous losses in the fluid. The dispersion equations for such viscous fluid systems have been calculated and numerically solved by Zhu and Wu (1995) . Thus, two distinctly different types of propagation are possible in this system, dependent upon the sealant thickness. Since, as was shown in chapter two, PRC sealant is highly attenuative in respect of the longitudinal and shear bulk waves, it was considered possible that, even with a relatively thin sealant layer, energy might not return to the plate. Such a sealant layer would then effectively constitute a half-space, resulting only in leaky propagation of plate modes. The first task therefore, was to determine which type of propagation was valid for the thickness of sealant that might be encountered in aircraft.

Figure 4.2 shows the phase velocity and attenuation spectra for the case of a plate with a half-space of sealant. The Scholte mode is seen as that having the lowest phase velocity. The figure compares viscous and non-viscous sealant, the latter being identical, except that the attenuation parameters have been set to zero. The phase velocity of the modes is virtually unaffected by the addition of viscosity and apart from the Scholte mode, there is also little difference in attenuation between the two cases. This indicates that for a sealant half-space the attenuation is almost entirely attributable to leakage. Unlike the other modes, however, the energy in the Scholte mode is carried primarily contained within the sealant layer, and does not leak away from the interface. In this case the viscosity of the sealant absorbs energy from the wave and there is consequently much greater attenuation when the sealant is viscous. A similar comparison between viscous and non-viscous sealant is shown in figure 4.3 for the case of a 1.4 mm layer of sealant. In this case there is a marked difference in the phase velocity spectra. The non-viscous case supports many more modes than the viscous case, because, in physical terms, the partial waves of these modes are not able to couple across a viscous layer of this thickness. In the attenuation spectrum there is, of course, a radical difference. All the modes of the non-viscous case, have zero attenuation, because there is no leakage from the system and no viscous loss. It is clear then that a 1.4 mm thick sealant layer does not effectively constitute a half-space, because the dispersion curves of figure 4.2b are completely different to those of figure 4.2a.

During aircraft assembly the sealant is usually spread onto the surface by hand with a spatula or brush and there is therefore a considerable variation in thickness. Figure 4.4 shows the effect of a 10% variation in sealant thickness above and below 1.4mm. The phase velocity spectrum shows that thickness changes only cause a shift in frequency, commensurate with the change in frequency-thickness product. The reason is that the more dense aluminium layer dominates the phase velocity of the modes. Perhaps more surprisingly a similar pattern is seen in the attenuation spectra, with little change in the minimum attenuation of each mode. In fact, with the exception of the two fundamental modes at low frequency, all of the modes shown in figure 4.4 have attenuations well in excess of 40 dB/m and so, from a practical point of view, there is apparently no mode with long-range propagation potential in this system. (This is not strictly so, since at much higher frequencies, some modes exist with little or no surface displacement at the sealant-aluminium interface. These modes include the Rayleigh wave on the unloaded surface and other modes coincident in phase velocity with the longitudinal bulk wave velocity in aluminium.) In general, aircraft may have a sealant thickness of as much as 5 mm in places. The attenuation spectrum of this case is shown in figure 4.5 where the pattern remains that of a system with two finite layers, the attenuation being attributable to viscous losses rather than leakage. The lowest attenuation in this case is roughly the same as that for much thinner layers of PRC. It is seen that the minimum attenuation increases with mode order, so that the lowest attenuation is found in the fundamental modes at low frequency.

Since it was found that considerable variation in the properties of the PRC sealant was likely, the effect of an error in the bulk wave velocities was investigated. The dispersion curves of figure 4.6 show the effect of a +/- 10% change in both longitudinal and shear wave velocity in the sealant. Once again, there is little change in the overall minimum attenuation though increasing the velocity by 10% increases the local attenuation minima by up to 16%, with a similar but opposite effect when the velocities are decreased. A small change is also seen in the phase velocity, particularly in the $A_{0,}$ mode at frequencies greater than 250 kHz. Both the phase velocity and attenuation spectra are also shifted in frequency, and the fact that figures 4.4a) and 4.6a) show a similar frequency shift is not really surprising and simply reflects the change in the time taken for the partial waves to cross the system. Before discussing the experimental validation of this system, it is interesting to note that the minima in the attenuation spectra closely correspond with points where the phase velocity coincides with that of a mode in the free plate system; the attenuation increases as the phase velocities in the two systems diverge. This is illustrated in figure 4.7, where the crosses mark coincidence with the A_0 mode in the free plate. These points define frequencies at which the ratio of strain energy density in the plate to that in the sealant layer are maximised. At such points, the mode shape within the plate section of the double-layer system most closely matches that of the corresponding mode in the free plate. This has important implications for the mode conversion that occurs when a mode in the free plate first encounters a sealant-loaded region.

In an initial validation of the dispersion curves of this system the attenuation and group velocity of propagating modes were measured using a local-immersion-wax-bath transmitter and a conical-transducer receiver (manufactured by Evans (1997) at Imperial College) in the pitch-catch arrangement shown in figure 4.8. Measurements were made at values of x between 110 mm, and 40 mm in increments of 10 mm. When x was less than 40 mm, the received signal had decayed such that it was buried in the noise floor. Two frequencies: 0.75 MHz and 0.98 MHz were chosen, which corresponded with attenuation minima. At 0.75 MHz a predominant S_0 mode was excited in the free plate region by setting the excitation transducer to an angle of 16° with respect to the plate normal, while at 0.98 MHz, using an excitation angle of 36°, a predominant A_0 mode was launched. Nevertheless, in both cases both S_0 and A_0 modes were evident and were temporally and spatially separated owing to the initial propagation in the free plate region. In the double-layer region mode **d** in figure 4.9 has a similar mode shape and phase velocity to the S_0 mode in the free plate, while modes **a**, **b**, and **c** have mode shapes and phase velocities more closely corresponding to those of A_0 in the free plate. Care was taken in the manufacture of the test specimen to obtain a sealant layer of consistent thickness (1.4 mm) and to avoid trapping air in the sealant. Table 4.1 compares the predicted and measured attenuation for the modes indicated on the dispersion curves for this system, shown in figure 4.9.

Mode	Predicted Attn (dB/m)	Measured Attn (dB/m)
a	1433	-
b	1077	903
c	2085	-
d	122	61

Table 4.1 Predicted and measured attenuation of modes shown in figure 4.9

At the leading edge of the sealant layer all of the modes of the double-layer system existing at the excitation frequency would be generated by mode conversion. However, most of the input energy is transferred to double-layer modes with similar phase velocity and mode shape to those of the incident mode in the free plate. Figure 4.10 illustrates the mode shapes of the modes indicated in figure 4.9. In the case of the input S_0 mode at 0.75 MHz, it is seen in figure 4.10 that the double-layer mode **d** has a very similar mode shape in the plate (the lower half) to that of the input mode. This mode would therefore be preferentially excited and the measured attenuation consequently fell closest to that of this mode. Considering the input A_0 mode, there are three possible modes of the double-layer system with similar phase velocities. These are marked **a**, **b**, and **c** in figure 4.9 and all three would be strongly excited. However, two of these modes, **a** and **c**, have considerably higher attenuation such that they rapidly decay to insignificance over a very short distance. Mode **b** is the most strongly generated mode, since in figure 4.9 and 4.10 it is seen that this mode has the closest phase velocity and mode shape in the plate to those of the input mode. It has been pointed out that such coincidence of phase velocity corresponds with a minimum in the attenuation spectrum and it is not surprising, therefore, that the experimental measurements at 0.98 MHz corresponded most closely with the parameters of this mode. The preferential excitation of certain modes, though interesting, is of small consequence in this system, since no mode could be found with a sufficiently low attenuation for long-range propagation. However, the same preferential excitation phenomenon is found in the double-skin systems, discussed later in this chapter, where it is of more practical importance. The measurements were fairly crude and the high frequency-thickness dependence of attenuation close to the measured mode points, means that small errors in the layer thickness or material specifications could account for the for lower measured attenuation than that predicted. Later in the project, having acquired the laser equipment described in chapter 2, further validation was carried out using a 200 kHz probe coupled directly to the edge of the plate with gel, to excite the S_0 mode over a band of frequencies from 170 kHz to 350 kHz. This method of excitation is able to couple the predominantly in-plane displacement of S_0 in this band. The laser was set-up to measure these in-plane displacements in a similar experiment to that already described. A comparison of the predicted and measured results is presented in figure 4.11, where the maximum error in both the phase velocity and attenuation is six percent. Below 200 kHz, the longer wavelength gave rise to interference with the reflected signal and above 300 kHz there was insufficient sensitivity in the probe bandwidth for reasonable measurement. The attenuation measurement of S_0 in this low frequency band further confirms that attenuation of less than 40 dB/m in this system is not obtainable.

4.3 Painted Skin

Existing finishes on current aircraft may be any one of several types, combinations of two or more types, or combinations of general finishes with special proprietary coatings. Most aircraft finishes are either cellulose, acrylic, or epoxy. Acrylic is currently the most common, but epoxy is becoming more popular owing to its high gloss and wear resistance [FAA (1976)]. A number of specimens were obtained painted with a military specification paint scheme either of epoxy or acrylic, and including primer and finishing coats. Measurement of the acoustic properties of the layers proved very difficult owing to the thickness of the coats, which ranged from 0.03 mm to 0.05 mm total thickness with a primer coat of roughly 0.02 mm. These thicknesses were determined by micrometer and from scanning electron microscope measurements of sectioned samples. Amplitude spectrum measurements using a 50 MHz probe, as described in chapter 2, indicated a bulk longitudinal wave velocity of 2500-3000 m/s across all samples, while the bulk shear wave velocity, measured with a 6 MHz shear probe, was 500-1300 m/s. The approximate values reflect the variation in paint types and the difficulty in establishing accurate paint thickness measurements. The acoustic velocities of Redux adhesive, detailed in chapter 2, are reasonably similar to those found for the paint samples and since these are also similar to the those of epoxy, it was felt reasonable to assume that the paint has the same acoustic properties as Redux. In order to estimate the likely attenuation of guided modes in a painted skin, the dispersion curves were plotted for the system of a 1.2 mm thick skin loaded on both surfaces with 0.03 mm and 0.05 mm of paint respectively. The phase and group velocity spectra differ from those of the free skin only in respect of the change in frequency-thickness product as was seen for the PRC loaded skin discussed previously. The group velocity and attenuation spectra for the paint-loaded case are shown in figure 4.12. Attempts made to validate the dispersion curves in respect of the fundamental modes between 0.8 and 1.5 MHz, by means of laser measurements, similar to those described for PRC, were only partially successful. Although measurement of group velocity provided excellent correlation with predictions, the attenuation measurements were less reliable. The attenuation was so low that it was necessary to duplicate the experiment on an unpainted plate and subtract the results from those of the painted plate, in order to remove the geometric attenuation due to beam spread. Nevertheless, the viscous attenuation of S_0 was less than its geometric attenuation, and consequently the viscous attenuation measurement was poorly conditioned and the results were unreasonable. More reasonable results were obtained for A_0 and these are indicated on the dispersion curves of figure 4.12. In conclusion, the dispersion curves of figure 4.12 b) give a reasonable estimate of the attenuation of modes propagating through painted skin. It is seen that at frequencies below 1 MHz, the attenuation of the fundamental modes is less than 6 dB/m. Above 2 MHz the attenuation of the fundamental modes rises sharply, tending, at high frequency, to that of a Rayleigh wave on each of the free paint surfaces (approximately 50 and 150 dB/m for the thin and thick paint surfaces respectively). The higher order modes generally have significant attenuation, with local minima where attenuation may fall to less than 6 dB/m. Thus the possible attenuation of paint layers must be taken into account when frequencies above about 2 MHz are considered. This investigation also indicates that a Rayleigh wave on the external fuselage surface (assuming that it could be generated practically), would not be capable of long-range propagation.

4.4 Double-skin systems

The semi-monocoque fuselage is commonly reinforced with added skin layers, particularly around hatches, doors and windows, as discussed in chapter 1. Double-skin systems fall into the multi-layer category and this section introduces two systems each comprising two skin layers separated by a jointing layer, and will consider general propagation in these systems. The important interaction between modes in the single skin and those in double-skin regions warrants a separate treatment that will be left until the next chapter, which deals primarily with joints. This section simply examines the dispersion curves of double-skinned systems with PRC sealant and Redux adhesive jointing at the interface. In both cases rivets are often used to fasten the skins together, however, this investigation was simplified by ignoring such fasteners, which would otherwise present a complicated scattering problem. Unlike the loaded skin case, the thickness of the sealant or adhesive in the double-skin case is far more constant and reliable (though thinning occurs close to fasteners). Considerable research has been directed to examination of systems of joined aluminium skins, similar to those detailed here. Much of this work focused upon propagation and defect detection in lap and stringer joints, which will be discussed in the next chapter. Some work, however, does deal more generally with propagation in the system, though there is little interest in attenuation and long-range propagation. For example, Alers and Thompson (1976) examined the related case of guided modes confined to the adhesive interlayer and identified modes sensitive to the interfacial properties of the joint and Mal, *et al.* (1989) found that for the bonded aluminium skin case, certain modes exhibit significant sensitivity to bond behaviour. Georgiou, *et al.* (1994) reported some finite-difference numerical modelling and experimental work, predominantly concerned with the propagation of Stonely waves in an adhesive joint between aluminium skins painted with primer.

4.4.1 Discussion of double-skin system dispersion curves.

The dispersion curves for PRC and Redux jointed double-skins, with a respective jointing layer thickness of 0.3 and 0.25 mm are presented in figures 4.13 and 4.14, and the lower order modes are picked out using different line-types for clarity. The group velocity spectra of the lower order modes will be presented in the next chapter. An interesting feature of both systems is the 'twinning' of modes in the phase velocity spectrum. That is to say, pairs of modes with similar phase velocity over a broad frequency band are generally evident, particularly at lower frequencies. Typical pairs of modes are marked **a**,**b** and **c**,**d** in figure 4.13 and **e**,**f** and **g**,**h** in figure 4.14. The reason for this mode twinning is that, as was also seen in the previous section, the phase velocity is dominated by the elastic properties of the much stiffer and thicker aluminium skin layers. In the previous section it was seen that the phase velocity of double-layer modes closely matched that of the free skin, and that the mode shape in the aluminium layer was very similar to the corresponding mode in the free skin. This three-layer system is similar, in as much as each pair of modes will also have a mode shape in the aluminium layers that resembles that of the corresponding mode of similar phase velocity in the free skin. The only difference between any pair of modes is a change of phase through the interface layer. This is illustrated in figure 4.15, which shows the mode shapes of the four pairs of modes indicated on figures 4.13 and 4.14. Thus, comparing the mode shapes in just the upper plates of any pair, they are also found to be similar, but phase reversed. This will be seen to have important implications at the transition from single to double skin and will be discussed further in the next chapter.

The attenuation spectra of figure 4.13b) and 4.14b), though somewhat confusing, indicate that, except for certain bands, attenuation is generally greater than 40 dB/m. In the loaded skin case, it was seen that attenuation minima corresponded with coincidence in phase velocity with a free-plate mode, but this is not the case with double-skin systems. Matching of the mode shape in one skin of the double-skin system with the corresponding single-skin mode generally does not constitute an attenuation minimum.

Above about 2 MHz in the Redux bonded case, and 1.5 MHz in the PRC jointed case the attenuation of all but one mode is greater than 40 dB/m and this mode becomes the equivalent of a surface wave propagating on each of the free aluminium surfaces at high frequency. Its sister mode, at 5 MHz, has a similar mode shape, but with an extra phase change in the interface layer, giving a greater attenuation. With respect to attenuation then, all of the potentially useful modes of these systems exist at frequencies below about 2 MHz. The problem is that the wavenumber proximity of twinned modes effectively prevents the excitation of just a single mode, irrespective of whether generation is by one of the transduction methods mentioned in chapter 2, or by mode conversion. For surface transduction, the degree of excitation of the twinned modes is related to the surface displacement (excitability) of the modes, outlined in chapter 2. However, for generation by mode conversion, the division of energy between the possible modes of the system is related to the degree of similarity in the mode shape and phase velocity of the incident mode. Further discussion of this is reserved for the next chapter. In either case, the input energy is divided primarily between the pair of twinned modes. Examination of the dispersion curves of figures 4.13 and 4.14 reveals that, at some frequencies, one of the two twinned modes has a much higher attenuation. In this instance one mode will rapidly decay to insignificance, leaving the more gradual decay of the second mode over a greater distance. This may usefully reduce the effective number of propagating modes; nevertheless, a large proportion of the input energy is lost and, as will be seen in the case of successive joints, this constitutes a further important attenuation mechanism. At frequencies where both of the twinned modes have a similarly low attenuation, they will propagate together over a considerable distance. In this instance, owing to the small difference between the phase velocities of the two modes, ‘beating’ occurs between the pair until they eventually become temporally and spatially separated. In joints, where the propagation distance is relatively short, this interference mechanism dominates the efficiency of transmission, as will be seen.

4.4.2 Validation of double-skin system dispersion curves.

The difficulty in obtaining single mode propagation of a non-dispersive mode, with reasonable attenuation, made validation of the dispersion curves of the double-skin systems very difficult and most attempts were plagued by interference between the twinned modes. Of course, techniques such as the two-dimensional Fourier transform, which might otherwise be used to separate interfering modes, are of little use in this case because the twinned modes have approximately identical wavenumbers. Nevertheless, in some of the experiments (described in the next chapter) made on PRC joints, using an A_0 input mode, the attenuation of one of the twinned pair was very much greater than the other. After sufficient propagation in a broad joint, one mode had decayed to insignificance, allowing a rough measurement to be made of the group velocity and continuing attenuation of the other. These measurements are presented in table 4.2 and the measured attenuations are marked by crosses in figure 4.13. Agreement between the theoretical and measured group velocity is considerably better than that between the theoretical and measured attenuation. This is because attenuation is much more difficult to measure accurately compared with group velocity that is relatively straightforward, as indicated in chapter 2. Despite errors of as much as 56%, the agreement between the predicted and measured attenuation is sufficient to confirm the acquired mode.

Input Mode	**Attenuation (dB/m)**		**Group Velocity (m/ms)**	
	Experiment	*Error*	*Experiment*	*Error*
	Theory		*Theory*	
A_0 at 0.54 MHz	14.77	12.8%	2.92	2.6%
	16.94		2.99	
A_0 at 1.1 MHz	23.28	56%	3.08	0.2%
	14.94		3.09	

Table 4.2 Measured points on dispersion curves of double-skin system with 0.3 mm PRC interlayer.

4.5 Conclusions

This chapter began by presenting the dispersion curves for the system of a skin loaded with a layer of sealant. It was shown that sealant layers commonly found in aircraft, are not sufficiently thick to form an effective half-space and consequently the attenuation in these systems is dominated by viscoelastic energy loss in the sealant, and not energy leakage. Apart from the fundamental modes at very low frequency, and a few high-order modes, all the modes of this system exhibited an attenuation of greater than 40 dB/m, and no mode suitable for practical long-range propagation could be identified. It has been shown that on encountering a region where the plate is loaded with sealant, the free plate mode, having a particular phase velocity and mode shape, will be mode converted preferentially to modes of the double-layer system that have a similar phase velocity and mode shape.

The related system of paint-loaded skin was also examined briefly and it was found that above about 2 MHz the viscous attenuation of paint layers may be significant and this should therefore be considered when working above the A_1 cut-off frequency. Surface waves (Rayleigh waves) on a painted skin surface have a high attenuation and are not a practical proposition for long-range propagation.

Finally, the dispersion curves of systems comprising two skins jointed by either a sealant or an adhesive layer were introduced. These systems exhibit an interesting ‘mode-twinning’ phenomenon that effectively prevents single mode excitation making validation of dispersion predictions difficult. The interference of these twinned modes will clearly have an impact on the propagation across small double-skin regions, and the efficiency of transmission across such regions, characterised by structural joints, will be a crucial issue in long-range propagation through fuselage structure. Lastly although general propagation through multi-layered regions has been examined the interaction of modes at the boundaries of multi-layered regions has not. These important issues will be addressed in the next chapter, which deals with aircraft joints.

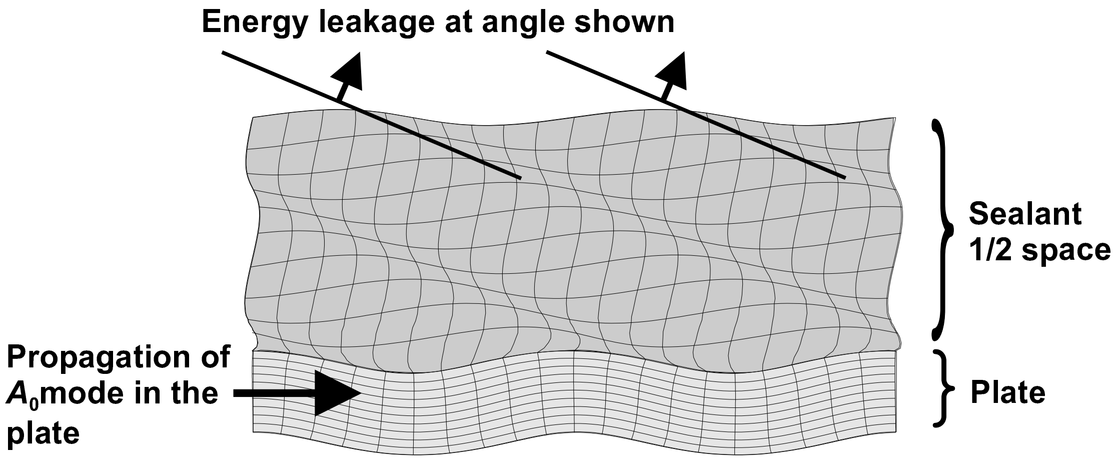

Fig 4.1 Leaky propagation of the A_0 *mode under a thick PRC layer.*

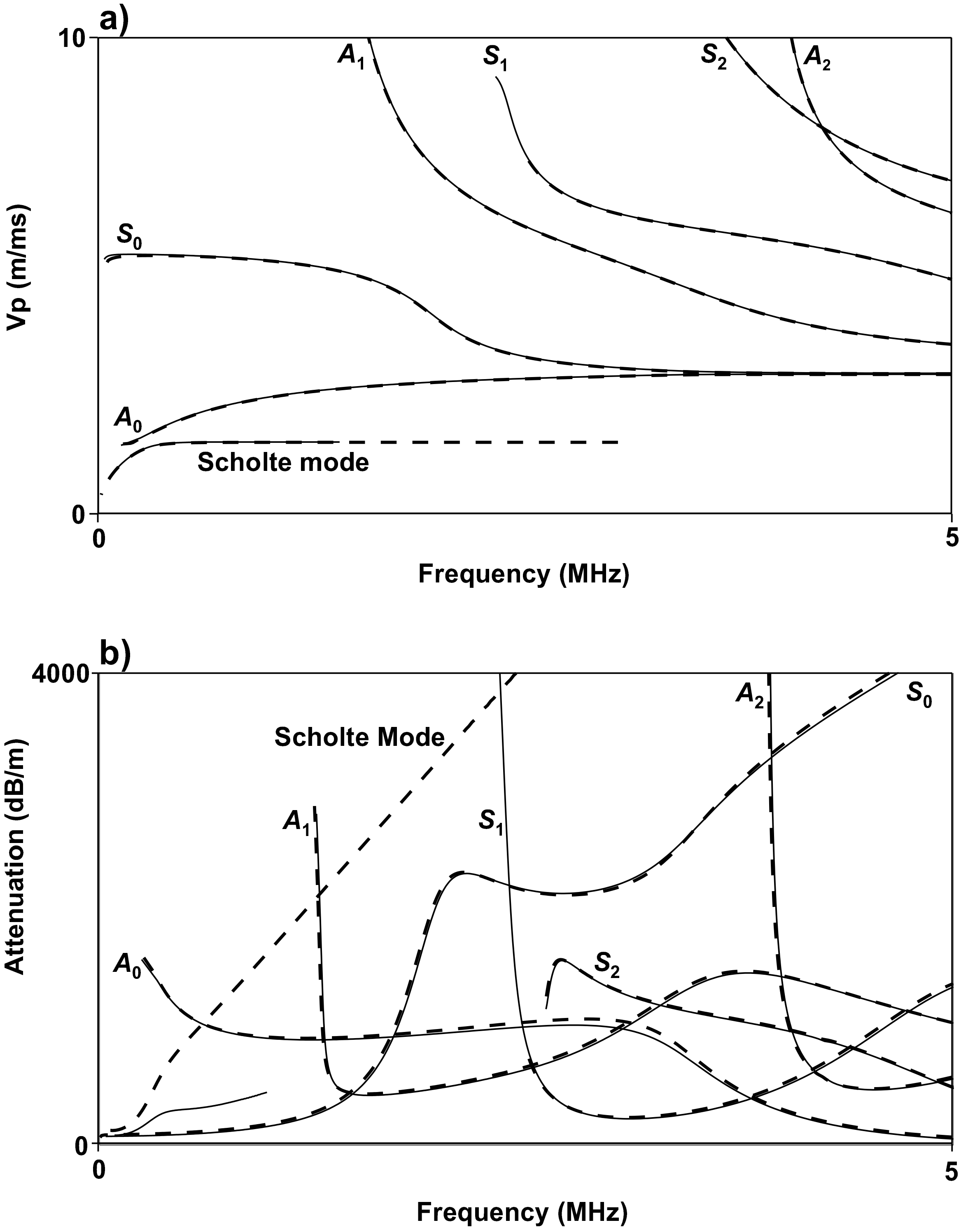

Fig 4. 2 a) Phase velocity and b) Attenuation spectra for the case of a 1.2 mm thick skin loaded with a half-space of PRC sealant comparing viscous (– – – – – – –) and non-viscous (————————) sealant. The A_0 and A_1 modes are truncated at their low frequency ends where the curve tracing algorithm becomes unstable. The Scholte mode in non-viscous sealant and the A_2 mode have been truncated to aid clarity.

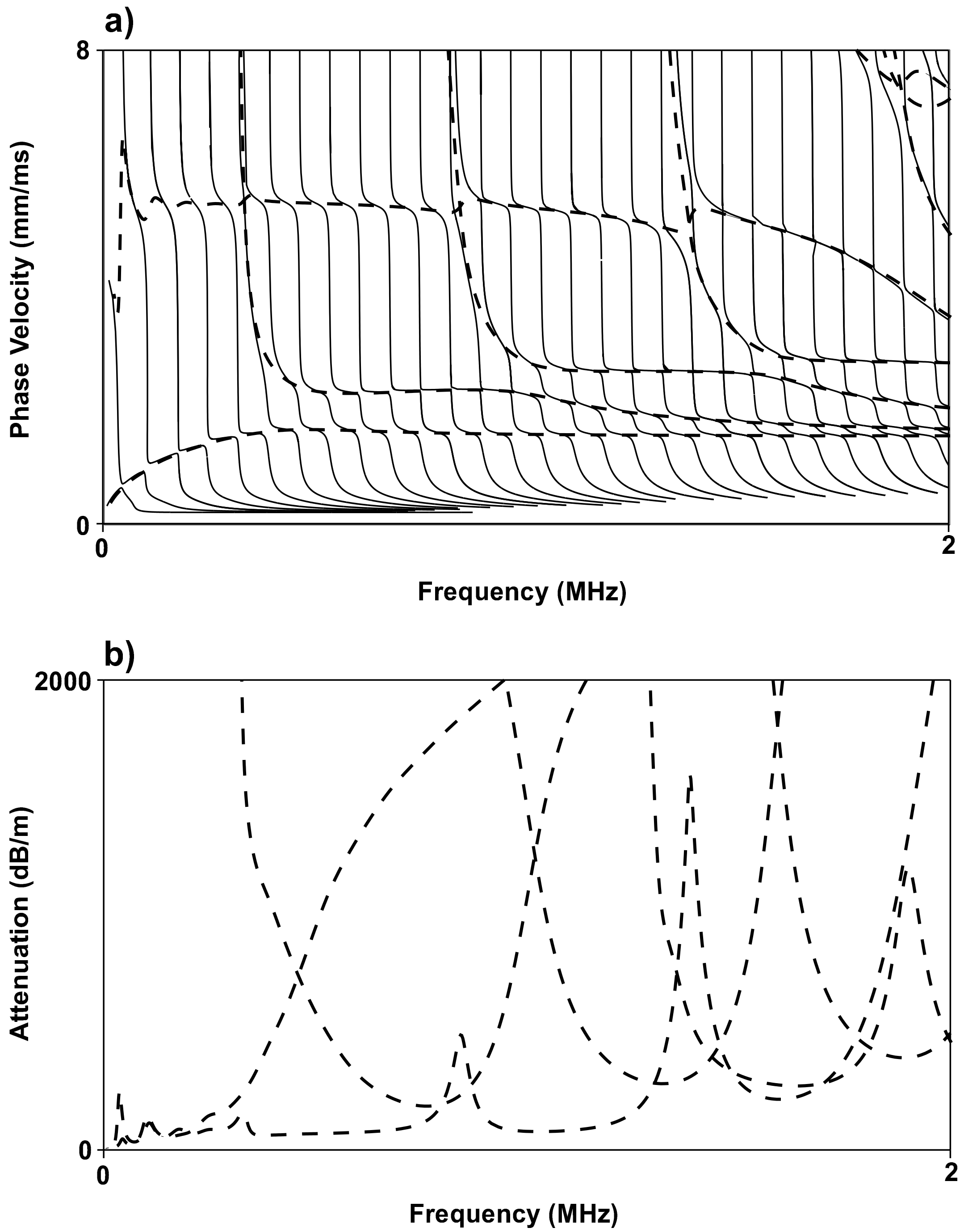

Fig 4. 3 a) Phase velocity and b) Attenuation spectra for the case of a 1.2 mm thick skin loaded with a 1.4 mm thick layer of PRC sealant comparing viscous (– – – – –) and non-viscous (————) sealant.

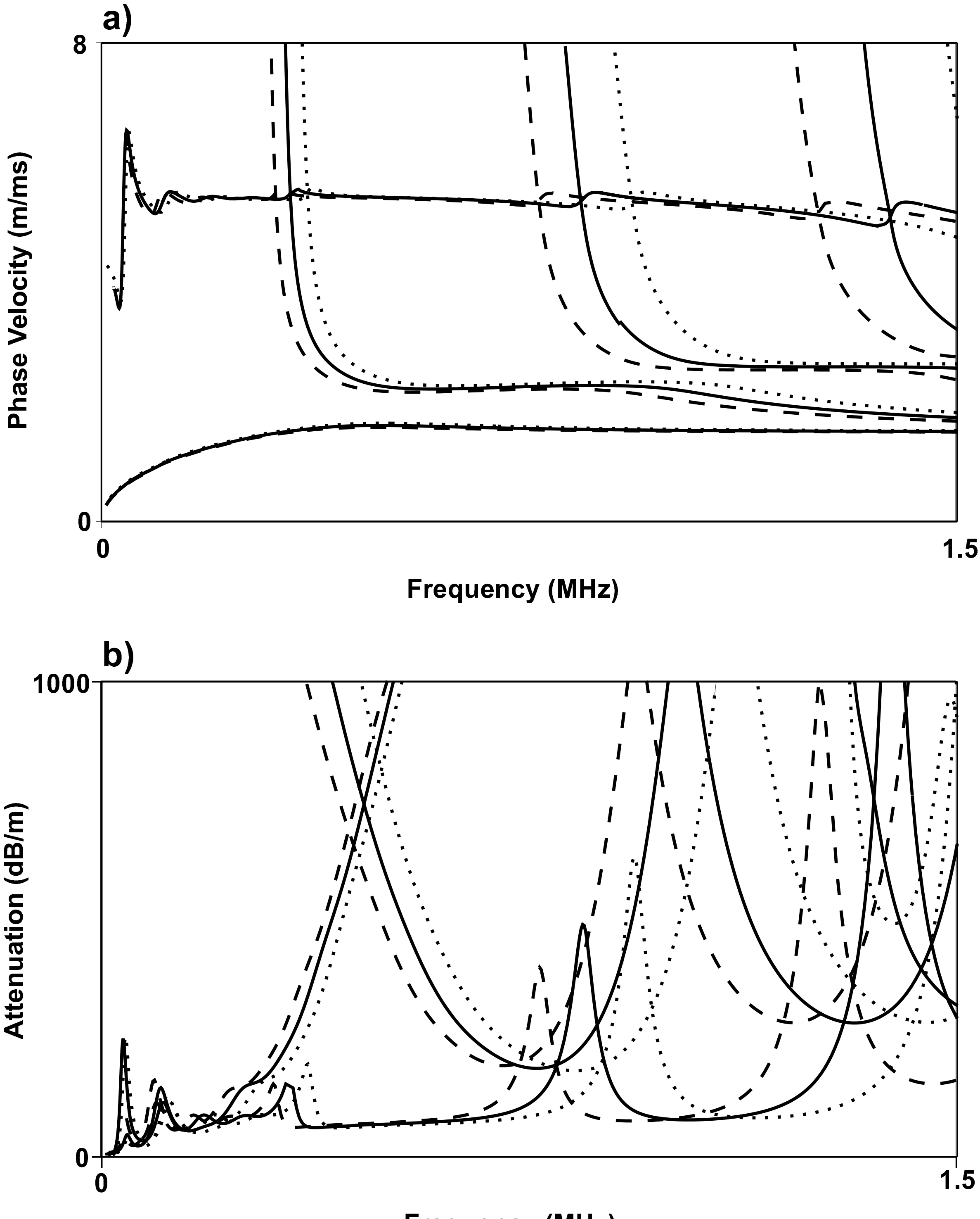

Fig 4. 4 a) Phase velocity and b) Attenuation spectra for the case of a 1.2 mm thick skin loaded with a 1.4 mm thick layer of PRC sealant (————), together with corresponding spectra for a 10% thinner (············), and a 10% thicker (– – – –) layer of sealant.

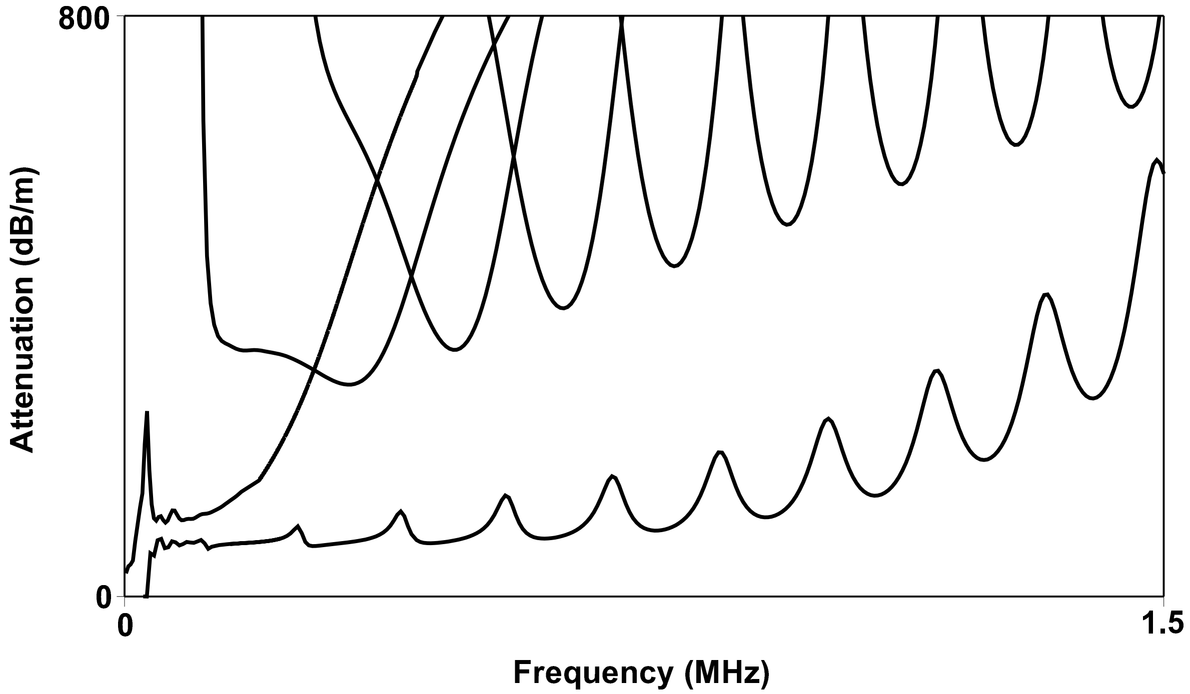

Fig 4.5 The attenuation spectrum for a 1.2 mm thick skin loaded with a 5 mm thick layer of PRC sealant.

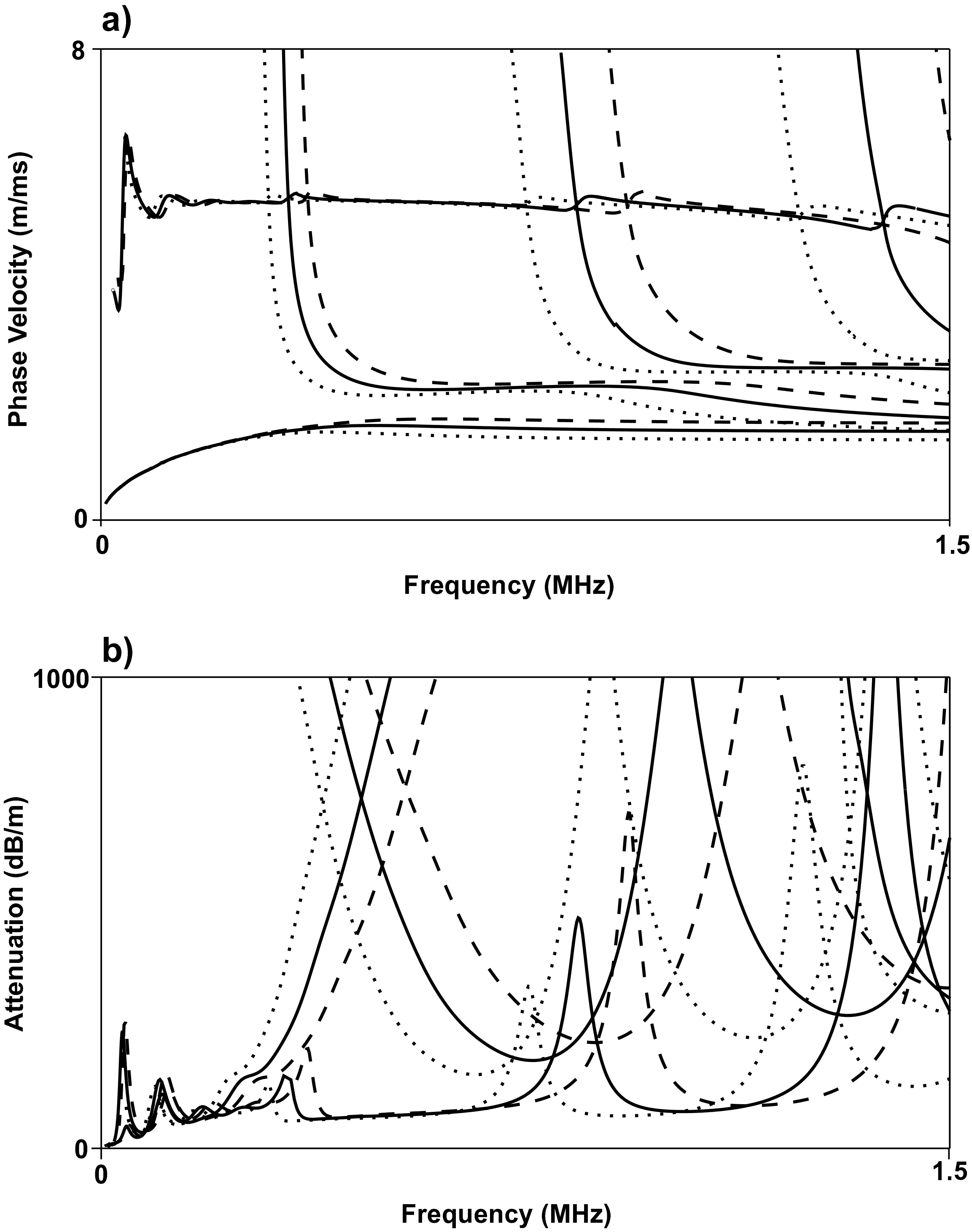

Fig 4.6 a) Phase velocity and b) Attenuation spectra for the case of a 1.2 mm thick skin loaded with a 1.4 mm thick layer of standard PRC sealant (————), together with corresponding spectra for sealant with 10% slower (··············), and 10% faster (– – – –) bulk longitudinal and shear velocities.

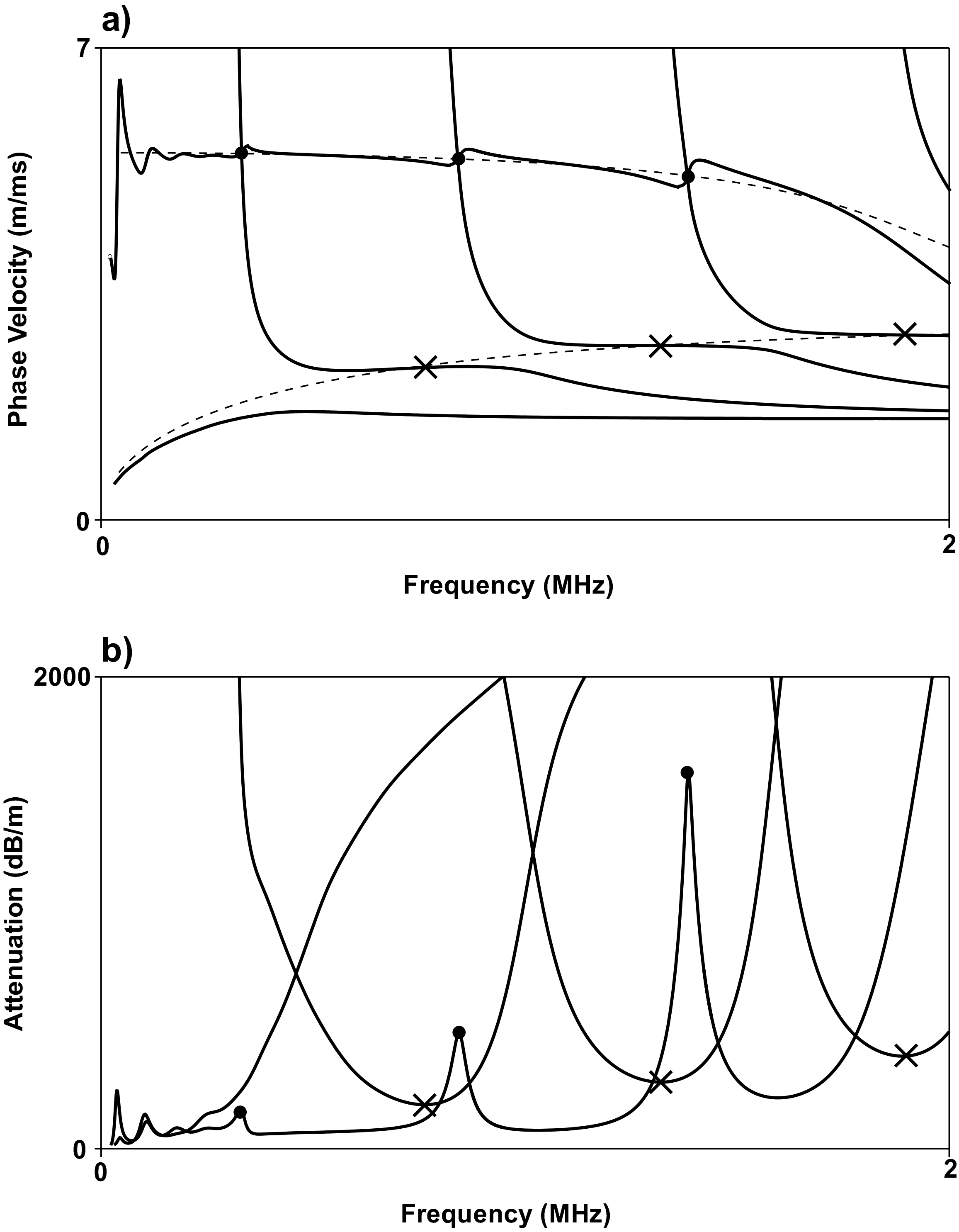

Fig 4.7 a) Phase velocity and b) Attenuation spectra for the case of a 1.2 mm thick skin loaded with a 1.4 mm thick layer of PRC sealant, compared with the corresponding spectra for the free plate case. Crosses indicate, for example, the points of coincident phase velocity on the A_0 curve, which correspond to attenuation minima. Dots indicate phase velocity crossing points on S_0 corresponding to attenuation maxima.

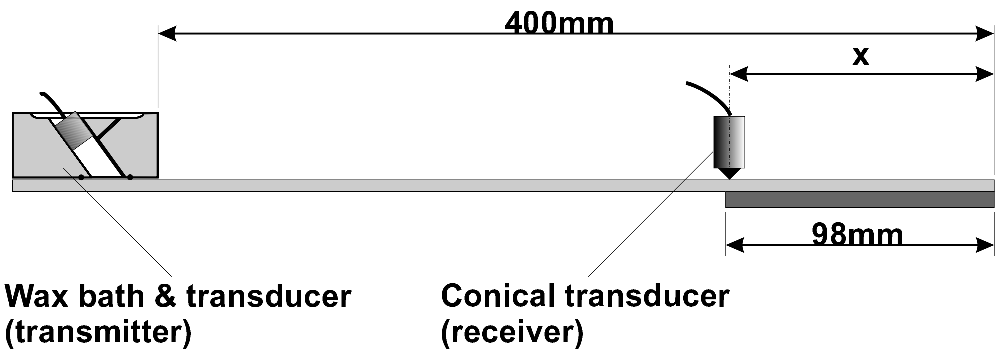

Fig 4.8 Schematic diagram of the pitch/catch arrangement used to measure group velocity and attenuation in the sealant loaded system.

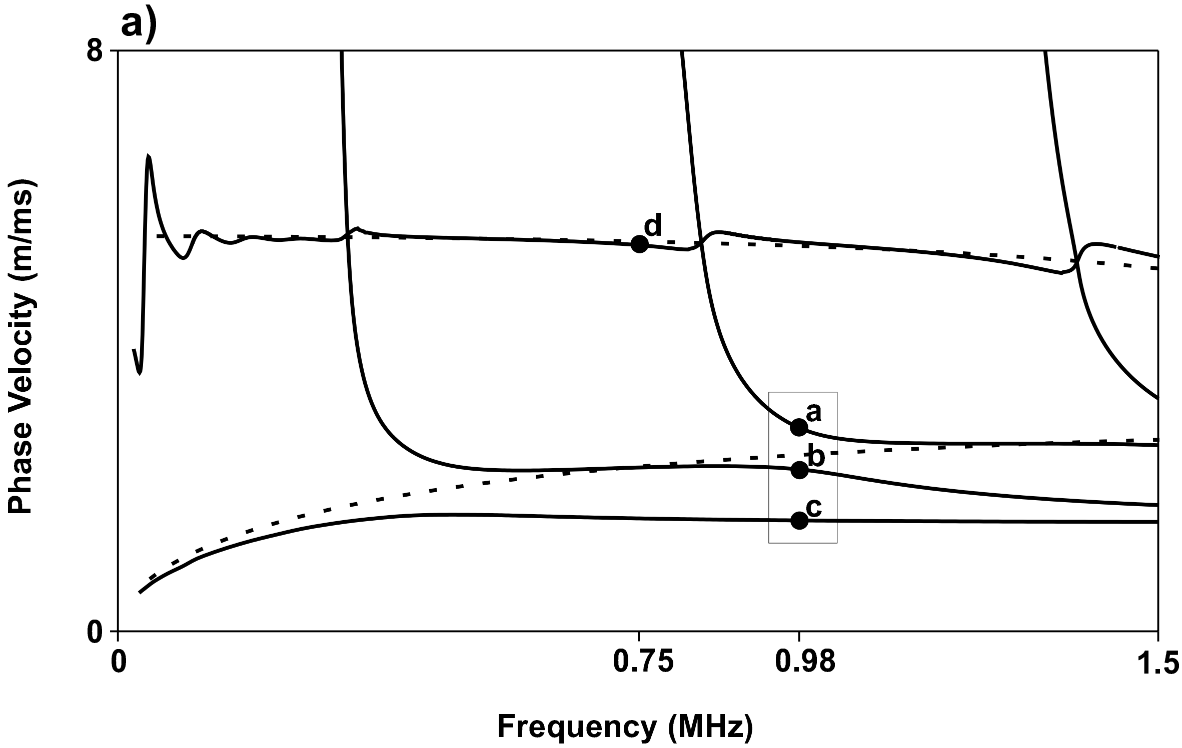

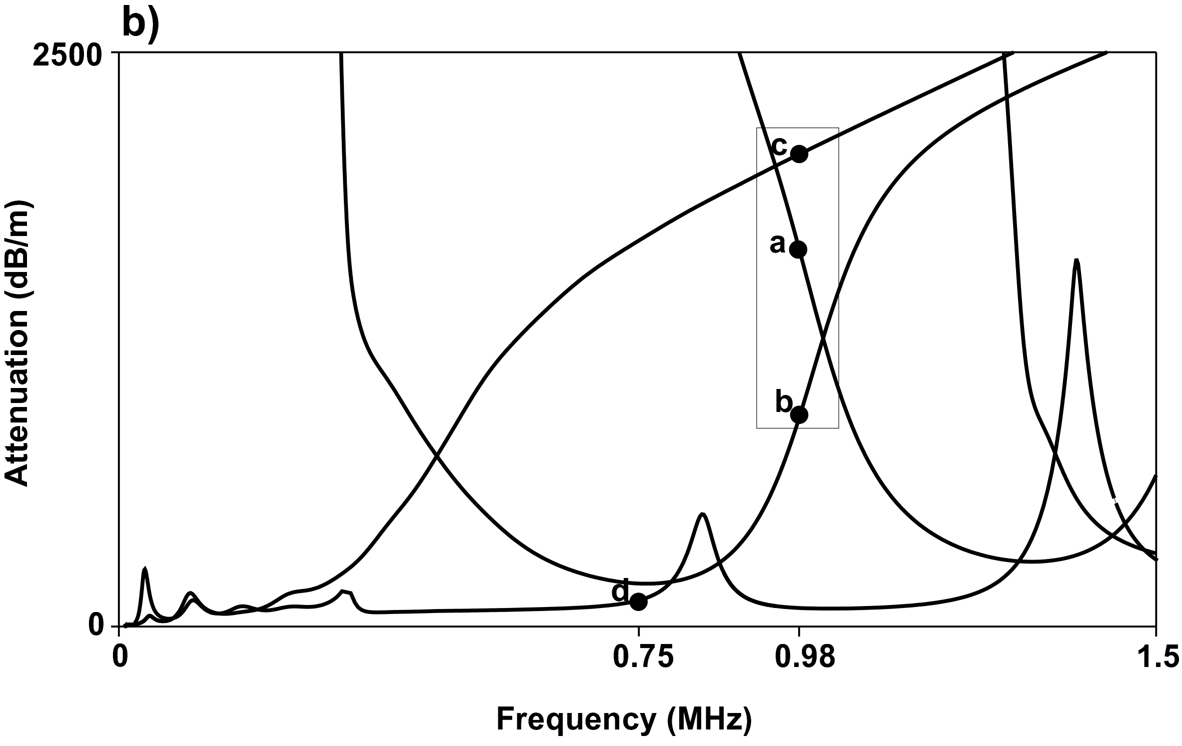

Fig 4.9 a) Phase velocity and b) Attenuation spectra for the case of a 1.2 mm thick skin loaded with a 1.4 mm thick layer of PRC sealant compared with the corresponding spectra for the free plate case. Modes ***a***, ***b***, *and* ***c*** *are strongly excited by an input* A_0 *signal at 1 MHz, while mode d is strongly generated by an input* S_0 *signal at 0.75 MHz.*

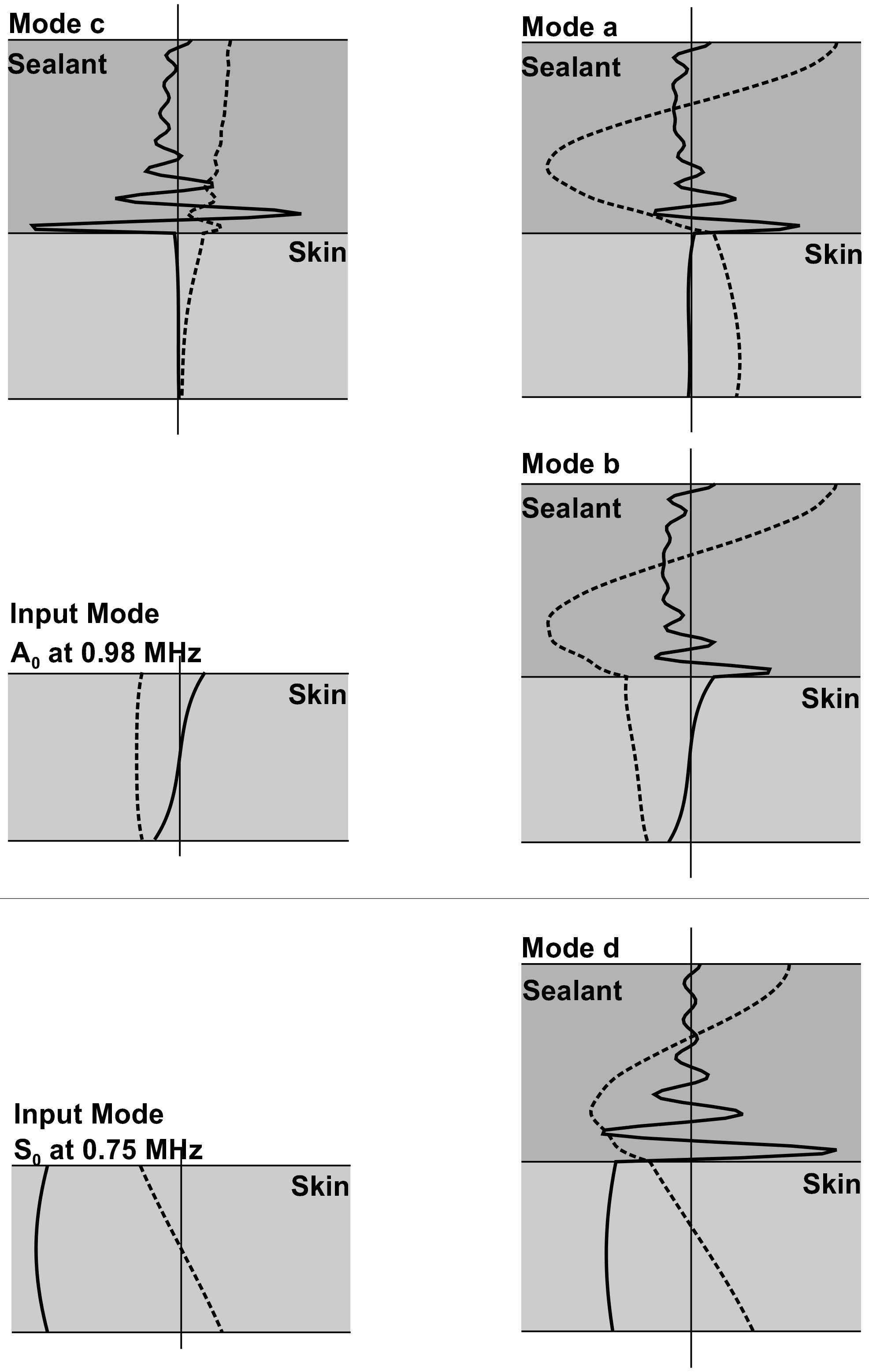

Fig 4.10 Mode shapes of modes indicated in figure 4.9.
——— In-plane displacement, – – – – – Out-of-plane displacement.

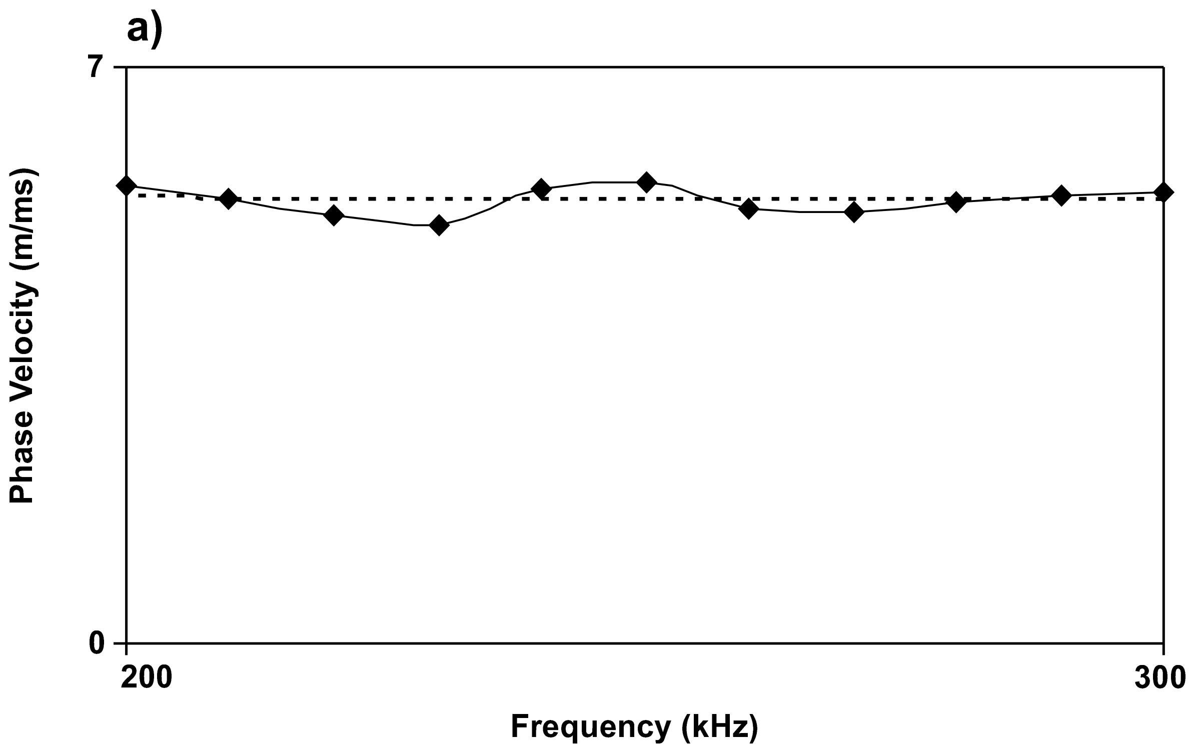

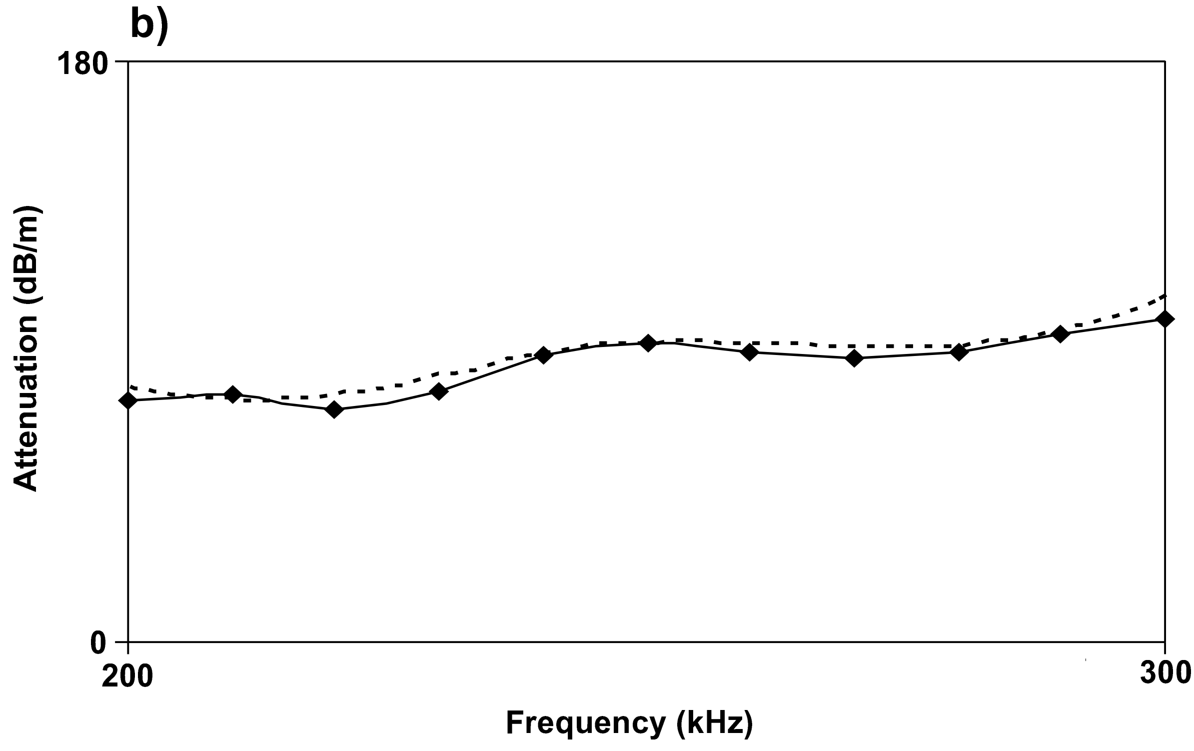

Fig 4.11 Results of validation of dispersion predictions for the sealant loaded plate with S_0 input at 200 kHz. a) Phase velocity spectrum b) Attenuation spectrum.
Measured —◆— *, Predicted* - - - -

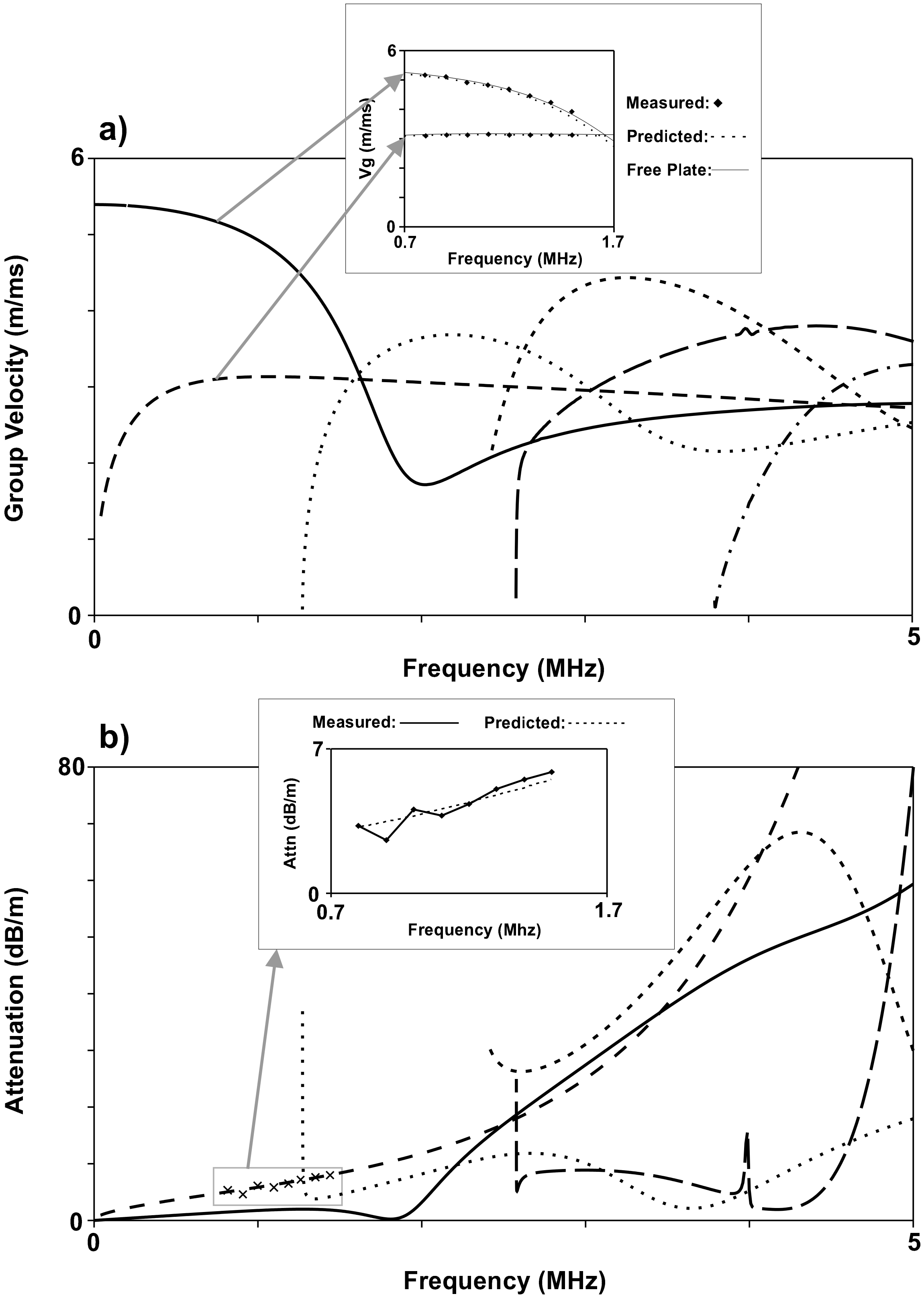

Fig 4. 12 a) Group velocity spectrum and b) attenuation spectrum for the paint loaded skin system. Measured values of group velocity and attenuation compared with dispersion predictions are shown in the insets for the modes indicated.

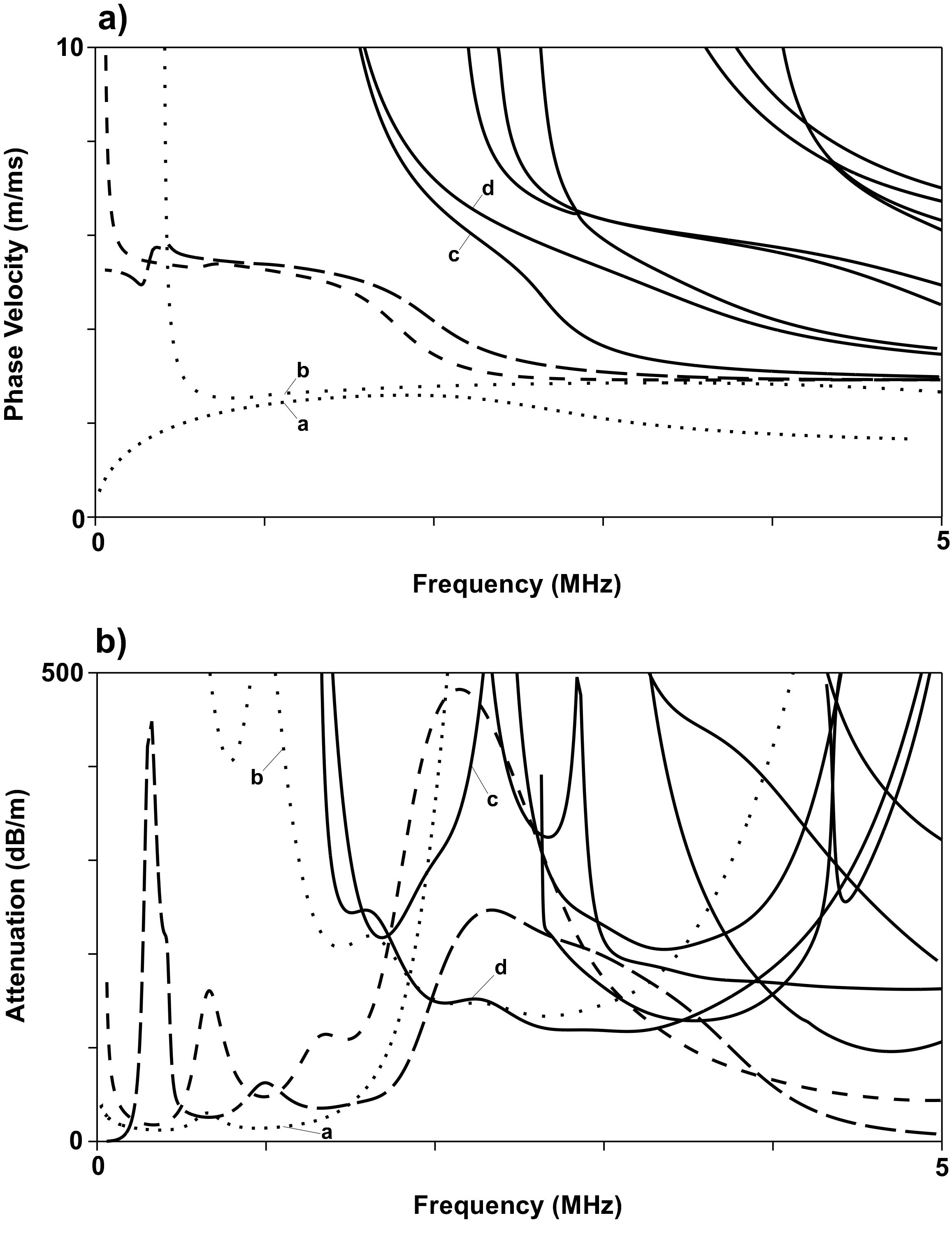

Fig 4.13 Dispersion curves for system of two 1.2 mm skins jointed by a 0.3 mm PRC sealant interface layer. a) Phase velocity spectrum b) Attenuation spectrum

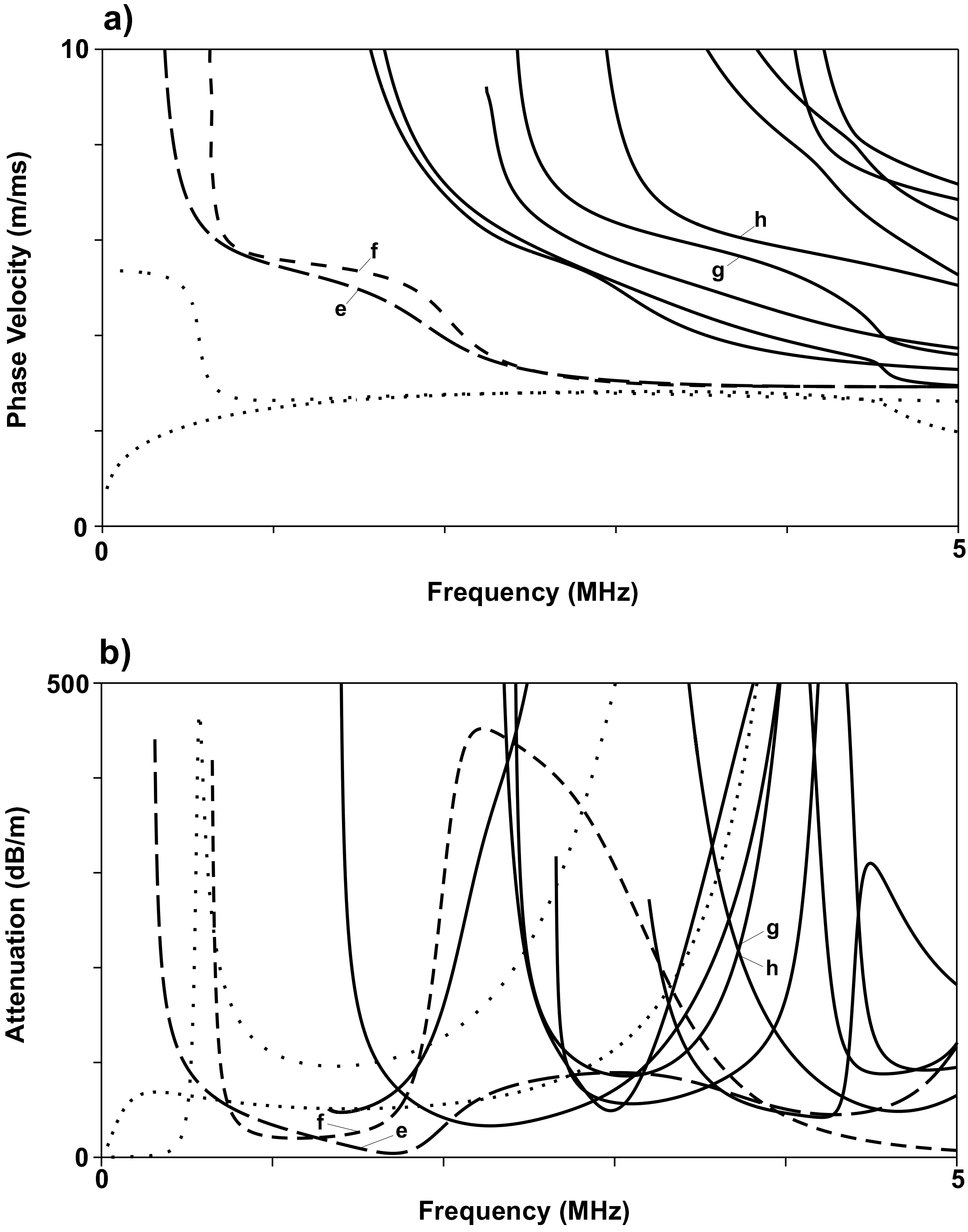

Fig 4.14 Dispersion curves for system of two 1.2 mm skins jointed by a 0.25 mm Redux adhesive interface layer. a) Phase velocity spectrum b) Attenuation spectrum

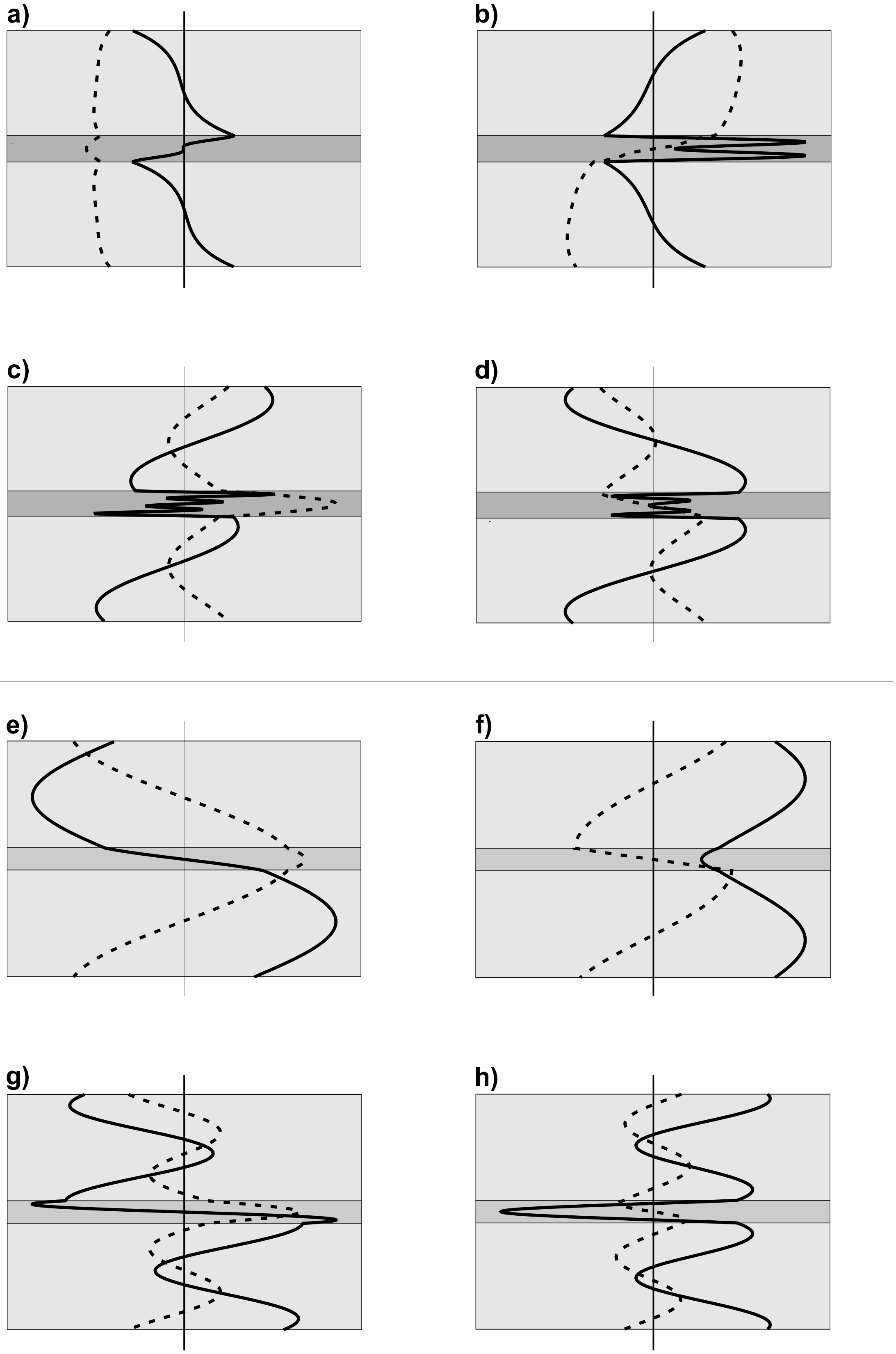

Fig 4.15 Comparison of mode shapes of 'twined modes in double-layer systems. a), b), c) and d): mode shapes of double-skin system with sealant interface at points indicated in figure 4.13. e) ,f), g), and h): mode shapes of double-skin system with adhesive interface at points indicated in figure 4.14.

5. Propagation across skin joints

5.1 Introduction

Until now, consideration has been given only to the behaviour of guided modes in continuous systems, whose behaviour can be modelled and analysed by plotting the dispersion curves of the system. This chapter examines the behaviour of guided waves propagating across aircraft joints. Two types of joint: the lap joint and the stringer joint, described in chapter 1 and illustrated in figure 1.1, are considered. Whilst the lap joint is found at the boundaries of fuselage skin plates, the stringer joint, which represents the point of attachment of support structure to the skin, occurs at regular intervals of about 100 mm along the fuselage longitudinal axis. Waves propagating through the skin would therefore be expected to encounter a high density of stringer joints. The interaction of guided waves with such discontinuous systems cannot be adequately analysed by dispersion curves alone. Some analytical study of joints with idealised geometry have been reported, where no interface (or jointing) layer was included and limiting boundary conditions of either slip or no-slip at the interface were imposed. [Rokhlin and Bendec (1983), Rokhlin (1991)] In general, however, difficulty in satisfying the boundary conditions on all the surfaces within the joint precludes any closed-form solution for practical cases. In such cases numerical techniques are utilised. Chang, *et al.* (1996) and Mal, *et al.* (1996) studied the case of a lap joint with no jointing layer using a hybrid finite-element technique, similar to that described in chapter 2. Since Rokhlin outlined the potential of Lamb waves for adhesive bond inspection, many workers have concerned themselves with the investigation of the defect detection aspects of guided wave interaction with joints. Pilarski, *et al.* (1992) proposed a mode selection criterion for the detection of interfacial weakness, based upon the multiplication of surface out-of-plane displacement and power, integrated over the region close to the interface. Recent experimental work on adhesively-bonded 'T' Joints by Challis, *et al.* (1996) showed that the bond dimensions could be derived from transmitted Lamb wave signals by careful signal processing. Considerable experimental work, directly concerned with aircraft joints, has been undertaken by Sun and Johnston [Sun and Johnston Sun (1992), Sun (1993), Sun and Johnston (1993)], with the aim of detecting delamination and corrosion in aircraft joints; some of this work even includes riveted joints [Sun and Johnston (1995)]. Much of the research mentioned showed encouraging results. However, despite the suggestion by Rose, *et al.* (1992), that the long-range characteristics and variety of mode shapes offered by guided waves may be exploited to improve the inspection efficiency of bonded joints, little attention was paid to the actual modes propagating in the jointed region. The generation and interaction of these modes has very important and far-reaching consequences for the transmission across joints, as will be seen, and such interaction will undoubtedly influence the results of defect detection in the bonded region. More recently, an important numerical study by Lowe and co-workers, examined the generation and interaction of modes in the joint region, for the estimation of bondline thickness [Lowe, *et al.* (1999)].

The dispersion curves for the bonded regions of the joints concerned were presented in the previous chapter, where it was noted that both of the double-skin systems exhibit a pairing or twinning of modes in the phase velocity spectrum. This chapter extends that work to examine the behaviour of these modes in both lap and stringer joints of finite width. The investigation is concerned with the influence of the interaction of these modes on the efficiency of transmission across the joint. It is shown that, for relatively narrow joints, typical of those formed between a fuselage skin and its support members, such interaction is the determining factor, and moreover, it crucially affects the transmission across a succession of narrow joints.

A dynamic finite-element model, of the type described in chapter 2, is used to examine the transient behaviour of the joint, including events at the leading edge. The modelled out-of-plane displacements over the bonded region are compared with corresponding experimental results and the chapter concludes by presenting the results of a simple pulse-echo experiment that graphically demonstrates the findings of this chapter. The concluding discussion explains the general difficulty in transmitting guided modes efficiently across a series of joints. This is most important, since it tends to dismiss the practical use of guided waves in an active structural-health-monitoring system for semi-monocoque fuselage structure.

5.2 Carrier Modes

Consider the interaction of a mode propagating in a single skin when it first encounters the leading edge of a joint. Figure 5.1 illustrates schematically an example of such an interaction, when the S_0 mode, propagating in the skin, encounters a lap joint with a 0.3 mm thick sealant interlayer. The leading edge area of the joint is illustrated in cross-section, in figure 5.1, by a light broken line, and the mode shape of the S_0 input mode is superimposed on the single-skin region. The change in section at the joint leading edge marks a step change in the elastic and geometric properties of the waveguide and this forces mode conversion of the input mode. The boundary conditions at the joint leading edge are satisfied by a combination of transmitted modes in the double skin, reflected modes in the single skin and a potentially infinite number of non-propagating, or evanescent modes in both systems. The influence of these evanescent modes extends only a short distance from the leading edge and it is assumed that they can be ignored. Nevertheless, Torvik (1967) has indicated that the influence of the non-propagating modes may extend further than was first realised. The numerical analysis, presented in this study, takes full account of these modes and is therefore valid. If the geometric transition from the single to double skin were symmetric, then the symmetry of partial wave reflections dictates that energy transfer could only occur between modes of similar type. (ie symmetric to symmetric and anti-symmetric to anti-symmetric) However, since in this case the geometric change is asymmetric, the input mode may be mode converted to any, or all, of the possible modes that can exist within the bandwidth of the input signal. In principle, all of the possible modes will be generated with differing amplitudes, such that the boundary conditions are satisfied. In fact, the more similar the mode-shape of a possible propagating mode in the joint, to that of the input mode, the more strongly it is likely to be generated by mode conversion. This is consistent with the 'Normal Mode Theory' discussed by Auld (1990) and has been found to apply strongly to joint systems such as these [Lowe, et al. (1999)]. This may appear somewhat inconsistent with the findings of Torvik (1967) in his early work on the interaction of guided modes with the normal boundary of a free plate. The redistribution of energy on reflection at a normal edge is frequency-thickness dependent, and over certain frequency bands the majority of energy in one symmetric mode may be transferred by mode conversion on reflection to another symmetric mode, rather than simply being reflected in the same mode. Indeed, he showed, for example, that at the first symmetric mode cut-off frequency, all the energy of an incident S_0 mode is transferred to the S_1 mode, and at the second symmetric cut-off frequency all the energy of an incident S_1 mode would be reflected in the S_0 mode. The boundary conditions that have to be satisfied at the normal boundary of a free plate are, of course, completely different from those that apply at the leading edge of a joint.

Returning to the example of figure 5.1, the double-skinned region of the joint with a 0.3 mm-thick sealant jointing layer was a system introduced in section 4.4 of the previous chapter. As was found generally in the multi-layered systems, discussed in the last chapter, the S_0 input signal will be predominantly mode-converted to the pair of modes with similar phase velocity and mode shape to that of the input S_0 mode. These are marked on the dispersion curves of figure 5.2. Other modes may have similar group velocity and attenuation to these modes, but it is the phase velocity and mode shapes that are important and the other modes are not excited. The modes that carry the energy of the incident mode across the joint may be termed carrier modes and the mode shapes of the two principal carrier modes for input S_0 at 0.98 MHz can be seen above the joint in figure 5.1. For each of these mode shapes, consider just the lower section, which represents the lower plate in the bonded region. It is clear that the mode shapes in the lower plate are very similar and closely resemble that of the input mode in the single-skin region. Both modes are therefore very strongly generated by mode-conversion at the leading edge. In the preceding chapter it was mentioned that the essential difference between a pair of twinned modes is an extra phase change in the interface layer. This is seen in both the in-plane and out-of-plane displacements in the carrier mode shapes in figure 5.1. In the upper plate, the mode shapes of the carrier modes are once again similar, but are in phase opposition owing to the phase change. When the two carrier modes are generated by mode-conversion at the leading edge, they are superimposed and the resulting displacement, which is the sum of the two mode shapes, is shown below the joint. The resultant shows that in the lower plate the displacements of the carrier modes sum constructively, while in the upper plate the displacements are largely destructive. There is consequently very little surface displacement amplitude at the joint leading edge. The displacement amplitude at the leading edge is not zero, however. Firstly, this is because the carrier mode shapes in the upper plate are not perfect, phase-reversed, copies of each other. Secondly, the diagram in figure 5.1 is schematic and in reality other modes within the bandwidth of the input signal are also excited to some extent, and the amplitudes of the principal carrier modes may not be exactly equal as implied by the figure. Finally, the numerical analysis, presented shortly, found that a surface wave is generated on the vertical leading edge of the upper plate, and this also contributes some surface displacement at the leading edge. Once generated, the two principal carrier modes propagate away from the leading edge with similar, but not equal, phase velocity. This difference in phase velocity results in a cyclic change in the resultant displacement as the modes propagate temporally and spatially through the double-skin region. The carrier modes are effectively 'beating' together, and the displacement amplitude on the surface of the upper plate in figure 5.1 changes cyclically between a destructive and constructive interference condition at spatial intervals along the plate surface; the opposite condition being found at any corresponding position on the lower plate. A similar 'beating' is found in the free plate at high frequency-thickness products, where the two fundamental modes, having very similar phase velocities, form what is usually termed the pseudo-Rayleigh wave. This mutual interaction is discussed by Auld (1990) who describes a coupling of the two modes across the plate, with energy being transferred in a temporal and spatial cyclic pattern from one surface of the plate to the other, over a spatial distance which he calls the 'coupling length'. This is similar to the carrier-mode conditions in the bonded region of a joint. As one might expect, increasing the carrier-mode phase velocity difference shortens the coupling length. Indeed, the coupling length (S_c) is simply related to the difference in wavenumber of the two carrier modes (k_1 and k_2) such that:

$$S_c = \frac{\pi}{|k_1 - k_2|} \tag{5.1}$$

Where signals of finite length are employed, as is always the case in NDE, the carrier-mode signals will eventually separate, given a sufficiently long propagation distance. In some cases, one of the principal carrier modes has a much greater attenuation than the other and its influence rapidly diminishes with distance from the leading edge, leaving just the decay of the other mode. Precisely the same carrier-mode generation and interference occurs in the bonded joint, since the dispersion curves, which are presented in figure 5.3, exhibit similar mode twinning in the phase velocity spectrum.

5.3 Experimental and Numerical Investigation

The experiments and numerical modelling that were carried out to investigate mode interaction in the aircraft joints are described below. Rather than presenting the results of the experimental and numerical modelling work separately, in this section, it is more convenient to present the results together, in section 5.4, enabling easier comparison of corresponding cases.

5.3.1 Experiments

This section describes the experiments that were conducted following consideration of the dispersion curves for the double-skin systems. It was felt that sufficient validation of the dispersion curves of the double-skin systems had been covered by the experiments detailed in the last chapter. The aim of this series of experiments was to illuminate the carrier-mode generation and interaction within the joint and to support the numerical analysis described later.

As in previous experimental work a small number of mode points were selected that might reasonably reveal the general interaction. Clearly, it was necessary to utilise only those modes that could be generated in the single plate with the available equipment and to aid subsequent analysis, dispersion was minimised. Consequently, the chosen points are generally those identified as having practical potential in a health-monitoring system.

It was initially supposed (perhaps somewhat naively) that the interaction of a single free-plate mode with a joint leading edge would generate a similar single mode in the double-skin region, with equal phase velocity. However, from the results of the initial experiments, this was clearly not the case, and an interference pattern between two or more modes was apparent in the double-skin region, the most likely candidates being the carrier modes identified previously.

The experimental work focussed upon the interference pattern appearing over the surface of the joints, which gives good insight into the carrier-mode interaction, and can be easily compared with corresponding results from the finite-element models. It is also the most simple and straightforward approach. The results were generally processed in the time domain by measuring the parameters of the interference pattern, particularly the 'coupling length'. Frequency-domain methods are not helpful in situations such as this, where interference between modes of similar wavenumber is occurring and modes are not separable by two-dimensional Fourier analysis. The experimental method was generally that described in chapter 2, recording the time domain signal at incremental intervals of 10 mm over the surface of the double-skin region of the joint, using local-immersion wax baths. Later, several experiments were repeated using the laser equipment, also described in chapter 2, to confirm the wax-bath results.

Four joint specimens were manufactured, the details of which are presented in table 5.1 below. Specimen A had only a 50 mm overlap, which proved to be insufficient with respect to measurements. It was also considered that reverberation might be significant in this specimen, and so the other specimens all feature a 150 mm overlap. The experiments reported in this thesis utilised only specimens B, C and D. Figure 5.4 illustrates an example of the experimental arrangement, in which the laser receiver is used to measure the out-of-plane surface displacements across specimen D, at distances from the leading edge denoted by *d*.

ID	Jointing Material	Type	Jointed Length (mm)	Bond thickness (mm)
A	PRC	Lap	50	0.23 +/- 20%
B	PRC	Lap	150	0.3 +/- 6%
C	Redux	Lap	150	0.25 +/- 4%
D	Redux	Stringer	150	0.26 +/- 2%

Table 5.1 Experimental specimens

Table 5.2 lists the modes examined, together with the specimen used in each case. This table also indicates the phase velocities (V_1, V_2) of the two carrier modes and their respective attenuations (α_1,α_2) derived from the dispersion predictions. The coupling length (S_c), defined in equation 5.1, is also shown.

Input Mode	Frequency (MHz)	Jointing Material	Type	Specimen	Predicted Parameters				
					Phase velocity V_1 (m/s)	Phase velocity V_2 (m/s)	Attenuation α_1 (dB/m)	Attenuation α_2 (dB/m)	Coupling length S_c (mm)
S_0	0.98	PRC	Lap	B	5371	5244	54	43	113
A_0	0.55	PRC	Lap	B	2787	2088	758	21	8
A_0	1.1	PRC	Lap	B	2662	2482	366	15	18
S_0	1.1	Redux	Lap	C	5557	5381	20	29	77
S_0	1.55	Redux	Lap	C	5309	4894	26	8	20
A_1	2.27	Redux	Lap	C	6369	6138	33	357	37
S_0	1.1	Redux	Stringer	D	5557	5381	20	29	77
S_0	1.5	Redux	Stringer	D	5309	4894	26	8	20
A_0	1.1	Redux	Stringer	D	2646	2523	103	53	25

Table 5.2 Experimentally examined modes.

The first experiments examined the four modes in the sealant jointed specimen (B in table 5.1) and, having observed the interference of the modes, subsequent experiments and modelling concentrated on just the S_0 mode in the frequency band between 1 MHz and 1.5 MHz. In this band an almost linear divergence in the relative phase velocity of the carrier modes is seen in figures 5.2 and 5.3.

The group velocity of the input signal was first calculated from its arrival time over the initial 300 mm of propagation in the free plate. This was then compared with that predicted for the desired mode, to confirm the correct input mode. The maximum amplitude of the signal envelope received at each location was established using the well-known Hilbert transform technique [Randall (1987)]. This amplitude was plotted against the distance from the joint leading edge, and the results were compared with the calculated coupling length and subsequently with those of equivalent numerical modelling exercises.

5.3.2 Numerical Modelling

Numerical modelling was carried out to reveal more clearly the interference across the thickness of the bonded region and to examine more closely events at the joint leading edge. Details of the method used can be found in chapter 2, which also mentions some of the limitations of the numerical analysis. An important limitation to be borne in mind is that the modelling software did not accommodate material damping. Furthermore, owing to the very large difference between the bulk longitudinal wave velocity in the aluminium alloy skin and the bulk shear wave velocity in the PRC sealant, it was not possible to model systems with PRC sealant layers. It will be recalled from chapter 2 that Blake's rules for stability in finite-element modelling dictate that the maximum element dimension is defined by the velocity of the slowest wave and the maximum time step is subsequently determined by the transit time of the fastest wave across an element. The very slow shear wave in PRC consequently demands a very small mesh size and when this is considered with the speed of the fast longitudinal wave in the skin, the time step becomes so small that many years would be required to run the model.

Figure 5.5 shows the three types of model run. A model with the same dimension as the experimental joint specimens, covering the entire joint, was not a practical proposition, because it would have required more elements than the arrays of the modelling software could accommodate and would have taken too long to run. The geometry of the first set of models was confined to just the input, single-skin region and the bonded region, seen in figure 5.5a). Since the position of the output region is not defined, these models apply to both lap and stringer joints, notwithstanding the fact that differences in the interaction with the joint trailing edge are likely. Providing they have a sufficiently long bonded region, such models should adequately model the mode interaction in this area. Considerable effort was spent in achieving an appropriate compromise between the model size and the required run time. The model size had to be sufficient to cover the experimental measurements and to remove unwanted reverberation effects, whilst the run time had to be restricted to a practical duration. The initial models had a bonded region of just 72 mm, that was subsequently extended to 158 mm to cover the same length as the experimental specimens. These extended models each required roughly six hours to run on a Unix workstation.

A further concern was the number of elements through the thickness of the adhesive layer. The mode shapes, such as those of the carrier modes in figure 5.1, for example, exhibit quite a complex pattern in the adhesive layer, owing to the phase changes. It was necessary to establish the number of elements that would be required through the thickness of this region, for reliable results. Models of type a) were run with two square elements through the thickness of the adhesive layer, and these were compared with similar models having four rectangular elements, having an aspect ratio of two, and the same length as those of the previous model, as shown in figure 2.9. Finding that the results were identical, all subsequent modelling was carried out using the two-element regime, except for the models employing the input mode A_1 at 2.27 MHz, which demanded much smaller elements.

In order to model the transmission across lap and stringer joints, further models, covering whole joints with both input and output single-skin regions, were run. These models, shown in figure 5.5 b) and c), featured a 25 mm bonded region, which is roughly comparable with joints most commonly found on aircraft. During the manufacture of the experimental specimens, described in the last section, care was taken to remove all adhesive and sealant that was squeezed from the joint, in order to preserve the correspondence between the experimental specimens and the models. Such practice is not normal procedure during aircraft manufacture, where joint spew may further complicate the mode interaction with real aircraft joints. Details of the various models run are shown in table 5.3 below.

Input Mode	Frequency (MHz)	Type of Model (refer of fig 5.5)
S_0	1.1	Leading edge (a), Stringer (b), Lap (c)
S_0	1.5	Leading edge (a), Stringer (b), Lap (c)
A_1	2.27	Leading edge (a)

Table 5.3 Numerical finite-element models of joints.

5.4 Results

5.4.1 Joints with a sealant interlayer

We begin by examining the results of the experiments on the lap joint with a sealant interface (specimen B). Figure 5.6 shows two examples of the signals received by the local-immersion wax bath at spatial intervals across the free surface of the output plate in the overlap region. These are presented in the form of ‘waterfall’ plots that highlight the differences between the signals at each location. For each time trace in the waterfall plots, the time axis originates at the centre (maximum amplitude) of the input tone burst. The input signals in both cases were of a similar frequency, but owing to the much lower group velocity of $A_{0,}$ a longer time scale is used in 5.6 b), giving the impression of a lower frequency. Both of the waterfall plots show very clean signals, which are free from the effects of bath reverberations owing to the use of the local-immersion wax baths. In the waterfall plot of figure 5.6.a) the amplitude of the signal is seen to be increasing with distance from the leading edge reaching a maximum at about 80 mm. In figure 5.6 b) the amplitude of the signal generated by A_0 at 1.1 MHz also increases from the leading edge, but is seen thereafter to change in a cyclic fashion. Figure 5.7 a) and b) plot the respective maximum amplitudes of the signals in Figure 5.6 a) and b) by means of a broken line. In addition, the corresponding results from later laser experiments are superimposed, using a solid line. The data in each series has been normalised by dividing by the mean of the amplitudes of the data points in the range common to both laser and local-immersion experiments. In both cases it is seen that the local-immersion and laser results are in close agreement, particularly in respect of the period of cyclic amplitude fluctuation. Differences in the amplitudes of laser and local-immersion results are thought to be attributable to the fact that the laser is a point measurement, whereas the local-immersion method effectively integrates over the area of the wax-bath aperture at the plate surface. Thus, the latter is less sensitive to more localised variations that may arise from any reverberation or reflection from the specimen sides. The coupling length of the carrier modes of S_0 at 0.98 MHz is seen in table 5.2 to be 113mm, but the maximum amplitude in figure 5.7 a) occurs at only 80 mm from the joint leading edge. However, just a 0.5% error in the phase velocity of one of the carrier modes would account for this disagreement and such an error is likely, given the variation in the PRC properties discussed in chapter 2.

In figure 5.7 b) the cyclic pattern generated by an input A_0 at 1.1 MHz is found to have a period that is not constant. The first amplitude maximum is found at 20mm, which is in reasonable agreement with the calculated coupling length of 18mm, given the varying PRC properties mentioned previously. However, subsequent cycles have much longer periods that vary in length. The cause of this is the much higher attenuation of one of the carrier modes (366 dB/m) compared with the other (15 dB/m). The high-attenuation mode would only have influence over a very short distance from the leading edge, before decaying to insignificance. A best-fit curve, fitted through all points located at greater than 40 mm from the leading edge, indicated a decay of 35 dB/m which compares favourably with the predicted decay of the less attenuative carrier mode. The reason for the oscillation in the decaying envelope amplitude is not known, but may be the result of interference with reflections from the plate boundaries.

A similar situation is found when A_0 is input at 0.55 MHz, where, once again, the attenuation of one of the carrier modes is much larger (409 dB/m and 16 dB/m). The joint surface amplitude for this case, obtained by local-immersion transduction, is shown in figure 5.8. Since data is only available for distances of greater than 40 mm from the leading edge, the influence of the high attenuation mode is not seen. In the experiments employing wax baths there was a likelihood that water would leak from the bath if it was brought too close to the joint leading edge and this is the reason that local-immersion measurements were not generally made for distances of less than 40 mm in this experiment. With hindsight, of course, this restriction could have been circumvented by performing the experiment on the opposite specimen face. Fitting a logarithmic curve to the points shown in figure 5.8 indicated an attenuation of 12 dB/m, which corresponds closely with the predicted decay of the remaining carrier mode. In this case, perhaps owing to the longer wavelength, there is no oscillation in the amplitude over the joint surface.

Except for the initial rise in amplitude close to the leading edge, the interference pattern produced by the two principal carriers was not clearly seen in the experiments on sealant jointed specimens, owing to the high attenuation of one mode. This was not the case however, for the bonded joints, which are considered next.

5.4.2 Joints with an adhesive interlayer.

The waterfall plots of figures 5.9 a) and b) show received signals for the case where the input mode to the bonded lap joint was S_0 at 1.5 MHz. In this case a 50 cycle Hanning-windowed tone was employed to avoid dispersion.

Figure 5.9a) shows the waterfall plot for the bonded region of the upper surface of the output plate, while 5.9b) shows the corresponding plot for the lower surface of the input plate in the bonded region (refer to figure 5.5 c)). In both figures the interference pattern is clearly seen. Comparing corresponding locations on the two figures one finds that positions where the envelope amplitude is greatest in one figure correspond with minimum envelope amplitude in the other figure. Thus, the swapping of energy from one side of the system to the other, with propagation distance was observed (described in section 5.2). In this case the predicted attenuation of the carrier modes was 8 dB/m and 26 dB/m, both of which are relatively low and so the interference pattern extends across the whole joint. A further example of the signals received across a bonded lap joint is seen in figure 5.10. In this case the input mode was A_1 at 2.27 MHz. This illustrates another case, similar to those in the sealant joints, where one carrier mode has a high attenuation (357 dB/m). Here, as before, the maximum signal amplitude is seen to fall with distance from the leading edge, the decay being governed by the carrier mode with least attenuation.

To illustrate the dependence of coupling length on the difference in the carrier-mode phase velocities and the correspondence with the coupling length, calculated from equation 5.1, the variation of maximum surface amplitude for an input S_0 mode at 1.1 MHz and 1.5 MHz are shown in figures 5.11 a) and b) respectively. Corresponding results from the numerical analysis are superimposed and show good agreement in both cases, particularly with respect to the period of cyclic variation. From table 5.2, the coupling distance for input S_0 at 1.1 MHz is seen to be 77mm. The period of amplitude variation in figure 5.11 a), however, is about 120 mm, implying a coupling length of only 60 mm. The dispersion curves from which the coupling lengths in table 5.2 were calculated assumed the nominal thickness of 0.25mm for the adhesive joint layers. However re-calculating the dispersion curves using the FE model adhesive layer thickness of 0.24 mm instead, results in a coupling length of only 68 mm. Thus a large proportion of the error is attributable to slight differences in the adhesive layer thickness. Further error is probably the result of slight differences in the dispersion of the two carrier modes over the bandwidth of the signal used in FE and experimental analysis. The simple calculation of equation 5.1 assumes continuous, single-frequency signals.

Table 5.2 indicates that at 1.5 MHz the coupling length for input S_0 reduces to 20 mm, owing to the increased relative difference in the carrier-mode phase velocities at this frequency. Figure 5.11 b) shows a cyclic amplitude variation with a period of about 40 mm, indicating a coupling length of 20 mm that corresponds with the predicted value. As expected, the pattern on the opposite surface of the jointed area showed a similar variation with an opposite phase.

The experimental results for the stringer joint were very similar, though the different thickness of the adhesive layer resulted in differences in the coupling lengths compared with the lap joint.

A final example of the surface amplitude variation is presented in figure 5.12, which plots the maximum signal amplitude (measured by laser) across the free surface of the attached plate in the stringer joint specimen, for the input mode: A_0 at 1.1 MHz. (Figure 5.4 illustrates the experimental arrangement, where *d* denotes the distances plotted in figure 5.12.) Once again the interference pattern is seen having a period of about 40mm, implying a coupling length of 20mm. The calculated coupling length in this case is 25mm, and the difference is probably caused, once again, by errors in the adhesive thickness or properties. Also the period of the cyclic variation in these results is not perfectly constant, perhaps owing to reverberation and/or other modes. Nevertheless, the clear cyclic pattern is undoubtedly caused by primary carrier-mode interference.

This interference pattern is very important, since it was found, in the experiments and modelling of whole joints, that it largely determined the efficiency of propagation across the joint. Optimum transmission will occur when the carrier-mode interference results in maximum amplitude in the output plate at the trailing edge of the joint. This mechanism is graphically illustrated in figure 5.13, which shows a snapshot in time from the full mesh output of the FE model for the case of an S_0 mode, input to a bonded lap joint at a frequency of 1.5 MHz. The input mode is a long twenty-cycle tone burst, so that the situation shown in the figure approximates the steady state condition. In order to see clearly the interference pattern in the jointed region only a small section of the mesh in the region of the joint is shown. At the leading edge of the joint there is relatively little amplitude on the surface of the output plate and large amplitude on the input plate surface below. This situation is the equivalent of that illustrated in figure 5.1 for the sealant joint. By the time the trailing edge of the joint is reached, the interference condition is reversed and a large amplitude is now seen on the output plate surface with very little amplitude on the corresponding input plate surface. Excellent transmission into the output plate is clearly seen and it is also apparent that there is very little reflection from the end of the input plate at the trailing edge. The latter is equally important, since it results in less joint reverberation.

The frequency dependence of the carrier mode interference is highlighted graphically in figure 5.14. This shows a series of snap shots in time and space of distorted mesh output from the bonded-joint FE models depicted in figure 5.5a) after a 20 cycle tone burst of the S_0 mode was input at the left-hand end. Figure 5.14 a) illustrates the carrier mode interference condition occurring at the joint leading edge, when the frequency of the input signal is 1.75 MHz. This shows the condition when the out-of-plane displacement reaches a maximum in the upper plate, which occurs, at a distance of 12mm from the joint leading edge at this frequency. The same view also shows the interference condition at the leading edge, where maximum out-of-plane displacement occurs on the free surface of the input plate, with little displacement on the surface of the upper plate. Figures 5.14 b) and c) illustrate the corresponding two conditions when the input frequency is reduced to 1.5 MHz, figure 5.14 b) showing the point of maximum out-of-plane displacement in the upper plate which is now 20mm from the leading edge and c) showing the leading edge condition. Figures 5.14 d), e), f), and g) illustrate the corresponding pairs for input frequencies of 1.25 MHz and 1.1 MHz. Together, these snap shots clearly illustrate the frequency dependence of the coupling length.

To further illustrate how the efficiency of transmission across a joint is determined by the carrier-mode interference, the ratio of input to output signal amplitude in the numerical models, featuring an S_0 input mode, is shown in table 5.4. Two-dimensional Fourier transform (2DFFT) analysis of the input and output signals in the single plate was employed and an example, for S_0 input at 1.1 MHz, is shown in figure 5.15. The input mode, whose amplitude was measured, can be seen centred on the intersection of the broken lines in figure 5.15a). The white lines superimposed on this graph are the dispersion curves of the free skin, plotted in wavenumber-frequency space. This indicates that just the S_0 mode was generated. In this case, the entire input time trace was processed and the dark area on the corresponding point with negative wavenumber is the reflection from the trailing edge of the joint. The trailing edge reflection can be gated out in the time domain, allowing any reflection from the leading edge to be seen. In both of the input S_0 models reflections from the leading edge were found to be insignificant. Figure 5.15 b) shows the 2DFFT plot of the output signal. Once again the output S_0 signal can be seen, but in addition, significant amplitude is evident on the A_0 mode line. This is the result of mode conversion at the joint trailing edge. The frequency and wavenumber spectra corresponding with the broken lines are plotted adjacent to the appropriate axes, and the amplitudes of the peaks corresponding with the input and output S_0 modes were used to find the transmission coefficient. However, these spectra were sometimes complicated by 'dips' in the amplitude such as can be seen, for example, in the frequency spectrum adjacent to the vertical axis of figure 5.15b). These 'dips' are caused by reverberation across the joint, resulting in a series of output signals that cannot be separated in the time domain. Such reverberation was only evident in cases of poor transmission such as this, where the reflection from the trailing edge was large. Although this makes the actual transmission ratios unreliable, lack of attenuation in the model means that they do not reflect the transmission across real joints in any case. Despite these limitations, the transmission ratios of table 5.4 clearly demonstrate that a frequency that gives good transmission across a lap joint will deliver poor transmission across a stringer joint of similar specification, and (vice versa) as expected. The table also suggests that the worst transmission ratio may be about half that of the optimum transmission case.

Joint Type	Frequency (MHz)	S_0 Transmission Ratio
Lap	1.1	0.66
Lap	1.5	0.99
Stringer	1.1	0.86
Stringer	1.5	0.48

Table 5.4 Joint transmission ratios for an input S_0 *mode, derived from finite-element models.*

Finally, as a practical illustration of these results, figure 5.16 presents two time-domain traces from the simple pulse-echo experiment described in section 5.3. Once again, this example shows the case of the S_0 mode input to the bonded lap joint shown above the graphs. Graph a) shows the worst transmission case at 1 MHz. In this graph a large reflection from the trailing edge of the joint is indicated in the figure. This is followed by some joint reverberation, after which a small reflection from the back wall of the output plate is seen, indicating a poor transmission across the joint. Simply changing the input frequency to 1.5 MHz results in the optimum transmission case shown in graph b). Here the reflection from the joint trailing edge has very much diminished in amplitude, while the reflection from the output plate back wall is significantly larger. This optimum transmission case is particularly encouraging when one considers that, since this is a pulse-echo experiment, the signal has traversed the 150 mm-wide bonded region twice. The same test, applied to the stringer joint specimen, found that although optimum transmission occurred at a frequency of 1.08 MHz, similar to the worst transmission frequency in the lap joint as expected, the best transmission frequency was not 1.5 MHz, but 1.2 MHz. This difference is consistent with differences in the bond thickness and material parameters of the two joints. The effect of such variations would be more apparent when, as in this case, the coupling length is short. Indeed, this problem with the short coupling length highlights a crucial problem that arises when transmission is attempted across a series of narrow joints.

Although these results are most encouraging in respect of a single joint, similar results were not obtainable from a series of joints, such as is presented by a succession of bonded fuselage stringers. A typical stringer joint is about 20 mm in width and optimum transmission is obtained only if the first constructive maximum occurs in the output plate at the joint trailing edge. In this case the optimum coupling length is only 10 mm. With such a short coupling length, small variations in the joint dimensions (and perhaps also adhesive properties) cause radical departure from optimum transmission across successive joints. This results in a cumulative degradation of the transmission efficiency over a series of joints. A number of practical laboratory tests were carried out on a specimen with several bonded stringers spaced at intervals of 100 mm. Transmission across more than four stringers, with an effective attenuation of less than 40 dB/m, was unobtainable when twinned carrier modes were present in the bonded regions, even though transmission across the first joint was about 90% efficient. At the time, this finding was somewhat perplexing, since the author knew of commercial acoustic emission systems that can receive signals that have propagated over several meters through metallic fuselage structure. Such signals can only be guided-wave modes and this issue will be dealt with in the next chapter.

5.5 Conclusions

This chapter has described the experiments and numerical models used to illuminate the generation and interaction of carrier modes within aircraft lap and stringer joints. Several examples of the experimental results were presented that illustrated two possible situations that arise. If one of the principal carrier modes has a much higher attenuation, it decays to insignificance over a very short distance in the joint, leaving the less attenuative mode. In this case, interference between the principal carrier modes was only evident close to the leading edge and the measured decay across the remainder of the joint width corresponded roughly with that of the least attenuative mode. This situation was more commonly encountered in experiments on joints with a sealant interface. Where both principal carrier modes exhibit low attenuation the experimental results demonstrated that beating occurs over a considerable distance across the joint, resulting in a clear pattern of surface displacement. It was shown that the cyclic period of this pattern could be simply calculated from the relative wavenumber of the carrier modes.

The finite-element models allowed the interference pattern to be seen in cross-section throughout the joint. It was demonstrated that, for either a lap or a stringer joint, excellent transmission is achieved by arranging for constructive carrier-mode interference in the output plate at the joint trailing edge. This condition also results in less joint reverberation. Conversely, destructive interference in the output plate at the trailing edge results in the poorest transmission. A simple pulse-echo experiment provided a practical demonstration of the importance of this phenomenon for joint transmission.

The chapter concluded by reporting that although excellent transmission across a single joint can be arranged, sadly, this was not found to be sustainable across a succession of narrow joints, such as are found in aircraft fuselage structure.

Finally, the chapter raised the important question of how it is that acoustic emission signals are apparently capable of long-range propagation through fuselage structure. This important issue, which appears to cast doubt on the credibility of the findings of this chapter, must be addressed. The joint investigation was therefore extended to include study of the transmission of AE signals and this phase of the project is reported in the next chapter.

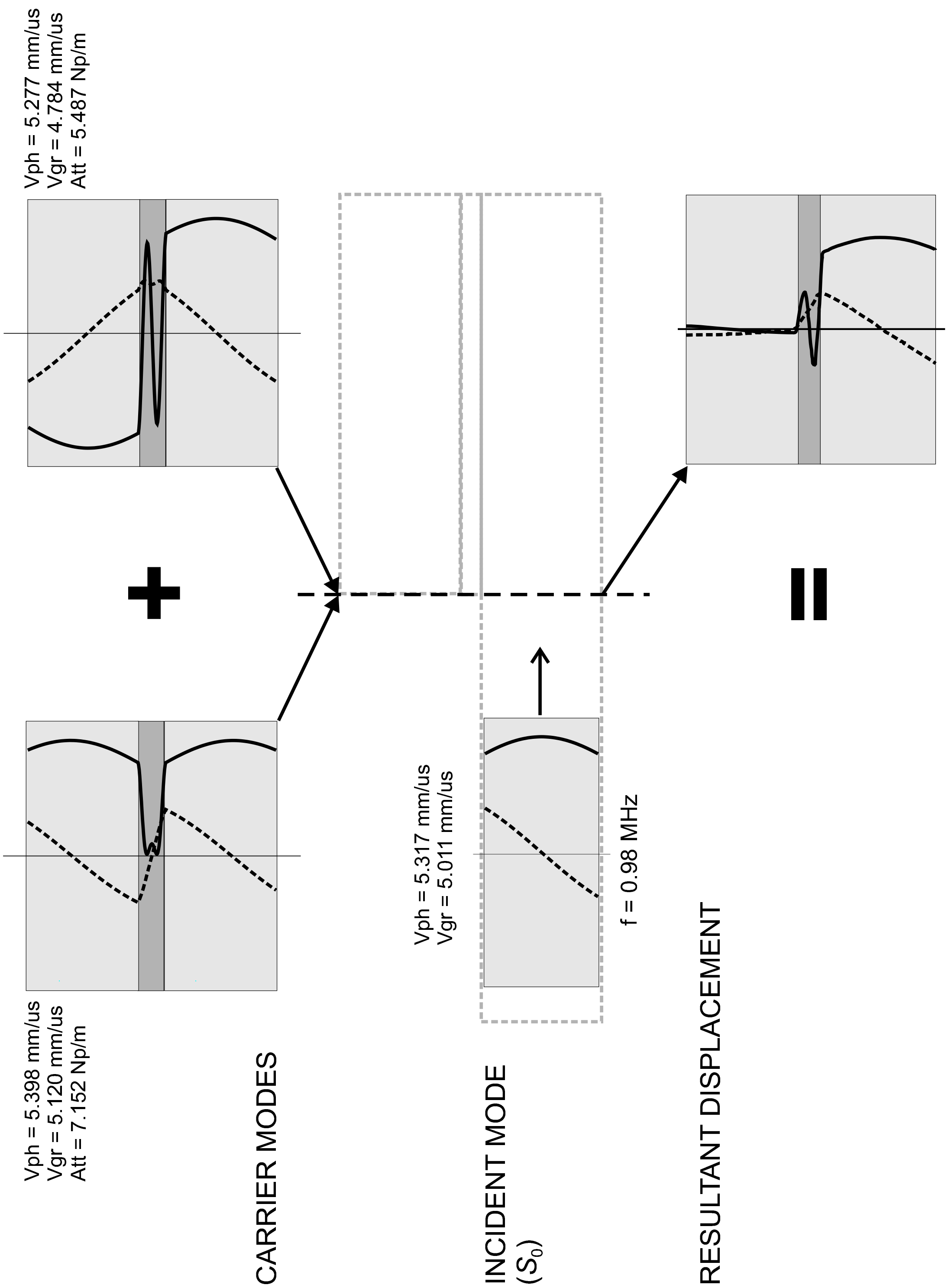

Fig 5.1 Schematic diagram of carrier-mode interference at the leading edge of a joint.
\- - - - - *Out-of-plane displacement;* ——— *In-plane displacement.*

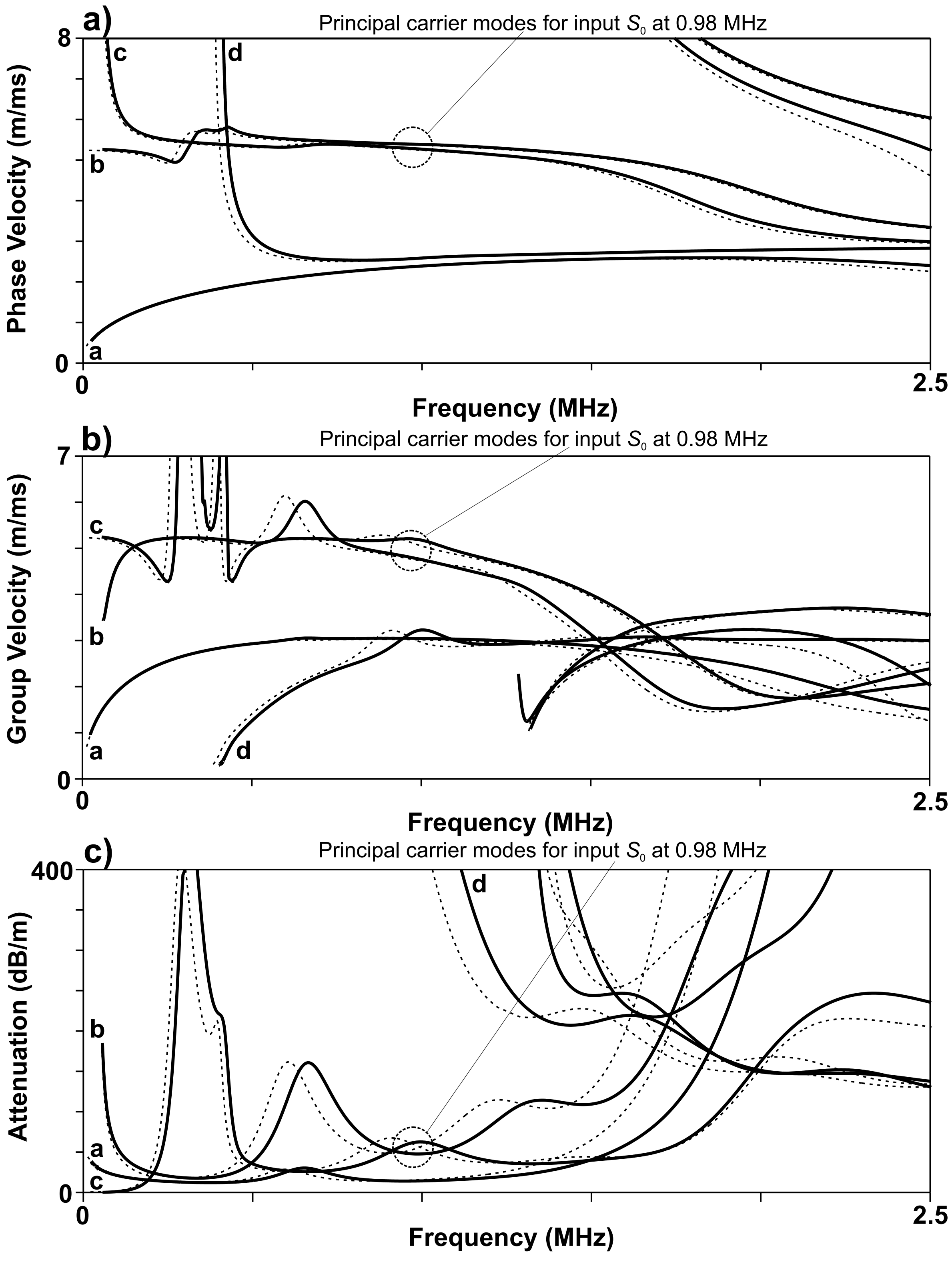

Fig 5.2 Dispersion curves for system of two skins joined by a PRC sealant layer. a) Phase velocity spectrum b) Group Velocity Spectrum c) Attenuation Spectrum.

0.3 mm sealant thickness -------------- *0.33 mm sealant thickness*

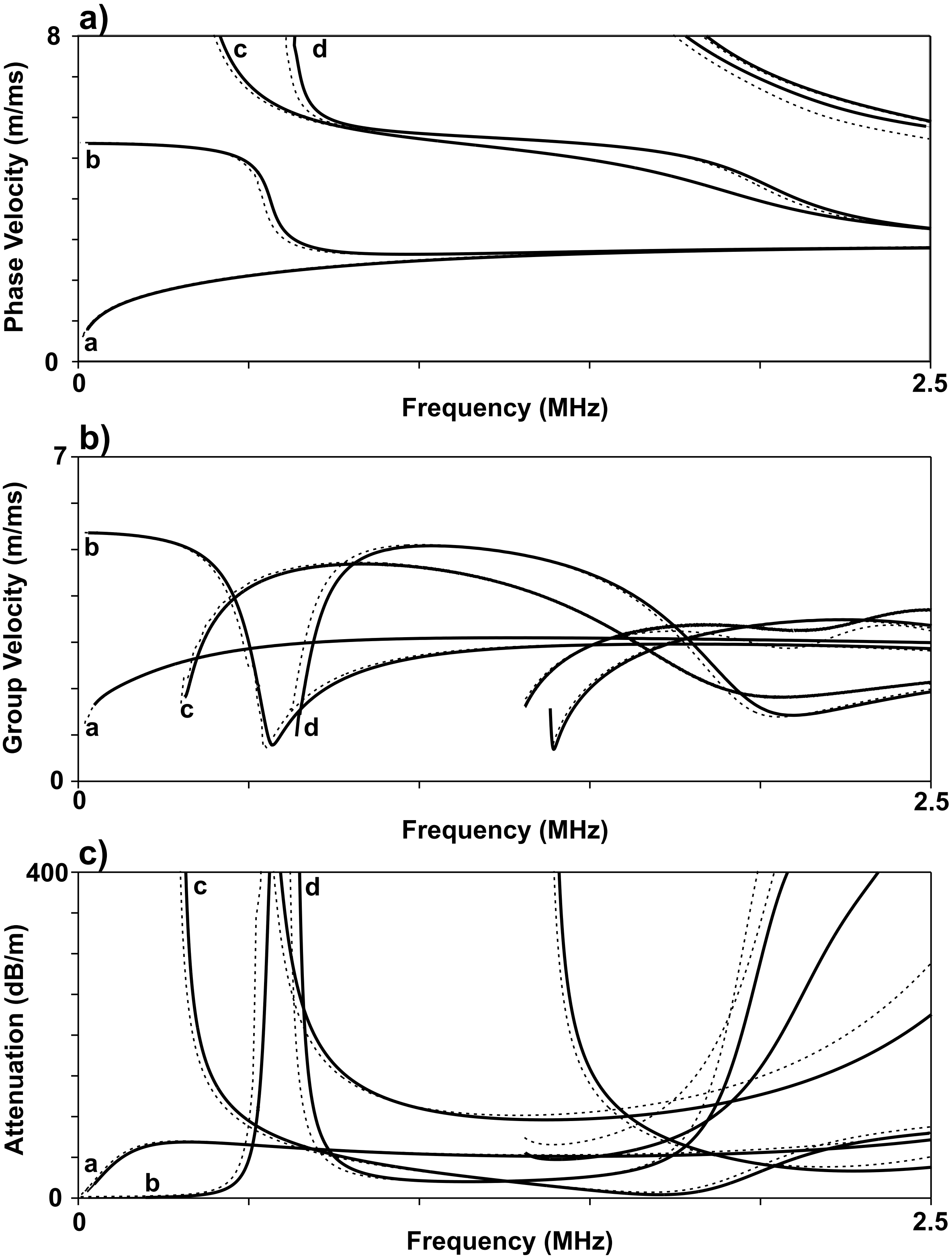

Fig 5. 3 Dispersion curves for system of two skins joined by a Redux adhesive layer. a) Phase velocity spectrum b) Group Velocity Spectrum c) Attenuation Spectrum.
0.25 mm adhesive thickness *0.275 mm adhesive thickness.*

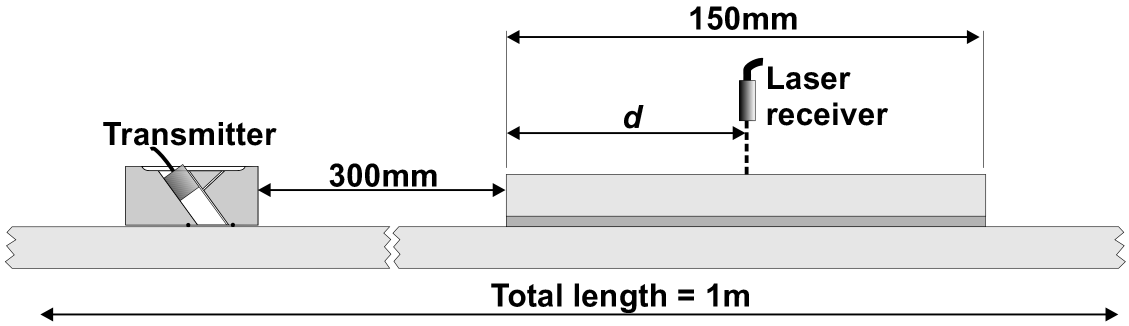

Fig 5.4 Experimental arrangement used to examine the interference pattern across specimen D. (refer to tables 5.1 and 5.2)

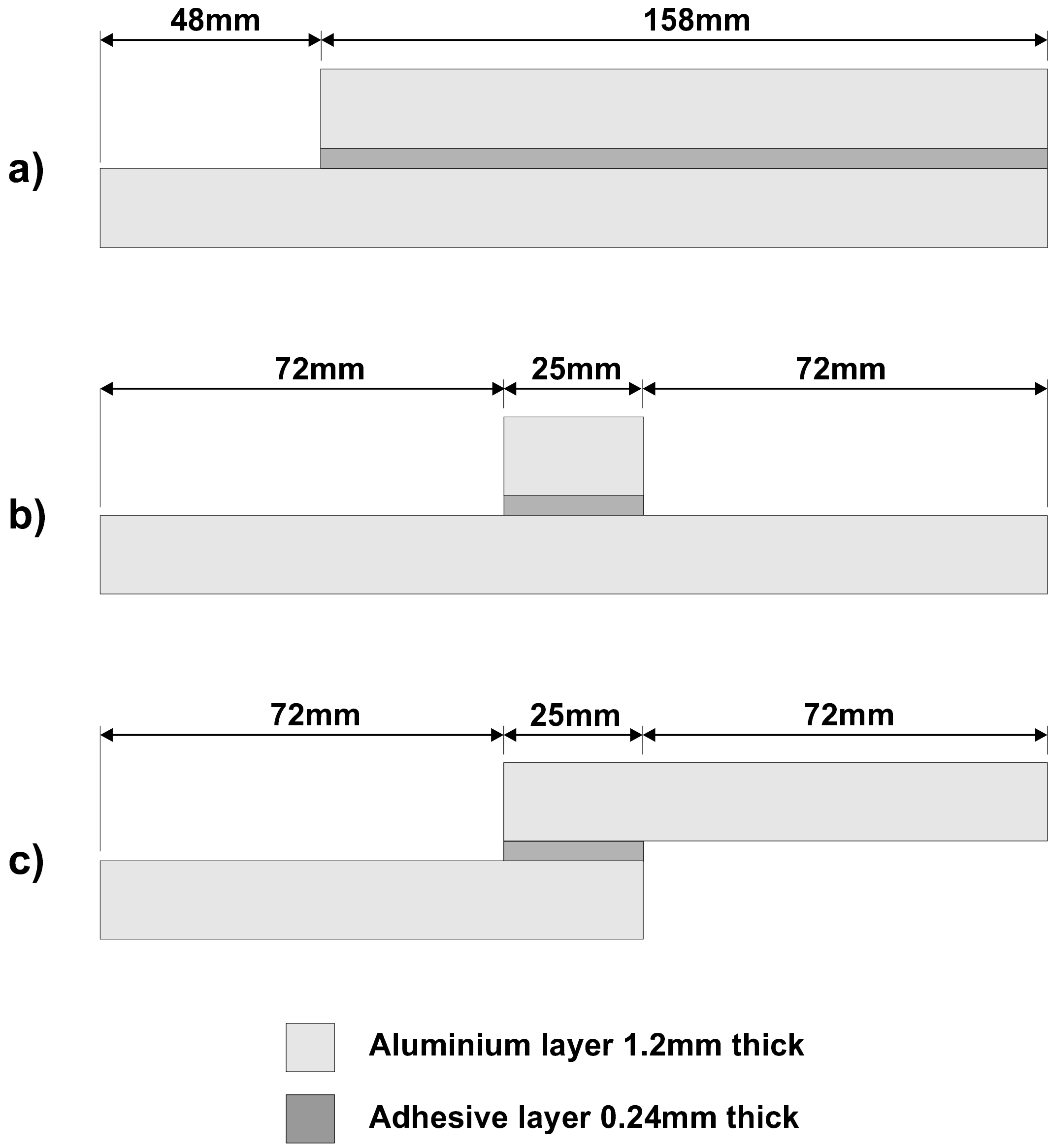

Fig 5.5 Diagram of finite-element models used a) leading edge common to both stringer and lap joints. b) Stringer joint c) Lap joint.

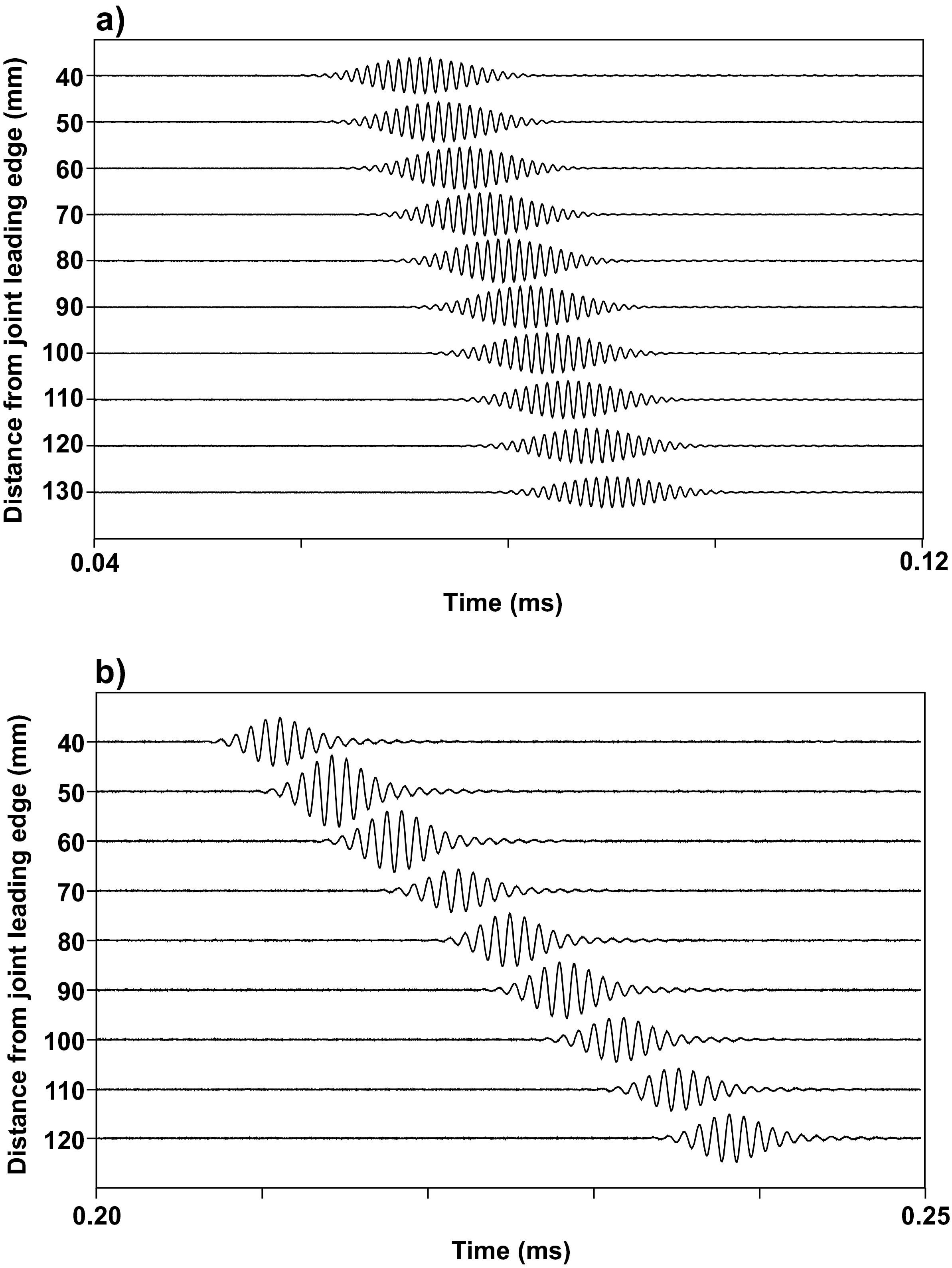

Fig 5.6 Two examples of experimental results obtained from the sealant jointed lap joint presented in the form of 'waterfall' plots for input modes: a) S_0 at 0.98 MHz b) A_0 at 1.1 MHz

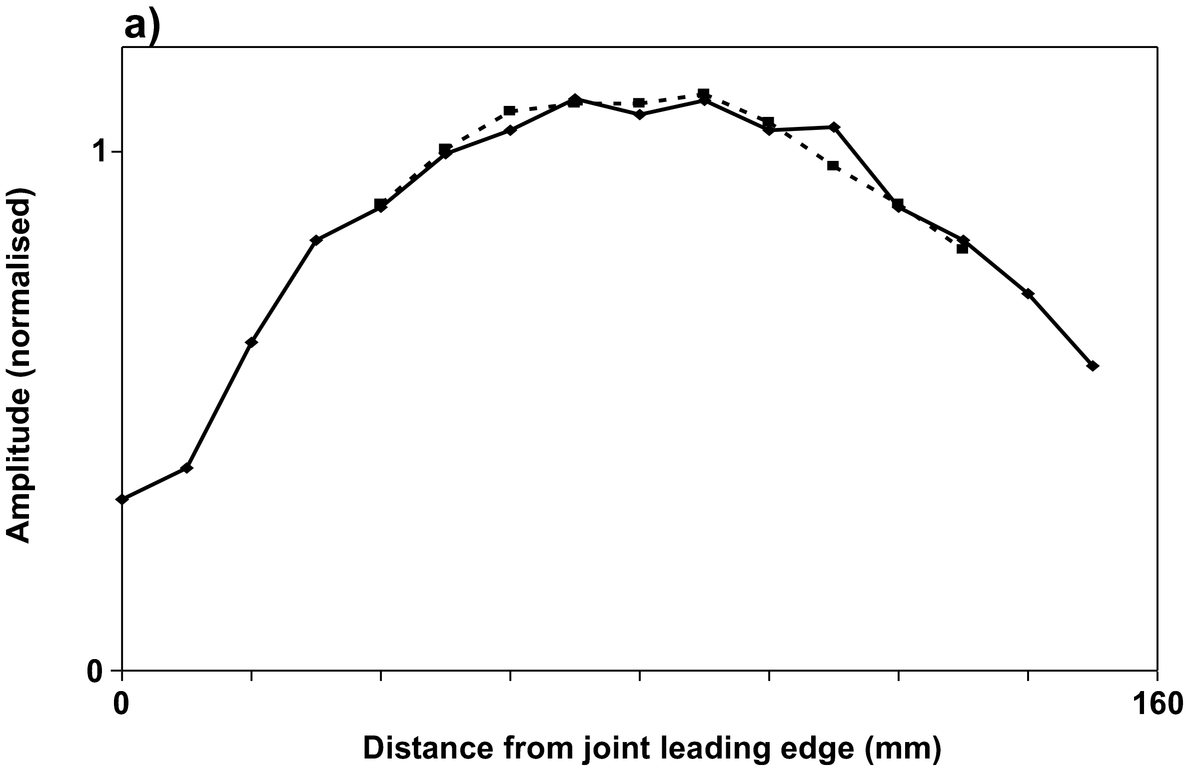

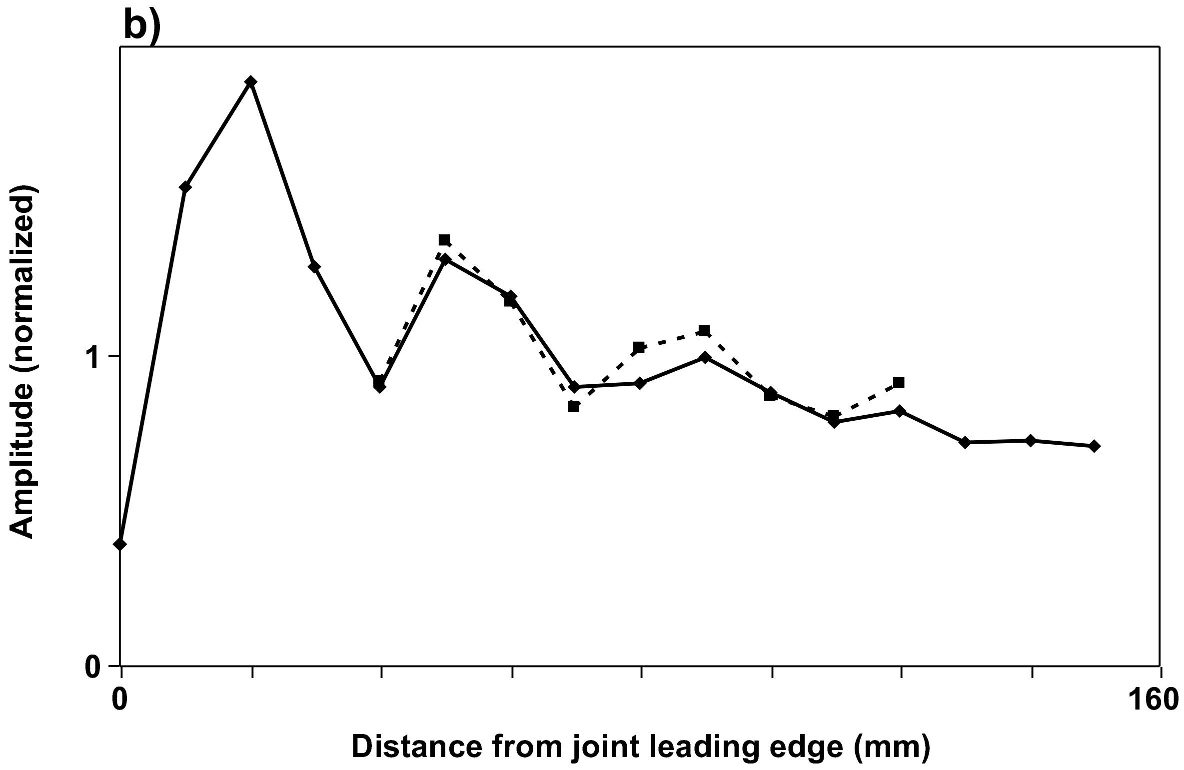

Fig 5.7 Comparison of results obtained by — — — local-immersion wax bath and ——— laser for the cases shown in figure 5.6 a) S_0 *at 0.98 MHz b)* A_0 *at 1.1 MHz. The data in each series has been normalised by dividing by the mean of the amplitudes of the data points in the range common to both laser and local-immersion experiments.*

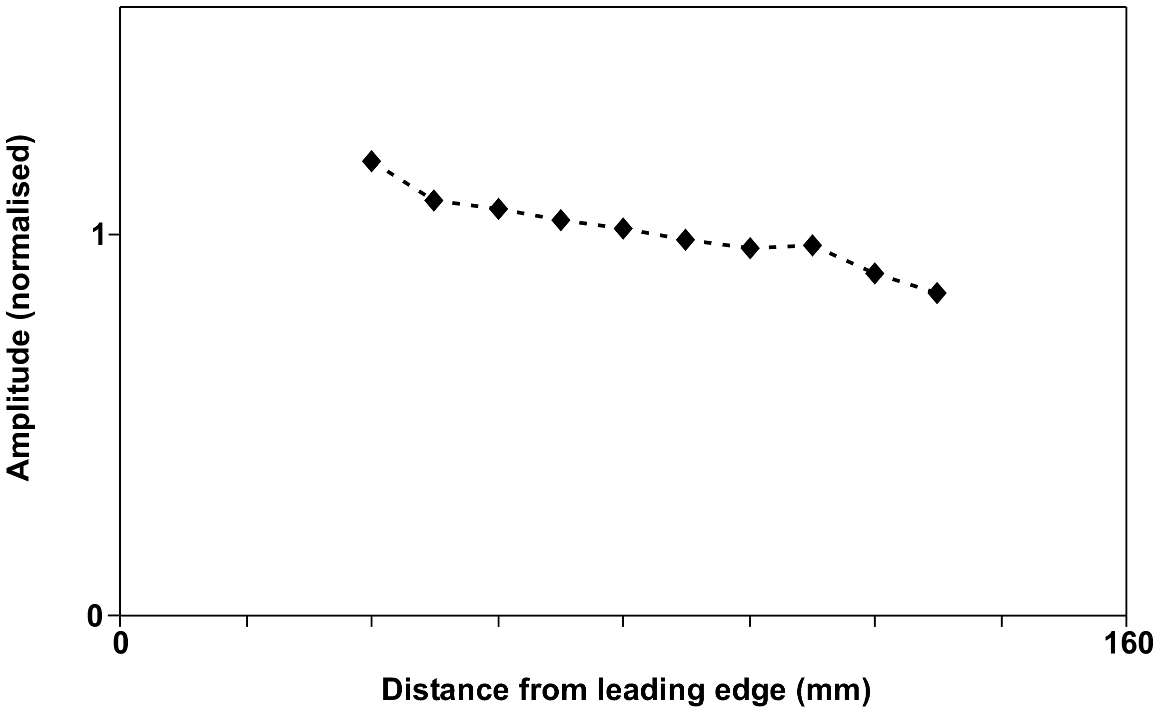

Fig 5.8 Experimentally measured surface amplitude across the overlapping region of a sealant jointed lap joint for the input mode: A0 at 0.55 MHz

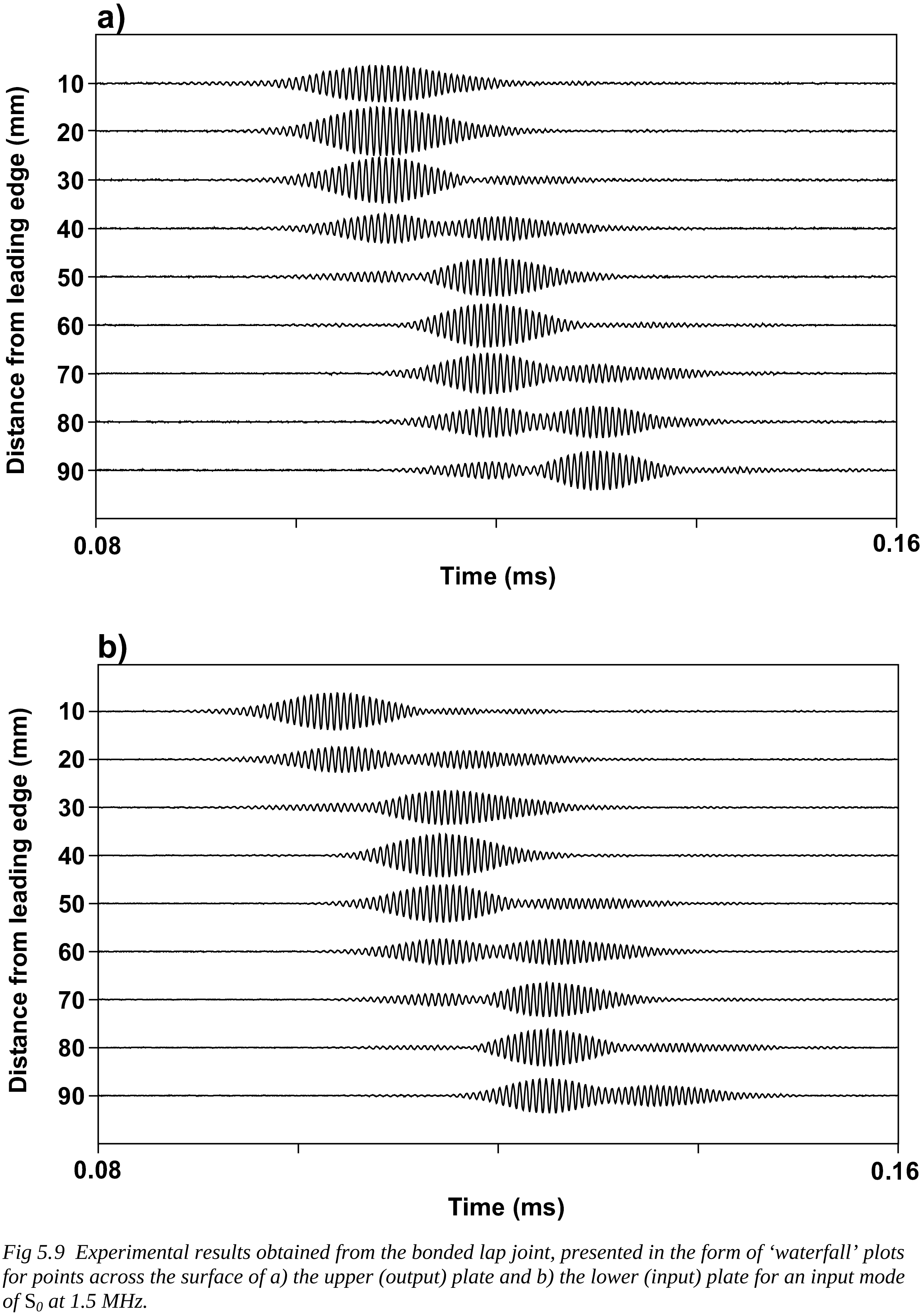

Fig 5.9 Experimental results obtained from the bonded lap joint, presented in the form of 'waterfall' plots for points across the surface of a) the upper (output) plate and b) the lower (input) plate for an input mode of S_0 at 1.5 MHz.

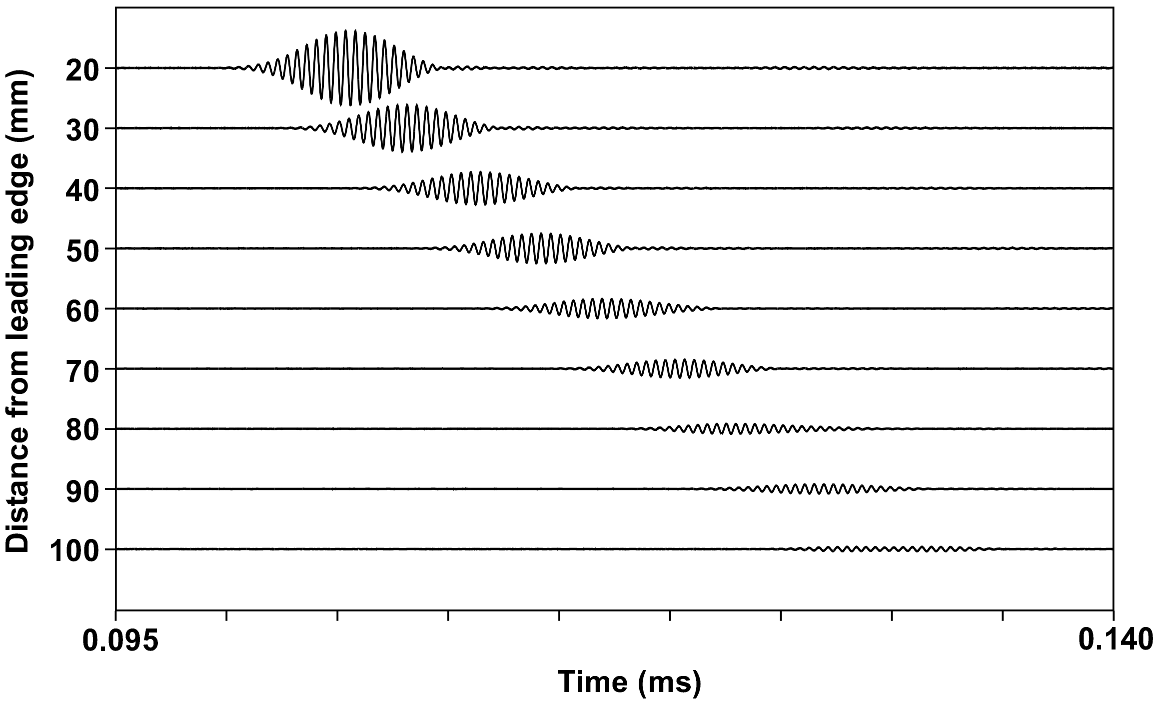

Fig 5.10 Waterfall plot of the time traces obtained at points along the free surface of the output plate in the overlap region of the bonded lap joint for the case of an input mode: A_1 *at 2.27 MHz.*

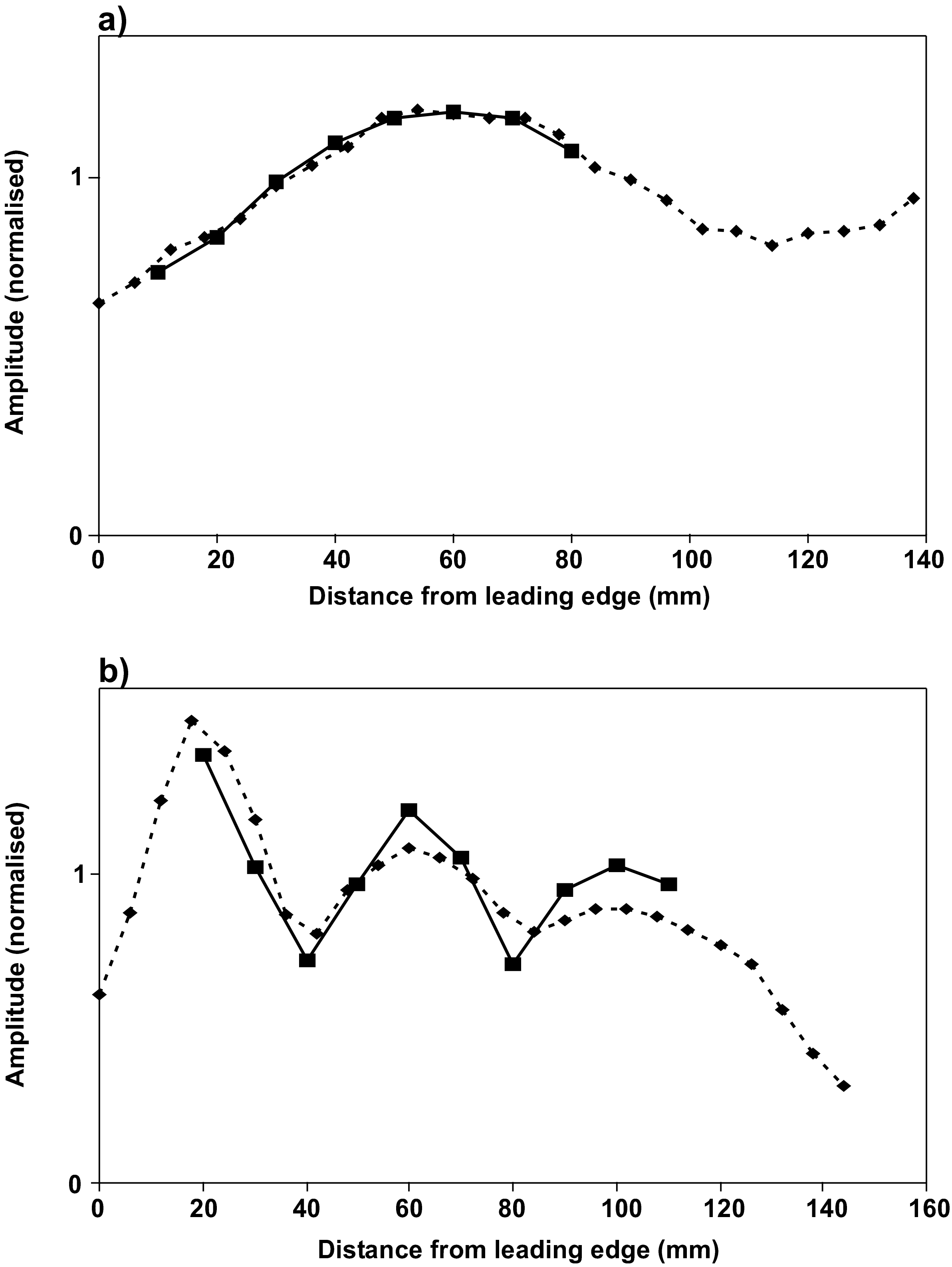

Fig 5.11 Graphs of surface amplitude for locations on the free surface of the output plate in the overlap region of the bonded lap joint for the cases of an S_0 *input mode at: a) 1.1 MHz and b) 1.5 MHz.*
: experimental results, : numerical predictions.
Results are normalised by dividing by the mean of the amplitude of points in the range common to both data sets.

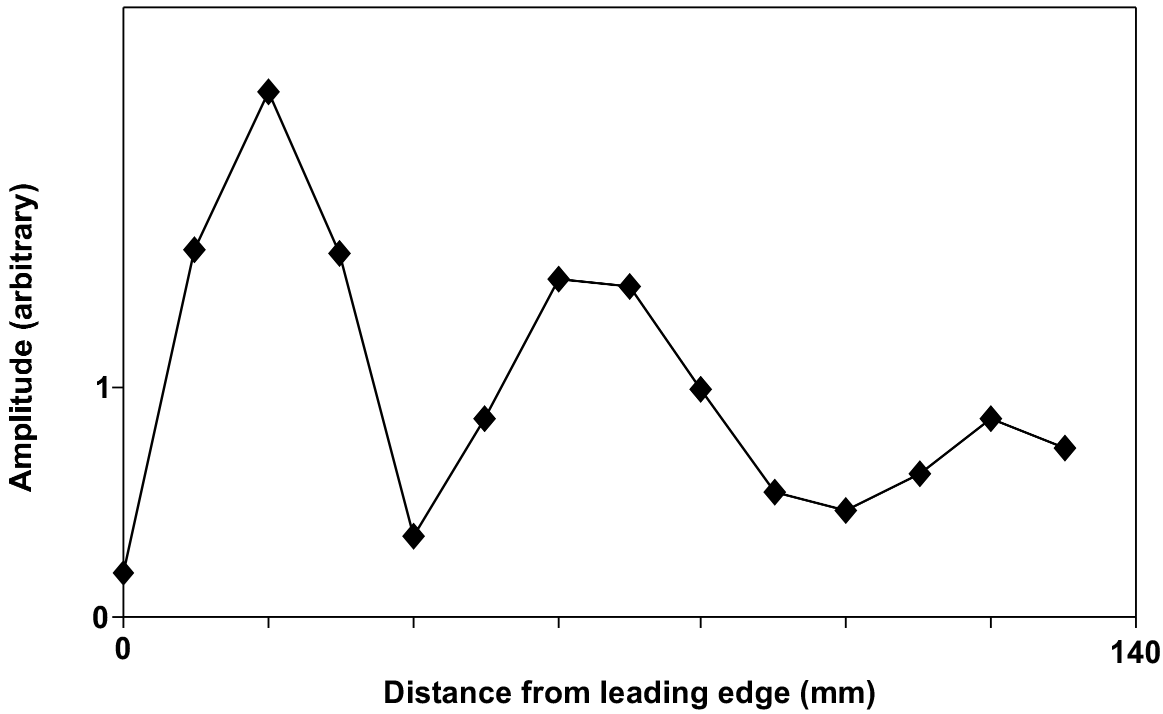

Fig 5.12 Graph of surface amplitude for locations on the free surface of the attached plate in the overlap region of the bonded stringer joint for the cases of an A_0 *input mode at 1.1 MHz.*

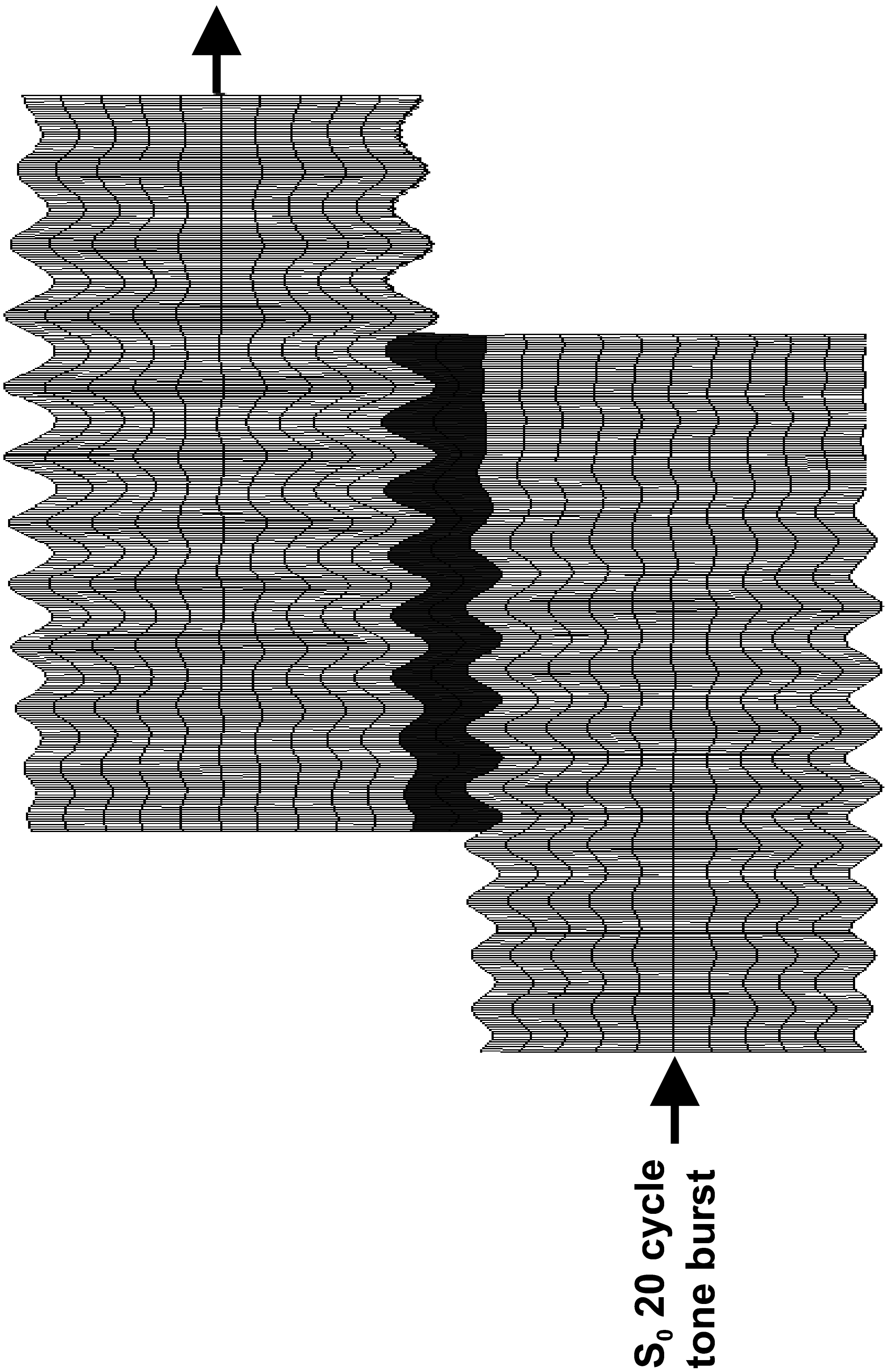

Fig 5. 13 View of the entire mesh of a finite-element model of a bonded lap joint, showing excellent transmission of a 20 cycle input tone burst of the S_0 *mode at 1.5 MHz.*

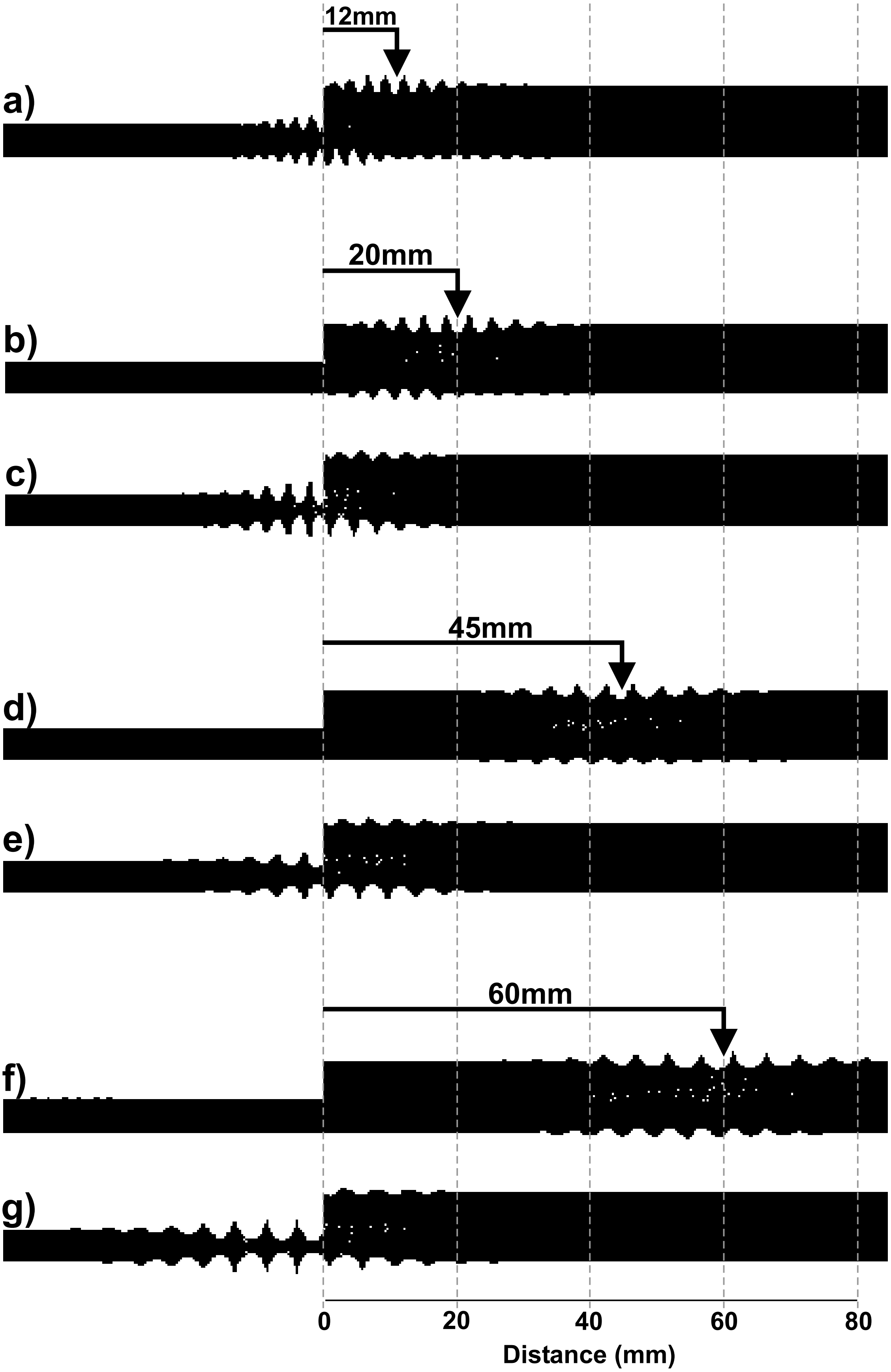

Fig 5. 14 Pairs of distorted mesh views of a bonded lap joint model with a 20 cycle S_0 *input tone, illustrating the leading edge condition and that occurring at the coupling length for input frequencies: a) 1.75 MHz, b) c) 1.5 MHz, d) e) 1.25 MHz, f) g) 1.1 MHz.*

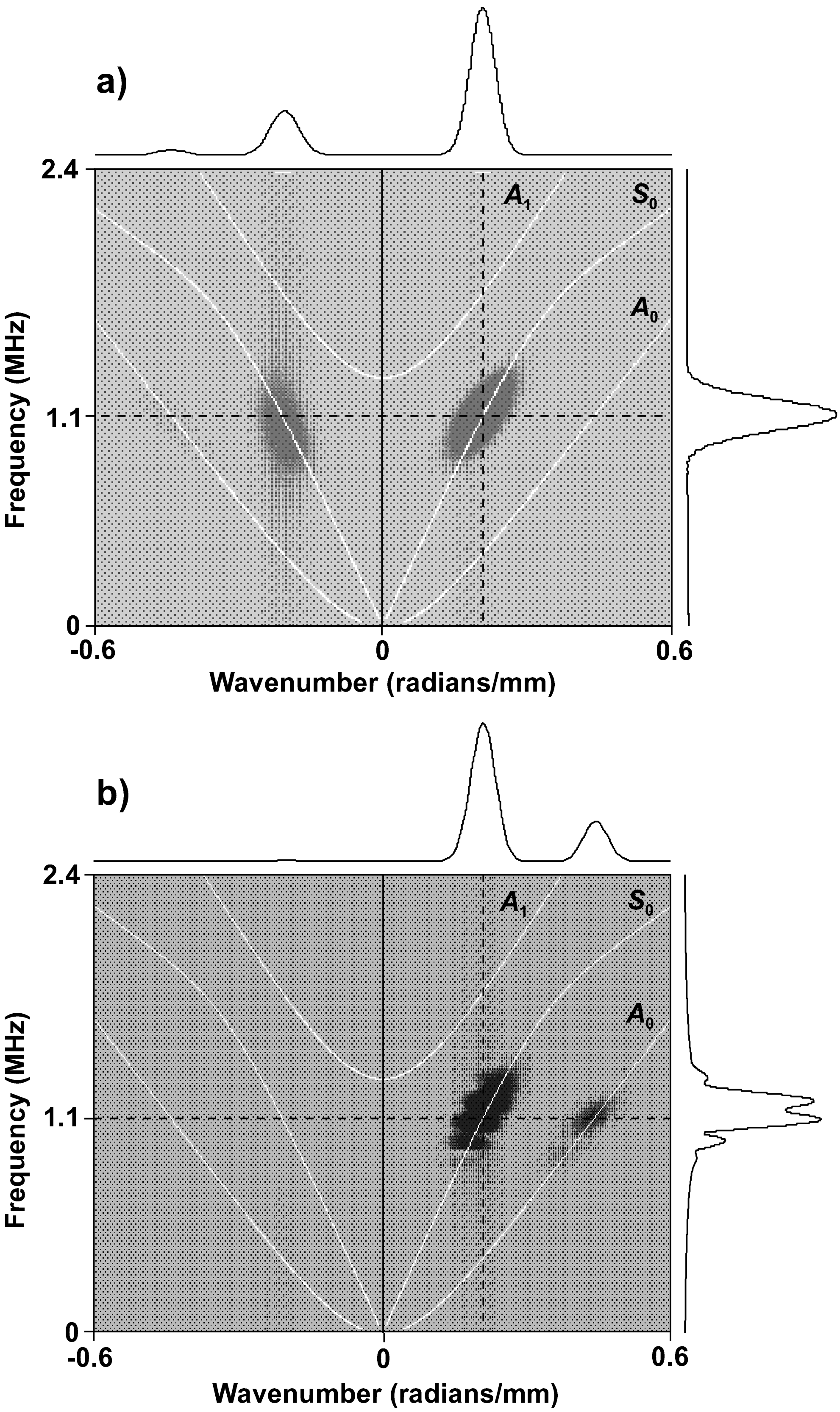

Fig 5.15 Example of the results of two-dimensional Fourier analysis of the transmission across a lap joint for the input mode case of S_0 *at 1.1 MHz. a) Wavenumber-frequency plot of the signal in the input plate b) Wavenumber-frequency plot of the signal in the output plate.*

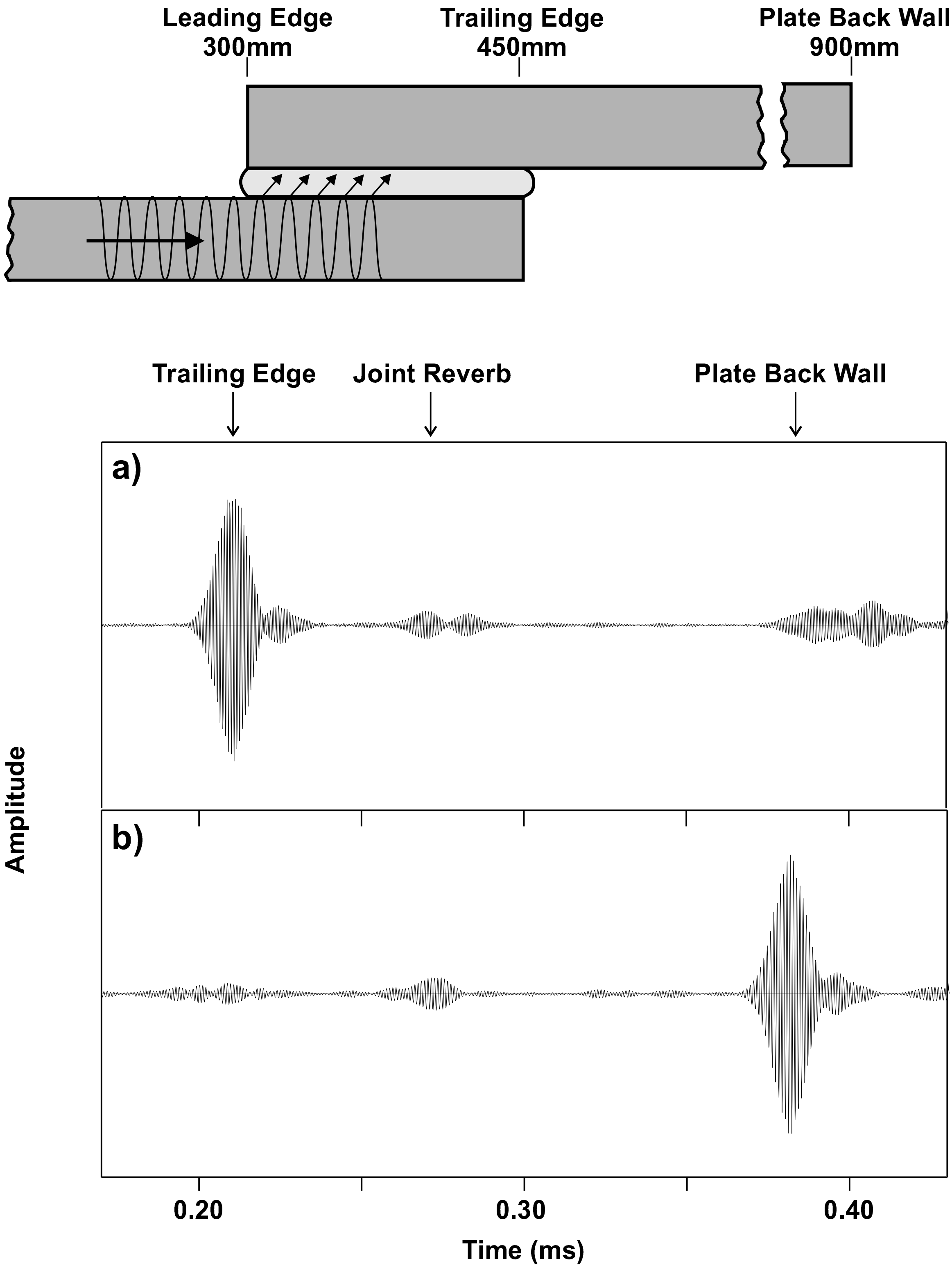

Fig 5.16 Results of a pulse-echo experiment showing: a) worst transmission across an adhesive lap joint at 1 MHz and b) optimum transmission at 1.5 MHz.

6. Acoustic emission

6.1 Introduction

In the previous chapter the difficulty in propagating modes across successive stringer joints was reported. This finding raised an important issue. Acoustic emission (AE) systems have been employed on aircraft since at least the late 1980's and the author has personal experience of an industrial system employed by the Royal Air Force that tracked fuselage crack propagation in VC10 aircraft during proof pressure testing [Odell (1991)]. This system employed roughly 200 acoustic emission transducers (PAC R15) arranged in a formation of triangular cells covering the entire fuselage, with a spacing between transducers of approximately one metre. The point is that crack propagation, or other acoustic emission events, generate guided waves in the fuselage structure. These events could certainly be received by transducers located several metres away from the source and yet these very low amplitude signals were able to propagate across numerous stringers, whilst maintaining sufficient amplitude to be received. This seemed to contradict the findings of the previous chapter and therefore warranted further investigation.

Acoustic emission has become a mature field with a vast literature base including many standard texts such as Williams (1980), for example. Much of this work was concerned with characterising defects from the profile of acoustic events (or 'counts') received; the development of algorithms for defect location and the filtering of noise continues to be a major problem. Until recently, however, little attention has been paid to the essentially modal nature of AE event signals. Although as early as 1972, Fowler and Papadakis (1972) indicated that 'plate mode analysis is a valid way of describing the dispersive nature of acoustic emission, pulses' it was not until Gorman's experimental work that 'modal acoustic emission' as it is now called, became properly established [Gorman (1991)]. In the meantime, Weaver and Pao (1982) presented a theoretical analysis of AE signals, which are effectively transient modes generated by a point source. Weaver's analysis was based upon the superposition of normal modes, evaluated numerically at several propagation distances. A similar analysis was conducted by Hsu, *et al.* (1977)

based, instead, on the more tedious derivation of the Green's tensor for the system, followed by a generalised ray expansion. Hsu's paper also includes some validation of the theory by idealised experiments. Following Gorman's work, interest in modal acoustic emission has increased, and although most work deals with continuous systems, Searle, *et al.* (1995) has worked on the location of cracks in lap joints by AE and discusses a method for distinguishing crack waveforms from those of fretting and noise.

This chapter is concerned with identifying how it is that AE signals can propagate across a series of bonded joints with low attenuation (<40 dB/m). The approach was:

a) To examine the waveforms of simulated AE events to establish which modes and frequencies are generated.

b) To generate simulated acoustic emission event signals and measure their attenuation across a series of stringer joints to confirm low attenuation (<40 dB/m).

c) To carry out FE modelling to measure the power transmission coefficient across a joint and establish what mode conversion occurs from the input modes established in a).

In the next section the experiments and numerical models will be described, and as in the previous chapter, the results of these will be presented together. The final section will summarise the conclusions from this work.

6.2 Acoustic Emission Experiments and Modelling

6.2.1 Experiments

The aim of the first series of experiments was to ascertain which modes are generated by a simulated AE source. Several schemes are widely used to simulate an AE source, and these are often generally referred to as Hsu-Neilsen sources. Comparatively sophisticated methods have been developed, such as, for example, the fracture of glass capillaries in a specially designed apparatus, reported by Breckenridge, *et al.* (1975), that produces very consistent signals. The simplest method, developed by Hsu (1976), involves breaking a 0.5 mm 2H pencil lead on the surface of the plate. This generates a surprisingly consistent, wide-band signal, of similar bandwidth to that produced by an advancing crack. In order to maximise consistency, however, it is necessary to adopt a standard procedure. About 2 mm of lead is extended from the pencil and the lead is held against the skin at an angle of about 10 °. The lead is then broken by slowly rotating the pencil. Some practice was needed to achieve signals with an amplitude tolerance of +/-10%.

The initial experiments simply captured the waveform of a simulated AE event produced by breaking a lead on the surface of a 1 m square plate and the experimental arrangement is shown in figure 6.1. A conical transducer, described in chapter 2, was used to trigger a digital oscilloscope. After propagating 850 mm through the skin, the signal was received, firstly by a PAC R15 transducer, and in a second test, by another conical transducer of the same specification as the trigger transducer. The waveform received by these transducers, was captured on the oscilloscope and subsequently stored and analysed on a personal computer (PC).

The PAC R15 is a highly sensitive resonant transducer with a centre frequency of 150 kHz. It is probably the most widely used transducer for current industrial AE work. Although it is available with an integral pre-amplifier, instead, a separate bespoke laboratory pre-amp with a gain of either 40 dB or 60 dB was used. The conical transducers were manufactured by M. Evans at Imperial College, for previous work in the field of acoustic emission [Evans (1997)]. They have a relatively flat bandwidth, particularly in comparison with that of the R15, with a roll-off at about 1 MHz. The waveforms received from both transducers were compared.

Following the example of Gorman, results were obtained for lead-breaks on both the top surface and on the side edge of the plate. The latter was shown by Gorman to generate greater in-plane displacement resulting in a proportionally stronger excitation of the S_0 mode with respect to that of A_0.

Ideally, a laser would have been used to capture the propagating signal from sufficient incremental spatial points to allow 2DFFT analysis. This would have revealed the mode distribution. Unfortunately, the laser requires considerable signal averaging to achieve a clear time trace, especially when the signals are of low amplitude as in this case. Clearly, this is not a feasible approach for transient waves generated by Hsu-Neilsen sources. Instead, since the frequency spectrum of the received signals indicated that virtually all the energy was concentrated below 300 kHz, where only the fundamental modes exist, it was simply necessary to allow sufficient spatial distance for the modes to separate, owing to their different group velocities.

The group velocity of the modes was measured by comparing the time-of-flight of equivalent points on the trigger and data signals over the appropriate distance (allowing for the source-to-trigger distance). Comparison was invariably made at a threshold amplitude point just above the noise floor, very close to the leading edge of the signal. When two conical transducers were employed these measurements were reasonably reliable, but they were less so when the signal was received by the R15 transducer. This is because the technique relies on a comparison of arrival times of corresponding points on two waveforms, which, when received from different transducers, are unlikely to be identical. The purpose of employing the R15 transducer, however, is simply to establish what waveforms are likely to be received by commercial AE systems. Since it was found that only the fundamental modes are propagating, sufficient accuracy to distinguish the A_0 and S_0 modes is all that is required.

Having established the modes generated by AE in the single skin, a simple experiment was carried out to ascertain which of these modes could be received after propagation under a series of stringers joints. This was followed by several experiments that attempted to measure the attenuation of the faster, non-dispersive S_0 mode under the stringers. For these experiments a multiple stringer specimen, shown in figure 6.2 a), was produced. This test specimen featured eight idealised stringers that were Redux bonded to a rectangular section of skin. The idealised stringers consisted simply of 20 mm wide strips of aluminium alloy of the same specification as the skin. Several different strategies, shown in figure 6.2 b)-d), were tried. The tests shown in figure 6.2 b) and c) are roughly equivalent but, whilst the former suffers only from variation in the lead-breaks, the latter is subject to both this and coupling variation in the R15. Consequently, the accuracy of these experiments must be treated with caution, though it was sufficient to meet the stated experimental aim. In the test illustrated in figure 6.2 d), a conical transducer, positioned at successive locations midway between the stringers, was driven with a 70 kHz, five cycle, Hanning-windowed tone burst from a Wavemaker, (described in chapter 2). The resulting signal was received by an R15 transducer. The conical transducer generates both S_0 and A_0 modes within the signal bandwidth. However, only A_0 is strongly generated, owing to its much greater surface out-of-plane displacement at this frequency, which couples with that produced by the conical transducer. The frequency of 70 kHz, chosen for this test, had previously been found to be the frequency of maximum energy in the simulated AE signals.

Finally, a further series of experiments was carried out with the aim of measuring the reflection and transmission of A_0 and S_0 across a single stringer, using the arrangement shown in figure 6.3. The test specimen was simply constructed of a 20 mm wide strip of aluminium alloy (L167) 1.2 mm thick, which was Redux bonded to a large plate 500 mm square. The strip, which represented a stringer, was roughly the same width as a typical aircraft stringer. Tests were made with both a one inch diameter, 500kHz immersion transducer (Panametrics V301-SU) and a conical transducer as transmitter, driven, in each case, with five-cycle, Hanning-windowed tone bursts of 50, 100, and 150 kHz from a signal generator. The 500kHz transducer was coupled to the plate with viscous couplant (treacle). This couples the small radial displacements in the transducer to the plate surface, exciting an S_0 mode of reasonable amplitude. Both transducers generated S_0 and A_0 modes within the signal bandwidth and the A_0 mode was more strongly generated, owing to its much greater surface out-of-plane displacement at these frequencies, which couples with the predominant out-of-plane forcing produced by the transducers. The two modes were isolated by separation in the time domain and were further highlighted by the arrangement of the laser used for measuring the received signals. The predominant in-plane displacement was measured with differential laser probes oriented at 30 ° to the plate normal as shown in the figure 6.3, while the predominant out-of-plane displacement of A_0 was measured using a single laser probe normal to the plate. The received signal from each mode was windowed and Fourier transformed, allowing frequency components at 50, 100 and 150 kHz to be recorded. Making two measurements, as shown in the figure, allowed the geometric attenuation due to beam spread to be subtracted, leaving just the decay due to reflection/transmission at the joints boundaries and the viscoelastic attenuation in the adhesive. This allowed a more direct comparison with the numerical results, which feature no attenuation.

6.2.2 Numerical modelling

Two-dimensional dynamic finite-element modelling, described in chapter 2, was used to analyse the interaction of the low frequency fundamental modes, identified in the experimental phase, with the bonded stringer joint, and employed a number of models with the geometry shown in figure 6.4. In order to establish the transmission and reflection ratios for each mode, A_0 and S_0 modes were input to these models with frequencies of 50, 100 and 150 kHz. The frequencies were chosen to cover the band containing most of the energy of the simulated AE signals, established by Gorman and confirmed by experiments. Within this bandwidth, the A_0 mode is highly dispersive. Rather than use a very broad band pulse, a five-cycle, Hanning-windowed tone burst was input and to avoid the interference of reverberations, the lengths of the single and double-skin regions were adjusted to accommodate the pulse-length of the mode with the longest wavelength. In these models the length of the bonded region did not correspond with that of a typical stringer joint (20 mm). The lengths of the input and output regions were usually set at 1.1 times the longest pulse-length and the bonded region was usually 0.6 times the longest pulse-length. Each model simply employed the centre frequency forcing regime, the nodes at the left hand edge of the models, shown in figure 6.4, being forced with an amplitude proportional to the local displacement determined from the mode shape. This is described more fully in chapter 2. In order to satisfy the array limitations of the modelling software, while maintaining a sufficiently long dimension in the propagation direction, it was necessary to employ rectangular elements with an aspect ratio of two, as discussed in the previous chapter. A mesh of 0.24 mm x 0.12 mm four-node quadrilateral elements was used and the time step was adjusted, such that both of Blake's rules (discussed in chapter 2) were satisfied. In all of the models, the in-plane and out-of-plane displacements were monitored at nodes on the mid-thickness line, in both input and output regions, as shown in figure 6.4. This strategy allows the separation of the two fundamental modes, since only the A_0 mode exhibits out-of-plane displacement on the mid-plane and only the S_0 mode exhibits in-plane displacement on the mid-plane. At least 64 nodes were monitored in the input and output regions, indicated in figure 6.4, to allow 2DFFT analysis.

6.3 Results

6.3.1 Initial experiments

Typical waveforms obtained from lead pencil breaks on the edge and surface of the plain skin are presented in figure 6.5 a) and b) respectively (These signals were received by the conical transducer). Both figures show clearly the arrival of two distinct modes. In figure 6.5 a) it is seen that breaking the lead on the edge of the plate significantly reduces the amplitude difference of the two modes, compared with the signal produced by the surface break, shown in figure 6.5b). Thus the faster signal is more clearly defined in 6.5 a) and appears to be predominantly a decaying non-dispersive signal. Gating this signal at the point where the second mode begins and applying a Fourier transform gives the frequency spectrum of the leading signal shown in fig 6.6 a). This indicates that the peak energy of this signal lies at 70 kHz with significant energy extending up to about 600 kHz. From its time-of-flight, the velocity of this signal was calculated to be 5.36 m/ms. The group velocity dispersion curve for the skin, given in figure 6.7, indicates that, at 70 kHz, the group velocity of S_0 is 5.54 m/ms, giving an error of -3.25%. It was concluded that the leading signal is that of the S_0 mode.

The amplitude of the second mode, seen in figure 6.5 a) and b), increases with time, as does its cyclic period. This indicates a highly dispersive mode, with high-frequency components travelling faster. It is very difficult to establish the group velocity of such a dispersive mode from a time-of-flight measurement, since the signal leading edge is obscured by the noise floor. In figures 6.5 a) and b) the leading edge of the dispersive mode is further complicated by the reflection of the S_0 mode from the plate boundary, and the superimposed S_0 mode can be seen in both figures. However, by applying ‘BluTack’ mastic to the plate edge and repeating the surface lead-break, the S_0 reflection was sufficiently damped to enable the second mode to be windowed and Fourier transformed, giving the spectrum shown in figure 6.6 b). Once again, most of the sensitivity is concentrated around the frequency of 65 kHz, though in this mode there is little sensitivity above 100 kHz. A rough estimate of the time-of-flight for the leading edge of the dispersive signal gives a group velocity of 1.73 m/ms. Considering the frequency spectrum of this signal, together with the predicted group velocity spectrum in figure 6.7, it is seen that although the group velocity of the central peak is 1.68 m/ms the frequency components up to 100 kHz have velocities of up to 1.95 m/ms and so the measured group velocity is consistent with propagation of the A_0 mode. Further verification was not considered necessary, since the bandwidth of the measured signals indicated that all the energy was concentrated below the cut-off frequency of the A_1 mode, where only the fundamental modes can exist. The conclusion that only low frequency fundamental modes propagate over significant distance in the skin agrees with Gorman's findings. However Gorman and others found that the A_0 mode exhibited predominantly lower frequency components than the S_0 mode. This was not observed in this case, though the energy in the S_0 mode did extend more significantly into higher frequencies. Since Gorman's paper does not present the frequency spectra for his tests on an aluminium plate, the results cannot be directly compared.

The experiments employing lead-breaks on the multi-stringer plate found that both of these modes were clearly seen after propagating across the eight stringers on the specimen. The result of the experiment shown in figure 6.2 d) indicated decay in the S_0 mode of 1.6 dB per stringer (13 dB across eight stringers). In the experiment of figure 6.2 c) the decay was apparently much greater, at 4.4 dB per stringer, although an error of +/- 13% is likely, owing to the varying amplitude of the lead-breaks. However, FFT analysis of the S_0 mode revealed that the R15 transducer had restricted the signal bandwidth, shifting the main energy peak to 180 kHz before the first stringer. This was further shifted by the filtering effect of propagation under the stringers to a frequency of 120 kHz measured after the eighth stringer. The attenuation of the 180 kHz component was found to be 32.5 dB/m, implying 3.2 dB per stringer. Although variation in the coupling of the R15 transducer over the series of tests in this experiment would have been responsible for some error, the results of these two experiments are not inconsistent, but merely indicate the varying transmission efficiency of S_0 with frequency. Therefore, the attenuation at 70 kHz, where most of the S_0 energy lies, is about 1.6 dB per stringer, while the apparent attenuation, seen by an R15 transducer in a practical AE test, would be considerably higher, at about 3.2 dB per stringer, because the R15 has a narrow bandwidth at a higher frequency.

6.3.2 Finite-element modelling predictions

Table 6.1 shows the results of the numerical modelling based on comparison of the out-of-plane amplitude component of the reflected and transmitted input signals, for three frequencies. It will be recalled that in the numerical models, the input and output amplitudes were monitored at the mid-plane; however, the transmission and reflection ratios in table 6.1 are based on the out-of-plane (OOP) amplitude component at the surface. For each mode, this was derived from the ratio of OOP surface displacement to the relevant mid-plane displacement component (in-plane for S_0 and OOP for A_0), which is simply established from the mode shape. Since the mode shape (obtained from the dispersion predictions discussed in chapter 3) varies with frequency, this ratio was found for each of the three frequencies. The models were made large enough to avoid reverberation problems and so it was generally possible to establish the amplitude of each reflected or transmitted mode simply by measuring the maximum amplitude of the appropriate displacement component at a monitoring node in the input or output region. These time domain measurements were then translated into OOP surface amplitudes, as previously described. (Identical transmission and reflection ratios were obtained when the centre frequency components of the mid-plane displacement signals were compared in the frequency domain. The long wavelength of S_0 at 50kHz necessitated the use of 2DFFT analysis of the input and output signals in order to separate reflections.)

In table 6.1 the transmission ratio of the input mode across the stringer joint is emphasised by a grey box. No results were obtainable for an A_0 mode at 50 kHz, because the severe dispersion of this mode led to a very much extended pulse length, which could not be accommodated within the model without wrap-round interference occurring. The table shows that the transmission coefficient of S_0 falls from 0.84 (-1.5 dB) at 50 kHz to 0.80 (-1.9 dB) at 150 kHz. This compares favourably with the results of the experiments discussed previously, which indicate a transmission of -1.6 dB at 70 kHz, and which also reflects the poorer transmission of S_0 at higher frequencies.

Frequency (kHz)	50	100	150
Incident Mode:		***A_0***	
R(A_0)	-	0.362	0.353
T(A_0)	-	0.839	0.834
R(S_0)	-	0.004	0.004
T(S_0)	-	0.003	0.003
Incident Mode:		***S_0***	
R(S_0)	0.313	0.317	0.331
T(S_0)	0.835	0.816	0.796
R(A_0)	-	7.499	4.828
T(A_0)	10.542	4.993	3.107

Table 6.1 Low frequency transmission ratios (T) and reflection ratios (R) bonded stringer; based on the surface out-of-plane amplitude component established by finite-element analysis. Omitted entries indicate where severe dispersion in the A_0 mode invalidated the results.

Having established the transmission and reflection of the incident modes, the transmission and reflection of mode-converted signals, indicated in table 6.1, is considered. Unfortunately, owing to its long wavelength at 50 kHz, the reflected A_0 signal, mode converted from S_0, interfered with the input signal and could not be obtained. From the table it appears that transmission and reflection of the S_0 mode from an input A_0 mode are both extremely small, while the transmission and reflection of the A_0 mode from an input S_0 mode are many times greater than those of the input mode. This is a distortion that arises due to the direct comparison of the out-of-plane amplitude component of two different modes. Although table 6.1 indicates the apparent reflection and transmission coefficients that would be indicated by field measurements, such direct comparison between modes is not valid owing to their different mode shapes. A much clearer picture is obtained by comparing the energy or power of the transmitted and reflected modes, and table 6.2 shows the same results presented in the form of power transmission and reflection ratios.

To obtain the power ratios, shown in table 6.2, it is necessary to find the relationship between displacement amplitude at a given point through the thickness of the plate and the power flow of the mode in the plate past this point. The power density can be found by integrating the acoustic Poynting vector over the cross-sectional area of the plate

[Auld (1990)]. Since the acoustic Poynting vector is the product of the stress and velocity vectors and since the stress vector is in turn simply related to the displacement vector, it is possible to relate the surface out-of-plane displacement of a given mode to the power density in the plate. This has already been implemented in the program Disperse, which gives the mode-shape displacements for unit power density. It was therefore a simple matter to calculate the power transmission and reflection ratios from the surface out-of-plane amplitude ratios.

The power transmission ratios of the input modes are the square of the amplitude transmission ratios, which is consistent with Parseval's theorem. It is apparent that for both A_0 and S_0, about 63-70% of the AE energy will be transmitted across a stringer joint and that there appears to be surprisingly little frequency dependence, considering the likely reverberation in the joint. Roughly 10-13% of the energy is directly reflected at the leading edge and less than 5% of the input energy is mode converted. Since the total reflected and transmitted energy amounts to about 79-89%, about 11-21% of the input energy reverberates across the joint. The reverberation energy is not seen in the table because the time duration of the model was not sufficiently long. Reverberation across the model joints would have resulted in signals emitted from the joint at a time too late to be seen. However, this reverberation energy will be received experimentally on narrow

Frequency (kHz)	50	100	150
Incident Mode:	$\boldsymbol{A_0}$		
R(A_0)	-	0.131	0.125
T(A_0)	-	0.703	0.695
R(S_0)	-	0.035	0.011
T(S_0)	-	0.016	0.006
Incident Mode:	$\boldsymbol{S_0}$		
R(S_0)	0.098	0.100	0.110
T(S_0)	0.697	0.667	0.634
R(A_0)	-	0.027	0.030
T(A_0)	0.009	0.012	0.013

Table 6.2. Low frequency power transmission ratios (T) and reflection ratios (R) for a bonded stringer; established by finite-element analysis.

joints. Of course, these figures take no account of the viscoelastic energy losses, but given the very low attenuation and narrow joint width, these are likely to lead to little change in the figures presented. The reverberation energy, not listed, will account for a large proportion of the viscoelastic losses. The power ratios now indicate that the proportion of energy lost through mode conversion from input A_0 and S_0 modes is roughly similar in both cases at 100 kHz.

In order to check the effect of changes in the thickness of the adhesive layer, the models were adjusted by increasing the adhesive thickness by one element (a 50% increase in thickness) and re-run for an input signal frequency of 100 kHz. Both the amplitude transmission/reflection ratios and the corresponding power ratios are presented together in table 6.3. The transmitted signal amplitude of the input mode remains at roughly 80% for both modes, corresponding to a power ratio of about 64%. The table suggests that slightly greater energy enters the thicker joint (there is less reflected energy), but that slightly less energy leaves it, implying a greater remaining reverberation energy. It is clear, however, that in contrast to the results of higher frequency transmission, the efficiency of transmission of these low frequency modes is much less dependent upon frequency and joint thickness.

	Surface amplitude ratios	**Power ratios**
Incident Mode:	$\boldsymbol{A_0}$	
R(A_0)	0.359	0.129
T(A_0)	0.815	0.665
R(S_0)	0.003	0.017
T(S_0)	0.002	0.011
Incident Mode:	$\boldsymbol{S_0}$	
R(S_0)	0.240	0.057
T(S_0)	0.816	0.666
R(A_0)	7.461	0.027
T(A_0)	4.932	0.012

Table 6.3 Low frequency power transmission ratios (T) and reflection ratios (R) for a bonded stringer with a 50% thicker adhesive layer than that of table 6.2; established by finite-element analysis.

6.3.3 Concluding experiments.

The results of the experiments aimed at measuring the transmission coefficients of the two fundamental modes at acoustic-emission frequencies, described in the previous section and illustrated in figure 6.3, are presented in table 6.4. The results for the 20 mm-wide joint differ from the numerically predicted results by no more than 0.09 and therefore show a reasonable correspondence. Nevertheless, such comparison must be treated with considerable caution. The possible variation of the parameters of the specimen joint from those assumed in the model, has been highlighted in previous chapters. Moreover, the fact that experimental results are subject to attenuation of both the directly transmitted signal and the reverberations, not present in the numerical results, has also been mentioned. The loss due to viscoelasticity at these low frequencies, in a joint of only 20 mm in width, is likely to be a small and this source of error should not be too great. However, the experimental results are, of course, also influenced by reverberations within the narrow joint that must have interfered with the measured signals. Such reverberations are inevitably found in practice and tend to complicate the received signal, especially when several joints are traversed. These sources of error may well account for all of the differences between the modelling and experimental results.

However, the experimental results show a 15% drop in the transmission of A_0 when the frequency is increased from 100 to 150 kHz, compared with only a 0.5% drop predicted by the model. This probably reflects the greater viscoelastic attenuation of the A_0 mode, which increases from 40 dB/m to 55 dB/m over this band, while the attenuation of S_0 only increases from 0.3 dB to 0.5 dB over the same band.

Frequency (kHz)	100	150
T(A_0) 20 mm stringer	0.90 (0.84)	0.76 (0.83)
T(S_0) 20 mm stringer	0.84 (0.82)	0.89 (0.80)

Table 6.4 Low frequency transmission ratios (T) for a bonded stringer; from experimental measurements. The numerical results from table 6.1 are reproduced in brackets for comparison.

6.4 Conclusions

This short exploration of the transmission of acoustic emission signals across joints has successfully established that acoustic emission energy is carried by the two fundamental guided modes in the skin, at frequencies predominantly below 100 kHz. These modes are able to propagate across stringer joints with an energy transmission efficiency of about 70%. Furthermore, a similar transmission efficiency was observed (for the S_0 mode) across a series of joints. The transmission of these low-frequency modes is not hampered by the carrier-mode interference phenomenon observed in higher-frequency transmission, discussed in chapter 5. Unfortunately, these modes are of little use in an active system, because the large wavelength of S_0 (approximately 100 mm) would give very poor defect resolution, and the A_0 mode is highly dispersive.

It can be seen from figure 4.14a) that the AE modes occupy a frequency band below that at which mode twinning occurs, and this is the main reason for their efficient propagation across successive joints. In addition, figure 4.14b) indicates the low attenuation of these modes; the A_0 mode exhibiting somewhat greater attenuation than the S_0 mode at these frequencies.

Finally, these results suggest a means of improving current acoustic-emission systems. Most structural health monitoring by acoustic emission is concerned with defect location, which is generally achieved by considering the time-of-flight between the defect and a spatially arranged array of surface mounted transducers (very often the PAC R15). Such transducers are primarily sensitive to out-of-plane surface displacement, and considering the mode shapes of A_0 and S_0 modes generated by AE events, the former exhibits about five times greater surface out-of plane displacement than the latter. These transducers are therefore far more sensitive to A_0 mode, as has been shown, yet the A_0 signal is highly dispersive. Time-of-flight is usually measured by setting a trigger signal level, which records a 'hit' when exceeded. Considering the rising amplitude of the A_0 signal in figure 6.5, it is apparent that the measured time-of-flight will largely depend on the level set and that this will, in turn, be dependent upon the propagation distance, owing to the general signal decay and dispersion. Large errors are therefore likely to result from triggering off this mode. Triggering from the leading edge of the S_0 mode offers much better accuracy, but the amplitude of the S_0 mode seen by current AE transducers is very small and the danger of triggering on noise arises if the trigger level is set too low. A possible solution would be the use of an omni-directional shear transducer that is sensitive to the predominant in-plane surface displacement of S_0. Indeed, consideration of through-crack propagation in a thin plate intuitively suggests predominant in-plane displacement and there is evidence suggesting that real AE signals from propagating cracks do, in fact, preferentially excite the S_0 mode [Carpenter and Gorman (1998)]. To date the author is unaware of any commercial AE scheme employing resonant, omni-directional, shear transducers.

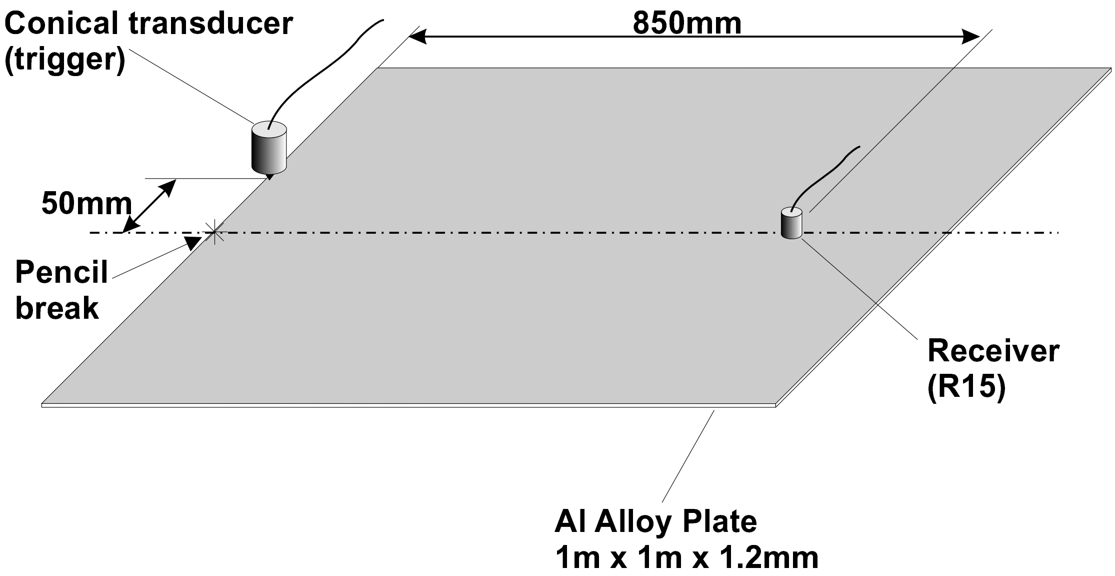

Fig 6.1 Experimental arrangement used to capture simulated acoustic emission signals propagating in the simple skin.

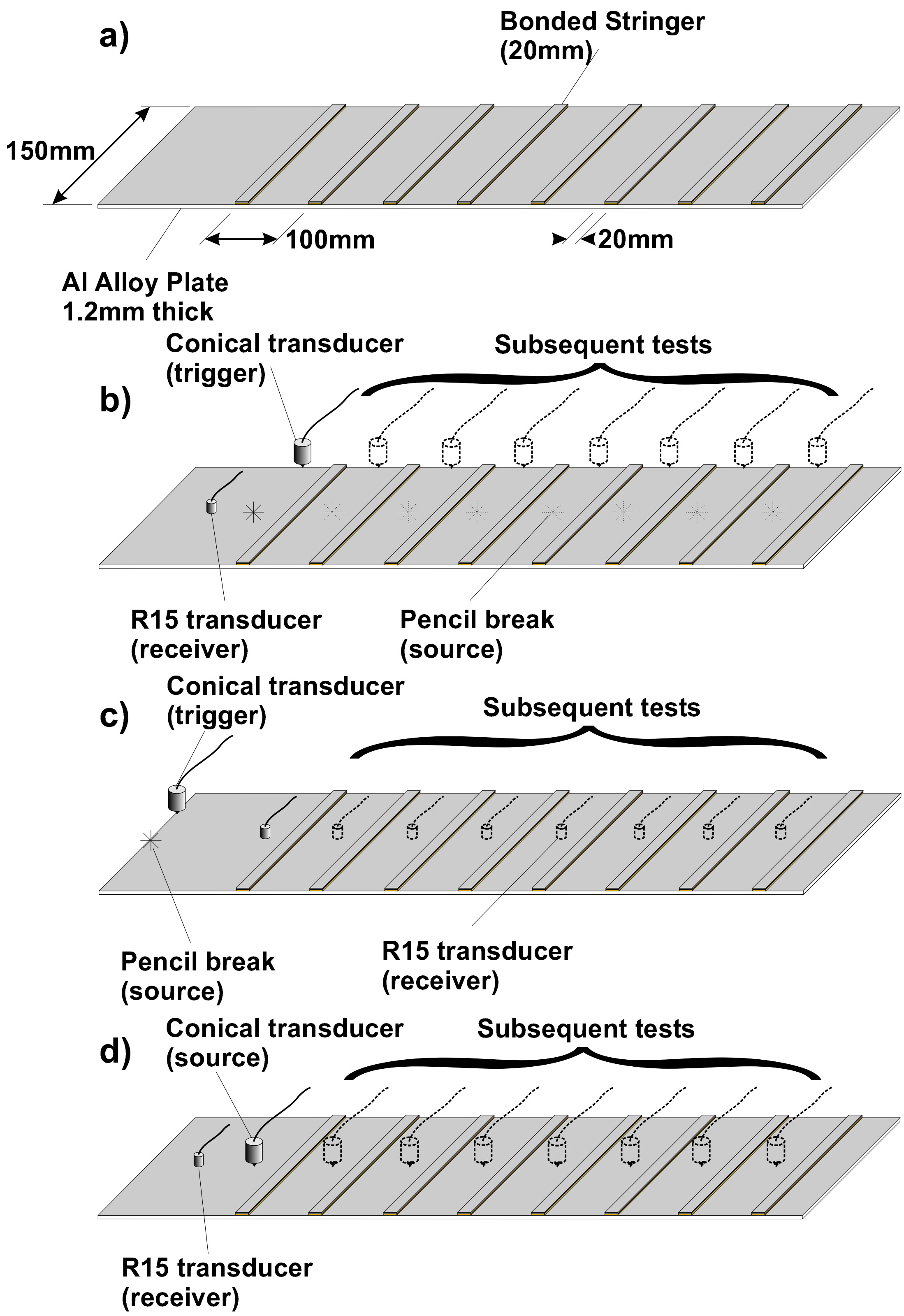

Fig 6.2 Experimental arrangements used to examine the propagation of AE beneath a series of stringer joints.

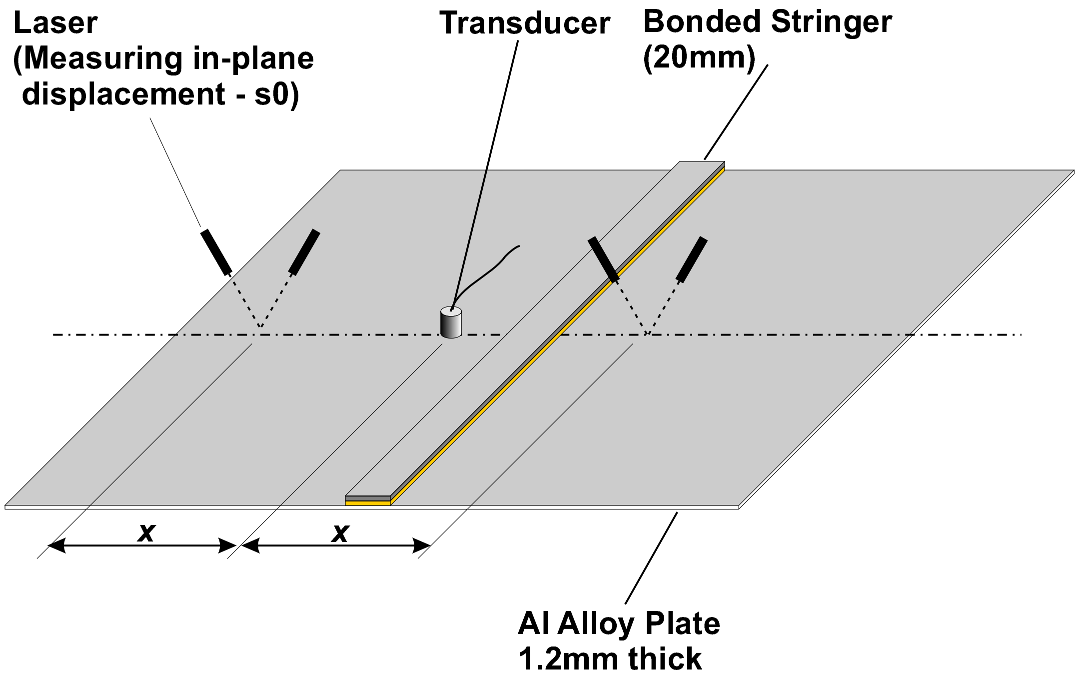

Fig 6.3 Experimental arrangement used to measure the transmission and reflection ratios associated with low frequency mode interaction with a single stringer joint.

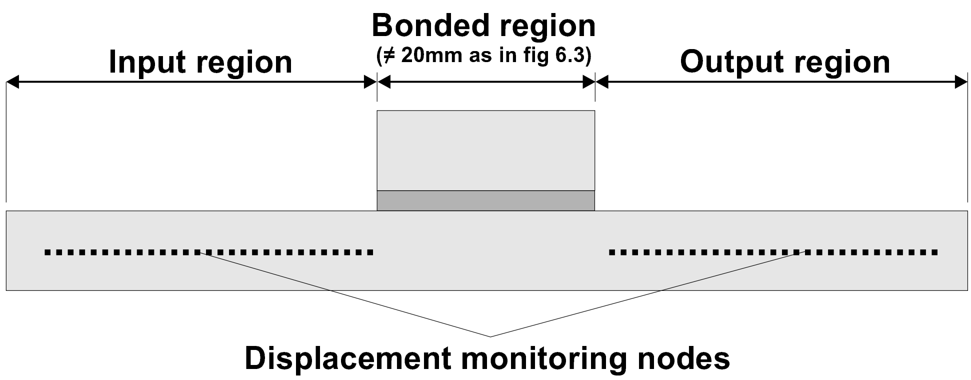

Fig 6. 4 Diagram of the geometry of finite-element models used to investigate the propagation of low frequency fundamental modes across a stringer joint.

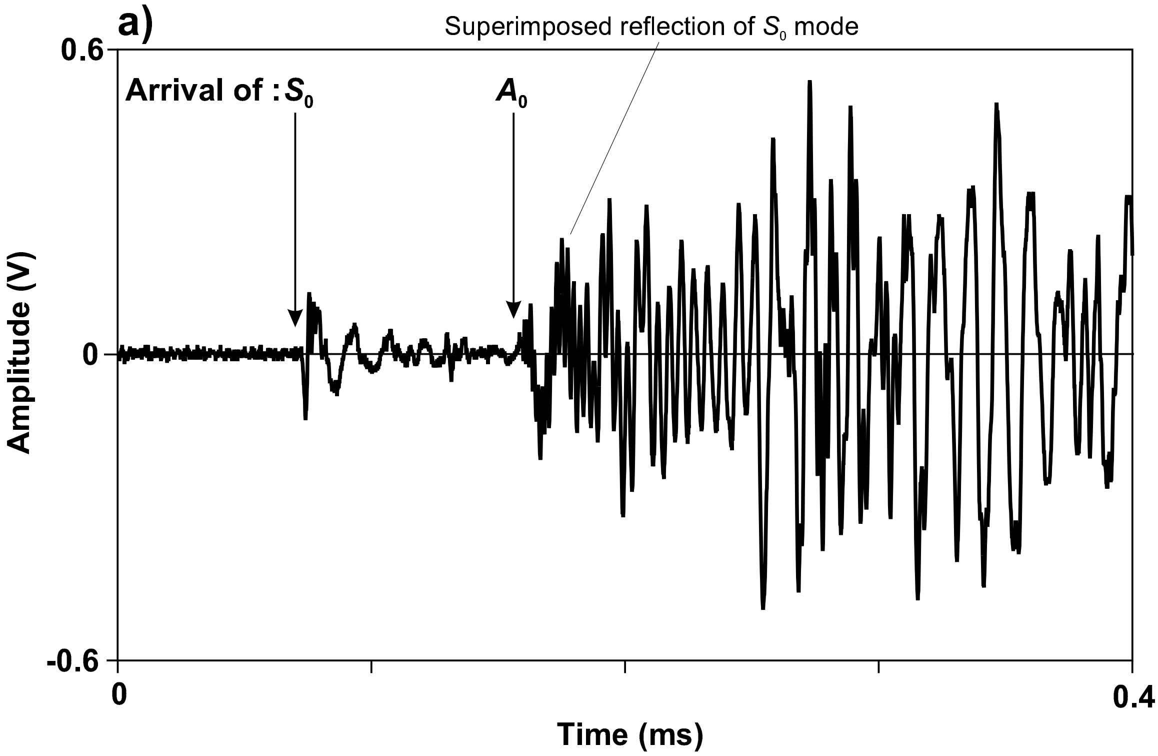

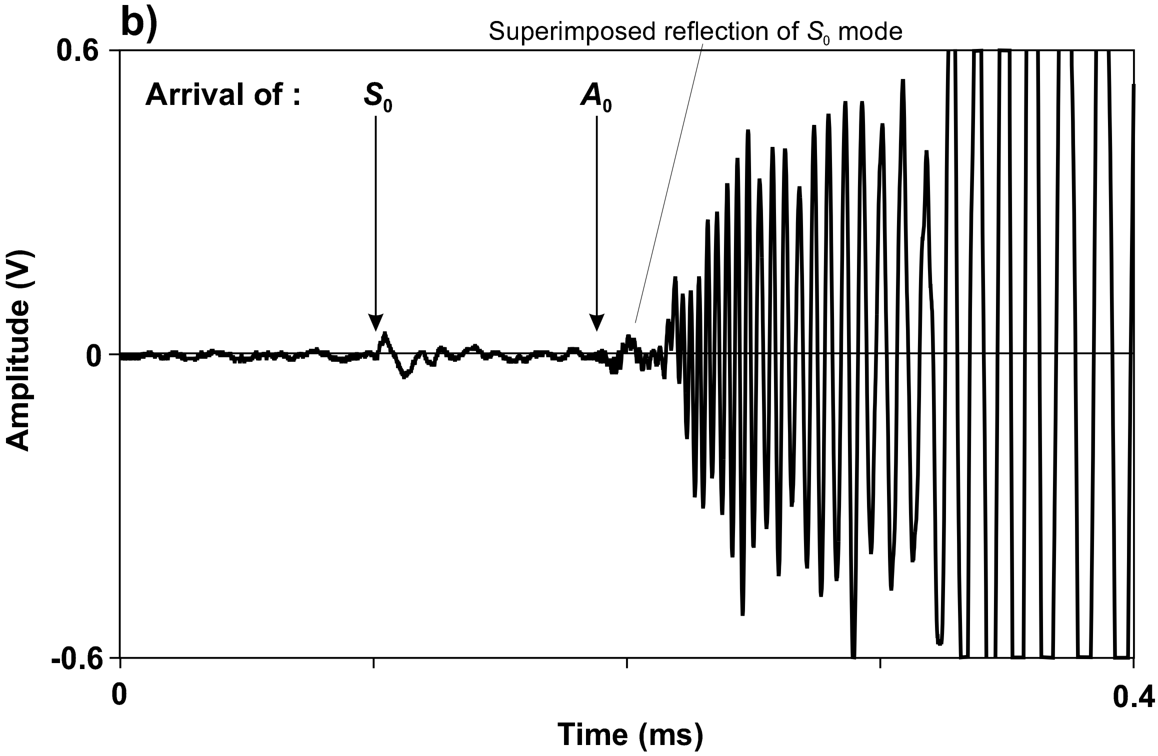

Fig 6.5 Simulated AE signal generated by breaking a 0.5 mm pencil lead on: a) the edge of the skin plate and b) the surface of the skin plate. The signals were captured by a conical transducer after propagation over 600 mm in the skin.

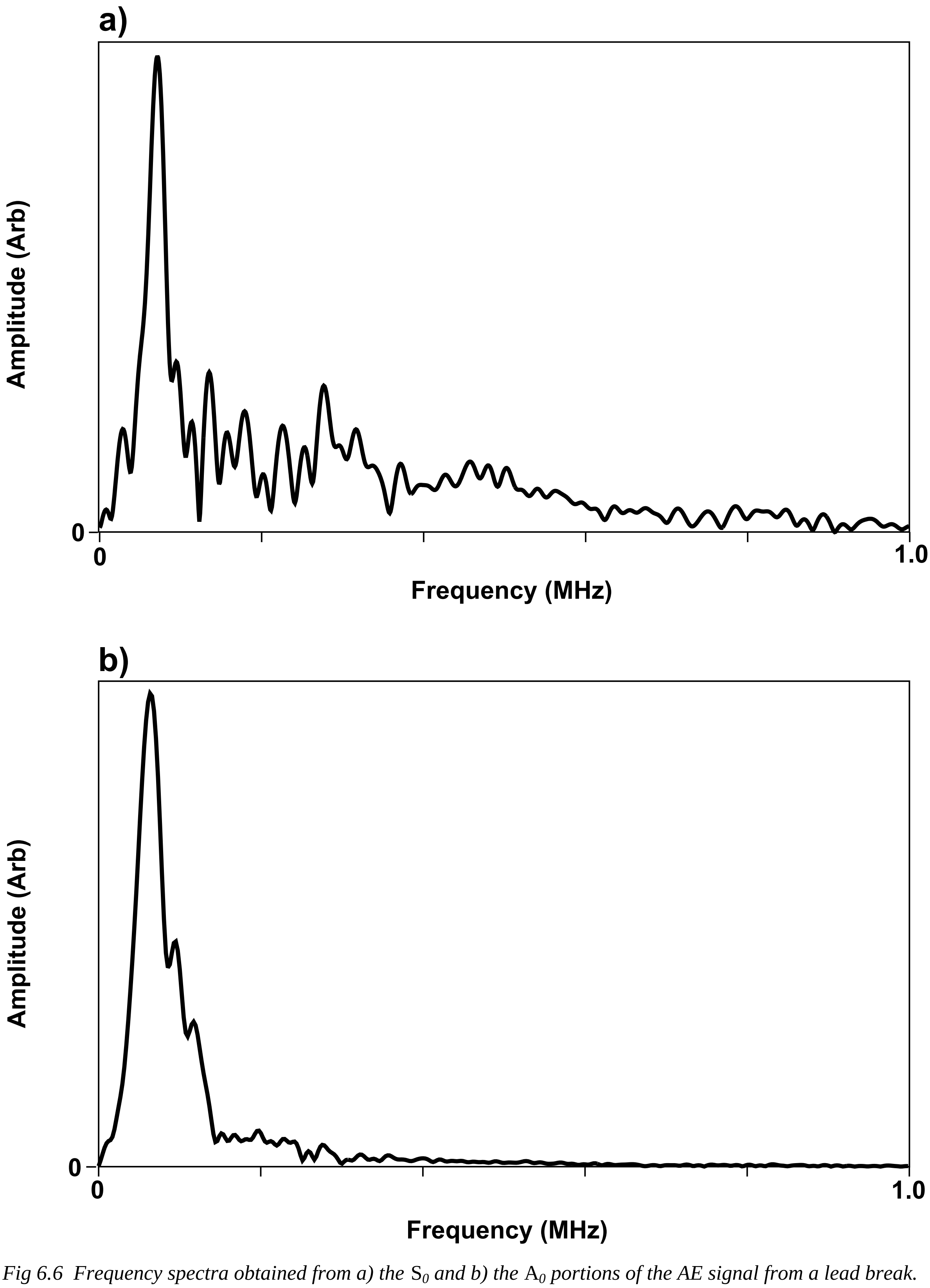

Fig 6.6 Frequency spectra obtained from a) the S_0 *and b) the* A_0 *portions of the AE signal from a lead break.*

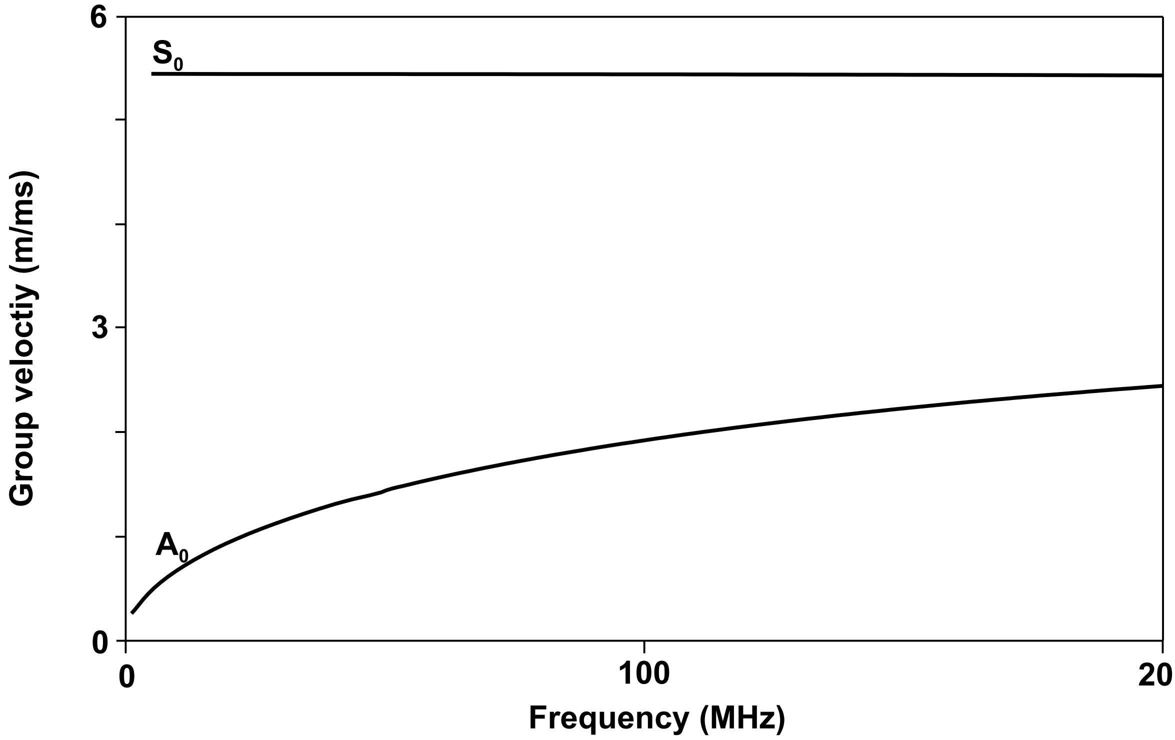

Fig 6.7 Single-skin group velocity spectrum for the low-frequency band covered by AE signals.

7. Conclusions and future work

The first task of this final chapter is to review the work that has been covered and its implications with respect to the aim of the project. Ultimately, a decision has to be made as to whether the use of guided waves is viable in an active, integrated, aircraft health-monitoring system, and it is important to understand clearly how the various elements of the project, presented in the chapters of this thesis, underpin this decision.

The second section of this chapter reviews the general method of the investigation, and considers the approach adopted, together with the important problems encountered. Clearly, time and resource constraints inevitably had some impact on the methods applied, and this section will review the limitations of the work in the light of these constraints and will justify the approach adopted.

This leads to consideration, in the final section, of further work that might be undertaken, either to reinforce or extend the work presented.

7.1 Review of thesis

Given the time and resource constraints of the project, it was necessary to limit the scope of the work, whilst ensuring that the main objectives of the project were met. These limitations were outlined in the opening chapter that confined the work to a study of guided wave propagation in the fuselage structure of metallic aircraft. Next, this structure was idealised by identification of the essential structural elements that were assumed to characterise metallic fuselage structure in general, and to further simplify the analysis fasteners were neglected. Lastly, chapter 1 considered the likely specification requirements of the proposed health-monitoring system and this led to maximum limits being defined for the attenuation and wavelength of modes (40 dB and 15 mm respectively) applied in subsequent mode selection.

In chapter 2 the materials from which the essential structural elements are commonly composed were identified and their acoustic properties measured. The frequency dependence of attenuation was seen to be approximately linear and this allowed a single wavelength-dependent parameter to be specified for the bulk longitudinal and shear wave attenuation in Redux and the bulk longitudinal wave attenuation in PRC. It was found that the PRC sealant was very highly attenuative and, essentially, would not support bulk shear wave propagation. It was further found that the acoustic properties of sealant layers were dependent upon the layer thickness, and batch factors, such as the quantity of air admitted during mixing. Establishment of the material properties was essential for the subsequent calculation of dispersion curves for the various waveguide systems involved. The chapter then went on to describe, in general terms, the experimental and numerical techniques employed throughout the investigation. (More specific details of particular experiments were given in other chapters).

Having set out the supporting details of the project, chapter 3 dealt with the simplest waveguide system: that of a single skin. It was considered that efficient propagation in this system should be a pre-requisite of all potentially useful modes, since this system forms so much of the fuselage structure. The chapter considered the factors of dispersion, attenuation, mode isolation, and wavelength, on which mode selection would be based. Apart from the wavelength limitation, which applies generally, dispersion is the only significant factor in this system, since the only other attenuating mechanisms are visco-elastic losses in the skin and beam spread, which are both small. Non-dispersive points on the lower order modes, identified from the dispersion predictions, therefore formed the basis of subsequent mode selection and the relative merits of each of these points was briefly outlined. The last section of this chapter briefly considered the effect of tapering skin regions and concluded that, for tapers with gradients of up to 1:5, the amplitude of the reflection should be less than 10% of the incident signal amplitude. In most cases examined numerically and experimentally, the reflections were insignificant. During propagation in the tapering regions, the mode characteristics are simply dictated by the local frequency-thickness product, which changes with propagation. No mode conversion takes place, provided that the mode is not forced below its cut-off frequency. The chapter concluded by noting that, providing dispersion is avoided, there is no difficulty in obtaining propagation with an attenuation of less than 40 dB/m.

Difficulties arise when further layers are added and this was the subject of chapter 4. Dispersion curves suggested that the application of a sealant to the skin, though not sufficiently attenuative to constitute a half-space, formed a system whose modes all exhibited attenuation of greater than 40 dB/m, except at very low frequencies. Furthermore, since the attenuation of all modes generally increases with sealant thickness, no mode was found suitable for long-range propagation.

Double-skin systems with sealant and adhesive jointing were also introduced in chapter 4 and these systems were found to exhibit an interesting ‘mode twinning’ phenomenon, in which pairs of modes have very similar phase velocity over a wide frequency bandwidth. This makes excitation of a single mode very difficult. A number of points on the low order modes offer attenuation of less than 40 dB/m. Such points could be exploited in cases where the other twin mode has a high attenuation, such that it is lost over a short distance.

In the last section of chapter 4 paint loaded skins were briefly examined. It was found that below 1 MHz, the attenuation of fundamental modes would be less than 6 dB/m, so that in such cases, paint layers could be ignored. However, in general the attenuation rises sharply with frequency, and this source of attenuation should be considered when working above the A_1 cut-off frequency.

Probably the most important findings were presented in chapter 5, which dealt with propagation across joints. It was found that in fairly narrow joints, such as those formed between the skin and structural support members, the efficiency of propagation across the joint is critically determined by the generation and interaction of twinned carrier modes, identified in chapter 4. Two modes are generated in phase opposition, by mode conversion at the joint leading edge, which results in a constructive interference condition on one of the free surfaces of the joint, and destructive interference on the opposite face. This changes in a cyclic fashion as the modes propagate across the joint, due to beating between the modes, so that the particular interference condition at the joint trailing edge largely dictates the transmission efficiency. Since the period of this cyclic interference is determined by the relative wavenumbers of the carrier modes, optimum transmission can be arranged, with very little reverberation or reflection from the joint.

In the cases, mentioned earlier, where one of the carrier modes has a much greater attenuation, the efficiency of transmission across a joint is determined simply by the decay of the low-attenuation mode, (assuming the joint is of reasonable width), since the other disappears over a short distance. However, roughly half the input energy is lost in this case and such losses may not be sustainable if propagation across a series of joints is required.

Although the use of carrier-mode interference enables very efficient transmission across a single joint to be achieved, it was found that propagation across successive narrow stringer joints was not possible, owing to the sensitivity of carrier-mode interference to small changes in the joint properties. This prevents the practical use of any of the potentially useful single-skin modes, identified in chapter 3, because generally stringers are pitched at intervals of only about 100 mm.

The work described in chapter 6 was necessary simply to solve a problem that arose from the findings of the previous chapter: namely, that acoustic emission event signals are known to propagate efficiently through aircraft skin and are not therefore hampered by carrier-mode interference. Experimental work using simulated AE signals found that AE events primarily excite the fundamental modes at frequencies predominantly below 100 kHz. In this frequency band, modes in the joint are not twinned and have low attenuation. Thus, only a single carrier mode is generated and interference does not occur. The numerical modelling indicated that these features of low frequency AE signals allow propagation across stringer joints with an energy efficiency of about 70%, giving an amplitude ratio across the joint of roughly 84%. This was validated by experiments that further indicated that such transmission efficiency is maintained over a series of joints. The issue concerning propagation of acoustic emission was thus resolved.

Having reviewed the work presented in the thesis, the next section will summarise the implications for aircraft health monitoring, which are the fundamental findings of the project.

7.2 Implications for aircraft health monitoring

Owing to their unique potential for long-range, in-plane propagation through thin plates, exploited in other applications, guided waves seemed to offer an obvious solution in the development of a global health-monitoring system for ageing metallic aircraft. An evaluation of this potential was the primary aim of this thesis.

7.2.1 Long-range active systems

The main conclusion that must be drawn from this project is that the combination and variation of structural features found in metallic aircraft generally precludes the selection of a single mode appropriate for long range propagation, since no mode was found that could negotiate each of the simplified structural features with sufficiently low attenuation and an appropriate wavelength.

Overlying sealant layers were seen to cause a severe damping problem, acting like a mechanical filter admitting only very low frequency modes. Sealant layers are used extensively for sealing and corrosion protection, and often have a thickness in excess of 1 mm with the result that all but the very low frequency fundamental modes are attenuated at a rate of more than 40 dB/m. The results have also demonstrated the problems of frequency thickness sensitivity of the propagation across aircraft skin joints, owing to mode interference. The use of extensive regions of multi-layered skin in large aircraft fuselage construction would result in wide variations in the path length of signals propagating through these regions, dependent upon the transducer location and direction considered. This means that the particular interference condition of the carrier modes cannot be optimised for transmission across the boundaries of multi-layer regions.

Consequently, it is hard to envisage a single mode, active system, employing current transducer technology. Perhaps the problem of ageing aircraft structural health assurance might be more practically addressed by monitoring just the integrity of structurally significant areas, or areas that present a difficult and expensive inspection problem. Although such a system may not provide sufficient battle damage information, this is probably a more efficient solution in civil aviation where it should radically reduce the problem of data transmission and reduction in large aircraft. The conclusions for short-range propagation are presented in the next section.

7.2.2 Short-range active systems

Despite the disappointing conclusions for long-range systems, the results support the view that guided waves do offer good potential for more localised monitoring of structurally-significant areas, where a higher transducer density can be tolerated. It has been demonstrated that excellent transmission across a single joint can be achieved by consideration of the carrier-mode velocities. In general, the fundamental modes offer the best choice for such applications, but other low-order modes are viable and may be more advantageous in particular circumstances.

It should be remembered that the results of the joint investigation show that points will exist at intervals across the joint where, owing to carrier-mode interference, there will be little or no displacement energy and consequently poor defect sensitivity. For example ,such a point is found at the leading edge of the joint, in the overlying plate. These ‘dead points may be accommodated by transmitting in both directions across the joint, or by employing more than one input mode, or frequency.

7.3 General achievements

Although each of the elements presented in the chapters of this thesis contributes towards the specific project aim, some elements also have a more general, independent value. The method used to measure the attenuation of PRC sealant detailed in chapter 2 demanded a variation on the standard techniques commonly employed. In the finite-element work on tapered skins, presented in chapter 3, the use of a tapering element scheme was shown to have considerable advantage in terms of computational efficiency, over the alternative arrangement of stepping elements to match the gradient. The local immersion method for excitation and receipt of guided waves was greatly improved by the development of wax baths, which enable much cleaner signals to be obtained by absorbing the reverberations that would otherwise exist in the fluid coupling. This will prove particularly useful in pulse-echo work were the effect of bath reverberations is more serious, owing to the use of just a single transmit/receive bath. The work presented in chapter 6 revealed that acoustic emission signals exist at frequencies below that at which mode twinning in the bonded regions occurs, and that this is primarily why they are able to propagate across many successive joints, where higher-frequency modes fail. Finally, the work on acoustic emission suggested that the development and use of resonant shear transducers, more sensitive to the S_0 mode, might significantly improve current defect location techniques, by allowing reliable triggering on the leading edge of a non-dispersive mode.

7.4 Critical review of project methods and approach

Throughout the course of this investigation many problems arose for which solutions were found, nevertheless, numerous simplifying assumptions and decisions had to be made in order to satisfy time and resource constraints. In addition to the work reported in this thesis some further work was undertaken in other areas associated with the project that proved largely unfruitful within the time allotted. It is appropriate therefore, to briefly consider some of the more important points and propose ways in which the investigation might have been improved, before the discussion of possible future work in the final section.

7.4.1 General

It could be argued that the investigation presented here has only examined the potential of a small proportion of the infinite number of modes that each of the waveguide systems can support. Vertically polarised guided modes with frequencies above 5 MHz have not been tested and no consideration has been given to the horizontally polarised shear modes. Whilst this is indeed the case, it was seen that higher order, higher frequency modes generally have greater attenuation, offering no viable solution. It might be supposed that surface waves could be made to propagate on the external free surface of the skin and thus escape the undesirable influence of the sub-structure. Unfortunately, consideration of the dispersion curves indicates that, at the Rayleigh wave frequencies (>18 MHz in the single skin), the attenuation of paint layers would be significant. Dispersion predictions suggest that the surface wave would be attenuated at a rate of about 900 dB/m, because most of its energy is concentrated in the paint layer. Other high-frequency modes with little or no surface displacement in the mode shape exist, and these would clearly not be perturbed by surface layers, but such modes cannot be excited or received, directly, by surface mounted transducers. A brief examination of the dispersion curves of the horizontally polarised shear (SH) modes indicates that they also offer no advantage, since they couple very efficiently to overlying layers and therefore generally exhibit similar, or greater attenuation when propagating beneath sealant. (All SH modes in the multi-layered features considered exhibit a predicted attenuation of greater that 40 dB/m, the lowest being the SH_1 mode at 2.25 MHz in the bonded skin system, which has an attenuation of about 40 dB/m) Nevertheless, it must be conceded that a full investigation of the potential of these modes has not been undertaken.

7.4.2 Experimental work

Essentially, the experimental work was undertaken to validate dispersion predictions, and for the most part, potentially useful mode points were chosen, in order to reinforce the results. Since local-immersion wax baths were used, only modes with sufficient out-of-plane surface displacement were selected. Consequently, little validation of modes with predominant in-plane surface displacement was undertaken, such as for example that of the S_1 mode at its maximum group velocity in the single skin and it would have been useful, therefore, to have some means of efficient, selective excitation of such modes. In the low frequency regime where only the fundamental modes exit, non-resonant techniques were adequately employed. For example, a standard PZT transducer was applied to the plate edge. Shear transducers, coupled to the plate surface with a shear couplant such as treacle, were also tried. These methods tend to generate unwanted modes and the shear transducers in particular were found to excite large SH mode signals, that inevitably interfered with measurements. Had such equipment been available, perhaps the best means of generating these modes in the laboratory might have been a high-power laser (employing a technique similar to that described by Costley and Berthelot (1992), or Huang, *et al.* (1992), to generate appropriately spaced in-plane surface tractions.

Laser signal measuring equipment that enabled more consistent point measurements to be made and which also allowed measurement of in-plane signal displacements was acquired fairly late in the project schedule. Although some previous measurements were repeated using this equipment, there was insufficient time to repeat all the experiments, nor was this warranted, since laser measurement were largely in agreement with those made using the local-immersion method. However, given more time, reliable measurements of precise transmission and reflection coefficients across joints might have been made using the laser; applying the two dimensional Fourier transform technique to separate modes converted at the joint boundaries. Such measurements would have reinforced the findings presented in chapter 5 and would have led to more quantitative results in this important area.

7.4.3 Modelling

Whilst the modelling was essential to reveal the interaction of modes with changes in waveguide geometry, the modelling has some important limitations that reduced its correspondence with the real system under consideration. Most serious was the lack of provision for viscoelastic damping, which would have led to an increasing modelling error with propagation distance through the attenuative adhesive. Despite this, the models did provide an adequate representation of events over the short distances associated with stringer transmission, and fulfilled their aim of illuminating the carrier-mode interference and leading edge effects. Had the finite-element application had provision for modelling liquid layers, (poisson's ratio = 0.5) then modelling of the systems with the sealant layers might also have been possible. The sealant was found to support virtually no shear wave propagation and it might, therefore, reasonably be assumed to be a liquid. This would have overcome the difficulties that arose from the large difference between the longitudinal wave velocity in the aluminium layers and the sealant shear wave velocity.

Considerable effort was spent in ensuring that reflections did not interfere with measured signals and this often led to large models with long computation times. The provision of non-reflecting boundaries in the modelling software would have been more expedient and would have prevented invalidation of the results in a number of cases.

It is most unlikely, however, that any of the previously mentioned improvements would have significantly altered the findings or conclusions of this project.

7.5 Future work

7.5.1 Aircraft structural health monitoring.

The conclusions of the work presented in this thesis do not recommend the use of guided waves in an integrated aircraft health-monitoring system demanding long-range propagation. Although this finding is unlikely to change, as long as the assumptions regarding transducer performance remain true, short-range health monitoring of structurally-significant features appears to be a viable option and is probably a more practical approach. Considerable development of such systems has already been done, particularly associated with defect detection in aircraft lap joints. However, these developments generally fall short of full integration into an on-board system, which demands consideration of the important issues of data transport, data reduction and data processing.

7.5.2 Excitation of modes with surface in-plane displacement for use in laboratory testing.

The previous section highlighted some development work that would be useful in the wider context of practical guided-wave analysis. Most urgent is the development of laboratory transduction systems that can conveniently generate unidirectional propagation of a single mode from in-plane surface tractions. This implies an interdigital transduction technique. The transducers currently under development at Strathclyde University and reported by Gachagan, et al. (1996) can generate in-plane surface tractions and seem to offer potential for the permanently installed system. Electro-magnetic acoustic transducers (EMATs) can also excite these modes. The drawback with these transducers is that they cannot be adjusted to excite different modes and are consequently less convenient to use for laboratory testing. One solution would be an interdigital transducer whose element spacing increment could be adjusted. Laser techniques are an alternative, though current systems are an expensive option, particularly in situations where several transducers are required.

7.5.3 Acoustic Emission

The investigation of acoustic emission was necessarily strictly limited and was sufficient only to resolve the apparent paradox associated with the propagation of AE event signals. This work did, however, suggest that aircraft AE systems, and perhaps other fields of AE, may benefit from the development of a resonant omni-directional shear transducer, that would be more sensitive to the predominantly in-plane S_0 mode generated by AE events. Use of such a transducer would allow triggering from a non-dispersive mode, rather than the dispersive flexural mode and this would undoubtedly improve defect location, which commonly relies upon a time-of-flight algorithm.

Appendix A.

A.1 Introduction

This appendix begins by reviewing the relationship between the longitudinal and shear bulk waves and the elastic properties of material before outlining relationship between these bulk waves and guided waves, particularly those of the free plate in a vacuum. This group of guided waves are more commonly known as Lamb waves after Professor Horace Lamb who reported their theoretical existence to the Royal Society of London in 1916 [Lamb (1917)]. Although the case of Lamb waves in isotropic material is comparatively simple, compared with those of multi-layered systems and those with anisotropic materials, it is nevertheless one of crucial importance in this project. Owing to the large difference in the elastic properties of aluminium alloy and air, Lamb's case, which yields an exact analytical solution, is a very close approximation to the case of a single skin in air. Consideration of the free plate is therefore an important practical case, but it also provides an essential basis for an understanding of more complex systems. To this end it is appropriate to present a brief outline of how the free plate dispersion analysis is approached. Such analysis is discussed more thoroughly in many texts such as Brekhovskikh (1980), Graff (1973), Victorov (1970) . The method of modal analysis for all but the simplest of systems is that of the global matrix method, which is implemented in the software program: 'Disperse'. The global matrix method requires a complete definition of the elastic properties of each layer of the system in order to determine the roots of the governing characteristic equation giving the modal solution.

A.2 Bulk Waves

From basic elastic theory the elastic constants of an arbitrary material form a six by six matrix, and thus there are 36 constants. Fortunately, the aircraft materials used in this project are essentially isotropic and homogeneous and in this case the elastic matrix ([c]) is reduced to

$$[c] = \begin{bmatrix} c_{11} & c_{12} & c_{12} & 0 & 0 & 0 \\ c_{12} & c_{11} & c_{12} & 0 & 0 & 0 \\ c_{12} & c_{12} & c_{11} & 0 & 0 & 0 \\ 0 & 0 & 0 & c_{44} & 0 & 0 \\ 0 & 0 & 0 & 0 & c_{44} & 0 \\ 0 & 0 & 0 & 0 & 0 & c_{44} \end{bmatrix} \tag{A2.1}$$

Since $c_{11} = c_{12} + 2c_{44}$ the elastic properties of an isotropic homogeneous material can be fully specified by just two constants from equation A2.1. These two constants are often expressed as the Lamé constants, μ and λ where:

$$\mu = c_{44}$$
$$\lambda = c_{12}$$

The velocities of the bulk transverse (shear) waves and bulk longitudinal waves in the material (c_T and c_L respectively), are simply related to these constants and the material density (ρ) by:

$$\begin{aligned} c_T &= \sqrt{\frac{\mu}{\rho}} \\ c_L &= \sqrt{\frac{\lambda + 2\mu}{\rho}} \end{aligned} \tag{A2.2}$$

More commonly however the elastic properties are expressed in terms of Youngs modulus (E) and Poissons ratio (ν) and these are related to the Lamé constants by:

$$
\begin{aligned}
E &= \frac{\mu(3\lambda + 2\mu)}{\lambda + \mu} \\
\nu &= \frac{\lambda}{2(\lambda + \mu)}
\end{aligned}
\qquad \text{(A2.3)}
$$

and in terms of E and ν the bulk wave velocities are given by:

$$
\begin{aligned}
c_T &= \sqrt{\frac{E}{\rho}\frac{1}{2(1 + \nu)}} \\
c_L &= \sqrt{\frac{E}{\rho}\frac{1 - \nu}{(1 + \nu)(1 - 2\nu)}}
\end{aligned}
\qquad \text{(A2.4)}
$$

For a lossless material, measurement of the two bulk wave velocities are sufficient to fully describe the material elasticity. Where energy losses in the material are significant, it is necessary to include parameters of attenuation. Energy losses arise from two sources:

- Scattering of energy due to the interaction with small imperfections in the material, such as grain boundaries and precipitation. In the case of guided waves, scattering also occurs at the system boundaries due to surface roughness. The scattered energy is lost from the propagating signal and is ultimately converted to heat by the viscoelastic mechanism.

- Viscoelasticity in the material causes a proportion of the displacement energy to be converted to heat.

For most materials it is found that signal amplitude decays exponentially with distance, so that, for a given material, a plane wave with an initial amplitude (A_i) will decay to an final amplitude of (A_f) over a distance (d), according the expression:

$$
\frac{A_f}{A_i} = e^{-\alpha d} \qquad \text{(A2.5)}
$$

where α is the attenuation constant or attenuation coefficient of the material expressed in Nepers/m.

Since viscoelasticity is generally velocity dependent, it is not surprising that viscoelastic attenuation is also frequency dependent. In order to specify a material constant expressing attenuation, α must be made independent of frequency. A convenient (though not necessarily accurate) method assumes that the attenuation coefficient is proportional to frequency and thus frequency independence is achieved simply by multiplying the established value of α by the wavelength. The roughly linear attenuation spectra, found experimentally for PRC sealant and Redux adhesive, largely validates this assumption in these cases.

A.3 Outline of elementary dispersion analysis of the free plate

The most intuitive consideration of Lamb waves is as the superposition of two sets of bulk waves (*ie* two longitudinal and two shear waves) reverberating between the thickness boundaries of a free plate. The wavelength of these contributory waves, termed 'partial waves', is comparable to the plate thickness and this, together with their angles of incidence with respect to the plate boundaries, determines the unique Lamb wave propagation characteristic, termed the 'mode'.

Consider the Lamb wave propagating in the plate of thickness (h), shown schematically (in cross-section) in figure A1. The two sets of longitudinal and transverse bulk waves are seen propagating with amplitudes (L) and (T) respectively and these are marked + and – to denote the sign of their x_2 component. The plate is considered to be infinite in the x_3 direction, so that conditions of plane strain can be assumed, and the analysis becomes conveniently two-dimensional. In other words, all points on the wave front lying parallel to x_3 have identical displacement and stress conditions, and there is no displacement in the x_3 direction. The wavenumbers ($k_{L/T}$) of the partial waves are related to their wavelength (λ) by:

$$k = \frac{2\pi}{\lambda} \tag{A3.1}$$

and these are represented in vector form in figure A1. Snell's law dictates that the x_1 component of wavenumber of each of the partial waves will be identical, and will be equal to that of the resultant Lamb wave (*k*).

Thus:

$$k = k_L \sin\theta_L = k_T \sin\theta_T$$

where θ_L and θ_T are the respective incident angles of the longitudinal and transverse partial waves, with respect to a line normal to the plate surface as shown. From simple consideration of the geometry it is also clear that

$$\begin{aligned} {k_L}^2 &= k^2 + p^2 \\ {k_T}^2 &= k^2 + q^2 \end{aligned} \qquad \text{(A3.2)}$$

and

$$\begin{aligned} p &= k_L \cos\theta_L \\ q &= k_T \cos\theta_T \end{aligned} \qquad \text{(A3.3)}$$

Considering just the two dimensions of this problem, the constitutive equation relating stress (σ) to strain (ε) is given by

$$\begin{bmatrix} \sigma_{11} \\ \sigma_{22} \\ \sigma_{12} \end{bmatrix} = \begin{bmatrix} c_{11} & c_{12} & 0 \\ c_{12} & c_{11} & 0 \\ 0 & 0 & c_{44} \end{bmatrix} \begin{bmatrix} \varepsilon_{11} \\ \varepsilon_{22} \\ \varepsilon_{12} \end{bmatrix} \qquad \text{(A3.4)}$$

where the elastic matrix is reduced from that of equation (A2.1).

The two-dimensional equations of motion are:

$$\begin{aligned} \rho \frac{\partial^2 u_1}{\partial t^2} &= \frac{\partial \sigma_{11}}{\partial x_1} + \frac{\partial \sigma_{12}}{\partial x_2} \\ \rho \frac{\partial^2 u_2}{\partial t^2} &= \frac{\partial \sigma_{21}}{\partial x_1} + \frac{\partial \sigma_{22}}{\partial x_2} \end{aligned} \qquad \text{(A3.5)}$$

Expressing the strains in equation (A3.4) as derivatives

$$\varepsilon_{11} = \frac{\partial u_1}{\partial x_1}, \varepsilon_{22} = \frac{\partial u_2}{\partial x_2}, \varepsilon_{12} = \frac{\partial u_1}{\partial x_2} + \frac{\partial u_2}{\partial x_1} \qquad \text{(A3.6)}$$

and the elastic constants in terms of the Lamé constants (λ and μ), defined in section A.1, expressions for $\sigma_{11,}\sigma_{22}$ and σ_{12} are found, and when substituted in (A3.5) give:

$$\rho \frac{\partial^2 u_n}{\partial t^2} = \mu \nabla^2 u_n + (\mu + \lambda) \frac{\partial}{\partial x_n} \left(\frac{\partial u_1}{\partial x_1} + \frac{\partial u_2}{\partial x_2} \right) : n = 1,2 \qquad \text{(A3.7)}$$

The two solutions of these equations, corresponding to the longitudinal and transverse bulk waves in figure A.1, are

$$u_L = \begin{Bmatrix} k \\ \pm p \end{Bmatrix} L^{\pm} e^{i(kx_1 \pm px_2 - \omega t)} \qquad \text{(A3.8)}$$

$$u_T = \begin{Bmatrix} \pm q \\ k \end{Bmatrix} T^{\pm} c^{i(kx_1 \pm qx_2 - \omega t)}$$

These are often more conveniently expressed in terms of field potentials (ϕ) and (ψ): $\phi = Le^{i(\mathbf{k} \bullet \mathbf{x} - \omega t)}$ and $\psi = Te^{i(\mathbf{k} \bullet \mathbf{x} - \omega t)}$, but for clarity the matrix form will be retained. Returning to figure A.1, the displacement at any location (x_1,x_2) may be found by summing the contribution of each of the four partial waves: L^+, L^-, T^+ and T^- and the result can be written in field matrix form:

$$[\mathbf{u}] = \begin{Bmatrix} u_1 \\ u_2 \end{Bmatrix} = \left[L^- \begin{pmatrix} k \\ -p \end{pmatrix} e^{i-px_2} + T^- \begin{pmatrix} -q \\ -k \end{pmatrix} e^{i-qx_2} + L^+ \begin{pmatrix} k \\ p \end{pmatrix} e^{ipx_2} + T^+ \begin{pmatrix} q \\ -k \end{pmatrix} e^{iqx_2} \right] e^{i(kx_1 - \omega t)} \qquad \text{(A3.9)}$$

The boundary conditions of the problem are that the normal stress (σ_{22}) and the shear stress (σ_{12}) at the plate surface are zero. Expressing σ_{22} and σ_{12} from equation (A3.4) in terms of the Lamé constants we have:

$$\sigma_{22} = \lambda(\varepsilon_{11} + \varepsilon_{22}) + 2\mu\varepsilon_{22} \tag{A3.10}$$

$$\sigma_{12} = \mu\varepsilon_{12}$$

Differentiating the expressions for u_1 and u_2 in equation A3.8 we obtain expressions for strains ε_{11}, ε_{22} and ε_{12} :

$$\varepsilon_{11} = \frac{\partial u_1}{\partial x_1}$$

$$\varepsilon_{22} = \frac{\partial u_2}{\partial x_2} \tag{A3.11}$$

$$\varepsilon_{12} = \frac{\partial u_1}{\partial x_2} + \frac{\partial u_2}{\partial x_1}$$

These are substituted into equation (A3.10) and the result is expressed in terms of k_L and k_T by use of equation (A3.2) giving:

$$\sigma_{22} = \left[iL^- \left\{ k_L^{\,2}(\lambda + 2\mu) - 2\mu k^2 \right\} e^{-ipx_2} + iL^+ \left\{ k_L^{\,2}(\lambda + 2\mu) - 2\mu k^2 \right\} e^{ipx_2} + 2i\mu qk \left(T^- e^{-iqx_2} - T^+ e^{iqx_2} \right) \right] e^{i(k_1 x_1 - \omega t)} \tag{A3.12}$$

$$\sigma_{12} = \left[-2ikpL^- e^{-ipx_2} + iT^- \left(k_T^{\,2} - 2k^2 \right) e^{-iqx_2} + 2ipkL^+ e^{ipx_2} + iT^+ \left(k_T^{\,2} - 2k^2 \right) e^{iqx_2} \right] \mu e^{i\left(k_1 x_1 - \omega t\right)} \tag{A3.13}$$

The expression for σ_{22} is then written in terms of the bulk shear wave velocity (c_T), defined in equation (A2.2) and applying the boundary conditions at the upper and lower plate surfaces,

$$\sigma_{22} = \sigma_{12} = 0 : x_2 = \pm h$$

the following matrix expression is obtained:

$$\begin{bmatrix} \sigma_{22(x_2=-h)} \\ \sigma_{12(x_2=-h)} \\ \sigma_{22(x_2=h)} \\ \sigma_{12(x_2=h)} \end{bmatrix} =$$

$$\begin{bmatrix} \omega^2 - 2c_T{}^2k^2e^{-ipx_2} & \omega^2 - 2c_T{}^2k^2e^{ipx_2} & 2c_T{}^2qke^{-iqx_2} & -2c_T{}^2qke^{iqx_2} \\ -2kpe^{-ipx_2} & 2pke^{ipx_2} & \left(k_T{}^2 - 2k^2\right)e^{-iqx_2} & \left(k_T{}^2 - 2k^2\right)e^{iqx_2} \\ \omega^2 2c_T{}^2k^2e^{ipx_2} & \left(\omega^2 - 2c_T{}^2k^2\right)e^{ipx_2} & 2c_{T^2}qke^{iqx_2} & -2c_T{}^2qke^{iqx_2} \\ -2kpe^{ipx_2} & 2pke^{ipx_2} & \left(k_T{}^2 - 2k^2\right)e^{iqx_2} & \left(k_T{}^2 - 2k^2\right)e^{iqx_2} \end{bmatrix} \begin{bmatrix} L^- \\ L^+ \\ T^- \\ T+ \end{bmatrix}$$

$$= 0$$

(A3.14)

The coefficient matrix is recast in trigonometric form and further simplified by removing common factors and adding and subtracting rows to give:

$$\begin{bmatrix} \left(\omega^2 - 2c_T{}^2k^2\right)\cos ipx_2 & \left(\omega^2 - 2c_T{}^2k^2\right)\cos ipx_2 & 2\left(c_T{}^2qk\right)\cos iqx_2 & -2\left(c_T{}^2qk\right)\cos iqx_2 \\ -i\left(\omega^2 - 2c_T{}^2k^2\right)\sin ipx_2 & i\left(\omega^2 - 2c_T{}^2k^2\right)\sin ipx_2 & -2\left(c_T{}^2qk\right)\sin iqx_2 & 2i\left(c_T{}^2qk\right)\sin iqx_2 \\ -2(kp)\cos ipx_2 & 2(kp)\cos ipx_2 & \left(k_T{}^2 - 2k^2\right)\cos iqx_2 & \left(k_T{}^2 - 2k^2\right)\cos iqx_2 \\ 2i(kp)\sin ipx_2 & 2i(kp)\sin ipx_2 & -i\left(k_T{}^2 - 2k^2\right)\sin iqx_2 & i\left(k_T{}^2 - 2k^2\right)\sin iqx_2 \end{bmatrix} \quad \text{(A3.15)}$$

A condition for a non-trivial solution to (A3.14) is that the determinant of the coefficient of the variable L$^-$, L$^+$, T$^-$, T$^+$ is zero. We thus require the determinant of (A3.15), which can be expanded into the product of 2 sub-determinants:

$$\begin{vmatrix} \omega^2 - 2c_T{}^2k^2\cos ipx_2 & 2\left(c_T{}^2qk\right)\cos iqx_2 \\ -2i(kp)\sin ipx_2 & \left(k_T{}^2 - 2k^2\right)\cos iqx_2 \end{vmatrix} \bullet \begin{vmatrix} k_T{}^2 - 2k^2\cos iqx_2 & 2i(kp)\cos ipx_2 \\ 2\left(c_T{}^2qk\right)\sin iqx_2 & \omega^2 - 2c_T{}^2k^2\sin ipx_2 \end{vmatrix}$$

$$= 0$$

(A3.16)

Setting each of these determinants to zero and simplifying, results in two frequency equations:

$$\frac{\tan iqx_2}{\tan ipx_2} = \frac{4ic_T{}^2 qpk^2}{\left(k_T{}^2 - 2k^2\right)\left(\omega^2 - 2c_T{}^2 k^2\right)} \tag{A3.17}$$

$$\frac{\tan iqx_2}{\tan ipx_2} = \frac{\left(k_T{}^2 - 2k^2\right)\left(\omega^2 - 2c_T{}^2 k^2\right)}{4ic_T{}^2 qpk^2} \tag{A3.18}$$

These are generally known as the Raleigh-Lamb frequency equations, and they effectively define the functional relationship between ω and k for two groups of modes in a material with a given poissons ratio. Equation (A3.17) defines the symmetric group, which are characterised by symmetric displacement about the median plane of the plate, while equation (A3.18) defines the anti-symmetric group having anti-symmetric displacements about the median plane.

For a given root defined by k and ω, the displacement components at any point, x_2, in the thickness of the plate, can be found by first calculating the partial wave amplitudes L^+, L^-, T^+, T^- (the eigenvector) in equation (A3.14), and then inserting these into equation (A3.8) with the desired value of x_2, to find u_1 and u_2. The displacement distribution for a given mode point is termed the mode shape.

The real roots of equation (A3.17) and (A3.18) give the propagating modes, while the non-propagating, or evanescent modes, are given by the imaginary and complex roots. Figure A.2 shows the loci of real roots for an aluminium plate plotted in dimensionless form:

$$kx_2 \text{ versus } \frac{fx_2}{c_T} \tag{A3.19}$$

A more useful plot of the modal phase velocity (c_p) is easily obtained since

$$c_p = \frac{\omega}{k} \tag{A3.20}$$

Practical guided wave testing generally employs a tone burst of finite duration. This tone or wave packet propagates through the plate, not at the phase velocity, but instead at the group velocity (c_g) given by

$$c_g = \frac{\partial \omega}{\partial k} \tag{A3.21}$$

Group velocity is therefore associated with the gradient of the phase velocity dispersion function. The phase velocity and group velocity spectra for the lower-order modes of an aluminium plate, are shown in figure A.2.

Only one symmetric and one anti-symmetric mode exist at all frequency-thickness products and these are termed the fundamental or zero-order modes denoted S_0 and A_0 respectively. At high frequency-thickness products these modes tend to the Rayleigh or surface wave, whose energy decays exponentially with plate depth. All the other modes have frequency cut-off points below which they are evanescent. The mode cut-off frequencies correspond with the through-thickness resonance of longitudinal and shear bulk waves, and at high frequency these modes subtend the shear wave phase velocity. The order of these modes, denoted by their subscript in figure A.2, describes number of phase changes of the mode shape through the plate thickness. Thus the complexity of the mode shape increases with mode order.

A.4 Outline of 'Global Matrix Method'

The dispersion curves for more complex systems involving multiple layers are generally calculated by Disperse using the global matrix method. This method does not suffer from instability at high frequency-thickness products that is a feature of the 'Transfer Matrix Method' developed by Thomson (1950) and Haskell (1953). Both approaches are explained in detail by Lowe (1995), and it is therefore intended simply to give a very brief outline of the global matrix method providing sufficient insight to support references to the method in the thesis chapters.

Consider the free plate system diagram of figure A.1 to be one of a series of layers forming a multi-layer system. At the layer boundaries: x = h and x = -h a matrix equation can be derived, as explained in the previous section, relating displacements (u) and stress (σ) with the partial wave amplitudes (L^+,L^-,T^+,T^-) such that

$$\begin{Bmatrix} u_1 \\ u_2 \\ \delta_{22} \\ \sigma_{12} \end{Bmatrix} = [\mathbf{D}] \begin{Bmatrix} L^+ \\ L^- \\ T^+ \\ T^- \end{Bmatrix} \tag{A4.1}$$

Re-annotating the displacement stress vector as [**u**] and the partial amplitude vector as [**A**] for simplicity this matrix equation can be written for the top and bottom boundaries of the layer separately. These are denoted by the subscripts (T) and (B) respectively.

$$[\mathbf{u}]_T = [\mathbf{D}]_T [\mathbf{A}]$$

$$[\mathbf{u}]_B = [\mathbf{D}]_B [\mathbf{A}] \tag{A4.2}$$

The partial wave amplitudes are identical in both equations. Numbering the layers from the top of the system to the bottom, the displacements are continuous across the layer boundaries so that

$$[\mathbf{u}]_{Bn} = [\mathbf{u}]_{T(n+1)} \tag{A4.3}$$

Therefore from (A4.2)

$$[\mathbf{D}]_{Bn}[\mathbf{A}]_n = [\mathbf{D}]_{T(n+1)}[\mathbf{A}]_{(n+1)} \tag{A4.4}$$

or

$$[\mathbf{D}]_{Bn}[\mathbf{D}]_{T(n+1)}\begin{Bmatrix}\mathbf{A}_n\\ \mathbf{A}_{n+1}\end{Bmatrix} = 0 \tag{A4.5}$$

Equation (A4.5) for each layer can be combined to form a global matrix equation for the entire system. For example, the global matrix equation for a four layer system would be:

$$\begin{bmatrix}[\mathbf{D}]_{1B} & [\mathbf{D}]_{2T} & & \\ & [\mathbf{D}]_{2B} & [\mathbf{D}]_{BT} & \\ & & [\mathbf{D}]_{3B} & [\mathbf{D}]_{4T}\end{bmatrix}\begin{Bmatrix}\mathbf{A}_1\\ \mathbf{A}_2\\ \mathbf{A}_3\\ \mathbf{A}_4\end{Bmatrix} = 0 \tag{A4.6}$$

It is seen however that this equation contains three displacement equations whilst there are four amplitude vectors. This is resolved for the modal solution because the incoming wave amplitudes at the top and bottom layers are zero so that in the top layer

$$\mathbf{A}_1 : L^+ = T^+ = 0$$

and in the bottom layer

$$\mathbf{A}_4 : L^- = T^- = 0$$

Thus four equations are removed and the global matrix equation is solvable. The global matrix equation, which is the equivalent of the free plate equation A3.14, does not generally yield an analytical solution, and must be solved numerically. Details of the numerical methods employed by Disperse are presented by Lowe (1995).

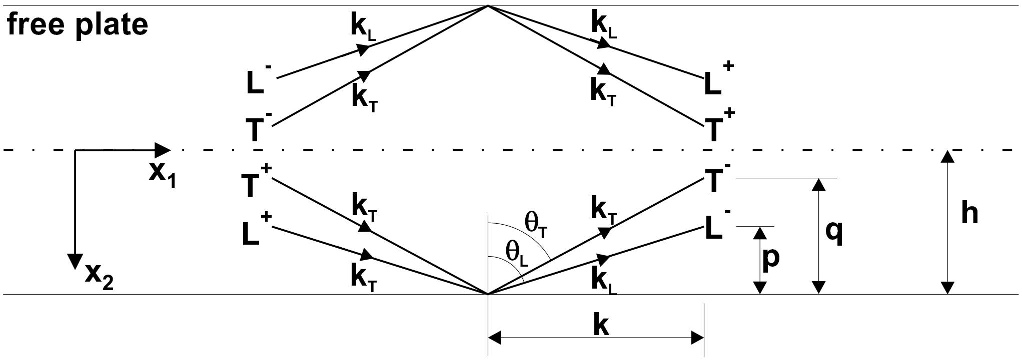

Fig A.1 Diagram of partial waves in a free plate.

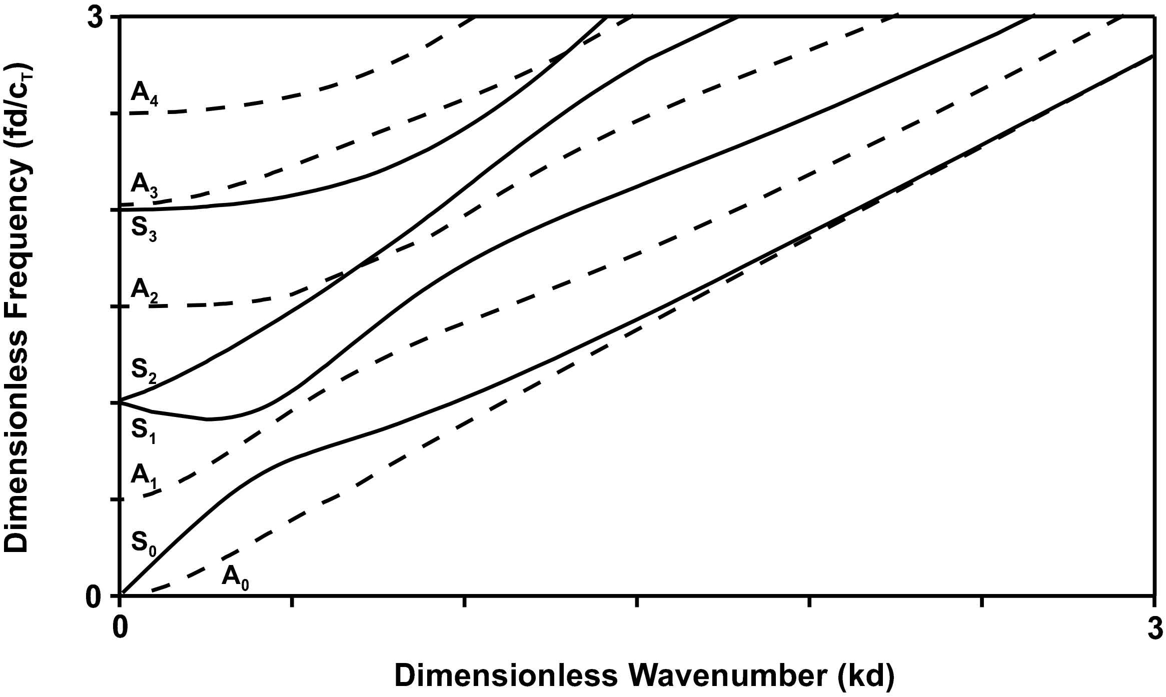

Fig A.2 Dimensionless dispersion curves for Lamb modes in a free aluminium plate.
— — — : Anti-symmetric modes. ——— : Symmetric modes.

Appendix B.

Although chapter 2 of this thesis presents the final results of the acoustic property measurements and discusses the adaptation of a standard method used to measure the attenuation of bulk waves in the PRC sealant, there is little mention of the measurement of the velocity of bulk waves in the Redux adhesive and the PRC sealant. This is entirely appropriate, because these measurements were achieved by means of standard tests that are easily found in the literature. However, since the accuracy of both the dispersion predictions and the numerical modelling, presented in this thesis, crucially depends upon the accuracy of these material acoustic parameters, it is appropriate to present some of the details of these measurements in this appendix.

B.1 Velocity measurements.

The phase velocity of bulk longitudinal and bulk shear wave propagation through Redux adhesive was measured using the Amplitude Spectrum Method described in detail by Pialucha, et al. (1989). This method was also used to find the longitudinal wave velocity in PRC sealant. The shear wave velocity in PRC had to be measured by a different method, which relied on a measurement of the reflection coefficient at the interface of the PRC specimen and another material. This method will be described later in this section.

B.1.1 Bulk wave velocities by amplitude spectrum method.

Specimens of PRC sealant were simply made by mixing a batch of the two-part mix and allowing a quantity to cure at room temperature between two sheets of glass. Aluminium separators of varying thickness were interspersed between the glass sheets to give specimens with parallel faces and several different thicknesses. In order to obtain specimens of Redux adhesive that were identical to those found in adhesively bonded joints, samples of Redux film were cured between two thick sheets of aluminium, under the pressure and temperature conditions stipulated for aircraft joints in DTD 775, using a hot press. The aluminium sheets, however, were lightly smeared with a release agent so that the cured adhesive layer could be removed after cooling.

In a simple pulse-echo test, a broadband pulse was transmitted through the specimen and the reflections from the front and back walls of the specimen were received and stored on the PC. The experimental arrangement for measurement of bulk longitudinal wave velocity by the amplitude spectrum method is shown in figure B.1. For both Redux and PRC specimens, measurements were made using a 5 MHz probe and a typical time-trace, showing the reflections from the front and back walls of a PRC specimen, is presented in figure B.2.

To obtain the velocity spectrum both the front and back wall reflections were windowed and fast Fourier transformed (FFT) to give a frequency spectrum. The spectrum of the two reflections, shown in figure B.2, is presented in figure B.3. Clear minima can be seen in the amplitude spectrum and these were used to establish the velocity at their respective frequencies, giving the velocity spectrum, as described below.

The Fourier transform of the sum of two reflections results in a spectrum that exhibits minima at frequencies corresponding with resonance across the specimen. Such resonance occurs whenever the difference in signal path length of the two reflections is an integral number of signal wavelengths (λ). Considering reflections from the front and back faces of a specimen, the path length difference is twice the sample thickness: (L) *ie:*

$$2L = \lambda m : m \in (1,2,3\ldots) \qquad \text{(B.1)}$$

Since phase velocity (c) is the product of frequency (f) and wavelength:

$$c = f\lambda \qquad \text{(B.2)}$$

then

$$c = \frac{2Lf}{m} : m \in (1,2,3,\ldots) \qquad \text{(B.3)}$$

It is therefore necessary to carry out Fourier transformation of the time interval enclosing the front and back face reflections and then calculate the phase velocity corresponding to each of the minima. These are plotted to from the velocity spectrum (or dispersion) of the material in respect of the bulk wave concerned.

In some cases, particularly where large impedance differences between the coupling and specimen result in large differences in amplitude between the front and back face reflections, the minima in the amplitude spectrum may be shallow and broad. In such cases, where it is difficult to determine the frequency of the minima, sharper minima can be obtained by multiplying the back face reflection (or dividing the front face reflection) by an appropriate constant before carrying out the Fourier transformation. It was also sometimes found useful to divide the amplitude spectrum of the front and back face reflections by that of the front face alone, to remove the transducer characteristic and thus provide a flat spectrum from which to read the minima.

A separate FFT of the windowed front face reflection, alone, was used to establish the limits of the bandwidth of valid results, which were deemed to be at points where the probe response had fallen to roughly -20dB of its centre frequency response.

A similar procedure was employed for the measurement of the shear wave velocity in Redux and PRC, except that, for these measurements, the specimens were not immersed. A 6 MHz shear transducer with a 10 mm acrylic stand-off was directly coupled to the specimen with a thin smear of shear couplant (Treacle).

The resulting velocity spectra for bulk longitudinal and bulk shear waves in Redux are shown in figures B.4 and B.5 respectively. Two sets of curves are shown in these figures. Concern over the possibility of changes in the material properties with age led to attempts to measure the acoustic properties of Redux in a joint specimen, obtained from a scrapped VC10 aircraft, approximately thirty years old. Since the aluminium skin layers in this specimen were painted, a 50 MHz probe was used for the measurement of longitudinal wave velocity, to provide sufficient resolution to separate the reflections from the paint layers. This resulted in a much wider bandwidth of measurements seen in the figure. The reflections of the slower shear wave were adequately resolved with the 6 MHz shear transducer. Velocity spectra for Redux, obtained from this specimen, are indicated by dotted lines in figures B.4 and B.5 and are seen to be roughly comparable with those of the new specimen.

For the longitudinal wave phase velocity in PRC, several spectra are presented in figure B.6. The three dotted lines indicate amplitude spectrum measurements made on three samples of different thickness. These show a variation of up to 15% at lower frequencies, which illustrates the likely scale of acoustic property variation in PRC. The two solid lines in figure B.6 indicate the longitudinal wave velocity spectra of two samples, calculated by a different method that was used to find the shear wave velocity in PRC. These curves were plotted in order to establish the validity of the method, which is discussed in the next section.

B.1.2 Bulk wave shear velocity from reflection coefficient.

The shear wave attenuation in PRC was so high that it proved impossible to obtain a reverberation signal using the shear probe available and so the preferred amplitude spectrum method could not be used. In this case, the velocity was calculated from the reflection coefficient at the interface between a block of polycarbonate (PC) bonded to a sample of PRC. The method for finding this reflection coefficient is the same as that used in the PRC attenuation measurement and is described in section 2.2.2.1 of chapter 2. At normal incidence, the reflection coefficient (R_{ca}) at the interface between coupling material (c) and specimen (a) is a function of the impedance of the two materials (Z_c and Z_a) respectively.

$$R_{ca} = \left| \frac{Z_c - Z_a}{Z_a + Z_c} \right| \tag{B.4}$$

Impedance is simply the product of velocity and density and the shear wave impedance was therefore found by multiplying the shear wave velocity in the PC, measured using the amplitude spectrum method, by the published density of PC. The density of PRC was simply measured and is indicated in table 2.1. For these shear wave measurements a 6

MHz probe was used throughout and a thin smear of shear couplant was applied to all the contacting surfaces. The resulting shear wave velocity spectra, for two of the thinner samples, are presented in figure B.7. The frequency band presented in figure B.7 represents the lower end of the transducer response, the higher frequencies being effectively filtered by the specimen.

Comparing the two solid lines in figure B.6, indicating the longitudinal velocity in two samples of PRC calculated by this method, with the dotted lines representing the same parameter calculated by the amplitude spectrum method, the calculation of velocity by reflection coefficient is generally about 7% lower than the mean of the amplitude spectrum results. It was concluded that the accuracy of this method is acceptable in this case, given the overall variation in the properties of PRC.

The measured shear wave phase velocity spectrum for the two PRC samples, shown in figure B.7, indicate dispersion of the shear wave velocity, which would complicate the modal analysis. However, when the shear wave attenuation was found to be so high that effectively shear waves would not propagate, it was felt that a single estimate of shear wave velocity would not cause undue error in the subsequent modelling. A mean value of 200 m/s was therefore ascribed.

B.2 Attenuation measurements in Redux adhesive.

Since the attenuation of Redux adhesive is much lower than that of PRC, it was possible to obtain several separated reverberations through the specimen. This enabled a simpler method to that described in chapter 2 for the measurement of attenuation in PRC to be employed, which Guo, et al. (1995) call the $F_0/B_1/B_2$ method. In this method no separate reference measurement is required. The ray diagram in figure B.8 shows the relevant ray paths using the notation of Guo, where F, B_1 and B_2 are the amplitudes of the front-face and the first and second back-face reflections respectively. It is seen that:

$$B_2 = B_1 R_{ca} R_{ab} A_\alpha{}^2 \qquad \text{(B.5)}$$

If A_α is the loss factor for a single transit through the specimen, and assuming that $R_{ab} = 1$ then:

$$A_\alpha{}^2 = \frac{B_2}{B_1}\frac{1}{R_{ca}} \tag{B.6}$$

It can be shown that

$$R_{ca}{}^2 = \frac{B_2/B_1}{B_2/B_1 - B_1/F} \tag{B.7}$$

so that A_α^2 can be calculated and the attenuation coefficient (α) can be established by applying equation 2.7 in chapter 2.

In practice, it proved very difficult to obtain consistent measurements of the attenuation properties of cured Redux adhesive. The thick samples were porous, with a lower density, while the samples cured under the standard conditions specified for aircraft joints were almost transparent and homogeneous, with a density of 1036 kg m^{-3}. Having very thin samples of about 0.25 mm caused poor conditioning of the attenuation measurement, which is highly sensitive to the thickness measurement, established using a micrometer.

For measurement of longitudinal wave attenuation, a 20 MHz probe was used in the experimental arrangement illustrated in figure B.9, and several clear backwall reflections were obtained from an airbacked specimen immersed in water. Air was simply trapped beneath the specimen, as shown in the figure. The shear wave attenuation, measurement was achieved using a 6 MHz shear probe with a 10 mm acrylic delay line. This was coupled to the specimen with a thin layer of treacle, commonly used for the purpose. The $F/B_1/B_2$ method was then used to process both the longitudinal and shear results in the frequency domain and the resulting attenuation spectra are shown in figure B.10.

A measurement was also made of the attenuation in the adhesive of the aged aircraft joint mentioned previously. In this case most of the energy was reflected at the first aluminium/adhesive interface; however, two backwall reflections were obtained for the longitudinal wave case. A cross-sectioned joint was used to find the adhesive thickness, which was measured by means of a scanning electron microscope. The result of this measurement is also shown in figure B.10, for comparison, and seems to indicate considerably higher attenuation in the aged sample. This prompted an ultrasound 'C scan' to be made of the joint, to check for variation in the joint thickness and any degradation of the joint interfaces at the test points. No anomalies were observed. The aged attenuation result must be treated with caution, however, owing to the likelihood of error in the thickness measurement and the associated sensitivity of the results.

A straight line best fit to the results for the bulk specimen was used to calculate the longitudinal and shear wave attenuation coefficients in terms of wavelength (0.12 and 0.2 Np/λ respectively) and these values were used in subsequent modelling.

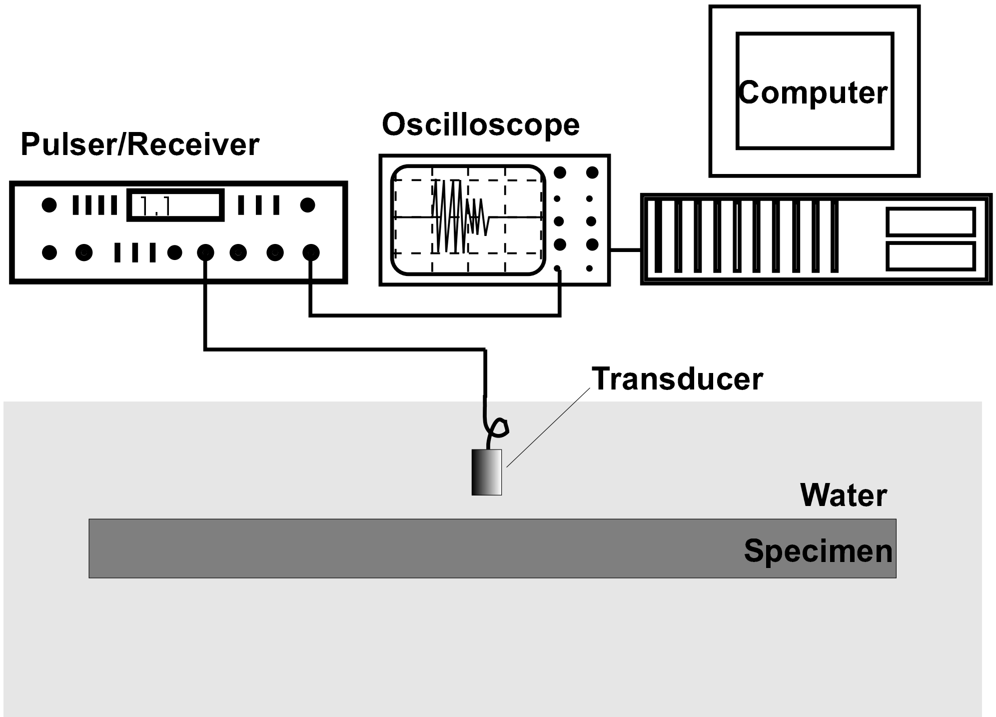

Fig B.1 Schematic diagram of the equipment arrangement for velocity measurements by the amplitude spectrum method.

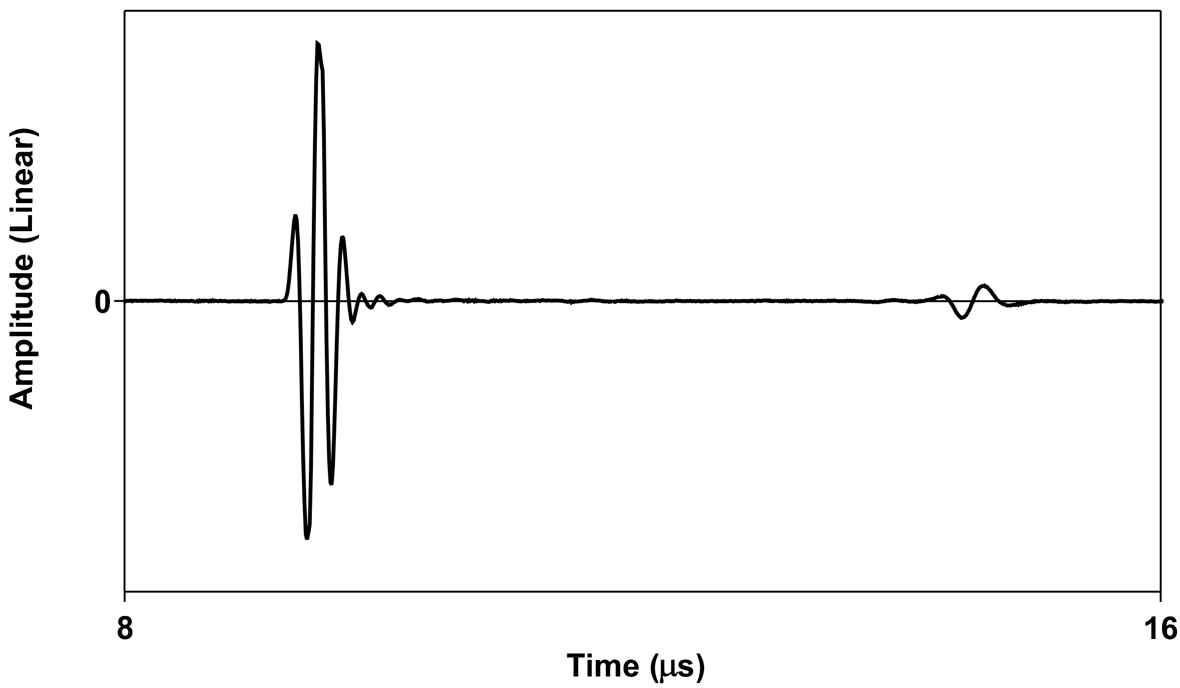

Fig B.2 Time trace obtained from a normal-incidence pulse/echo test on a specimen of PRC sealant using a 5 MHz probe.

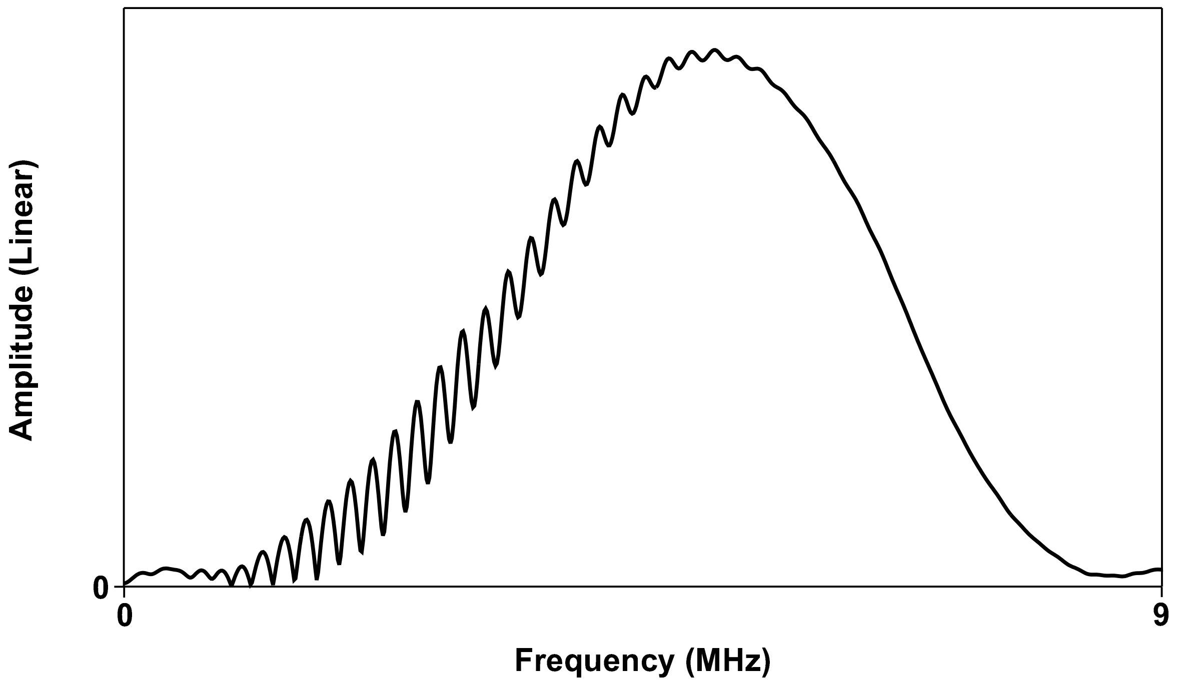

Fig B.3 Spectrum of front and back face reflections used for calculation of longitudinal bulk wave phase velocity in PRC.

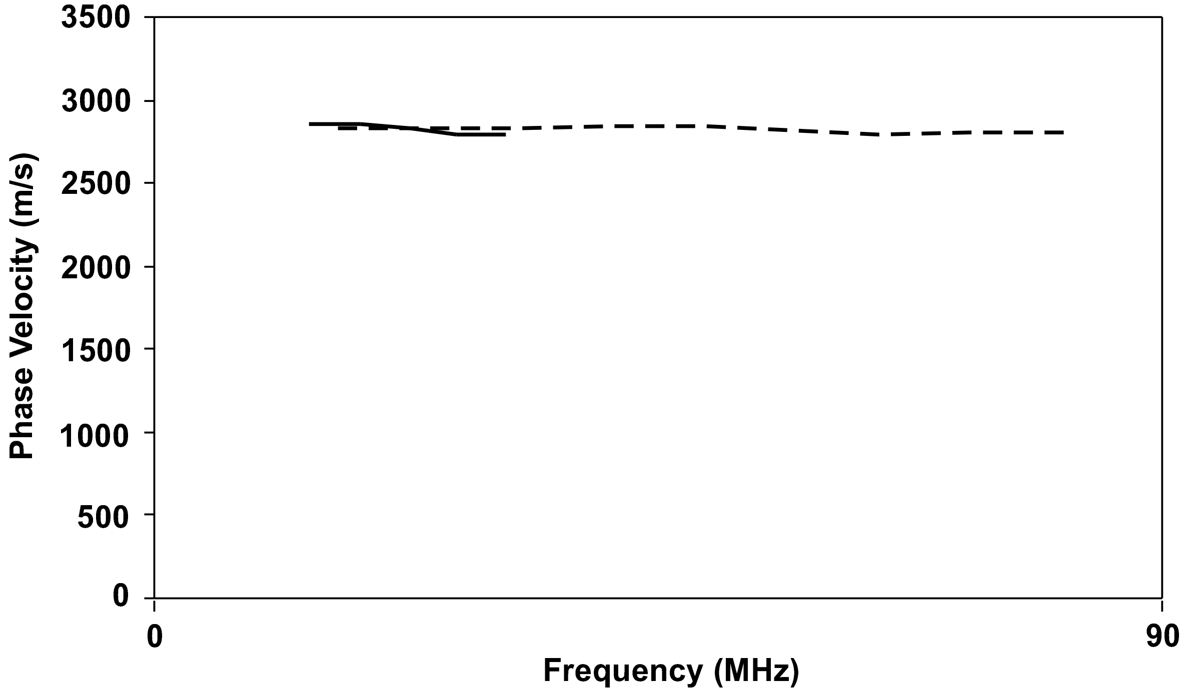

Fig B.4 Spectra of bulk longitudinal wave phase velocities in Redux adhesive.
New sample: ———————, *Old aircraft joint sample:* – – – – – –

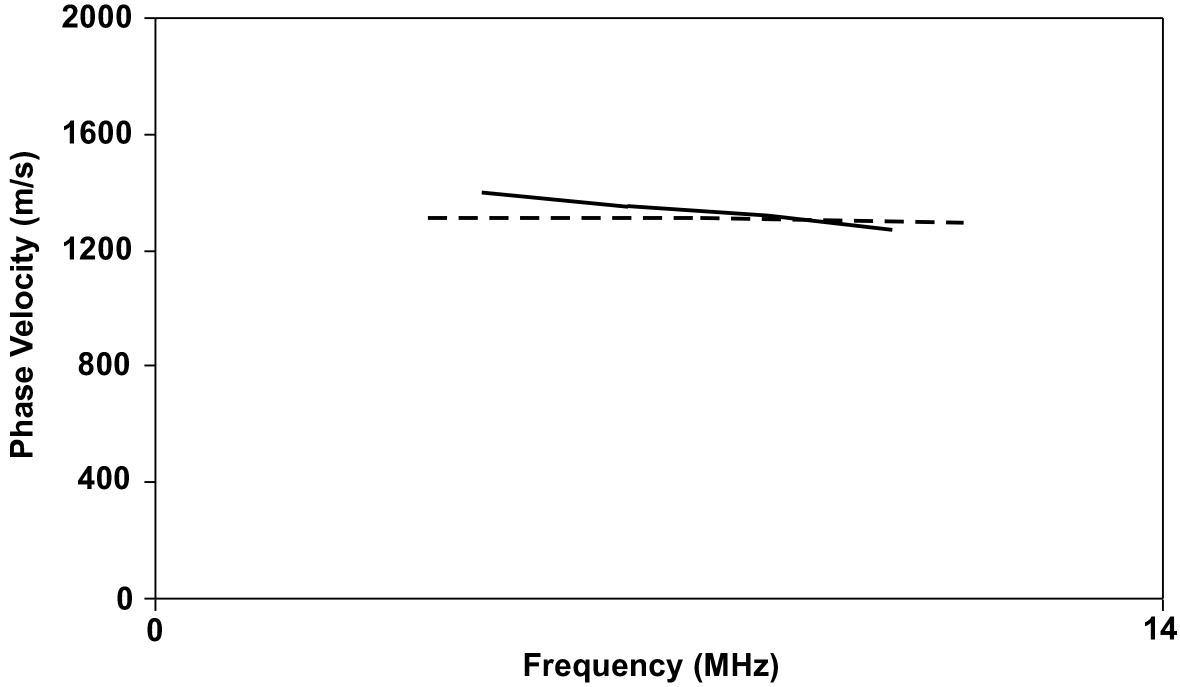

Fig B.5 Spectra of bulk shear wave phase velocities in Redux adhesive.
New sample: ———————, *Old aircraft joint sample:* – – – – – –

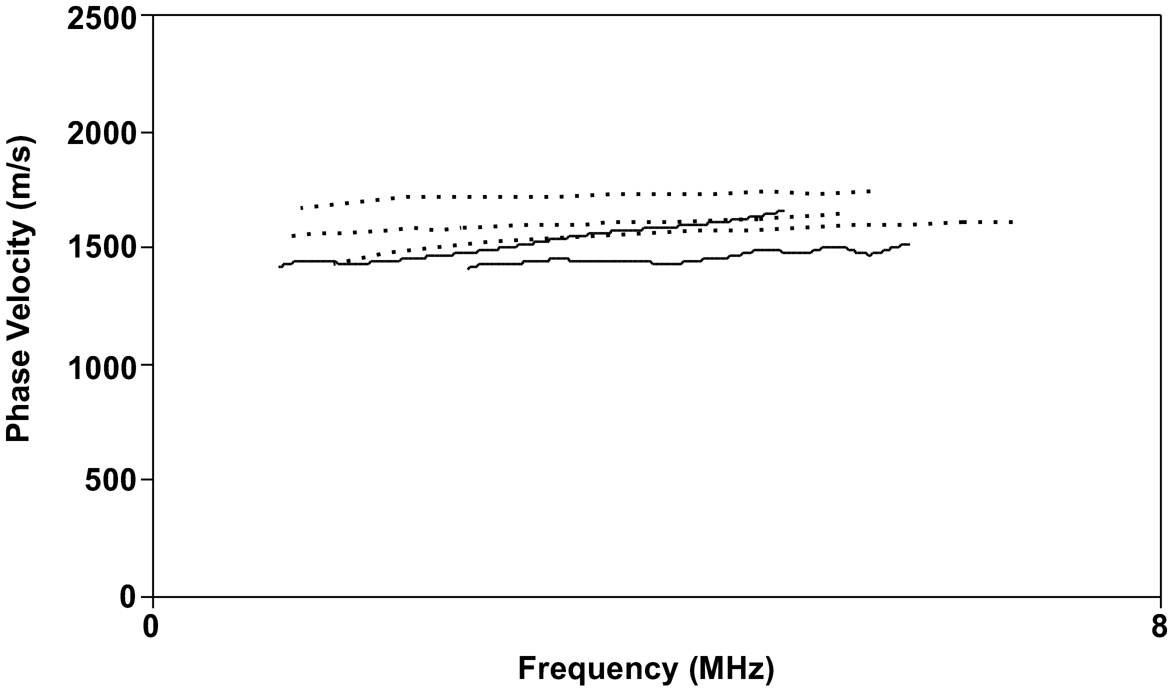

Fig B.6 Spectra of bulk longitudinal wave phase velocities in PRC sealant showing the variation between three specimens. The phase velocity for two specimens, calculated by means of reflection coefficients, are also shown for comparison.
Amplitude spectrum method: .... , *reflection coefficient method:* ————

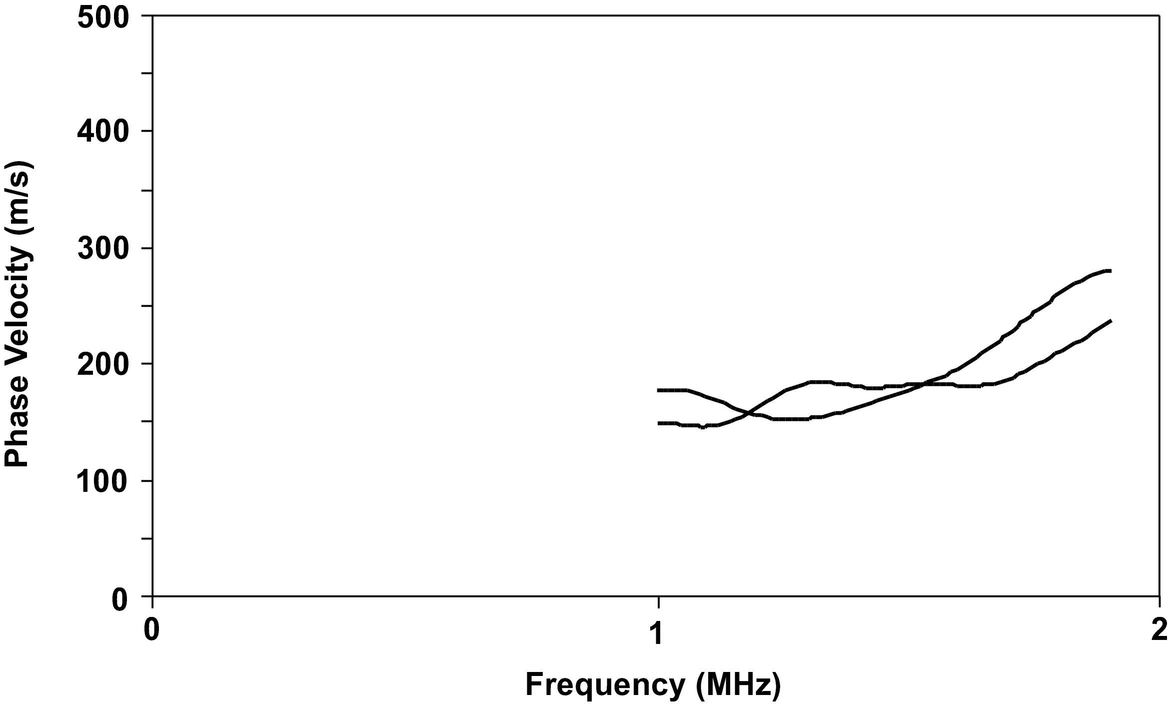

Fig B.7 Spectra of bulk shear wave velocities found using the reflection coefficient method for two samples of PRC sealant.

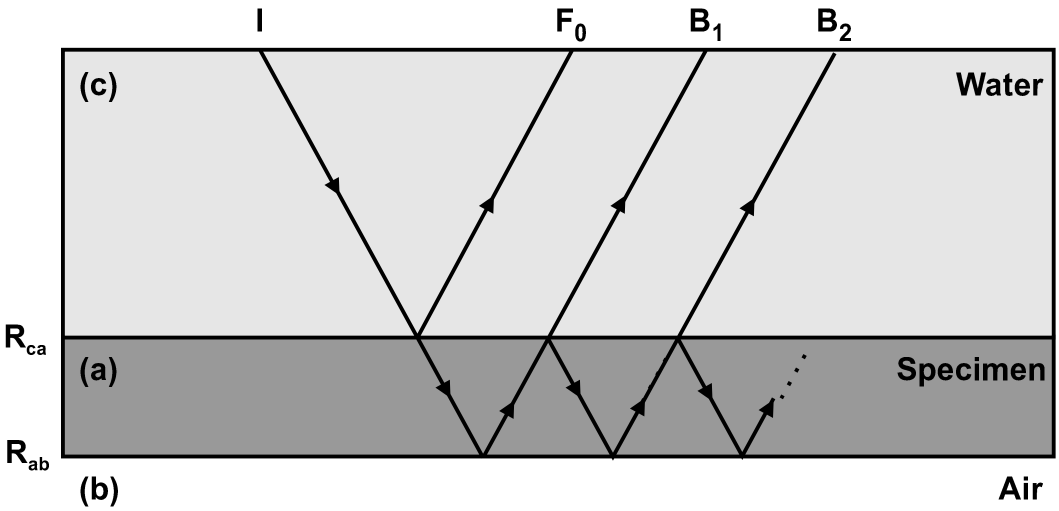

Fig B.8 Schematic diagram of the paths of received signals in the F0/B1/B2 method of attenuation measurement. The signal paths are normal to the interfaces, but are shown inclined for clarity.

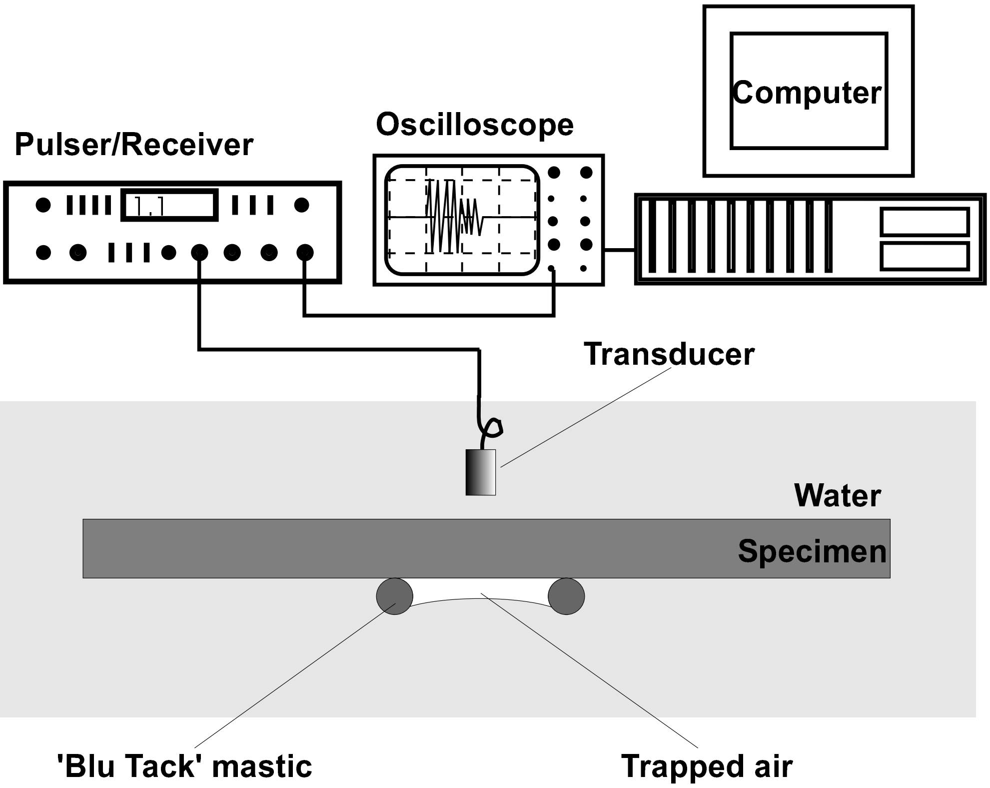

Fig B.9 Schematic diagram of the equipment arrangement used in the measurement of the longitudinal wave attenuation by the F/B_1/B_2 method.

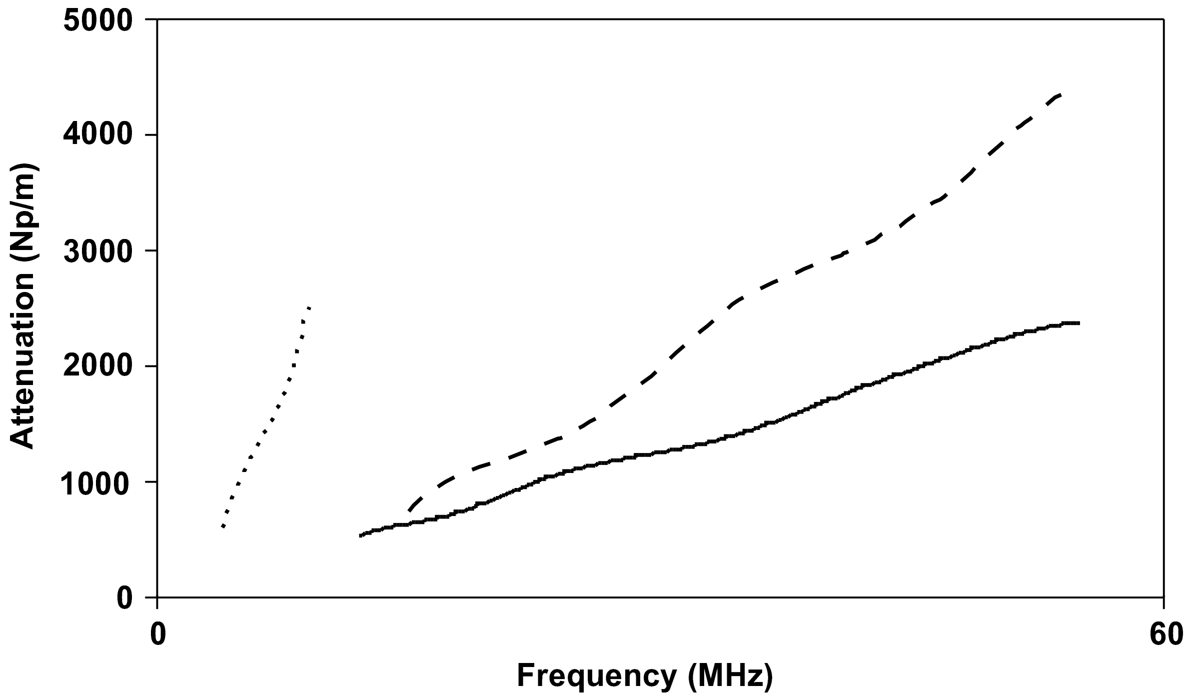

Fig B.10 Spectra of longitudinal and shear bulk wave attenuation in Redux adhesive.
Longitudinal wave attenuation in new specimen.
Longitudinal wave attenuation in aged specimen.
Shear wave attenuation in new specimen.

References

Alers, G. A. and Thompson, R. B., (1976), "Application of trapped modes in layered media to the testing of adhesive bonds", in *IEEE Ultrasonics Symposium, Annapolis, MD*, pp. 138-143

Alleyne, D., Lowe, M., and Cawley, P., (1996), "The inspection of chemical plant pipework using Lamb waves : defect sensitivity and field experience", in *Annual review of progress in quantitative NDE*, edited by D. O. Thompson and D. E. Chimenti, Plenum Press, New York , pp. 1859-1866

Alleyne, D. N., (1991), "The nondestructive testing of plates using ultrasonic Lamb waves", PhD thesis, Department of Mechanical Engineering, Imperial College of Science Technology and Medicine, London

Alleyne, D. N. and Cawley, P., (1991), "A two-dimensional Fourier transform method for the quantitative measurement of Lamb modes", in *Annual review of progress in quantitative NDE*, edited by D. O. Thompson and D. E. Chimenti, Plenum Press, New York , pp. 201-208

Alleyne, D. N. and Cawley, P. , **(1992)**, "The interaction of Lamb waves with defects", *IEEE transactions on ultrasonics, ferroelectics, and frequency control* , vol. 39, pp. 381-397

Alleyne, D. N. and Cawley, P. , **(1992)**, "Optimization of Lamb wave inspection techniques", *NDT and E international*, vol. 25, pp. 11-22

Alleyne, D. N. and Cawley, P., (1994), "The practical excitation and measurement of Lamb waves using piezoelectric transducers", in *Annual review of progress in quantitative NDE*, edited by D. O. Thompson and D. E. Chimenti, Plenum Press, New York , pp. 181-188

Atkinson, D. and Hayward, G., (1999), "Embedded acoustic fibre waveguides for Lamb wave NDE", in *NDT '99 and UK Corrosion '99*, *Poole, England*, British Institute of Non-Destructive Testing , pp. 95-96

Auld, B. A., (1990), "Acoustic Fields and Waves in Solids", vol. 1, Krieger Publishing Company, Florida

Balasubramanyam, R., Quinney, D., Challis, R. E., and Todd, C. P. D., **(1996)**, "A finite-difference simulation of ultrasonic Lamb waves in metal sheets with experimental verification", *Journal of physics, D applied physics*, vol. 29, pp. 147-155

Beevers, A., (1995), "Forensic Studies Part 2: A forensic analysis study of adhesive bonded joints from a 30-year old bonded aircraft structure", Contract report, 7, Sept 1995, Oxford Brookes University, Oxford

Blake, R. J., (1988), "Numerical models of Rayleigh wave scattering from surface features", PhD thesis, Department of Dept of Electronic and Electrical Eng, University of London (University College), London

Breckenridge, F. R., Tschiegg, C. E., and Greenspan, M., **(1975)**, "Acoustic emission: some application of Lamb's problem", *Journal of the acoustical society of America*, vol. 57, pp. 626-631

Brekhovskikh, L. M., (1980), "Waves in layered media", Academic Press, New York

Briers, R., Leroy, O., and Shkerdin, G., **(1997)**, "A liquid wedge as generating technique for Lamb and Rayleigh waves", *J. Acoust. Soc. Am.*, vol. 102, pp. 2117-2124

Carlyle, J. M., **(1989)**, "Acoustic Emission Testing The F111", *NDT international*, vol. 22

Carpenter, S. H. and Gorman, M. R., **(1998)**, "A comparison of AE measurements from aluminoum alloys and glass/epoxy composites with different AE techniques", in *Annual review of progress in quantitative NDE*, edited by D. O. Thompson and D. E. Chimenti, vol. 17, pp. 509-516

Castaings, M. and Cawley, P., **(1996)**, "The generation, propagation, and detection of Lamb waves in plates using air-coupled ultrasonic transducers", *Journal of the acoustical society of America*, vol. 100, pp. 3070-3077

Castaings, M. and Hosten, B., **(1998)**, "The use of electrostatic, ultrasonic, air-coupled transducers to generate and receive Lamb waves in anisotropic, viscoelastic plates", *Ultrasonics*, vol. 36, pp. 361-365

Challis, R. E., Bork, U., and Todd, P. C. D. , **(1996)**, “Ultrasonic NDE of adhered T-joints using Lamb waves and intelligent signal processing”, *Ultrasonics*, vol. 34, pp. 455-459

Chang, Z., Guo, D., and Mal, A. K., **(1996)**, “Lamb Wave Propagation across a Lap Joint”, in *Annual review of progress in quantitative NDE*, edited by D. O. Thompson and D. E. Chimenti, Plenum Press , vol. 15, pp. 185-191

Cho, Y. and Rose, J. L. , **(1996)**, “A boundary element solution for a mode conversion study on the edge reflection of Lamb waves”, *Journal of the acoustical society of America*, vol. 99, pp. 2097-2109

Chopra, I. , **(1996)**, “Review of current status of smart structures and integrated systems”, *SPIE*, vol. 2717, pp. 20-62

Costley, R. D. and Berthelot, Y. H. , **(1992)**, “Laser generation of Rayleigh and Lamb waves for ultrasonic testing”, *Journal of the acoustical society of America* , vol. 92, pp. 2294

Culshaw, B., **(1996)**, “Smart structures activities worldwide”, *SPIE*, vol. 2717, pp. 3-17

Culshaw, B., **(1996),** “Smart structures and materials”, Artech House, Boston and London

Ditri, J. J., Pilarski, A., Rose, J. L., and Pavlakovic, B., **(1994)**, “Generation of guided waves in a plate by axisymmetric normal surface loading”, in *Annual review of progress in quantitative NDE*, edited by D. O. Thompson and D. E. Chimenti, Plenum Press, New York , vol. 12A, pp. 133-140

Drinkwater, B. W., **(1995),** “Use of dry coupling in ultrasonic non-destructive testing”, PhD thesis, Department of Mechanical Engineering, Imperial College of Science Technology and Medicine, London

ESDU, (1969), “ESDU 69023 average gust frequencies subsonic transport aircraft”, Sep 1969 (amended Mar 1989), ESDU (Engineering Science Data Unit) International Plc

Evans, M. J., (1997), “The use of diffuse field measurements of acoustic emission”, PhD thesis, Department of Mechanical Engineering, Imperial College of Science, Technology and Medicine, London

FAA, (1976), " Federal Aviation Administration - airframe handbook", 2nd ed, US Department of Transportation, Washington

Fowler, K. A. and Papadakis, E. P. , **(1972)**, "Observation and analysis of simulated ultrasonic acoustic emission wave in plates and complex structures", *American society for testing and materials (ASTM)*, vol. STP 505, pp. 222-237

Gachagan, A., Reynolds, P., Hayward, G., and McNab, A., **(1996)**, "Construction and evaluation of a new generation of flexible ultrasonic transducers", *IEEE Ultrasonics Symposium*, pp. 1-4

Georgiou, G. A., Lank, A. M., and Munns, I. J., (1994), "Mathematical modelling of ultrasound wave propagation in adhesively bonded joints", in *Annual review of progress in quantitative NDE*, edited by D. O. Thompson and D. E. Chimenti, Plenum Press, New York , vol. 13B, pp. 1515-1522

Ghandi, M. V. and Thompson, B. S., (1992), "Smart materials and structures", Chapman and Hall, London

Gorman, M. R. , **(1991)**, "Plate wave acoustic emission", *Journal of the acoustical society of America*, vol. 90, pp. 358-364

Graff, K. F., (1973), "Wave motion in elastic solids", Dover Publications inc., New York

Guillet, A., Kettani, M., and Luppe, F. , **(1999)**, "Guided waves' propagation in an elastic plate of linearly varying thickness", *Journal of the acoustical society of America* , vol. 105, pp. 1340

Guo, N., Lim, M. K., and Pialucha, T. , **(1995)**, "Measurement of attenuation using a normalized amplitude spectrum", *Journal of non-destructive evaluation*, vol. 14, pp. 9-19

Hagemaier, D. J. , **(1991)**, "Nondestructive testing developments in the aircraft industry", *Materials evaluation*, vol. 49, pp. 1470-1478

Hahn, S. L., (1996), "Hilbert transforms in signal processing", Artech House, London

Han, X., Fauro, L. D., Ouyang, Z., Wang, L., Wang, X., Zhang, F., Kuo, P. K., and Thomas, R. L., (1997), "Quantitative thermal wave imaging of corrosion on aircraft", in

Annual review of progress in quantitative NDE, edited by D. O. Thompson and D. E. Chimenti, vol. 116, pp. 353-364

Haskell, N. A., **(1953)**, "Dispersion of surface waves on multilayered media", *Bulletin of the American Seismological Society*, vol. 43, pp. 17-34

Hickman, G. A., Gerardi, J. J., Feng, Y., **(1991)**, "Application of smart structures to aircraft health monitoring", *Journal of intelligent material systems and structures*, vol. 2, pp. 411-430

Hitchings, D., (1995), "FE77 user manual", Internal Report, Imperial College, London

HMSO, (1955), "Civil aircraft accident - report of the court of enquiry into the accidents to Comet G-ALYP on 10th January 1954 and Comet G-ALYY on 8th April 1954", Her Majesty's Stationary Office, London

Hsu, N. N., (1976), "Acoustic emissions simulator", Patent No: 4018084, May 1976, Lockheed Aircraft Corp, United States

Hsu, N. N., Simmons, J. A., and Hardy, S. C., **(1977)**, "An approach to acoustic emission signal analysis - theory and experiment", *Materials evaluation*, pp. 100-106

Huang, J., Krishnaswamy, S., and Achenbach, J. D., **(1992)**, "Laser generation of narrow-band surface waves", *Journal of the acoustical society of America*, vol. 92, pp. 2527-2531

Hutchins, D. A., Lundgren, K., and Palmer, S. B., **(1989)**, "A laser study of transient Lamb waves in thin materials", *Journal of the acoustical society of America*, vol. 85, pp. 1441-1448

Jia, X., **(1997)**, "Modal analysis of Lamb wave generation in elastic plates by liquid wedge transducers", *Journal of the acoustical society of America*, vol. 101, pp. 834-842

Kino, G. S., (1987), "Acoustic waves: devices, imaging and analogue signal processing", Prentice-Hall Inc., New Jersey

Klein, M. B. and Bacher, G. D., **(1998)**, "Robust laser-based detection of Lamb waves using photo-emf sensors", *SPIE*, vol. 3399, pp. 12-17

Koshiba, M., Karakida, S., and Suzuki, M. , **(1984)**, "Finite-element analysis of Lamb wave scattering in an elastic plate waveguide", *IEEE transactions on sonics and ultrasonics*, vol. SU-31, pp. 18-25

Krautkramer, J. and Krautkramer, H., (1983), "Ultrasonic testing of materials", Springer-Verlag, Berlin, Heidelberg and New York

Kudva, J. N., Alper, J. M., and Paul, (1994), "Guidelines for Smart Structural Health Monitoring Systems For Military Aircraft - Lessons Learned From The SSCORE Contract", in *Smart Structures and Materials* , *Orlando*, edited by Sirkis, vol. 2191, pp. 210-215

Kudva, J. N., Marantidis, C., and Gentry, J. , **(1993)**, "Smart structures concepts for aircraft structural health monitoring", *Smart structures and intelligent systems SPIE* , vol. 1917, pp. 964-971

Lamb, H., (1917), "On waves in an elastic plate", in *Conference of the Royal Society* , *London*, vol. XCIII, pp. 114-128

Lowe, M. J. S. , **(1995)**, "Matrix techniques for modeling ultrasonic waves in multilayered media", *IEEE transactions on ultrasonics, ferroelectrics and frequency control*, vol. 42, pp. 525-542

Lowe, M. J. S., Chan, C. W., and Challis, R. E., (1999), "Estimation of bondline dimensions in adhered metal joints using ultrasonic Lamb waves: finite element studies of underlying physical phenomena", in *Annual review of progress in quantitative NDE* , edited by D. O. Thompson and D. E. Chimenti, vol. 18, pp. 1509-1516

Mal, A., Chang, Z., Guo, D., and Gorman, M. , **(1996)**, "Lap joint inspection using plate waves", *SPIE*, vol. 2945, pp. 128-137

Mal, A. K., Xu, P. C., and Bar-Cohen, Y. , **(1989)**, "Analysis of leaky Lamb waves in bonded plates", *International journal of engineering science*, vol. 27, pp. 779-791

Megson, T. H. G., (1990), "Aircraft structures for engineering students", 2nd ed, Edward Arnold, London

Monkhouse, R. S. C., Wilcox, P. D., and Cawley, P. , **(1997)**, "Flexible interdigital PVDF transducers for the generation of Lamb waves In structures", *Ultrasonics*, pp. 489-498

Morse, P. M., (1948), "Vibration and sound", 2nd ed, McGraw Hill, New York

NTSB, (1989), "NTSB\AAR-89/03", Aviation Accident Report, NTSB\AAR-89/03, National Transport Safety Board, Washington USA

Odell, J. H. , **(1991)**, "Monitored proof testing - a method of insuring structural integrity", *Air Clues*, pp. 416-419

Osborne, M. and Hart, S. , **(1945)**, "Transmission, reflection, and guiding of an exponential pulse by a steel plate in water 1. Theory", *Journal of the acoustical society of America*, vol. 17

Osborne, M. and Hart, S. , **(1946)**, "Transmission, reflection, and guiding of an exponential pulse by a steel plate in water 2. Experiment", *Journal of the acoustical society of America*, vol. 18

Papadakis, E. P., (1990), "The measurement of ultrasonic attenuation", Physical acoustics, vol. XIX, Academic Press, New York, pp. 107-155

Pavlakovic, B., Alleyne, D., Lowe, M., and Cawley, P., (1998), "Simulation of Lamb wave propagation using pure mode excitation", in *Annual review of progress in quantitative NDE*, edited by D. O. Thompson and D. E. Chimenti, vol. 17, pp. 1003-1010

Pavlakovic, B., Lowe, M., Alleyne, D., and Cawley, P., (1997), "Disperse : a general purpose program for creating dispersion curves", in *Annual review of progress in quantitative NDE*, edited by D. O. Thompson and D. E. Chimenti, Plenum Press, New York , vol. 16A, pp. 155-192

Pavlakovic, B. N., (1998), "Leaky guided ultrasonic waves in NDT", PhD thesis, Department of Mechanical Engineering, Imperial College of Science, Technology and Medicine, London

Pialucha, T., Guyott, C. C. H., and Cawley, P. , **(1989)**, "Amplitude spectrum method for the measurement of phase velocity", *Ultrasonics*, vol. 27, pp. 270-279

Pilarski, A., Rose, J. L., Ditri, J., Jiao, D., and Rajana, K., (1992), "Lamb wave mode selection for increased sensitivity to interfacial weaknesses of adhesive bonds", in *Annual review of progress in quantitative NDE*, edited by D. O. Thompson and D. E. Chimenti, Plenum Press, New York

Randall, R. B., (1987), "Frequency Analysis", Bruel and Kjaer

Rokhlin, S. and Bendec, F., **(1983)**, "Coupling of Lamb waves with the aperture between two elastic sheets", *Journal of the American ceramic society,* vol. 73

Rokhlin, S. I., **(1991)**, "Lamb wave interaction with lap-shear adhesive joints: theory and experiment", *Journal of the acoustical society of America,* vol. 89, pp. 2758-2765

Rose, J. L., (1995), "Recent advances In guided wave NDE", in *IEEE Ultrasonic Symposium, Seattle, USA*, pp. 761-770

Rose, J. L., Ditri, J. J., Gallela, D., and Grant, T., (1992), "Adhesive bond inspection utilizing ultrsonic Lamb waves", in *15th Annual meeting of the adhesion society*, *Hilton Head SC*, pp. 181-183

Scholte, J. G., **(1942)**, "On the Stoneley wave equation", *Proceedings of the Koninklijke Nederlandse Akademie Van Wetenschappen,* vol. 45, pp. 20-25, 159-164

Schubert, W., Gowan, J., and Rothwarf, F., (1997), "A portable TV-holography system for QNDE", in *Annual review of progress in quantitative NDE*, edited by D. O. Thompson and D. E. Chimenti, vol. 16, pp. 641-647

Searle, I. R., Ziola, S. M., and Rutherford, P. S., (1995), "Crack detection in lap-joints using acoustic emission", in *Smart structures and materials*, edited by W. B. Spillman, SPIE - The International Society for Optical Engineering, vol. 2444, pp. 212-223

Sessarego, J. P., Sageloli, J., and Gazanhes, C., **(1997)**, "Two Scholte-Stoneley waves on doubly fluid-loaded plates and shells", *Journal of the acoustical society of America*, vol. 101, pp. 135-142

Smith, C., D., **(1996)**, "Federal Aviation Administration aircraft inspection research and development program", *SPIE,* vol. 2945, pp. 200-209

Spencer, F. W., (1996), "Visual inspection reliability of transport aircraft", in *Non-destructive Evaluation of Aging Aircraft, Airports, and Aerospace Hardware*, *Scottsdale,* *Arizona*, edited by R. D. Rempt and A. L. Bronz, SPIE - The International Society for Optical Engineering , vol. 2945, pp. 161-171

Spillman, W. B., **(1996)**, "Sensing and processing for smart structures", *Proceedings of the IEEE,* vol. 84, pp. 68-77

Spillman, W. B. and Durkee, S. , **(1994)**, "Non-contact power/interrogation system for smart structures", *Smart structures and materials,* vol. 2191, pp. 362-372

Spillman, W. B. J., Sirkis, J. S., and Gardiner, P. T. , **(1996)**, "Smart materials and structures: what are they?", vol. 5, pp. 247-254

Sun, K. J., Johnston, P. H., (1992), "Mode conversions of Lamb waves for inspection of disbonds", in *IEEE Ultrasonics Symposium*, pp. 763-766

Sun, K. J., Johnston, P. H., (1993), "Feasibility of using Lamb waves for corrosion detection in layered aluminium aircraft structures", in *IEEE Ultrasonics Symposium*, pp. 733-736

Sun, K. J. and Johnston, P. H., (1993), "Disbond detection in bonded aluminum joints using Lamb wave amplitude and time-of-flight", in *Annual review of progress in quantitative NDE*, edited by D. O. Thompson and D. E. Chimenti, vol. 12, pp. 1507

Sun, k. J. and Johnston, P. H., (1995), "Effect of rivet rows on propagation of Lamb waves in mechanically fastened two-layer aluminum plates", in *Annual review of progress in quantitative NDE,* edited by D. O. Thompson and D. E. Chimenti, vol. 14, pp. 1569-1575

Thomson, W. T. , **(1950)**, "Transmission of elastic waves through a stratified solid medium", *Journal of applied physics,* vol. 21, pp. 89-93

Torvik, J. P., **(1967)**, "Reflection of wave trains in semi-infinite plates", *Journal of the Acoustic Society of America,* vol. 41, pp. 346-353

Victorov, I. A., (1970), "Rayleigh and Lamb Waves", Plenum Press, New York

Viktorov, I., **(1965)**, "Ultrasonic Lamb waves (review)", *Soviet Physics - Acoustics*, vol. 11, pp. 1-14

Weaver, R. L. and Pao, Y.-H., **(1982)**, "Axisymmetric elastic waves excited by a point source in a plate", *Journal of applied mechanics*, vol. 49, pp. 821-836/699-700

Whiteley, S., Girma, D., Hayward, G., and Smith, D. G., (1999), "A Novel Wireless Sensor for Wireless NDE", in *NDT '99 and UK Corrosion '99*, *Poole, England*, British Instiute of Non-Destructive Testing , pp. 349-350

Wilcox, P. D., (1998), "Lamb wave inspection of large structures using permanently attached transducers", PhD thesis, Department of Mechanical Engineering, Imperial College of Science, Technology and Medicine, London

Williams, R. V., (1980), "Acoustic emission", Adam Hilger, Bristol

Worlton, D. C., **(1957)**, "Ultrasonic testing with Lamb waves", *Non-destructive Testing*, vol. 15, pp. 218-222

Zhu, Z. and Wu, J., **(1995)**, "The propagation of Lamb waves in a plate bordered with a viscous liquid", *Journal of the acoustical society of America*, vol. 98, pp. 1057-1064